Dissertation
submitted to the
Combined Faculty of Mathematics, Engineering and Natural Sciences
of Heidelberg University, Germany
for the degree of
Doctor of Natural Sciences

Put forward by
Martin, Richter
born in: Heidelberg
Oral examination: 18.12.2024

Ultrafast Dynamics of Optically Excited States in Organic Semiconductors

Referees: Prof. Dr. Rüdiger Klingeler
Prof. Dr. Petra Tegeder

Abstract

Excited state dynamics of organic materials were studied using time-resolved spectroscopic techniques. The processes involved, such as charge separation (CS), charge recombination (CR) and singlet fission (SF) play a key role in developing and improving organic electronics such as light-harvesting devices. To study the impact of the relative orientation of organic chromophores on singlet fission (SF), substituted pentacene (PEN) was used as linker in a surface-anchored metal-organic framework (SURMOF). This allowed to arrange the PEN molecules in a slip-stacked configuration. It was found, that the SF dynamics were altered appreciably. The SF rate was slowed down by almost two orders of magnitude and the triplet life time was increased by more than three orders of magnitude. Furthermore, CS and CR dynamics were investigated in a porphyrin-based SURMOF, incorporating C_{60} in the pores. The CS occurred via a direct pathway without the population of the porphyrin triplet state. The CS was found to be very fast with a time constant of $\sim$300 fs and the CR took place with time constants between 200 and 400 ps. CS and SF were further investigated in bilayers of PEN with strong acceptors. In the ground state, formation of ion-pairs as well as the formation of charge transfer complexes were observed. The SF dynamics in PEN were only marginally slowed down to 158-222 fs. Within a few dozens of picoseconds, CS at the interface between PEN and the acceptor layer was identified by observation of a shift in optical absorption due to the Stark effect. Lastly, second-order non-linear optical properties of chiral cage compounds were investigated. Second-harmonic generation rotatory dispersion experiments reveal a rotation over 20°. The explanation of the data obtained regarding the interaction with circularly polarised light required magnetic dipole contributions.

Zusammenfassung

Die Dynamik angeregter Zustände organischer Materialien wurde mit zeitaufgelösten spektroskopischen Methoden untersucht. Die beteiligten Prozesse wie Ladungstrennung, Ladungsre kombination und Singulett-Spaltung (engl.: SF) spielen eine Schlüsselrolle bei der Entwicklung und Verbesserung organischer Elektronik, z.B. von Solarzellen. Um die Auswirkungen der relativen Ausrichtung organischer Chromophore auf den SF Prozess zu untersuchen, wurde substituiertes Pentacen (PEN) als Linker in einem oberflächenverankerten metallorganischen Gerüst (engl.: SURMOF) verwendet. Dies ermöglichte die Anordnung der Pentacenmoleküle in einer parallel, versetzten Orientierung. Es wurde festgestellt, dass dies die SF-Dynamik maßgeblich beeinflusst. Die SF-Rate wurde um fast zwei Größenordnungen verlangsamt, während die Triplett-Lebensdauer um mehr als drei Größenordnungen zunahm. Weiterhin wurde die Dynamik der Ladungstrennung und der Rekombination in einem Porphyrin-basierten SURMOF untersucht, wobei der Akzeptor C_{60} in die Poren eingeschlossen wurde. Die Ladungstrennung erfolgt über einen direkten Weg ohne Beteiligung des Porphyrin-Triplettzustands. Es wurde eine schnelle Ladungstrennung mit einer Zeitkonstante von $\sim$300 fs gefunden. Die Ladungsrekombination findet mit Zeitkonstanten zwischen 200 und 400 ps statt. Des Weiteren wurden Ladungstrennung und SF in Bilagen aus PEN mit starken Akzeptoren untersucht. Im Grundzustand wurden sowohl die Bildung von Ionenpaaren als auch von Ladungstransferkomplexen beobachtet. Die SF Zeitkonstante in PEN wurde nur geringfügig auf 158-222 fs verlangsamt. Innerhalb einiger Dutzend Pikosekunden wurde die Ladungstrennung an der Grenzfläche zwischen PEN und der Akzeptorschicht beobachtet, was durch eine Verschiebung der optischen Absorption aufgrund des Stark-Effekts identifiziert werden konnte. Ferner wurden die nichtlinearen optischen Eigenschaften zweiter Ordnung chiraler Käfigverbindungen untersucht. Experimente zur rotatorischen Dispersion zeigten eine Rotation von mehr als 20°. Die Erklärung der erhaltenen Daten bzgl. der Interaktion mit zirkular polarisiertem Licht erforderte die Beteiligung von magnetischen Dipolbeiträgen.

Contents

1 Acronyms

AFM	atomic force microscope
B3LYP	Becke, 3-parameter, Lee-Yang-Parr
CB	conduction band
COM	center of mass
CR	charge recombination
CS	charge separation
CT	charge transfer
CTC	charge transfer complex
cw	continuous-wave
DADS	decay associated difference spectra
DFG	difference frequency generation
DFT	density functional theory
EADS	evolution associated difference spectra
EA	electro absorption
$\mathbf{E_{EA}}$	electron affinity
ET	electron transfer
ESA	excited state absorption
F4-TCNQ	2,3,5,6-tetrafluoro-7,7,8,8-tetracyanoquinodimethane
F6-TCQNNQ	2,2′-(perfluoronaphthalene-2,6-diylidene)-dimalononitrile
FTIR	Fourier transform infra-red spectroscopy
FWHM	full width at half maximum
GA	global analysis
GIWAXS	grazing incident wide-angle X-ray scattering
GSB	ground state bleach
HOMO	highest occupied molecular orbital
HWP	half wave plate
IC	internal conversion
ICT	integer charge transfer
IE	ionisation energy
IP	ionisation potential
IRF	instrument response function
ISC	inter system crossing
IVR	internal vibrational relaxation
LUMO	lowest unoccupied molecular orbital
MOF	metal-organic framework
Nd:YAG	neodymium-doped yttrium aluminum garnet
NIR	near infra-red (spectral range)
OLED	organic light emitting diode
OFET	organic field-effect transistor
OPA	optical parametric amplifier
OPV	organic photovoltaics

OSC	organic semiconductor
PEN	pentacene
PIA	photo-induced absorption
QWP	quarter wave plate
RegA	regenerative amplifier
SAM	self-assembled monolayers
SE	stimulated emission
SF	singlet fission
SFG	sum frequency generation
SHG	second harmonic generation
SHG-CD	SHG circular dichroism
SHG-ORD	SHG optical rotatory dispersion
SURMOF	surface anchored metal-organic framework
TA	transient absorption
TD-DFT	time dependent DFT
TQY	triplet quantum yield
TR	time resolved
TTA	triplet-triplet annihilation
UV	ultraviolet (spectral range)
VB	valence band
VIS	visible (spectral range)
VR	vibrational relaxation
XRD	X-ray diffraction
ZnTPP	(5,15-bis-(3,4,5-trimethoxyphenyl)-10,20-bis-(4-carboxyphenyl) porphyrinato zinc(II))

2 Introduction

The research in organic semiconductors (OSC) has made great advances in the last few decades. Since the 21st century, organic electronic devices have found their way into our daily lives. The first commercial use was by organic light-emitting diodes (OLED) in 2002 for a display panel [1] and the first working OLED was already produced in 1987 by Tang and Slyke [2].

Today OSCs are used in OLEDs for displays, and solar cells and organic field effect transistors (OFET) are on their best way to commercialisation. There is such a great interest in OSC as they promise a variety of outstanding benefits, such as mechanical flexibility, printable and low-cost electronics [3]. As the functionality of the materials can be adjusted by chemical modification, they open up a huge space of applications. Moreover, many OSC materials exhibit better bio-compatibility for utilisation in life, health and bio-sciences [4].

A field that is today more pressing than ever is the design of efficient light harvesting systems. Organic photovoltaics (OPV) have been improved immensely and single junction solar cells surpass power conversion efficiencies of 20% [5]. In comparison to that the best performing silicon based solar cell has a conversion efficiency of 26.7% [6]. Of course, transferring the results for OPVs away from laboratory conditions is still challenging. The large scaled fabrication and lifetime of the devices need to be improved further. For the systems there exists a theoretical maximum: the Shockley-Queisser limit [7]. It depends on the band-gap and for silicon it amounts to $\sim 33\%$ [7]. The underlying argument for the existence of such a limit is easily understood. Any photon with lower energy than the band-gap does not get absorbed and photons with higher energy lead to thermal losses while the created excitons relax to the conductance band edge.

An interesting mechanism that can improve the efficiency of OPV systems is called singlet fission (SF). In this process, a high-energy singlet exciton is converted into two lower-energy excitons. These states with lower energy are triplets that are spin coupled to have an overall spin multiplicity of $m = 1$, i.e. the coupled state is still a singlet state. Thus this process is spin allowed and can be very fast. For pentacene which is a model system to study SF and also studied in this thesis, SF can be on a time scale of 100fs. The benefit from that process is, that it creates two excitons and hence potentially four charge carriers. Combining it in an energetically suitable alignment with the semiconductor of a solar cell can reduce thermal losses drastically, with a theoretical limit of 44% [8]. Although the fields of application for organic and inorganic semiconductor materials coincide in many cases there are essential differences in the basic working principles.

OSC materials can be divided into polymers and small-molecule OSCs. Both have in common, that their conductivity results from delocalised electrons arising from bond conjugation in the chemical structure, which describes alternating single and double bonds between carbon atoms [4]. Through hybridisation molecular orbitals (σ and π) form, and the system of alternating bonds is called π-conjugated system.

Moreover, OSCs often exhibit less order than the crystalline inorganic semiconductors. This is due to the type of interactions in the material. The intramolecular forces are strong, as these are covalent bonds, but the relative order of the molecules is mostly determined

by weak van der Waals interactions. This greatly impacts the optical and especially their electronic properties. Inorganic semiconductors exhibit a conduction and valence band with a clearly defined band gap. Organic semiconductors show discrete molecular energy levels since the weak interactions do not allow for a wide electronic delocalisation. The difference between the highest occupied molecular orbital (HOMO) and the lowest unoccupied molecular orbital (LUMO) serves as an analogue to the band gap. Overcoming this energy barrier creates electron-hole pairs called excitons. Regarding the case of OSCs, excitons have greater binding energy due to a low dielectric constant and the electron and hole are located on the same molecules. After exciton dissociation, as a first step to charge separation, the electron-hole pair resides on neighbouring molecules, which is called a charge transfer (CT) exciton. The separation of electron-hole pairs into free charge carriers is an intensively studied field, especially due to its relevance for OPV performance. To study the underlying mechanisms, time-resolved spectroscopic techniques such as transient absorption (TA) and second harmonic generation (SHG) are employed. This allows for the observation of exciton dynamics from the microsecond down to the femtosecond time scale.

The subject of this thesis is to investigate the exciton dynamics, charge separation and SF in small-molecule semiconducting materials. As pointed out, aside from the chemical structure, the relative molecular arrangement has a striking impact on many properties. One aspect covered, is molecules that are integrated in a well defined structure. This is achieved with surface anchored metal-organic frameworks (SURMOF). These systems provide a grid-like structure of metal atoms that are connected with functionalised organic linkers. With this approach highly structured systems are produced and the impact of the geometry on the excited state dynamics can be studied. This includes dynamics of charge separation as well as SF dynamics that have been significantly altered in the SURMOF structure compared to their native thin film structure. Specifically, SURMOFs using pentacene as the organic linker were found to yield an exceptional prolonging of triplet exciton lifetime. The SF process is slowed down in turn, but only marginally. A second system used a porphyrin based linker in the SURMOF, while the pores could be packed with fullerene (C_{60}). The charge separation and recombination dynamics could be analysed. Another aspect of optimizing OSC materials is doping. For inorganic semiconductors this is a well established process that is understood theoretically and the experimental methods to dope conventional materials like silicon or gallium arsenide are optimized to a high degree. In organic semiconductors introducing electron donors and acceptors is not only used to alter the charge carrier concentration, but it is essential for charge separation, as the excitons are stronger bound in OSCs. It is also called molecular doping as the dopants are organic molecules. In some cases unexpectedly high concentrations were needed for effective doping, which was explained by the generation of charge transfer complexes (CTC). A CTC is a new molecular electronic state that arise from hybridisation of molecular orbitals. CTCs do not increases the charge carrier density directly, but the energy gap of the newly hybridised orbitals is smaller. The CTC can be ionized more easily to yield charge carriers in the OSC [9]. Pentacene together with the acceptor F4-TCNQ is a system believed to be at the border of creating ion-pairs or CTCs. This system was revisited by studying blends of this donor/acceptor system [10]. Here, this investigation was extended by examining the properties in bilayers of F4-TCNQ and a

stronger acceptor F6-TCNNQ with PEN. The fs-TA the SF dynamics could be characterised, as well as the CS in the PEN/F4-TCNQ bilayers. The charges create a static electric field at the interface that induce a shift if the optical absorption that is identified in the TA spectra.

A topic which certainly has not reached public attention (yet), are the non-linear properties of organic molecules. Due to their electronic structure, the optical properties often have greater non-linear contributions than inorganic solids [11]. Possible applications include optical gates for computing, two-photon absorption for 3D-printing or optical limiting [11, 12, 13]. Laser systems producing beams with high intensity electric fields are necessary to go beyond the linear regime and probe the materials. Here, the existing setup for SHG was extended to investigate the non-linear response of chiral molecules. The SHG analogue to optical rotatory dispersion (SHG-ORD) yielded a rotation of linear polarised light by an angle $(24.15 \pm 0.15)^\circ$ and $(-22.43 \pm 0.31)^\circ$ for the different enantiomers, with respect to the fundamental beam. By studying the interaction of chiral molecules with circular and elliptically polarised light, it is possible the draw conclusions about the second-order susceptibilities of the material. It could be demonstrated that magnetic-dipole interactions need to be assumed to fit the data.

Outline The fundamental principles to describe organic molecular systems are treated in chapter 3. This is followed by the theoretical background to understand the experimental techniques with a focus on transient absorption and second harmonic generation. The experimental setups are described and characterised in chapter 4. The results are discussed starting with the description of SF dynamics in a pentacene based SURMOF in chapter 5. The systems is further investigated by theory including steady state as well as time dependent calculations based on density functional theory (DFT). Chapter 6 starts with an introduction to the broad field of porphyrin and fulleren based systems. Subsequently, TA measurements are presented and the charge separation dynamics are discussed. Chapter 7 revisits the systems pentacene with dopants F4-TCNQ and F6-TCNNQ with a focus on the bilayer structure to elucidate the formation of CT complexes or ion pair formation. In Chapter 8 the extension to the laboratory setup for non-linear optics is presented with first results on chiral cage compounds. Finally, chapter 9 gives a summary of the work presented in this thesis.

3 Theoretical Background

This chapter covers fundamentals of the electronic structure of organic molecules and solids. Furthermore, processes in organic semiconductor materials, especially after optical excitation are discussed in section 3.1.1. The process of singlet fission is the subject of a separate paragraph. The theoretical basis for the experimental methods of transient absorption and SHG are explained in section 3.3.1 and 3.3.2.

3.1 Organic semiconductors

Organic molecules are based on carbon. This usually includes compounds with the elements hydrogen, oxygen, nitrogen, sulphur and halogens. Why some organic compounds have a high electrical conductivity and how this can be specifically increased has once again become the focus of scientific attention in recent decades and continues to be the subject of current research. We want to recapitulate how molecular bonds can be described. The bond between atoms in molecules can be described using the molecular orbital (MO) theory. MOs are represented by linear combinations of suitable basis functions. A good choice can be, for example, the unperturbed atomic orbitals (AO). This approach describes the LCAO theory (Linear Combination of Atomic Orbitals) [14, 15].

A schematic representation of these linear combinations of AOs and the resulting MOs is shown in Fig.3.1 a) to c). A distinction is made between σ-type MOs and π-type orbitals. From Fig.3.1 a) and b) one could conclude that σ MOs are formed from s AOs and π MOs from p AOs. However, the decisive factor is that σ-type MOs have a rotational symmetry with respect to the connecting axis of the molecules. In contrast, π-type MOs consist of a combination of AOs that are perpendicular to this molecular axis or at least have a node in a plane that contains the molecular axis. This means that the π-type MO also has an electron density that is lateral to the axis. Most π-type MOs are based on p and d orbitals. As shown in Fig.3.1 c), a σ bond is also formed by a linear combination of hybridised AOs, here e.g. from sp^n, which in turn are a linear combination of the unperturbed AOs. For both types of bonds, there is an antibonding orbital σ^* or π^* and a bonding orbital σ or π. Under simplifying assumptions, the energy of the orbitals can be estimated by:

$$E_{s,a} = \frac{H_{aa} \pm H_{ab}}{1 \pm S} \tag{1}$$

Here, $S = \int \phi_a^* \phi_b dV$ is the overlap integral of the AOs $\phi_{a,b}$ of atom a and b, $H_{aa} = \int \phi_a^* H \phi_a$ and $H_{ab} = \int \phi_a^* H \phi_b$ is the exchange integral [15].

It can be seen that the amount of decrease in the energy of the binding orbital is equal to the gain in energy of the antibonding orbital if the overlap integral is small $S << 1$. As p orbitals of two atoms tend to have a smaller overlap, it should also be apparent that the energy splitting of σ MOs is greater than of π MOs, as illustrated in Fig.3.1. The arrows in the figures indicate the spins of the electrons that occupy the orbitals. Occupation of binding σ or π MOs lead to a lower total energy compared to occupying the individual AOs. This bond is therefore stabilising, meaning that molecule formation is favoured in principle.

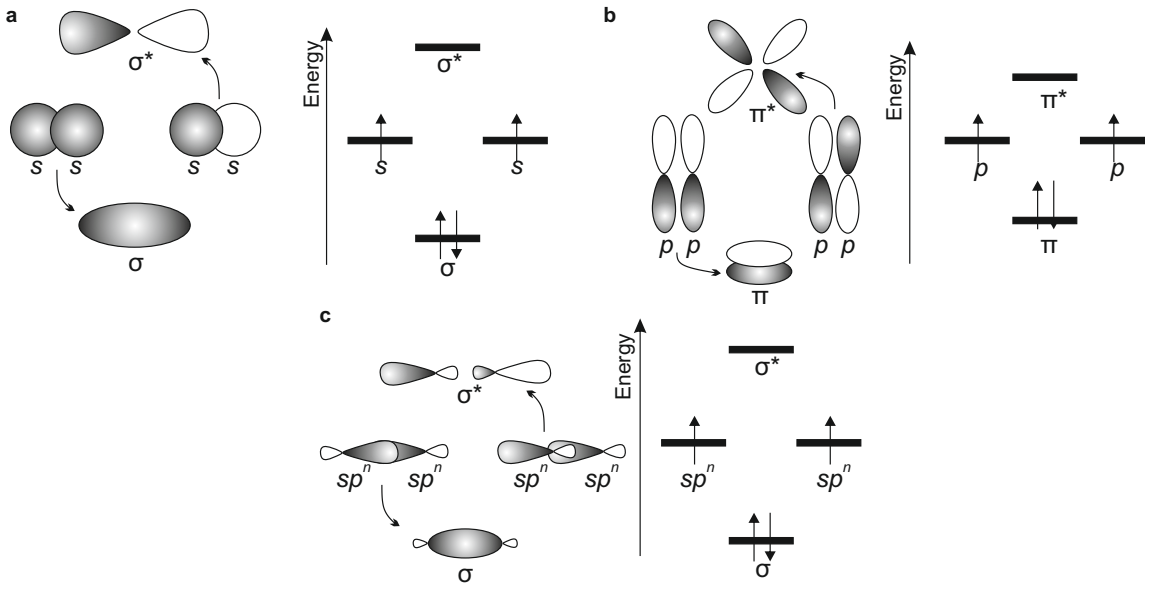

Figure 3.1: Hybridisation to form bonding and antibonding **a** σ-orbitals from atomic s-orbitals, **b** π-orbitals from atomic p-orbitals and **c** σ-orbitals from hybridised sp^n-orbitals [16].

In the next step, we want to see how the electronic structure of a solid consisting of organic molecules can be described. Fig.3.2 illustrates the successive build-up of structure, starting with one molecule. According to the frontier molecular orbital theory [17], the so-called frontier orbitals are the most important to describe intermolecular interactions. These are the highest occupied molecular orbital (HOMO) and the lowest unoccupied molecular orbital (LUMO). The lower energies (core level) belong to orbitals that can be represented by AOs, since high inter atomic potentials do not allow the formation of MOs. Fig.3.2 b) and c) show the formation of energy bands (HOMO/LUMO band) through intermolecular interaction. In the case of strong interactions, the bands can increase in width ($> 0.2\,\mathrm{eV}$) and, as in solid-state physics, are referred to as valence (VB) and conduction bands (CB). The atoms form covalent bonds within the molecules, but the weak intermolecular - mostly Van der Waals interaction - is not sufficient to form broad bands. Furthermore, in organic materials, the degree of crystallinity is often lowered by structural imperfections or mixing with amorphous regions. Then, the electronic structure remains similar to that of the molecule and HOMO and LUMO levels are of interest instead of VB and CB. For charge transport this means that the band model can only be applied to a limited extent and other theories must be used instead, such as the hopping mechanism [18, 19]. Here, the reorganisation energy is an important parameter that describes the energy difference that the molecule experiences during charge transfer. This energy difference is due to the conformational change of the molecule [19, 20].

Before the charges are transported, they must be generated. In inorganic semiconductors such as silicon, for example, a Wannier-Mott exciton is created by the incidence of light. An

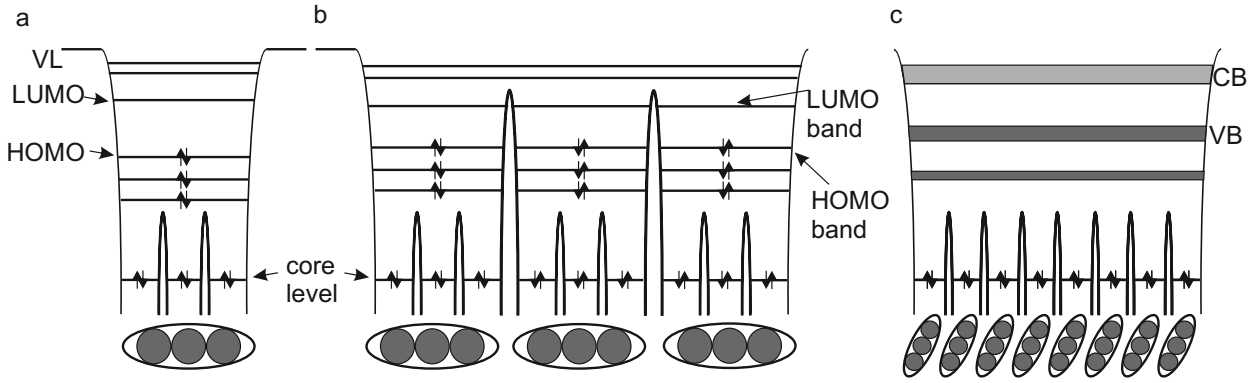

Figure 3.2: Electronic structure of **a** a single molecule and a solid with weak **b** and strong **c** intermolecular interaction. Vl: vacuum level, VB: valence band, CB: conduction band [3].

exciton describes a bound electron-hole pair. Excitons can be categorised depending on their binding energy and localisation [4, 21, 22]:

1. **Wannier-Mott exciton**: The electron-hole pair is only weakly bound, since the electrical permittivity ϵ is high in inorganic semiconductors and the associated Coulomb force $F \sim 1/\epsilon$ between electron and hole is low (charge screening). Typically, the binding energy is of the order of $E_B \sim 0.01\,\mathrm{eV}$, so that the thermal energy at room temperature $E_{th} \sim 0.025\,\mathrm{eV}$ is sufficient to separate electron and hole. Wannier-Mott excitons are more strongly delocalised (e-h distance 10 nm for $E_B = 4\,\mathrm{meV}$ in germanium), which means that the electron and hole are usually not on the same lattice site.

2. **Frenkel exciton**: The electron-hole pair is strongly bound with $E_B \sim 1\,\mathrm{eV}$ or greater and accordingly strongly localised. In molecular solids, the Frenkel excitons are often localised on the same molecule. They can be easily identified with optical absorption measurements, as they differ greatly in energy from the transition between VB and LB.

3. **Chrage transfer (CT) exciton**: CT excitons have a binding energy between Frenkel and Wannier-Mott excitons. The electron-hole pair is located on neighbouring molecules. They play a special role in organic electronics and often occur at interfaces between organic semiconductors. They are often referred to as charge transfer states. CT states are usually not observed in optical spectra as their absorption is weak and their energy is close to the $S_0 \rightarrow S_n$ transition [23].

As previously mentioned, in inorganic semiconductors, the energy at room temperature is sufficient to separate Wannier-Mott excitons and generate free electrons and holes, which can then migrate to electrodes. This is not the case with the binding energies of Frenkel and CT excitons and a further driving force is required to separate the charges. This is achieved with a donor-acceptor structure, with suitable energy levels of the frontier orbitals, as shown in Fig.3.3 a). Here, an electron is transferred from the LUMO of the donor (D) to the LUMO of

the acceptor (A). The transfer is driven by the energy difference ΔE between D-LUMO and A-LUMO as described in the Marcus theory [19, 20]. The dissociation at the D/A interface appears to be analogous to the p-n transition in inorganic semiconductors, as shown in Fig.3.3 c). However, the D/A interface is usually mandatory to cause charge separation at all, which occurs in inorganic semiconductors even without the p-n junction. However, the p-n junction is important to avoid charge recombination. In both cases, therefore, only the boundary layer is significantly involved in charge carrier generation. Moreover, it is important that electron transfer takes place faster than competing processes.

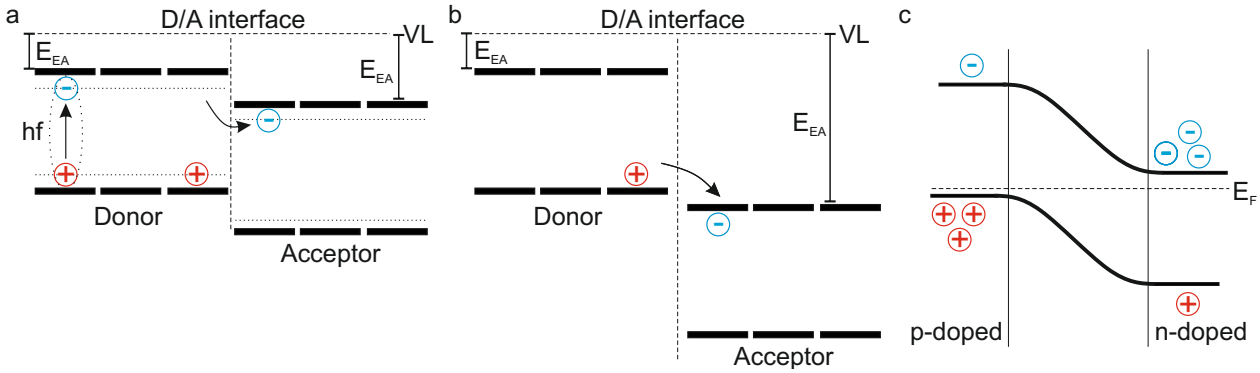

Figure 3.3: Illustration of **a,b** a donor/acceptor interface with different electron affinities (E_{EA}). p-n junction of a doped inorganic semiconductor. E_F: Fermi-level [21, 24]

3.1.1 Excited state dynamics

This section provides an overview of the processes that can occur after the absorption of a photon in addition to charge carrier generation. This is usually illustrated in Jablonski diagrams (after Aleksander Jabłoński) as shown in Fig.3.4. Here, the vertical solid lines describe the absorption or emission of a photon. The Born-Oppenheimer (BO) approximation is used to describe these processes theoretically. This involves the assumption that, due to the large mass difference between atomic nuclei and electrons, their state functions can be separated [15]. The BO approximation forms the basis for the Franck-Condon principle, according to which the transition probability from the initial state $\langle\psi|$ to the final state $|\psi'\rangle$ is calculated from

$$P(\psi \to \psi') = \int \psi_e'^* \mu_e \psi_e d\vec{r}_e \int \psi_v'^* \psi_v d\vec{r}_n \int \psi_s'^* \psi_s d\vec{r}_s \tag{2}$$

The indices e, n, s show that the functions depend on electronic, atomic or spin coordinates and μ_e is the sum of the electronic dipole contributions. From this, basic rules for radiative transitions can be derived. Transitions that follow these rules are called dipole allowed. Other selection rules apply to quadrupole transitions that can play a role at higher light intensities, e.g. in SHG experiments [25].

The first factor is the transition dipole moment and describes the transition of the electronic states. In addition to a spatial overlap of the functions ψ_e and ψ'_e, they must have different parity, since μ_e has negative parity, i.e. behaves like $\mu_e \rightarrow -\mu_e$ under the spatial reflection $\vec{r} \rightarrow -\vec{r}$. Otherwise the integral will vanish.

The second term describes the overlap of the vibrational states. Usually, molecules in the electronic ground state are also in the lowest vibrational state, since the energy differences between vibrational states are of the order of 100-400 meV, i.e. they are not excited by the thermal energy at room temperature. Assuming that the atomic nuclei do not change their coordinates during the radiative transition (BO approximation), transitions to higher vibrational states $0 \rightarrow n$ (e.g $n = 1, 2, 3$) are usually more likely than $0 \rightarrow 0$.

The third term provides the spin selection rules under the dipole approximation. According to this, only transitions without changing the spin $\Delta S = 0$ can take place. This means that absorptions from the ground state lead almost exclusively to higher singlet states. Similarly, *fluorescence* is the spin-allowed radiative transition back to the ground state from higher singlet states. This occurs within approx. 10^{-9} to 10^{-6}s. The fact that the spin selection rule can be violated is observed by *phosphorescence*, which describes the radiative transition from triplet states $T_1 \rightarrow S_0$ to the singlet ground state. Since this transition is dipole forbidden, it happens on long time scales, typically 10^{-4} to 20 s [22].

After absorption into higher excited states S_n ($n > 1$), a radiationless transition to the state S_1 usually follows within picoseconds. This entails transferring energy to vibrations, which ultimately means heat is produced. This process is called *internal conversion* (IC). The spin state is not affected in this process. A transition between the spin manifolds is called *intersystem crossing* (ISC). ISC is based on the spin-orbit coupling, i.e. interaction of the electron spin with the magnetic field generated by the current of the electron around the nucleus. This increases with the nuclear charge number, consequently the ISC rate increases with the atomic number. This can be observed well in porphyrins with and without a central metal atom, for example. In the case of tetraphenylporphyrin, the ISC rate increases from 1/12ns to 1/2ns [26, 27].

In addition to intramolecular processes, interactions with other molecules are possible as well. Triplet-triplet annihilation (TTA) should be mentioned here in particular. This process can be described by the reaction mechanisms $T_1 + T_1 \rightarrow S_0 + T_n$ with subsequent IC to T_1 and $T_1 + T_1 \rightarrow S_0 + S_n$ with subsequent IC to S_1. In both cases, this leads to a reduction in the number of excitons in the T_1 state. The TTA can be described by

$$\frac{\mathrm{d}[T_1]}{\mathrm{dt}} = -k_T[T_1] - \gamma[T_1]^2, \tag{3}$$

where k_T is the rate of mono-molecular decay and γ describes the bi-molecular annihilation process. This non-linear relationship makes it possible to draw conclusions about this process in experiments with different excitation densities. In addition, the so-called *delayed fluorescence* can be observed, which can be attributed to the fluorescence of the resulting singlet after TTA. Similarly, singlet-singlet annihilation (SSA) involves the fusion of two singlet excitons $S_1 + S_1 \rightarrow S_0 + S_n$, which also leads to reduced fluorescence.

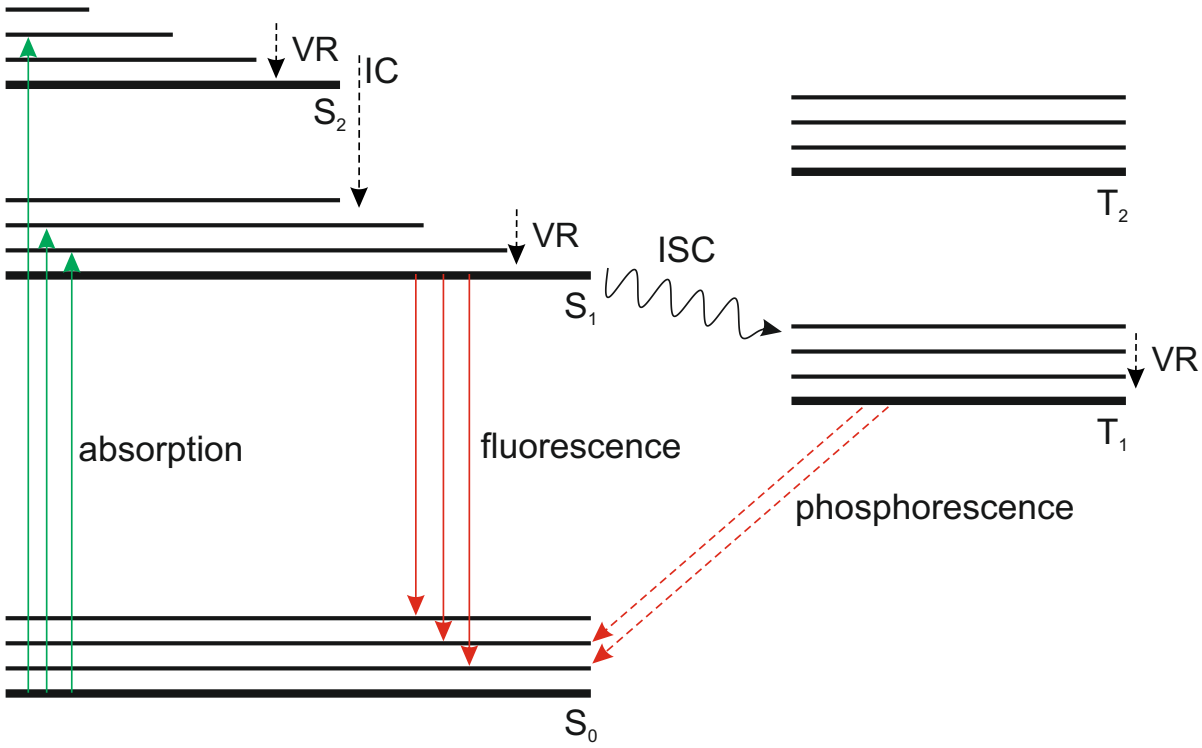

Figure 3.4: Jablonski Diagram depicting possible electronic states and transitions between them. VR: vibrational relaxation, IC: internal conversion, ISC: intersystem crossing [21].

Singlet Fission Since SF is an integral part in the systems investigated, a more in depth view is presented here. An overview of the mechanism will be given and the principle ideas for implementation in solar cell devices to enhance the efficiency will be discussed. As this is however and extensive and active field of research, further literature is given for a comprehensive picture [28, 29, 30, 31, 32, 33, 34, 35, 36, 37, 38, 39].

SF describes the process where a singlet exciton is converted into two lower-energy triplet excitons. In contrast to ISC discussed before, this is not a spin forbidden transition, since an excited pair of spin-correlated triplets is created that have an overall spin multiplicity of $m = 1$. Therefore SF can be much faster than ISC. For the mechanism the following criteria are crucial: (1) energy level matching at the single molecular level: $E_{S_1} \geq 2E_{T_1}$ and $E_{T_2} \geq 2E_{T_1}$ [40], which ensures that the splitting of a singlet excitation into two triplets is thermodynamically feasible, while triplet-triplet annihilation (TTA) is not; (2) strong electronic coupling [37] and (3) the spin-correlated triplet pair $^1(\mathrm{T_1T_1})$ should efficiently separate into two independent triplets $\mathrm{T_1}$.

The energetic criterion is not strict in the sense that exothermic and endothermic SF exist as well, where energy ΔE is given to or taken from the evironment. The energy differences range between $\Delta E \sim \pm 300\,\mathrm{meV}$. Exothermic SF is substantially faster because it does not need to get thermally activated, however energy is lost that would contribute to the

device efficieny. Prototypical examples for exothermic and endothermic SF are pentacene and tetracene with SF rate constants of $\sim 100\,\mathrm{fs}$ ($\Delta E = -110\,\mathrm{meV}$) and $\sim 145\,\mathrm{ps}$ ($\Delta E = +188\,\mathrm{meV}$), respectively [41, 42, 43].

The most common and agreed on description for pentacene to date is as follows [32, 44, 45]:

$$(S_0S_1) \xrightarrow{(1)} {}^1(T_1T_1) \xrightarrow{(2)} {}^1(T_1 \cdots T_1) \xrightarrow{(3)} 2T_1, \tag{4}$$

Here, $^{\mathrm{m}}$(TT) specifies triplets on adjacent chromophores both in an excited triplet state. The four electrons involved in this picture spin-couple to have a multiplicity of $m = 1, 3$ or 5. The spin-coupled state must retain spin multiplicity m=1 initial to the generation of the triplet pair to ensure conservation of angular momentum. (S_0S_1) indicates a singlet excitation on one of the two chromophores, $^1(T_1 \cdots T_1)$ describes a spin-coupled triplet pair that is spatially separated and has lost electronic coherence, and $2T_1$ are two uncoupled triplet excitons. The rate of the first step – the triplet-pair generation – is extremely fast with 70-100 fs in PEN thin films [41]. The second and third steps are more elusive and an unambiguous assignment of kinetic rates is difficult. Some studies report the rate of the second step on the ps-ns time scale for PEN derivatives [44, 46]. Spatially separated triplet excitons have been reported to give a different photo-induced absorption (PIA) [44, 47]. In the end two uncorrelated triplets are created. The overall lifetime of the triplets in PEN thin films is more well-founded with a few nanoseconds [48].

The first step that creates the coupled triplet ^{1}(TT) is studied extensively both experimentally and theoretically. The general assumption is, that there are three possible pathways as shown in Fig.3.5. A charge transfer (CT) state can participate in a direct or indirect manner and a direct transition can take place.

The direct mechanism is determined by the coupling of the ^{1}(TT) and the S_1S_0 states, which tends to be small [39]. Therefore, it is most often the case in competitive SF, that a CT state is involved. If the energy is of the CT state is higher than that of S_1S_0, the CT state can interact as virtual state via the so-called super-exchange mechanism, which can accelerate the reaction. If the energy is lower than S_1S_0, CT states can act as real intermediates. This would in include an electron transfer to form the CT state and a back electron transfer to form ^{1}(TT). In contrast, it is also possible that strongly stabilized CT states may interfere as trap states and inhibit ^{1}(TT) formation [49].

There is emerging consensus on the mediated mechanism with a varying degree of CT character [35, 49].

Recent publications indicate that prior to the emergence of free triplets, quintet states ^{5}(TT) are populated [33, 50, 51, 52, 53] Lubert-Perquel et al.[51] proposed that a parallel orientation of the chromophores favours the formation of quintets and ultimately free decorrelated triplets. In addition, the displacement along the long molecular axis Δx in a slip-stacked configuration is also of crucial importance. Pensack et al.[54] reported that without a displacement, i.e. $\Delta x = 0$ the triplet quantum yield (TQY) is almost zero.

As pointed out in the introduction to this thesis, SF is particular interesting since it promises to increase the efficiency of photovoltaic devices up to 44% which surpasses the Shockley-Queisser limit [7, 8]. The efficiency of a solar cell could thus be enhanced if the

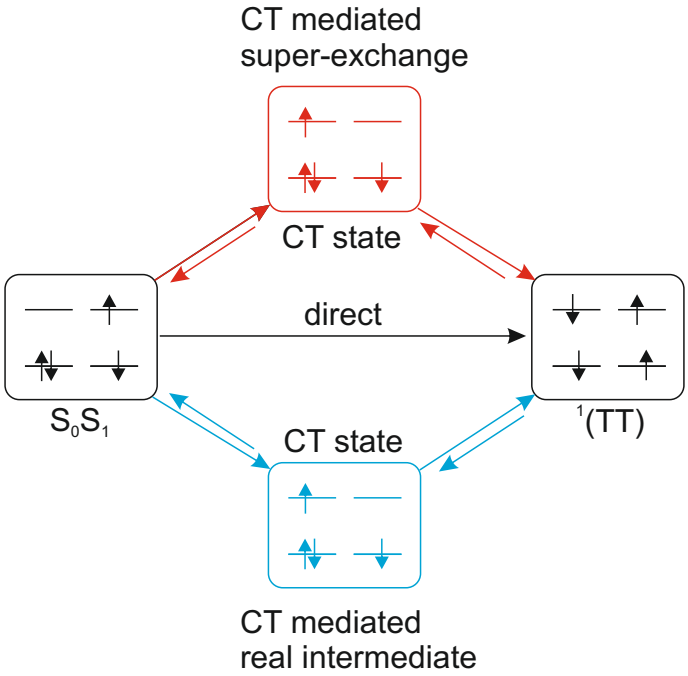

Figure 3.5: Illustration of CT mediated and direct SF. CT: Charge transfer [31].

triplet energy level of the SF material is comparable to the semiconductor band gap, provided that the energy can be transferred. Harnessing this process, high-energy photons can be utilized whose energy would otherwise be lost in dissipative processes. The basic idea how to use the SF material in solar cells is as follows [35]: Assuming the SF material had the same band gap E_g as the ordinary semiconductor, the charges and hence the generated current would be twice as much, but at the same time the potential is lowered by half. With that the provided power $P = UI$ would maximally be the same as in the ordinary semiconductor. If however, the band gap is approximately twice as big and therefore the triplet state energy is aligned with the CB of the semiconductor, any photon with higher energies than E_g (of the SF material) can get absorbed an produce two triplet excitons. These excitons would then need to be transferred to the ordinary semiconductor of the solar cell. Thus high-energy photons can be used, which would otherwise dissipate heat. For commercialisability it is therefore beneficial to design SF materials with twice the band gap of typical semiconductors used for photovoltaic applications as silicon (1.1 eV), cadmium telluride (1.5 eV) or copper indium gallium (di)selenide ($1 - 1.7$ eV) [35]

Fast SF is in general desired, since it needs to out compete other decay mechanisms. Therefore, ideal time-scales are on the picosecond to femtosecond time scale. In addition to a fast SF and high TQY, a long lifetime of the generated triplets and a high diffusion coefficient is of great importance, since it increases the probability of harvesting the charge carriers.

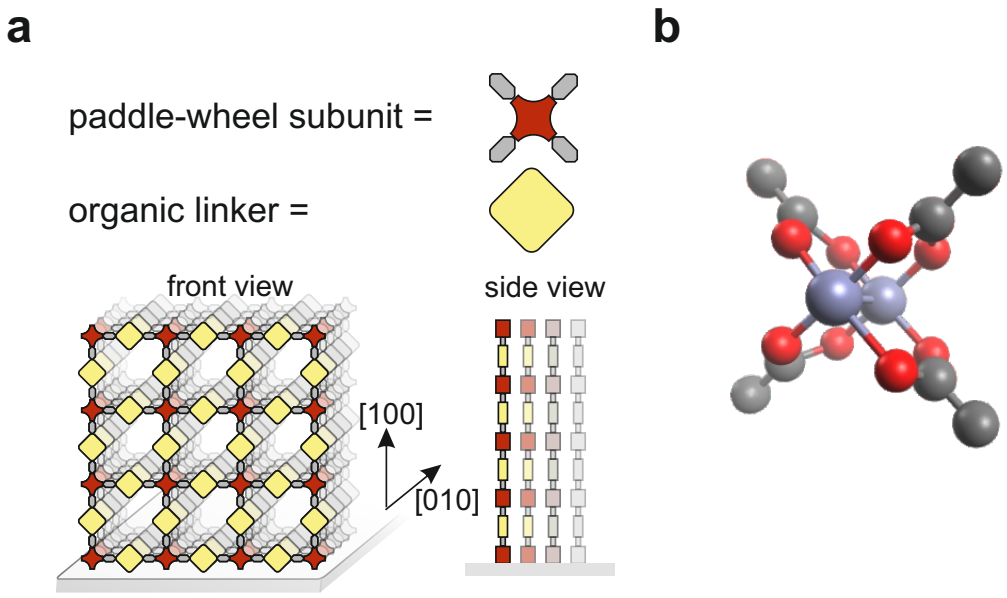

Figure 3.6: **a** Front and side view of the structure of SURMOFs build from subunits and organic linkers. The surface functionalisation is not shown. **b** Molecular structure of the paddle-wheel subunit. Grey: carbon, red: oxygen, blue: zinc

3.2 Metal-Organic Frameworks

As metal-organic frameworks (MOFs) are investigated in two projects of the thesis, a brief general overview will be given here. The specific samples are then described in more detail in the corresponding section.

MOFs form nano porous crystalline structures as shown in Fig.3.6 a). Here, metal or metal-oxo clusters form the vertices, which are connected to each other by linkers. The linkers are organic molecules that have been functionalised with coupling groups, such as carboxylic acid groups. These form a coordinative bond with the metal atoms, see Fig.3.6 b). There are different structures of metal clusters at the nodes. The tetragonal paddle wheel unit as shown is relevant to this thesis. The metal atoms used are often Cu or Zn, but there is almost no limit to the choice of organic molecules, so that an enormous number of systems have already been fabricated. In 2017, 70,000 structures had already been characterised [55] and the possibilities are almost unlimited. The areas of application are therefore also wide-ranging: gas storage, gas separation [56, 57, 58], catalysis, data storage, electronic conductivity, drug delivery [59] and optical applications [60].

The surface mounted metal-organic frame works (SURMOF) investigated in the thesis are deposited on a functionalised surface. This surface can be functionalised e.g. by deposition of self-assembled monolayers (SAM), which serve as nucleation seed for the following layers of the MOF [61]. The SURMOFs have several advantages. They form a thin film and not a powder, so they are better suited for the investigation of optical properties as they scatter

less. Furthermore, the connection to the surface is suitable for attaching electrical contacts and thus investigating electrical properties such as conductivity [62].

3.3 Ultrafast time-resolved spectroscopy

The theoretical foundation for lasers was established by Albert Einstein in 1916, who described stimulated emission. Another 44 years had to pass before the first laser was realised. However, the precursor of today's transient absorption was actually developed as early as 1950 [63]. A flash tube provides a short light pulse, which ultimately made it possible to achieve a temporal resolution of around 50 µs. Around 1965, the first mode-locked lasers were developed, which made it possible to generate laser pulses from a continuous beam. Today, the shortest pulses are in the range of 40-50 attoseconds [64].

Time-resolved measurement can be realised by taking snapshots at specific points in time. In the light of time-resolved spectroscopy, these snapshots are realised using ultrashort laser pulses. In concrete terms, this means that a laser pulse interacts with the sample and is then detected. This laser pulse is called probe. Another laser pulse, called pump, is used to excite the sample. With that a pump-probe experiment is designed. The time offset between pump and probe indicates the time after excitation of the sample.

How good the temporal resolution of the experiment is, depends largely on the width of the laser pulses used. But how do you determine the length of the pulse? In principle, this is easy, as we have just discussed: Once again, short snapshots are needed to scan the laser pulse. However, the pulses to be measured are the shortest time intervals accessible to us. The solution is to use the pulse itself to measure it. This method is called autocorrelation. The principle will be briefly explained here, as the pulse width was determined daily before the TR-SHG measurement, as the pulse width can vary during manual adjustment of the various optical devices.

Fig.3.7 a) shows a schematic of an autocorrelator. The incoming beam is split into two beams at a beam splitter, one of which is guided via a delay stage. Both beams then meet in a non-linear crystal. When the two beams are superimposed, photons of twice the frequency are produced by SHG. In the non-collinear arrangement shown, the frequency-doubled beam can be detected in isolation; the measurement is therefore background-free. A typical measurement signal is shown in Fig.3.7 b). Mathematically this represents the convolution of the two pulses. This poses a problem for the exact determination of the pulse width, as not all information is obtained during the measurement in order to reconstruct the original pulse. For example, the asymmetrical pulse in 3.7 c) results in a symmetrical autocorrelation again. However, in our experimental setup, we can approximately assume a Gaussian pulse In this case, the pulse width Δt results from

$$\Delta t = \frac{\mathrm{FWHM}}{\sqrt{2}}, \tag{5}$$

with the full width half at half maximum (FWHM) of the auto-correlated signal.

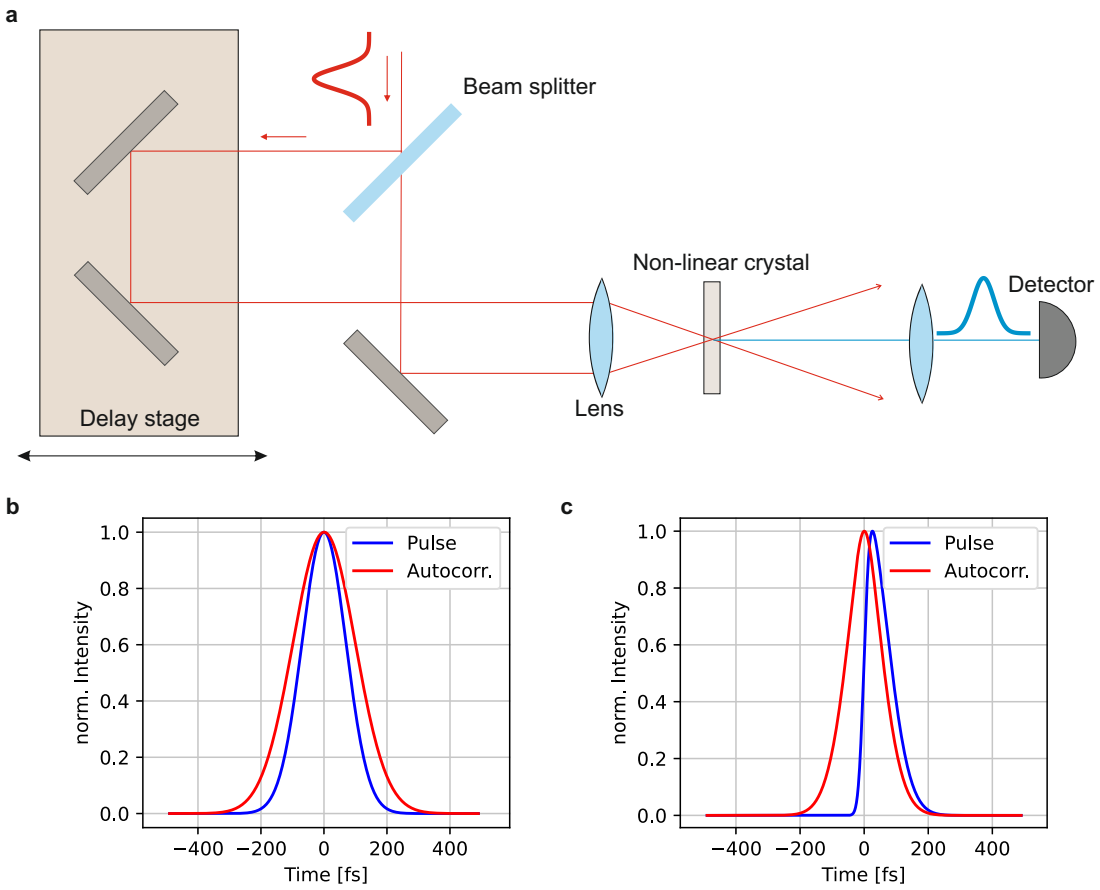

Figure 3.7: **a** Schematic setup of a non-collinear autocorrelator. The incoming beam is a pulsed laser beam. In the non-linear crystal the blue beam is created by SHG. **b** Exemplary gaussian pulse and its autocorrelation. **c** An asymmetric pulse represented by a skewed gaussian. Note that the autocorrelation is symmetric again.

3.3.1 Transient absorption

TA is a pump-probe experiment as described above. The probe beam is a white light supercontinuum, which means that the spectral width is extremely broad, typically a few hundred nanometres. The detected signal is the difference in absorbance of the sample after excitation and the sample in the ground state:

$$\Delta A = -\log \frac{I}{I_0} \tag{6}$$

Here I is the detected probe intensity at a specific delay time between pump and probe. I_0 is the intensity without exciting the sample. This is a simplified equation, since in the actual setup reference signals are included to account for fluctuations of the incoming beam intensity.

The principle processes that contribute to the acquired signal are illustrated in Fig.3.8 a). For these processes it can be assumed that the probe beam does not influence the population of the excited states, since it is much weaker than the pump beam.

1. After excitation usually 2-20% [65] are excited. This means that the absorption from the ground state reduces accordingly, as long as the chromophore is in the excited state. Therefore, the Ground State Bleach (GSB) gives rise to a negative contribution in the difference absorption spectrum, as the transmission is increased. The GSB can easily be identified by comparison to the steady-state absorption [21].

2. A second negative contribution arises from Stimulated Emission (SE). The excited states can be depopulated by interaction with the photons of the probe beam. In contrast to spontaneous emission, SE is coherent to the photon of the probe beam. Specifically, it travels always in the same direction, and hence will be detected as well. These additional photons give rise to a negative signal. They can be identified by comparison to photoluminescence spectra and they are located in the red, i.e. at lower energies as the GSB [21].

3. If the sample is in an excited state, further transitions can occur from there. This usually involves the excitation of the S_1 state to energetically higher states. It is therefore called excited state absorption (ESA) or photo-induced absorption (PIA). But in principle, any new state can cause additional absorption. Examples of this are triplet states, charge transfer states or isomerised states. This is sometimes listed separately as *product absorption* [65]. In both cases, a positive signal is obtained, as photons of the probe pulse are absorbed in this process.

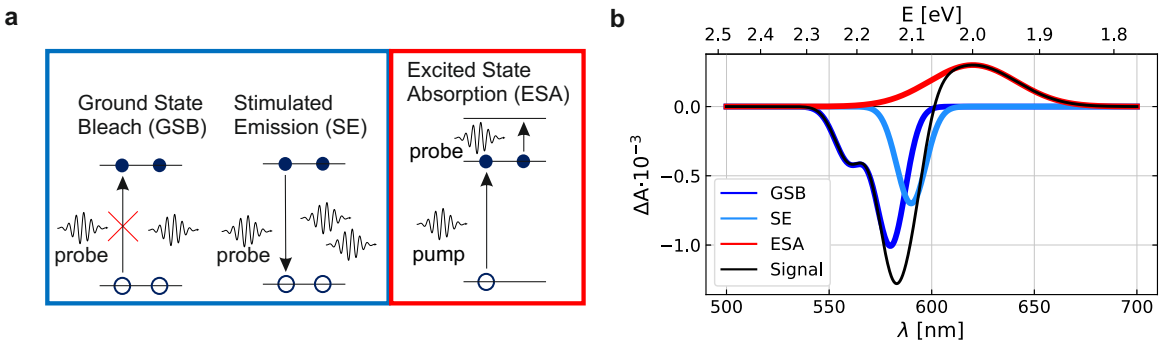

Figure 3.8: **a** Basic processes that contribute to changes in absorption in TA measurements. Empty and filled circles represent unoccupied and occupied states, respectively. **b** Exemplary TA spectra split up by their contributions to the total signal. GSB: ground state bleach, SE: stimulated emission, ESA: excited state absorption.

3.3.2 Nonlinear optics

Second harmonic generation (SHG) is a non-linear optical process. Such processes are not very common in everyday life as they only occur at very high electric field strengths. The most frequent contact with it is probably when using green laser pointers, in which the frequency of an Nd:YAG laser is doubled. Shortly after the invention of the laser, Franken et al.[66] published the first results on SHG in 1961, which could only be realised with an intense, focused laser beam. The description below is based on the books and publications by Boyd, Sutherland, Kärtner and Mücke [67, 68, 69] as well as previous dissertations in this group [70, 71, 72]. The following relationship applies in linear optics:

$$\tilde{P}(t) = \epsilon_0 \chi^{(1)} \tilde{E}(t) \tag{7}$$

Here $\tilde{P}(t)$ describes the macroscopic polarisation caused by the electric field $\tilde{E}(t)$. ϵ_0 is the Vacuum permittivity and $\chi^{(1)}$ is the first-order electric susceptibility. Equation (7) describes the response of a material to an electric field with non-resonant excitation. It is assumed that the electrons of charge q move away from the atomic nucleus by the distance l due to the electric field, creating a dipole. The macroscopic polarisation is then the average over an ensemble of microscopic dipoles $|\vec{p}| = ql = \alpha|\vec{E}|$, with the atomic polarisability α. Here, the restoring force is described by a harmonic potential. For large deflections, however, this no longer applies and Eq.(7) must be extended:

$$\tilde{P}(t) = \epsilon_0 \left[\chi^{(1)} \tilde{E}(t) + \chi^{(2)} \tilde{E}(t)^2 + \chi^{(3)} \tilde{E}(t)^3 + \cdots \right] \tag{8}$$

The second- and third-order non-linear susceptibilities are $\chi^{(2)}$ and $\chi^{(3)}$. Then we denote $\tilde{P}^{(2)}(t) = \epsilon_0 \chi^{(2)} \tilde{E}(t)^2$ as the second-order non-linear polarisation and correspondingly $\tilde{P}^{(3)}(t) = \epsilon_0 \chi^{(3)} \tilde{E}(t)^3$ as the third-order non-linear polarisation. With the image of the deflection of electrons in the atomic potential, one can imagine that the correction terms become relevant at the latest at a field strength that corresponds to the atomic field strength. This allows us to make an initial estimate on the values of $\chi^{(2)}$ and $\chi^{(3)}$. Due to the relationship between the electrical susceptibility $\chi^{(1)}$ and the refractive index n

$$n^2 = (1 + \chi), \tag{9}$$

we know that for materials with $n \sim 1 - 3$, $\chi^{(1)}$ is of the order of 1. With a field strength $E_{at} = \frac{q}{4\pi\epsilon_0 a_0^2}$ at a distance of the Bohr radius $a_0 \sim 0.5$ Åwe would now expect that

$$\chi^{(2)} \sim \frac{\chi^{(1)}}{E_{at}} = 1.94 \cdot 10^{-12} \mathrm{m\,V^{-1}} \tag{10}$$

and

$$\chi^{(3)} \sim \frac{\chi^{(1)}}{E_{at}^2} = 3.78 \cdot 10^{-24} \mathrm{m^2\,V^{-2}}. \tag{11}$$

In fact, these values are of the right order of magnitude. With the second-order non-linear polarisation term $\tilde{P}^{(2)}(t)$ we can describe some non-linear optical phenomena. If the electric

field strengths $\tilde{E}_1(t)$ and $\tilde{E}_2(t)$ of two laser beams with frequencies $\omega_{1,2}$, which we represent as plane waves, are superimposed, we can use

$$\tilde{E}(t) = \mathbf{E}_1(t)e^{-i\omega_1 t} + \mathbf{E}_2(t)e^{-i\omega_2 t} + c.c. \tag{12}$$

to calculate the second-order non-linear polarisation:

$$\begin{aligned} \tilde{\mathbf{P}}^{(2)}/\epsilon_0\chi^{(2)} = &\left(\mathbf{E}_1^2 e^{-i2\omega_1 t} + \mathbf{E}_2^2 e^{-i2\omega_2 t} + \text{c.c.}\right) && \text{(SHG)} \\ &+ 2\left(\mathbf{E}_1\mathbf{E}_2 e^{-i(\omega_1+\omega_2)t} + \text{c.c.}\right) && \text{(SFG)} \\ &+ 2\left(\mathbf{E}_1\mathbf{E}_2 e^{-i(\omega_1-\omega_2)t} + \text{c.c.}\right) && \text{(DFG)} \\ &+ 2\left(\mathbf{E}_1^2 + \mathbf{E}_2^2\right) && \text{(OR)} \end{aligned} \tag{13}$$

The complex conjugate is denoted by c.c.. Each of the four lines can be assigned to a specific effect. In all processes, the energy must of course be conserved and the so-called phase matching condition must be fulfilled. The latter can ultimately be traced back to the conservation of momentum. The conditions are usually not fulfilled simultaneously for the various effects. The first term includes components with the doubled frequency of both electric fields. This ultimately leads to the observation of radiation with frequencies ω_1 and ω_2. Therefore, this term describes second harmonic generation (SHG), which we will discuss in more detail below. The next term involves the addition of the frequencies and describes sum frequency generation (SFG). This process is often used to obtain tunable radiation in the UV range, generated by SFG of two lasers in the visible range, one of which must be tunable within a certain range. The third term describes difference frequency generation (DFG) and is, among other applications, used in optical parametric amplifiers (OPA) together with SHG, to obtain laser light with adjustable output frequencies. The DFG not only produces radiation with the frequency of the difference $\omega_3 = \omega_1 - \omega_2$ ($\omega_2 < \omega_3$, as otherwise energy would be destroyed). But also radiation of the frequency ω_2 is generated, which serves as input and is thus amplified, which explains the name of the OPA. The last term describes the optical rectification (OR), where a constant electric field is created.

Second Harmonic Generation Optically non-linear second-order processes are only possible with non-inversion-symmetric materials. For an inversion-symmetric material, the second-order polarization

$$\tilde{\mathbf{P}}^{(2)} = \epsilon_0\chi^{(2)}\tilde{\mathbf{E}}^2 \tag{14}$$

must transform under inversion $\tilde{\mathbf{E}} \to -\tilde{\mathbf{E}}$ in the same way due to symmetry:

$$-\tilde{\mathbf{P}}^{(2)} = \epsilon_0\chi^{(2)}(-\tilde{\mathbf{E}})^2 \tag{15}$$

That implies $-\tilde{\mathbf{P}}^{(2)} = \tilde{\mathbf{P}}^{(2)}$ and hence $\tilde{\mathbf{P}}^{(2)} = 0$, which can only be fulfilled by $\chi^2 = 0$. Therefore, SHG is in particular a surface-sensitive process, since inversion symmetry is always broken at the surface. Moreover, this means that a material with a symmetric bulk does not provide a background contribution. Assuming this, the detected SHG signal in the dipole approximation can be described by Eq.(16).

$$
\begin{aligned}
I_{\mathrm{SHG}}(2\omega) &\propto |\mathbf{P}^{(2)}(2\omega)|^2 \\
&\propto |\chi^{(2)} E(\omega) E(\omega)|^2 \\
&\propto \left(|\chi^{(2)}|^2 + \chi^{(2)*}\Delta\chi^{(2)} + \chi^{(2)}\Delta\chi^{(2)*} + |\Delta\chi^{(2)}|^2\right) I^2(\omega) \\
&\approx I_0(2\omega) + \Delta I_0(2\omega) + \Delta I_{\mathrm{ind}}(2\omega, \Delta\chi^{(2)}),
\end{aligned}
\tag{16}
$$

Here, it is assumed that the excitation causes a change $\Delta\chi^{(2)}$ in the susceptibility, which is, however, small compared to $\chi^{(2)}$. This means that the quadratic term $|\Delta\chi^{(2)}|^2$ can be neglected and the observed intensity is linear with the change $\Delta\chi^{(2)}$. In principle, electric quadrupole transitions and magnetic dipole transitions can also contribute to the signal. However, these are usually weaker than electric dipole transitions. In the next section, however, we will see that these transitions must be taken into account in certain cases [73].

SHG from chiral molecules Chiral molecules are intrinsically not inversion symmetric. Therefore we can expect SHG from materials with chiral molecules. Particularly, SHG circular dichroism (SHG-CD) and rotation of linear polarized light, termed optical rotatory dispersion (SHG-ORD) can be observed. Before discussing these phenomena, a recapitulation of linear optical processes for chiral molecules is given. A thorough description can be found in the Refs.[25, 74, 75, 76] for example.

Chiral molecules are known to display optical activity. This describes the rotation of linearly polarized light by an angle Φ_0. The enantiomers show opposite behaviour meaning that, if the right handed molecule rotates by Φ_0, then the left handed rotates by $-\Phi_0$.

This can be understood by that fact that the enantiomers have different indices of refraction n_l and n_r for left and right handed circular polarized light. If we consider a wave of linearly polarized light, we can treat it as a superposition of left and right circular polarized light:

$$
\vec{E} = E_0 \begin{pmatrix} 1 \\ 0 \end{pmatrix} e^{i(\vec{k}\vec{r}-\omega t)} \tag{17}
$$

$$
= E_0 \begin{pmatrix} 1 \\ i \end{pmatrix} e^{i(\vec{k}\vec{r}-\omega t)} + E_0 \begin{pmatrix} 1 \\ -i \end{pmatrix} e^{i(\vec{k}\vec{r}-\omega t)} \tag{18}
$$

Here, the first term in the second line describes right circularly polarized light. The factor i in the y-component shows that the y-component is 90° ahead of the x-component. Similarly, the second term describes left circularly polarized light. When the wave passes through the medium, the phases that depend on the thickness d of the material and the refractive index $n_{r,l}$ change according to

$$
\psi_r = k_r d - \omega t = \omega \frac{n_r d}{c} - \omega t \tag{19}
$$

$$
\psi_l = k_l d - \omega t = \omega \frac{n_l d}{c} - \omega t \tag{20}
$$

So the phase difference $\Delta\psi = \frac{2\pi f d}{c}(n_l - n_r)$ (with $c = f\lambda$), resulting in a rotation of the linearly polarized light by the angle

$$\Phi_0 = \frac{\Delta\psi}{2} = \frac{\pi d}{\lambda}(n_l - n_r) \tag{21}$$

The origin of the difference between the refractive indices n_l and n_r is non-trivial and can not be explained within the electric dipole approximation [77]. For a deeper understanding a derivation in the framework of electromagnetic theory is given in Ref.[78].

Some non-linear chiroptical processes can in contrast be explained with electric dipole transitions only [79]. In other cases magnetic transition were needed to explain the observed data [73]. An illustration of the experimental scheme is shown in Fig.3.9 a) and c). A film of chiral molecules is deposited on a substrate. The substrate is assumed to behave linear. The direction of p- and s-polarisation are determined by the plane that is spanned by the incident and reflected beam.

The SHG analogue to linear optical rotation is SHG-ORD. Here, a linearly p-polarized beam is incident on the surface. The analyser behind the sample is rotated and any detected s-polarized light of the second harmonic is a sign of chiral molecules on the surface [74].

When rotating a quarter wave plate (QWP) in front of the sample, the non-linear interaction of elliptically polarised light with chiral molecules needs to be considered. For the following description the surface is taken to be isotropic, so that a rotational symmetry C_∞ can be assumed.

In the case where electric and magnetic dipole transitions have to be taken into account, the non-linear polarisation of second order is given by:

$$P_i^{(2)}(2\omega) = \sum_{jk} \left[\chi_{ijk}^{eee} E_j(\omega)E_k(\omega) + \chi_{ijk}^{eem} E_j(\omega)B_k(\omega)\right] \tag{22}$$

Additionally, a non-linear magnetization is generated by:

$$M_i^{(2)}(2\omega) = \sum_{jk} \chi_{ijk}^{mee} E_j(\omega)E_k(\omega) \tag{23}$$

The upper indices e and m indicate that the respective subscripts refers to a component of an electric or magnetic transition moment [73]. The contribution of the magnetic dipole moments is in general only a few percent of the response of electric dipole effects [80].

Now, we start from the fundamental p-polarized light, that traverses the QWP that is rotated by an angle ϕ. By transformation to the rotated system of the QWP, adding the phase shift induced by the plate and back transformation, the resulting electric field can be described with:

$$\vec{E}(\omega) = A\sin(\phi)\cos(\phi)(1-i)\vec{e_s} + A(\sin^2(\phi) + i\cos^2(\phi))\vec{e_p} \tag{24}$$

Now the resulting electric field $E(2\omega)$ needs to be calculated. From Eq.(22) we see that terms of the form E_i^2 and E_iE_j $(i \neq j)$ will appear, if we calculate the electric field from the

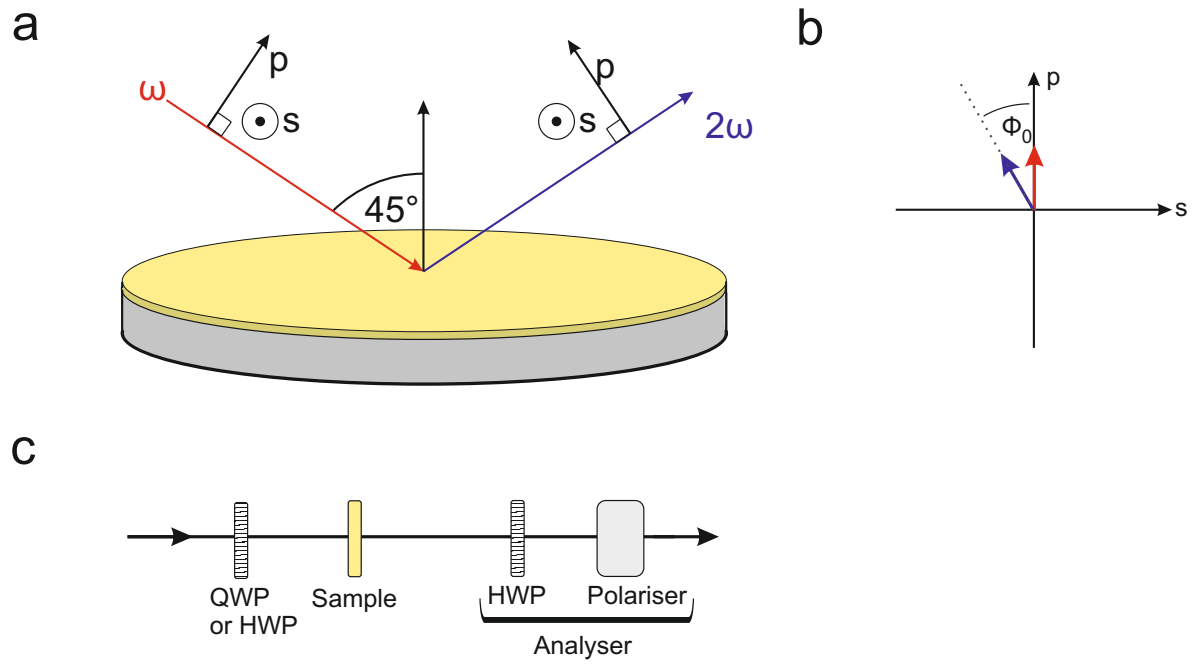

Figure 3.9: **a** Incident fundamental and reflected SHG beam and assignment of the direction of p- and s-polarisation. **b** Rotation of incident p-polarised light by an angle of Φ_0. **c** Schematic of the experiment including only the most important optical components.

magnetic induction by $B(\vec{\omega}) = \frac{\vec{k}\times E(\vec{\omega})}{|\vec{k}|}$. Then pure geometric considerations - i.e. projecting the E-field on the Cartesian components x, y and z - will lead to the bilinear combinations:

$$E_x^2(\omega) = \cos^2(\theta)F(\phi), \quad E_y^2(\omega) = G(\phi), \quad E_z^2(\omega) = \sin^2(\theta)F(\phi), \tag{25}$$

$$E_x(\omega)E_y(\omega) = \cos(\theta)H(\phi), \quad E_x(\omega)E_z(\omega) = \sin(\theta)\cos(\theta)F(\phi), \tag{26}$$

$$E_y(\omega)E_z(\omega) = \sin(\theta)H(\phi) \tag{27}$$

where the functions F, G and H only depend on the angle of rotation of the QWP and are given by:

$$F(\phi) = A^2\left(sin^2(\phi) + icos^2(\phi)\right)^2 \tag{28}$$

$$G(\phi) = A^2 sin^2(\phi)cos^2(\phi)(1-i)^2 \tag{29}$$

$$H(\phi) = A^2 sin(\phi)cos(\phi)\left(sin^2(\phi) + icos^2(\phi)\right)(1-i) \tag{30}$$

$$\tag{31}$$

Finally the SHG signal can be expressed as

$$|E(2\omega;\phi)|^2 = |fF(\phi) + gG(\phi) + hH(\phi)|^2, \tag{32}$$

where f,g and h are complex valued fit parameters. These fit parameters are determined by the non-linear susceptibilities of the material. Hence, from determining f,g and h, conclusions on the tensor elements of $\chi^{(2)}$ can be drawn. The exact form of the parameters is given in the chapter 8.1.3 and literature [73]. From the obtained model parameters, the angle of rotation in SHG-ORD experiments could in principle also be derived. For more details see Ref.[25].

4 Experimental setup

This section describes the experimental setups used in the framework of the thesis. Transient absorption (TA) is described in the following section and the setup for Second harmonic generation (SHG) in section 4.2.

4.1 Transient absorption

The transient absorption measurements were carried out with commercially available setups for fs-TA and µs-TA (HELIOS and EOS, Ultrafast Systems). The setup is shown in Fig.4.1 The output of a Ti:sapphire amplifier (Coherent Astrella) at 800 nm and a repetition rate of 4 kHz was used in a commercial optical parametric amplifier (TOPAS Prime, Light Conversion) to create the excitation pulse. The excitation or pump beam is directed into the HELIOS system, where it passes a chopper. This chopper is set to a frequency 2 kHz to block every second pulse, such that the desired comparison of spectra with and without excitation can be measured. Subsequently, it passes an achromatic half-wave plate to adjust the polarisation and is then focused on the sample. The relative polarisation between pump and probe beam were set either to have polarisations parallel, perpendicular or with an angle of 54.7°. This corresponds to the magic angle and is typically chosen to avoid effects of anisotropy in solution.

The spectra of the excitation pulses that were used to excite the samples investigated in this work are presented in Fig.4.2 a). The autocorrelation of the excitation pulse centred at 605 nm was about 94.5 ± 0.2fs corresponding to a pulse width of ~ 67 fs assuming a gaussian pulse shape, measured with a commercial autocorrelator (pulseCheck, APE).

To generate the probe beam, the output of a Ti:sapphire amplifier at 800 nm enters the HELIOS system and passes through a delay stage of up to 8 ns, which was controlled by a motorised delay stage. Thereafter, a half-wave plate is used to set the polarisation of the beam. In the next step the a broad spectrum covering several hundred nanometres (supercontinuum) is created. The creation is based on a non-linear effect called self-phase modulation. For a detailed description see [81] for example. For fs-TA the setup can be adjusted to give a supercontinuum (or white light spectrum) in several spectral regions. The normalised spectra a depicted in Fig.4.2 c). To achieve a white light probe spectrum in the range from 320 nm to 650 nm the Ti:sapphire output was focused into a CaF_2 crystal. Similarly, focusing on a sapphire crystal yielded a spectrum of 440 nm to 800 nm and the NIR white light spectrum enables measurements from 820 nm to 1500 nm. The beams have a diameter at the position of the sample of ~ 100 µm (probe) and ~ 300 µm (pump).

To observe longer time-dynamics up to 200 µs an electronically operated delay was employed. In this case, an external laser system (Leukos) generates a white light spectrum from 350 nm-900 nm, compare Fig.4.2 c). The cross-correlation for this setup is about 350 ps.

The sample holder is placed on a micrometer stage to drive the sample along the z-axis (beam direction) into the focus of the probe beam. It can also be displaced in the x- and y-direction by motorised stages. They can be controlled by the software, to randomly select positions on the sample while measuring. This will minimize beam damage and allows for

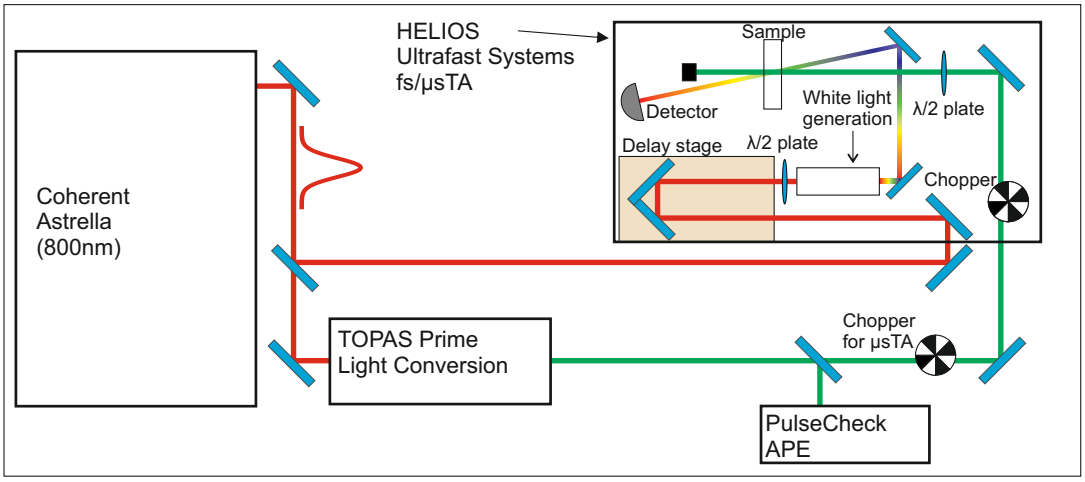

Figure 4.1: Illustration of the setup used for TA measurements. The output of the Astrella laser (red) is a pulsed laser beam centred at 800 nm. This is used as probe after whitelight generation and as input for the OPA to generate the pump beam (green). The pump beam is blocked by the chopper every second pulse.

averaging in case of an inhomogeneous sample.

4.1.1 Data processing:

As a result of the self-phase modulation, the probe beam is chirped, with short wavelengths in the front of the pulse. Furthermore, the dispersion of the optics used in the setup add to the chirp. This is reflected in ultra short measurements that are spectrally resolved. An exemplary data set is shown in Fig.4.3 a). This map encodes the difference absorption ΔA in the color, the ordinate represents the delay time between pump and probe and the abscissa the wavelength. The red line named chirp fit, captures the position of t_0, i.e. the delay time at which pump and probe coincide temporally. It can be seen that t_0 varies with the wavelength, shifting over almost one picosecond. For both visualisation and analysis the data are corrected such that t_0 is the same for all wavelengths. The analysis software Glotaran [82] fits a polynomial of n-th order. For visualisation the polynomial is adapted, such that the signal onset at every wavelength lies within ± 50 fs of a set t_0, compare Fig.4.3 b). Furthermore, the data is corrected for the background signal by subtracting the average of 15-30 data points before the earliest t_0. By comparing Fig.4.3 a) and b) it can be seen that the negative (blue) signal at ~ 528 nm disappears with the background correction. This signal is based on scattered pump beam light. In this case the pump beam wavelength was set to 264 nm. In the process of generating the pump beam, use of SHG is made. Hence, the signal at 528 nm stems from the fundamental beam of that SHG process. In most cases the scattered light saturates the detector and the background correction does not work in the spectral range of the pump beam. In that case the data will be omitted for analysis.

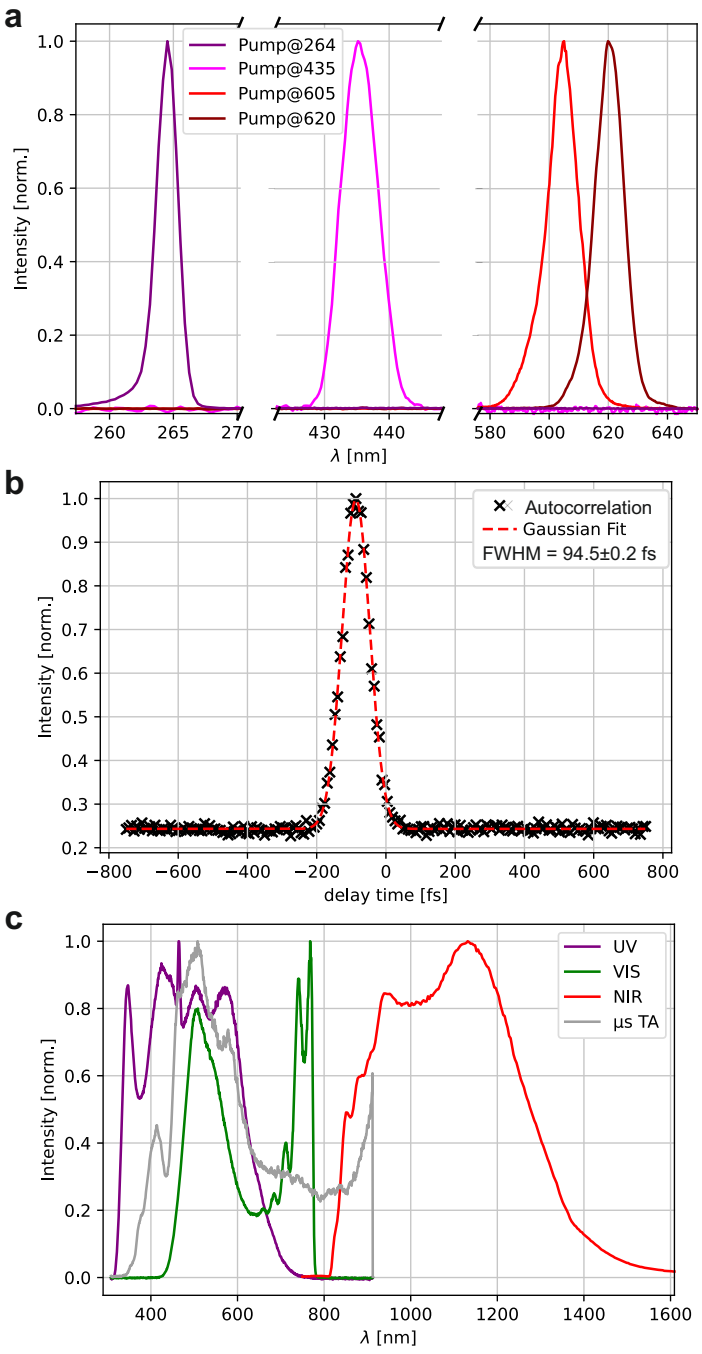

Figure 4.2: **a** Spectra of the pump beams. **b** Autocorrelation function of the pump beam at a wavelength of 605 nm. **c** Supercontinuum white light spectra used for probing the absorption. The spectra cover the ultra violet (UV, purple), visible (VIS, green) and near infra-red (NIR, red) spectral regions. The grey spectrum (µs TA) is used in experiments for probing long time delays in the micro second range.

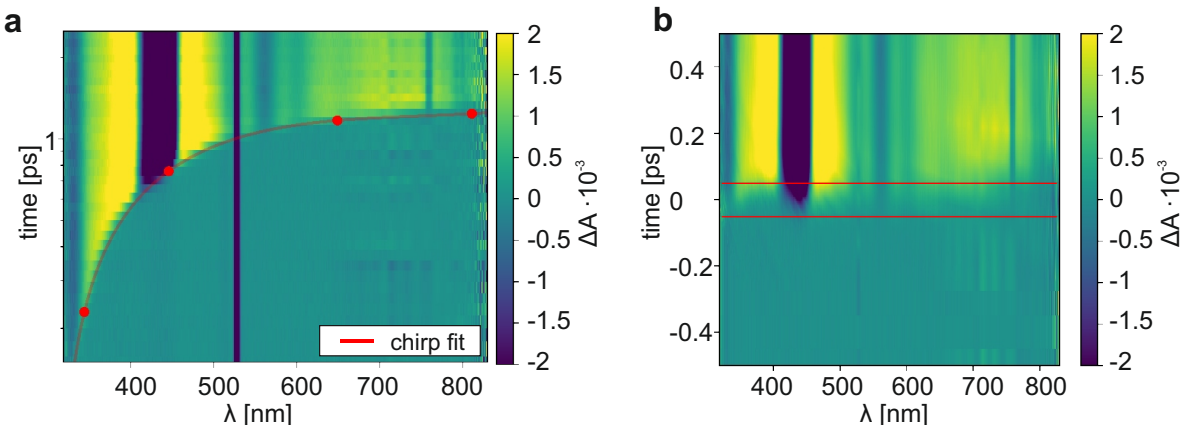

Figure 4.3: **a** Difference absorption ΔA before correcting for the chirp of the white light supercontinuum and without background correction. The red curve is described by a third-order polynomial. **b** Corrected data. The red horizontal lines mark the times ± 50 fs.

4.1.2 Data analysis

The analysis is executed with the free software Glotaran [82]. The basic concepts are covered here, but for a comprehensive description see Refs.[83, 84, 85, 86]. The following description closely follows the review by Stokkum et al.[85]. To model the absorption, it is assumed, that the spectroscopic properties of the sample are a superposition of the spectroscopic properties of the individual n components. This is described with the following equation:

$$\psi(t, \lambda) = \sum_{l=1}^{n} c_l(t)\epsilon_l(\lambda) \tag{33}$$

The concentration c_l of the component l depends on time t and the extinction coefficient ϵ_l depends on the wavelength λ. The number of components n does not only count the number of different molecules, but more generally species that are spectrally or dynamically distinct, or both. Equation (33) assumes separability of time and wavelength dependence. This is however a simplification, as has been discussed above, time zero t_0 depends on the wavelength and with that also $c_l(t; t_0)$.

To account for this, the concentration profile is convolved with the instrument response function (IRF). In case of pump-probe experiments the IRF is given by the convolution (denoted by $*$) of pump and probe pulses and can be modelled by a Gaussian function $i(t)$.

$$c_l(t; k_l, t_0, \sigma_{IRF}) = \exp(-k_l t) * i(t), \qquad \text{with} \tag{34}$$

$$i(t) = \frac{1}{\sqrt{2\pi}\sigma_{IRF}} \exp\left(-\left[\frac{t - t_0}{\sigma_{IRF}}\right]^2\right) \tag{35}$$

The resolution of the system is limited by the width σ_{IRF} , which lies between 50 to 100 fs for the TA setup, depending on the pump and probe beams used. The

Without further knowledge of the dynamics, a singular value decomposition (SVD) gives first indications on the number of components involved, as well as their spectral and time dependant shape. For that, we rewrite Eq.(33) in matrix notation $\Psi = CE^T + \Sigma$. Here, C contains the concentration profiles as columns, E contains the spectra as columns (T denotes the transpose) and Σ is a matrix representing the noise.

The SVD yields

$$\Psi = USW^T \tag{36}$$

with orthogonal matrices U and W, whose columns are left and right singular vectors. The matrix S allows to extract the singular values s_i from the diagonal elements. If there was no noise, this would exactly return as many singular values as the number of components n. Otherwise, both singular vectors and values will be perturbed and additional non-zero singular values s_i $(i > n)$ and vectors will be obtained. Then the numbers of components can be estimated from the singular values that are distinctly different from zero and from the number of singular vectors that are different from white noise.

Global analysis, as carried out by Glotaran, is restricted to first order kinetics and the solution will in general be a sum of exponential decays. With an estimate from SVD on the number of components, the first attempt is to extract the so called decay associated difference spectra (DADS). For that, the underlying model is a sum of independent exponential decays as described by Eq.(33). This will also be called parallel model/scheme or model/scheme with parallel decays. An unbranched unidirectional model $(1 \rightarrow 2 \rightarrow \cdots \rightarrow n)$ describes the evolution of the spectra and the resulting $\epsilon_l(\lambda)$ will be called evolution associated difference spectra (EADS). This might describe a system such as the dynamics $S_2 \rightarrow S_1 \rightarrow S_0$ for example. The results of the sequential and parallel scheme will only differ in the fitted spectra, whereas the decay constants k_l will be the same. In many cases, however, a detailed kinetic model involves branching and possibly back reactions. In this case the retrieved spectra and concentration profiles can describe the actual properties of the components involved. The obtained spectra from this co-called target analysis are termed species associated difference spectra (SADS).

4.2 Second harmonic generation

The next pages describe the experimental setup used for time-resolved SHG as well as polarisation resolved SHG experiments. Furthermore, the key parameters characterising the experiment are given. The setup is described in more detail in other works [70, 71, 72]. As the thesis was written, parts the setup were replaced by new devices. The seed laser was replaced by the Vitara Modelocked Ti:Sapphire Laser (Coherent) and the Verdi V18 Laser (Coherent) providing the continuous-wave (cw) Laser light was renewed. As this was not used in the thesis, the previous system is described.

4.2.1 Laser Setup

In Fig.4.4 the whole setup is displayed, which can roughly be divided into three parts. First, the generation beams and their subsequent preparation, to serve as pump and probe beam. Second, the measurement chamber, where the beams coincide on the sample and lastly, the detection and data acquisition.

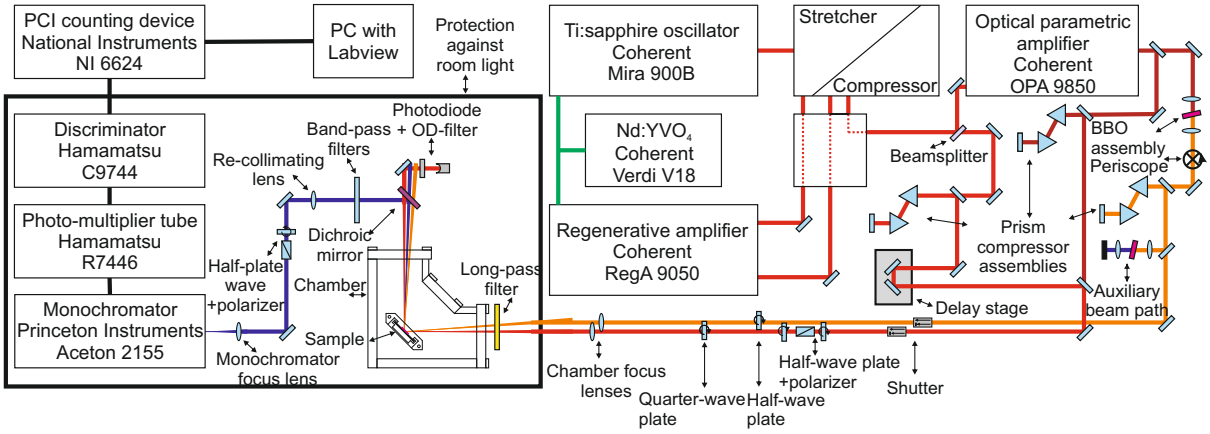

Figure 4.4: Schematic of the setup. On the right the beams are prepared. The box on the lower left contains the measurement chamber together with the light detection setup. Adapted from [70].

Beam preparation: Cw-Laser light is generated by frequency-doubled Nd:YVO4 laser (Coherent Verdi V18) at a wavelength of 532 nm and a power of 18 W. The beam is split up (12 W/6 W) and directed to a regenerative amplifier RegA (Coherent RegA9050, 300 kHz, 800 nm) and passive mode-locked Ti:sapphire oscillator (Coherent Mira 900 B) that serves as seed for the RegA. The output has a repetition rate of 76 MHz, an output power of roughly 400 mW and the pulses have a width of 60-80 fs. The beam is split (50%/50%) and guided to a spectrometer and to the stretcher. The stretcher extends the width of the pulse to a few tens of picoseconds, to prevent beam-induced damage inside the regenerative amplifier from too high laser peak powers. The regenerative amplifier is pumped by 12 W cw-light and uses

a Ti:sapphire crystal as gain medium. The output of the regenerative amplifier ($1.5 - 2\,\mathrm{W}$ passes through a compressor using a grating pair to yield pulses of width 60-80 fs again.

Subsequently, the beam is split again. One part will serve as probe beam and is directed through a pair of dispersive prisms (Thorlabs AFS-FS) for pulse compression and then passes a piezo-driven delay stage (Physcical Instruments M-505.4DG). The delay stage has a maximal range corresponding to 667 ps, with a resolution well below the cross-correlation of the pump-probe system. The other part of the beam is steered to an optical parametric amplifier (Coherent OPA 9850). Through generation of a white light supercontiuum and DFG, an output of 1050 to 1350 nm is generated and subsequently frequency-doubled by passing through a β-barium borate (BBO) crystal. With that the pump beam is tunable from 540 to 660 nm. For pulse compression, it passes a pair of dispersive prisms (Thorlabs AFS-FS). An auxiliary beam path creates the second harmonic of the pump beam and to optimise the compression, the power of the second harmonic is maximised.

Before entering the sample chamber, a combination of half-wave plate (HWP) (Thorlabs, AHWP10M-980), polarizer (Thorlabs GTH10M) and another HWP, allows to adjust both the power and the polarisation of the probe beam. The power of the pump beam, is reduced by moving the BBO crystal (behind the OPA) out of focus and an achromatic HWP (Thorlabs, AHWP10M-600) is used to set the polarisation.

Sample chamber: The sample chamber and all optics and devices thereafter are enclosed in a housing to prevent stray light from entering while taking a measurement. The sample itself is placed in a chamber to establish an inert gas atmosphere (nitrogen). The beams can enter through optically polished, 3 mm thick CaF_2 windows. Both beams get focused on the sample by biconvex lenses (N-BK7, LB1391-A and B) with a focal length of 400 mm. The beam profiles are shown in Fig.C.1.

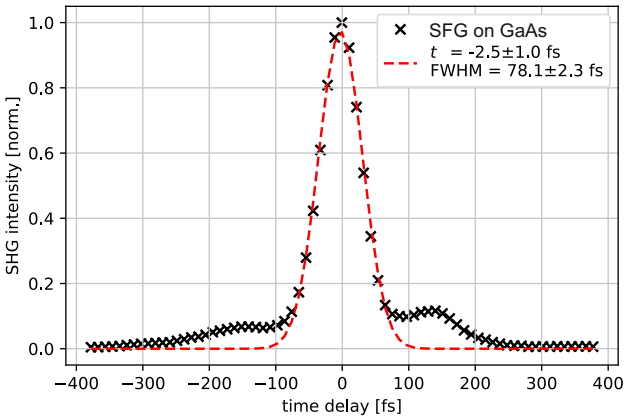

Figure 4.5: SFG cross correlation of pump and probe beam.

To separate the SHG beam that was generated in the sample from the fundamental a dichroic mirror (Thorlabs DMLP505) is used. The fundamental is detected by a photodiode

(Thorlabs SM1PD1A), while the SHG beam is directed through a set of filters (FGS900, FGB25 and FGB37) to remove light of wavelength > 400nm.

Data acquisition: To detect the SHG or SFG signal, the beam passes a monochromator and is detected by a photomultiplier (PMT). A discriminator is used to reduce the background noise and a counting units (Hamamatsu C9744) converts the electrical signal to a digital signal. The converted signal is captured by a PCI data acquisition card (National Instruments NI 6624) and processed by a personal computer.

4.2.2 Characterisation

On a daily basis the TR-SHG experiments require to measure the cross-correlation of pump and probe bean, which is depicted in Fig.4.5. The data is obtained by observing the SFG signal of the pump and probe beam on GaAs. The FWHM of the cross-correlation depends on the beam preparation and the wavelength of the pump beam, therefore it can vary. Typical values are between 50 and 90 fs.

An exemplary spectrum of the pump beam at 565 nm generated by the OPA is shown in Fig.4.6 a). The corresponding SFG signal of pump and probe and the SHG signal of the probe (800 nm) are shown in Fig.4.6 b) and are obtained be sweeping the monochromator. The profiles can be well-modelled by two Gaussian functions.

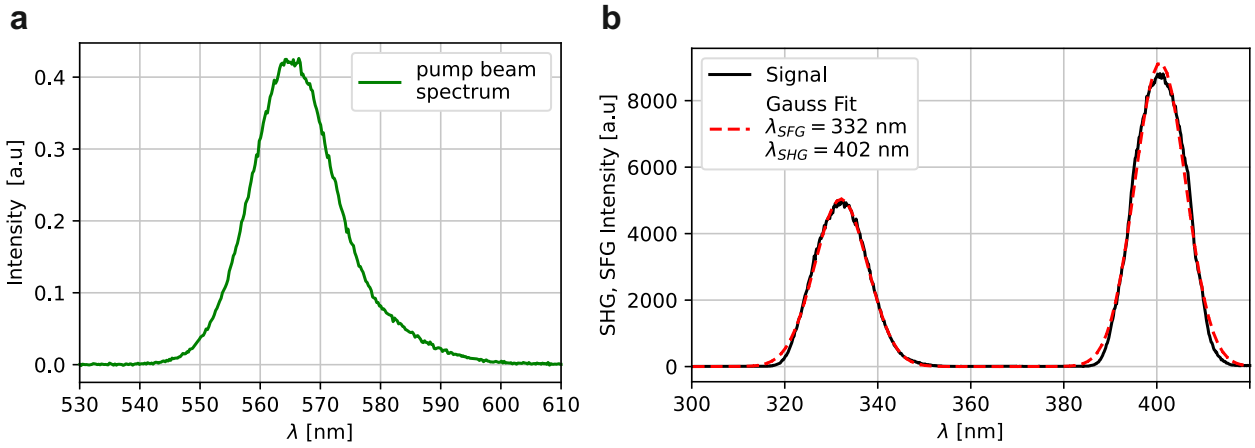

Figure 4.6: **a** Spectrum of the pump beam centred around 565 nm. **b** Sum frequency signal of pump and probe beam and SH of the probe beam on GaAs.

4.2.3 Data analysis

For the description of TR-SHG data, first order kinetics are assumed. The model function is obtained from the solution of the coupled equations (37), describing a sequential decay with

N_i being the amount of species i and k_i its corresponding decay rate.

$$\begin{aligned} N_1^{'}(t) &= -k_1 N_1(t) \\ N_2^{'}(t) &= -k_2 N_2(t) + k_1 N_1(t) \\ &\dots \end{aligned} \tag{37}$$

In the case of three components with initial values $N_2(t=0) = N_3(t=0) = 0$ and assuming $k_3 = 0$ (which can be assumed, if the decay of N_3 is not observed within the available time scale), the solution is given by:

$$N(t) = N_1(t) + N_2(t) + N_3(t) \tag{38}$$

$$= N_1^0 e^{-k_1 t} + N_1^0 \frac{k_1}{k_2 - k_1}(e^{-k_1 t} - e^{-k_2 t}) + N_1^0 (1 - \frac{k_2}{k_2 - k_1} e^{-k_1 t} + \frac{k_1}{k_2 - k_1} e^{-k_2 t}) \tag{39}$$

The actual applied model $A \rightarrow B \rightarrow C$ reads

$$N(t) = A e^{-k_1 t} + B \frac{k_1}{k_2 - k_1}(e^{-k_1 t} - e^{-k_2 t}) + C(1 - \frac{k_2}{k_2 - k_1} e^{-k_1 t} + \frac{k_1}{k_2 - k_1} e^{-k_2 t}) \tag{40}$$

Here, the additional parameters A, B and C are introduced because they also include the non-linear optical contrast of the species. For example, if the initially excited state did not result in a significant change $\Delta\chi$, only the first term would vanish, by finding $A = 0$. In case of only two species the model $A \rightarrow B$ reads:

$$N(t) = A e^{-kt} + B(1 - e^{-kt}) \tag{41}$$

Similarly to the procedure of the fs-TA, the final model function needs to be convolved with the IRF, which is described by a Gaussian function and the FWHM obtained from the cross-correlation.

4.2.4 Chiral SHG

SHG-ORD are collected by setting an analyser angle and then sweeping the monochromator in front of the photo multiplier tube (PMT). With a fundamental light beam at 800 nm an intensity profile around 400 nm is recorded and fitted with a Gaussian function. The fitted amplitude is taken as a data point for the specified angle of the analyser. The measurements can be complicated by the degradation of the samples. To account for that, the SHG intensity is monitored over several minutes at the same spot on the sample without rotating the analyser. If appreciable degradation is observed the measurement procedure is adapted as follows: Only three angles were measured on the same spot of the sample for 30 seconds each. The fitted linear decay over time is used to correct the data points. In case of inhomogeneous samples, such that the SHG intensity varies with the location on the sample, the data are normalised to a reference. Therefore, along with each batch of three angles, a measurement at $\phi = 0$ is recorded to serve as normalisation, i.e. $I(\phi)_{\text{norm.}} = \frac{I(\phi)}{I(\phi=0)}$.

The measurement procedure for experiments with a rotating QWP is the same, except for rotating the QWP and setting the analyser angle to either detect p- or s-polarised light.

5 Enhancing singlet fission lifetimes through molecular engineering

This chapter is presented as manuscript. The contributions to this work are as follows: Philipp Ludwig synthesized the pentacene dicarboxylic acid. Zhiyun Xu fabricated the SURMOFs. Christian Huck fabricated the neat pentacene thin films. Transient absorption spectroscopy was carried out by Martin Richter and Pavel V. Kolesnichenko. Martin Richter carried out the data analysis. Simulations were carried out by Muhammed Jeneesh Kariyottukuniyil. The paper was written by Martin Richter and Muhammed Jeneesh Kariyottukuniyil (theoretical modelling) with contributions from Pavel V. Kolesnichenko, Wolfgang Wenzel and Petra Tegeder.

The main part of the manuscript is unchanged, however the supplementary info (except for TR-SHG measurements) is shown in Appendix A and the references are included in the list of references at the end of the thesis.

Enhancing singlet fission lifetimes through molecular engineering

Martin Richter[1], Muhammed Jeneesh Kariyottukuniyil[2], Zhiyun Xu[3], Philipp Ludwig[4], Pavel V. Kolesnichenko[1], Christian Huck[1], Uwe Bunz[4], Christof Wöll[3], Wolfgang Wenzel[2] and Petra Tegeder[1]

[1] *Physikalisch-Chemisches Institut, Ruprecht-Karls-Universität Heidelberg, Im Neuenheimer Feld 253 , 69120 Heidelberg, Germany*

[2] *Institute of Nanotechnology, Karlsruher Institut für Technologie, Hermann-von-Helmholtz-Platz 1, 76131 Karlsruhe, Germany*

[3] *Institut für Funktionelle Grenzflächen, Karlsruher Institut für Technologie, Hermann-von-Helmholtz-Platz 1, 76131 Karlsruhe, Germany*

[4] *Organisch-Chemisches Institut, Ruprecht-Karls-Universität Heidelberg, Im Neuenheimer Feld 271, 69120 Heidelberg, Germany*

Abstract

Singlet fission (SF) is a process where a singlet exciton is converted into two triplet excitons, significantly enhancing charge generation in organic solar cells. It has been shown that the rate of SF and the lifetime of the generated triplets strongly depend on the molecular arrangement. In thin films of small molecules the SF efficiency is determined by the crystal structure.

Using a molecular engineering approach, we here exploit the design space accessible in metal-organic frameworks to enhance SF lifetimes. A cofacial orientation of pentacene molecules is achieved by embedding organic linkers which contain a pentacene unit in a surface-anchored metal-organic framework. Transient absorption spectroscopy and a quantum mechanical analysis have been used to analyze the ultrafast exciton dynamics as well as long-lived states after photoexcitation. The observed absorption spectra indicate that after the initial excitation, a singlet excited state generates a correlated triplet pair within a few picoseconds that retains singlet character. Subsequent dynamics show the formation of a long-lived species (40 µs) with triplet character. This exceeds by far the observed lifetime of triplets generated in pentacene thin films and may enhance triplet harvesting capabilities in photovoltaic cells.

5.1 Introduction

The interest in the use of solar energy has increased significantly in the last decade. Exploitation of singlet fission (SF) promises to increase the efficiency of photovoltaic junctions up to 44%, which surpasses the Shockley-Queisser limit [7, 8]. In SF materials, a singlet exciton is converted into two lower-energy triplet excitons ($E_{S_1} \approx 2E_{T_1}$). The efficiency of a solar cell could thus be enhanced if the triplet energy level of the SF material is comparable to the semiconductor band gap, provided that the energy can be transferred. Harnessing this process, high-energy photons can be utilized whose energy would otherwise be lost in dissipative processes. In addition to a fast SF and high triplet quantum yield (TQY), a long lifetime of the generated triplets is of great importance, since it increases the probability of harvesting the charge carriers.

Charge transfer (CT) states occur in a direct or indirect manner and especially the multiexcitonic state ^{m}(TT) plays a key role in the SF process [33, 50, 51, 52, 53]. Here, ^{m}(TT) specifies triplets on adjacent chromophores both in an excited triplet state. The four electrons involved in this picture spin-couple to have a multiplicity of $m = 1, 3$ or 5. The spin-coupled state must retain spin multiplicity m=1 initial to the generation of the triplet pair to ensure conservation of angular momentum. Many studies report the following model for SF [32, 44, 45]:

$$(S_0S_1) \xrightarrow{(1)} {}^1(T_1T_1) \xrightarrow{(2)} {}^1(T_1 \cdots T_1) \xrightarrow{(3)} 2T_1, \tag{42}$$

where (S_0S_1) indicates a singlet excitation on one of the two chromophores, $^1(T_1 \cdots T_1)$ describes a spin-coupled triplet pair that is spatially separated and has lost electronic coherence, and $2T_1$ are two uncoupled triplet excitons. The rate of the first step – the triplet-pair generation – is extremely fast with 70-100 fs in PEN thin films [41]. The second and third steps are more elusive and an unambiguous assignment of kinetic rates is difficult. Some studies report the rate of the second step on the ps-ns time scale for PEN derivatives [44, 46]. Spatially separated triplet excitons have been reported to give a different photo-induced absorption (PIA) [44, 47]. In the end two uncorrelated triplets are created. The overall lifetime of the triplets in PEN thin films is more well-founded with a few nanoseconds [48]. For the above mechanism the following criteria are crucial: (1) energy level matching at the single molecular level: $E_{S_1} \geq 2E_{T_1}$ and $E_{T_2} \geq 2E_{T_1}$ [40], which ensures that the splitting of a singlet excitation into two triplets is thermodynamically feasible, while triplet-triplet annihilation (TTA) is not; (2) strong electronic coupling between molecular aggregates i.e, $S_1 \rightarrow {}^1(T_1T_1)$[37] and (3) efficient excitation dynamics, including that the correlated triplet pair $^1(T_1T_1)$ evolves into two independent triplets T_1 that can physically separate from each other. These criteria are referred to as (1) energetic, (2) coupling, and (3) separation criterion, respectively.

Recent publications indicate that prior to the emergence of free triplets, quintet states ^{5}(TT) are populated [50, 51]. Lubert-Perquel et al.[51] proposed that a parallel orientation of the chromophores favours the formation of quintets and ultimately free decorrelated triplets. In addition, the displacement along the long molecular axis Δx in a slip-stacked configuration is also of crucial importance. Pensack et al.[54] reported that without a displacement, i.e. $\Delta x = 0$ the TQY almost disappears.

Here, we investigate PEN embedded in a surface-anchored metal-organic framework

(SURMOF), which we denote by ZnPn. The PEN linker forms a coordination bond with the Zn^{2+} dimer nodes, creating a parallel orientation with $\Delta x \neq 0$. The difference in geometry compared to the PEN thin film has an enormous impact on both the observed dynamics and electronic properties. The geometry provides one-dimensional channels for charge transport, which may also favour the separation of triplet pairs. In addition, anchoring at the surface produces a high crystalline order and also facilitates attaching electrical contacts for device applications in comparison to a MOF powder [87]. Regarding the SF properties, the sample exhibits extraordinarily long triplet lifetimes compared to other bulk materials with PEN as SF chromophore, which is beneficial for light harvesting devices. At the same time, the slowdown in triplet exciton generation is less drastic. Additionally, the prominent triplet-pair absorption of the PEN thin film in the near-infrared (NIR) spectral region is almost absent in the ZnPn.

5.2 Results

5.2.1 Steady state characterization

The UV/vis absorption spectra of ZnPn compared to a PEN thin film on a glass substrate are shown in Fig. 5.1b). The $S_0 \rightarrow S_1$ transition in the PEN thin film, shows Davydov splitting with absorption maxima at 670 and 632 nm [88, 89, 90]. Furthermore, peaks at 585, 545 and 500 nm are observed, which probably stem from a vibronic progression or CT transitions [88, 91]. In contrast to the thin film, the ZnPn sample does not show a Davydov splitting, a vibronic progression with maxima at 525, 565 and 610 nm is observed. As in the PEN thin film there are two molecules in a unit cell, but in ZnPn they are separated by the Zn-oxo-metal node. Apparently, there is no significant coupling across the node to lift the degeneracy of energy levels. However, there is a substantial coupling between the PEN linkers in [001] direction expected, since a hypsochromic shift of 50 meV compared to linkers in solution was found [87]. For the theoretical models we can confirm the energetic requirements $E_{S_1} \geq 2E_{T_1}$ and $E_{T_2} \geq 2E_{T_1}$ for SF. For the pentacene molecule TD-DFT calculations using B3LYP/def2-TZVP- with D3 Correction yield $E_{S_1} = 1.81\,\text{eV}$, $E_{T_1} = 0.69\,\text{eV}$ and $E_{T_2} = 1.92\,\text{eV}$. For the pentacene linker in the MOF $E_{S_1} = 1.85\,\text{eV}$, $E_{T_1} = 0.62\,\text{eV}$ $E_{T_2} = 1.93\,\text{eV}$.

5.2.2 Excited state dynamics

Before presenting and discussing the ZnPn results we will revisit the characteristic features of the thin film structure whose fs-TA spectra are shown in Fig. 5.2a). The ground state bleach (GSB) is located at 670 nm and the bleach at 584 nm likely stems from a vibronic sideband [93, 94]. The broad positive signal ranging from 750 to 1050 nm is associated with the $T_1 \rightarrow T_2$ transition [41, 93, 95, 96]. It is surmised that it is enhanced in the solid state compared to PEN in solution [93]. The $T_1 \rightarrow T_3$ transition can be observed at 540 nm and becomes stronger when the angle of incidence of the probe beam is not perpendicular to the substrate surface (see also Fig. SA.2) [95, 97]. This is because the transition dipole moment is aligned along the long axis of the molecule, which itself arranges upright on the substrate, i.e. long molecular axis and surface normal are almost parallel. This PIA is delayed and

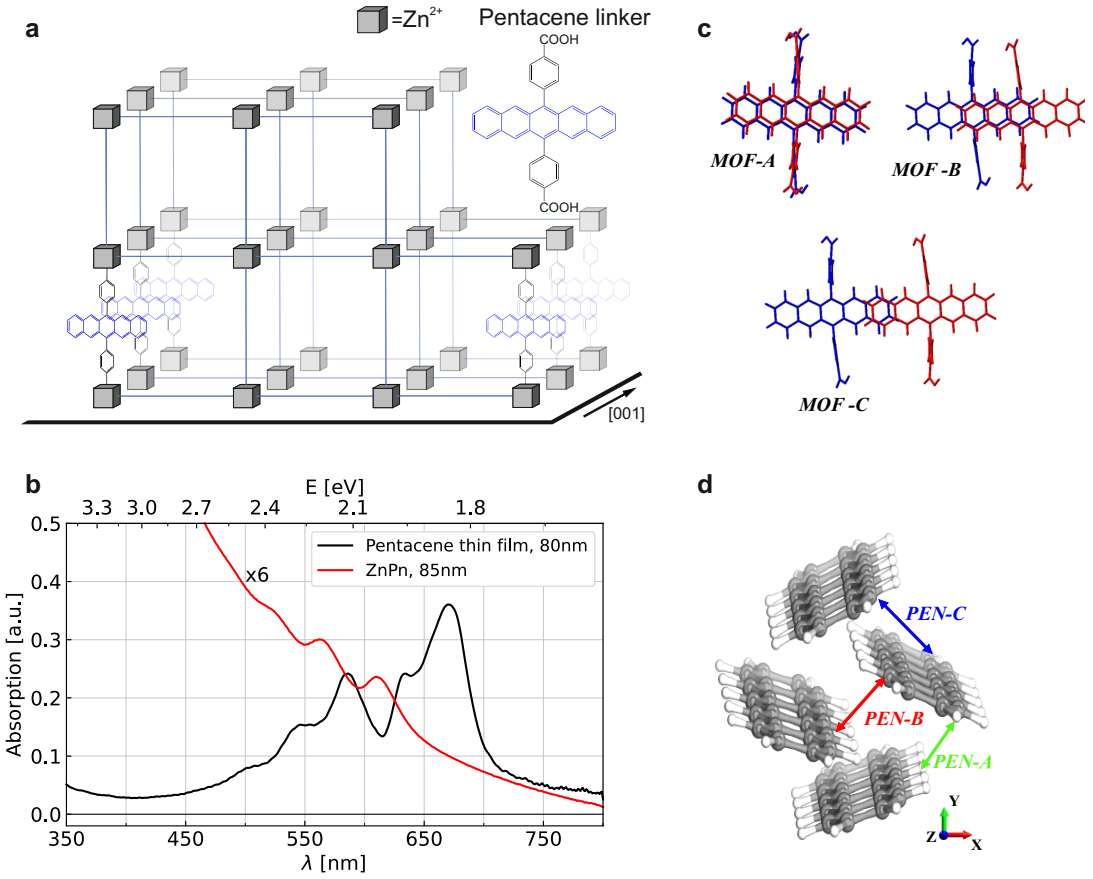

Figure 5.1: a) Schematic of the ZnPn SURMOF structure. Blue lines indicate the PEN linkers. Adaptation from Ref.87. b) Absorption spectra of PEN thin film (black) and ZnPn (red) on quartz substrates. c) Dimer pair geometries considered in the computational part of this work. The MOF-A, B and C models were constructed by placing the pentacene linkers in a coplanar geometry at a distance of 3.58 Å and then stacking both linkers with respect to the xy plane (see Table 2). d) The pentacene dimers PEN-A, B and C were obtained from the experimental crystal structures of PEN [92].

has a rise time of approximately 1 ps [97]. Interestingly, in addition to the known $T_1 \rightarrow T_3$ and $T_1 \rightarrow T_2$ transitions, we also observe a PIA centred at 340 nm. To our knowledge, this PIA has not been detected with TA before. We propse that it is related to a triplet-triplet transition (see SI for detailed information).

We will now turn to the discussion of the ZnPn sample. Fig. 5.2c) shows transient absorption spectra of ZnPn with an excitation wavelength of 605 nm for selected pump-probe delays and Fig. 5.2b) compares the dynamics of the PEN thin film and ZnPn. At first sight, it is obvious that the TA data do not resemble those of the thin film, but these spectral features

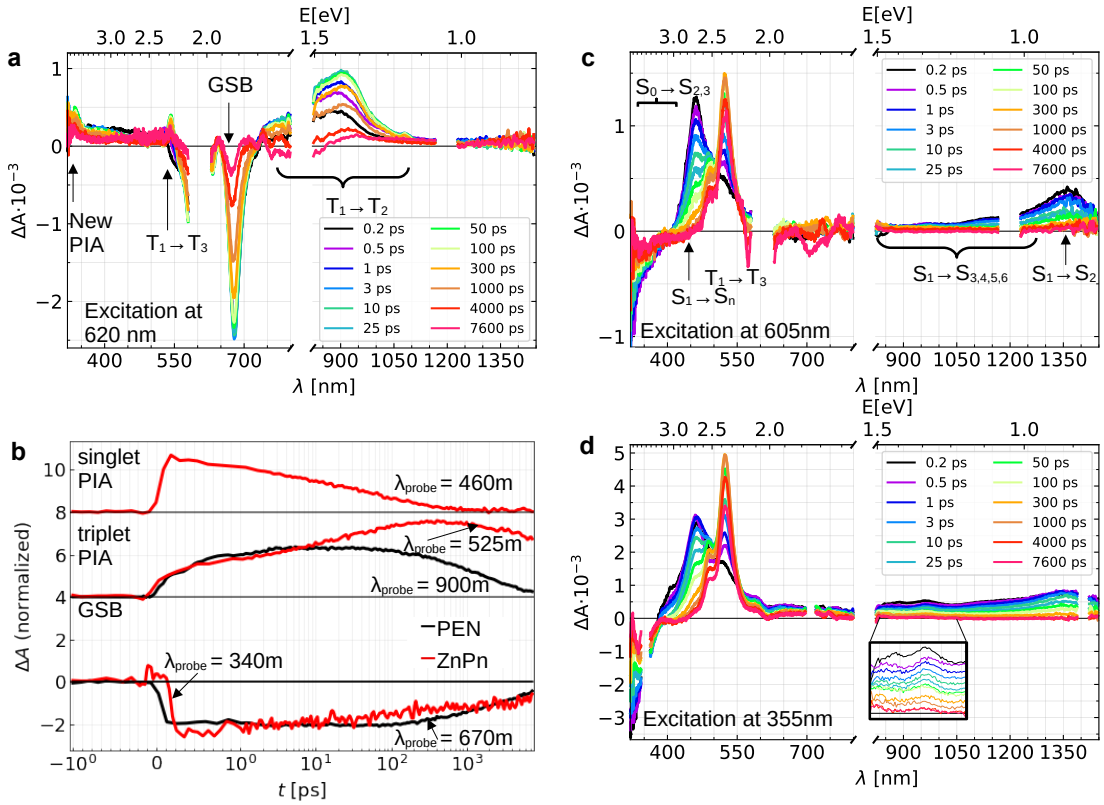

Figure 5.2: a) fs-TA spectra of PEN thin film excited at 620 nm. The visible spectrum was probed at 50° angle of incidence (424 µJ cm^{-2}) and the NIR spectrum at 0° angle of incidence (495 µJ cm^{-2}). b) Kinetics with normalized signal comparing characteristic wavelengths corresponding to PIAs of singlets or triplets and the GSB in ZnPn and the PEN thin film. Note that especially the PIA of triplets at 525 nm for ZnPn is overlaid with the PIA of singlets. c) fs-TA spectra of ZnPn excited at 605 nm (424 µJ cm^{-2}). d) ZnPn excited at 355 nm (141 µJ cm^{-2}.) The inset highlights the region where triplet-induced absorption is anticipated.

are fairly well-known for PEN in solution, especially for linked dimers which have been studied extensively [30, 98, 99, 100, 101, 102]. Most prominently a transformation of the initially formed PIA peaking at 460 nm to a state with maximum absorption at 525 nm is apparent. We attribute the PIA centred around 460 nm to the $S_1 \rightarrow S_n$ transition and the PIA at 525 nm to $T_1 \rightarrow T_3$ in accordance with literature [100, 101, 102, 103, 104]. Furthermore, a broad PIA can be observed in the NIR region, with a main absorption at 1360 nm corresponding to the $S_1 \rightarrow S_2$ transition, based on our calculations and literature [101]. The nearly identical decay of the PIAs at 460 nm and 1360 nm (Fig. SA.6) also confirms that these spectra originate from the same states. This is also verified by global analysis (GA). The PIA between 700-1000 nm is the most prominent sign of triplet excitons in the PEN thin film and an according signal can not be identified in ZnPn for an excitation wavelength of 605 nm. In the range from 900 to 1100 nm a weak absorption can be seen for ZnPn. Still, it shows the same dynamics as for

1360 nm and in comparison to our calculations, it is likely that it corresponds to excitations to higher singlet states ($S_{3,4,5,6}$; compare Table SA.15). Calculations in a PEN dimer in face-to-face orientation predict a weak triplet PIA in this spectral region and enhanced intensity with increasing intermolecular coupling [53]. For higher excitation energies (355 nm) we observe a weak PIA that outlasts the singlet PIA. Our measured values for fs-TA can be well modelled with three sequential exponential decays. The obtained Evolution Associated Difference Spectra (EADS) are shown in Fig. 5.3.

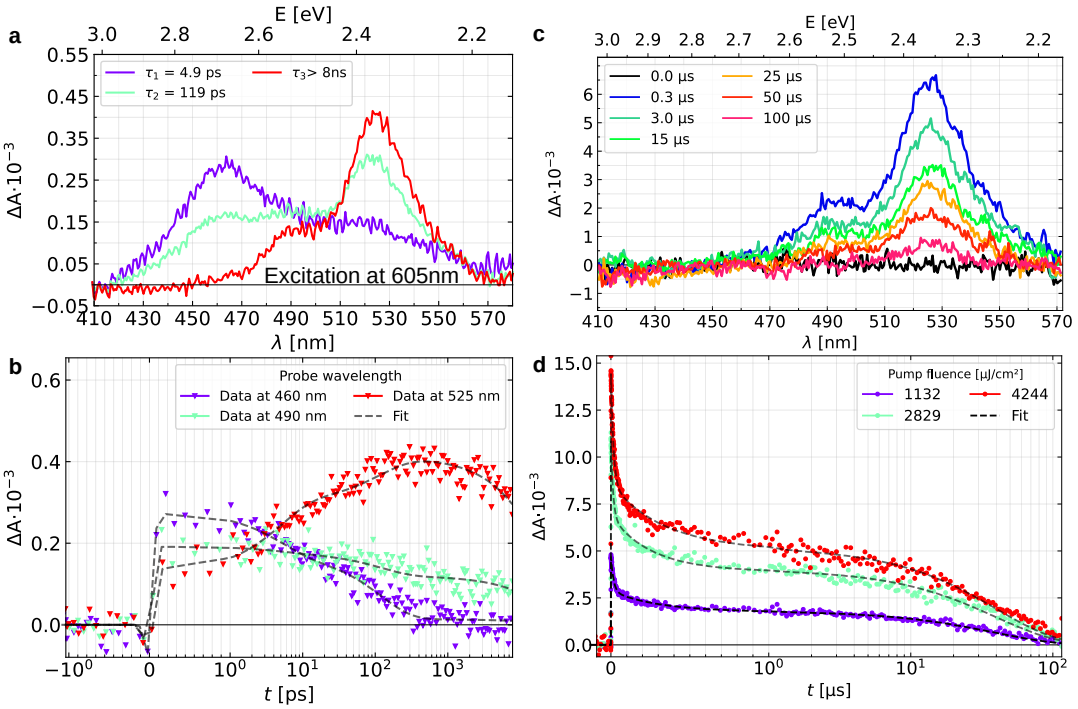

Figure 5.3: a) EADS of ZnPn excited at 605 nm with 141 µJ cm^{-2}. The data are fit with three sequential exponential decays. The transient spectra are assigned to the singlet excited state (S_1S_0) (purple), the intermediate state ^{1}(TT) (green) and the triplet excited state ^{m}(TT) (red). b) Time traces of fs-TA data of ZnPn excited at 605 nm with 141 µJ cm^{-2} at selected wavelengths. Data at 460 nm and 525nm are associated with singlet and triplet PIA, respectively. Note that the time is plotted semi-logarithmic with a linear scale between −1 ps and 1 ps. c) µs-TA spectra of ZnPn excited at 605 nm with a pump fluence of 3540 µJ cm^{-2} at selected time frames d) µs-TA kintetics of ZnPn excited at 605 nm for different pump fluences probed at 525 nm, associated with triplet PIA. The dotted line is a fit with three parallel decays from GA.

We attribute the first EADS, which appears immediately after excitation to the singlet excited state (S_0S_1) due to its main absorption at 460 nm. It decays with a time constant of approximately 4.9 ps into a state showing characteristics of both singlet and triplet excited state absorption. Therefore we are inclined to assign the second EADS to the $^1(T_1T_1)$ intermediate state. The decay at 460 nm and concomitant rise of the triplet signature at

525 nm can be clearly seen in Fig. 5.3. It was proposed before that $^1(T_1T_1)$ exhibits spectral features of both species [28, 35]. With that we argue the rate for triplet-pair generation to be on the order of a few picoseconds (4.9 ps) in ZnPn, whereas in the PEN thin film triplet-pairs are created within 70-100 fs. The comparative slowdown in this rate is most likely explained by a weaker electronic coupling in ZnPn which in turn results from a higher CT state energy, as computed in our theoretical study. Ritesh et al.[87] have shown that the SURMOF structure allows for frustrated rotations, and hence fluctuating electronic coupling is possible. From the analysis we conclude that the $^1(T_1T_1)$ state decays with a time constant of ∼119 ps. For a selection of PEN derivatives the decay of the $^1(T_1T_1)$ state has been observed to be ∼ 1 ps, which again demonstratesthe slower dynamics in ZnPn [44]. The third EADS exhibits a vibronic structure peaking at 525 nm and 490 nm. We assign this spectrum tentatively to the $^5(T_1T_1)$ state. As outlined above, from the parallel alignment of the chromophores the generation of the quintet pair state might be promoted [51].

The maximum delay of the fs-TA setup is 7.8 ns, therefore the third time constant is given as >8 ns and µs-TA measurements were conducted to probe the long lived excitations. Fig. 5.3c) shows the µs-TA of ZnPn at an excitation wavelength of 605 nm. The spectra show the known signature for triplets and essentially no change in shape – apart from amplitude – can be seen over the whole time range.

Most remarkable is the long lifetime of the triplets, which is four orders of magnitude larger than the lifetime in the PEN thin film 10 ns [48]. In the semi-logarithmic plot, it is easy to see that at least three time constants are involved in the dynamics. In fact, the data can be fitted well with a model of three parallel exponential decays. The time constants obtained from GA are τ_3 =20 ns, τ_4 =350 ns, and τ_5 = 40 µs. As the numbering suggests, we assign the slowest time constant from the fs-TA data with the fastest of the µs-TA measurements. We chose to use a parallel decay instead of sequential decays, due to the following argument: Assuming that the different triplet states can not be distinguished spectrally, no change should be detected until the free triplets decay to the ground state. In this case, a monoexponential decay would be expected after the emergence of the triplets. The observation of further time constants together with the decrease of the PIA at this stage, points to loss channels between the transformation of different triplets states. In particular, in the process with time constant τ_3 =20 ns, many triplets are lost. Compared to 1 ns, only about 45% are still present after 100 ns.

Triplet-triplet annihilation: We could observe a fluence dependence, which becomes especially clear in Fig. SA.8 with normalized signal intensities. There, only the triplet population decreases with higher fluence whereas the singlet signal intensities are unaffected. This lets us conclude that we do not observe singlet-singlet annihilation but instead triplet-triplet annihilation (TTA). Faster decays with increasing fluence are detected also in PEN thin films and crystals, which is attributed to TTA, and therefore is an indicator of free triplets [93]. We expect free triplets, since in a highly ordered bulk structure – like this SURMOF considered here – delocalization and entropy are driving factors for separation [30, 105].

Dynamics including higher excited states: To test for a dependence on the excitation wavelength, we excited the sample with 355 nm. Fig. 5.2d) shows the TA spectra for selected

delays. The broad PIA extending from the NIR to the visible range is enhanced. In addition, the ratio of the maxima at 525 nm and 460 nm is larger than that for an excitation with 605 nm. Since the singlet and triplet PIAs overlap considerably it is better to compare the ratio $R_{T/S}$ of the maxima of the EADS from GA, which are listed in table 1. From the larger ratios we conclude, that the TQY is increased by approximately 21% compared to an excitation with 605 nm. Furthermore, a decrease in $R_{T/S}$ with increasing fluence is apparent, which is consistent with the fluence dependence due to TTA discussed earlier. The broad PIA in the NIR region decays simultaneously with the PIA at 1360 nm, except for two peaks at 950 nm and 855 nm, which outlast it; see inset of Fig. 5.2d). We attribute these peaks to the $T_1 \rightarrow T_2$ transition that has been missing in the spectra when exciting with light at a wavelength of 605 nm.

However, there is no concomitant rise in signal strength following the triplet feature in the visible range. It has to be noted that also the PEN cation absorbs in this spectral range [106]. To compare the dynamics, kinetics with normalised intensity are shown in Fig. SA.9. There are only slight deviations, e.g. at 460 nm, which we attribute to the difference in TQY together with the normalisation of the data. As the time evolution remains essentially the same, it suggests either that the initially excited state does not need to relax before undergoing SF, as Wilson et al.[41] have argued as well for the PEN thin film or that a relaxation to S_1 is ultrafast.

$\lambda_{ex} = 605$ nm		$\lambda_{ex} = 355$ nm	
Fluence [µJ cm^{-2}]	$R_{T/S}$	Fluence [µJ cm^{-2}]	$R_{T/S}$
141	1.41	14	1.71
283	1.44	42	1.75
566	1.36	57	1.71
1061	1.30	89	1.71
1415	1.25	141	1.68
4244	1.12		

Table 1: Ratio $R_{T/S}$ of maxima of EADS associated with triplets and singlets obtained from global analysis for different excitation energies and pump fluences.

5.2.3 Modelling Results

To better understand the influence of the partially unresolved structure on the electrooptical properties we have undertaken a comprehensive quantum mechanical analysis of the exciton dynamics in singlet fission for both pentacene, which serves as a reference system, and models of potential dimer configurations in the metal-organic framework. In the following sections, we explain how the molecular models influence the rate of singlet fission and the lifetime of triplets.

Choice of slip-stacked model: A minimal morphology model comprising at least two chromophores is necessary to study the SF process. Since the geometric configuration

of the MOF dimer pairs remains experimentally unavailable, we have therefore created a series of possible configurations based on the known constraints from the MOF structure and subsequently subjected to quantum chemical calculations. The dimers in these models are placed in a slip-stack configuration and denoted as MOF-A, MOF-B and MOF-C. The π-π distance $d_{\pi\pi}$ is kept constant at 3.58 Å for all dimers and the displacement Δy in the direction of the short molecular axis is initially set to Δy=0 and the geometry optimization resulted in small displacements of $\Delta y \sim 1.1\text{-}1.2$ Å for all dimer models. The main parameter to monitor the changes in photophysical properties is the "slip" Δx along the long molecular axis. This was varied from 1.81 Å for MOF-A to 6.87 Å for MOF-B and finally 9.48 Å for MOF-C. For MOF-A this results in almost face-to-face π stacked dimers. The strong interaction between the chromophores in this configuration, promotes efficient electronic coupling and charge transfer processes, facilitating rapid excitation dynamics and triplet generation. MOF-B shows face-to-face as well as edge-to-face interaction. In contrast, MOF-C exhibits the maximal stacking displacement, resulting in the least π-π interaction. Instead, edge-to-face interaction and interaction via short C$\cdots$H contacts become more prominent. In the subsequent analysis, we also analyse the three known relative dimer orientations for the PEN thin film for comparison. The three dimer orientations in PEN exhibit different π-π distances and orientations resulting from variations in the relative orientation of pentacene molecules in the herringbone crystal lattice. As shown in Fig.5.1d), PEN-B forms a slip-stacked herringbone with a π-π interaction, while the PEN-C and PEN-A dimers feature a herringbone arrangement with a CH-π interaction (see also Table 2).

Dimer pair	Long axis (Δx)	short axis (Δy)	$\pi - \pi$ (Δz)
PEN-A	1.81	5.73	7.58
PEN-B	1.72	6.72	5.98
PEN-C	1.78	3.21	5.75
MOF-A	1.81	1.21	3.58
MOF-B	6.87	1.05	3.58
MOF-C	9.48	1.18	3.58

Table 2: Relative shift along x, y and z axes (Å) in for dimer pairs of PEN as obtained from the crystal structure and MOF dimer models.

Characteristics of Charge Transfer Excitations: In accordance with the methodology described by Berkelbach et al (Eq.43) for the superexchange mechanism, it is helpful to analyse the charge transfer characteristics (CT) in a donor-acceptor (D-A) dimer, because CT intermediates are likely to influence the SF process. To explore the significant impact of charge transfer characteristics in D-A dimers the transition dipole and spatial overlap are computed for up to six excited states of a molecule as represented schematically in Fig. SA.14. In PEN a high transition dipole moment and low spatial overlap are associated with S1 (2.3 D) and S6 (14.7 D) while for the MOF models, we find 2.01 D for S_1 which means, the corresponding states can develop favourable CT excitations upon geometrical shift. Finally, we illustrate the CT character with respect to the frontier molecular orbital (FMO)

energies of both systems in Fig.5.4, aiming to understand the CT mechanism from an orbital perspective. Visual representations of FMO character and charge density plots help in comprehending the distribution of charge density during excitations, thereby offering insight into the CT process.

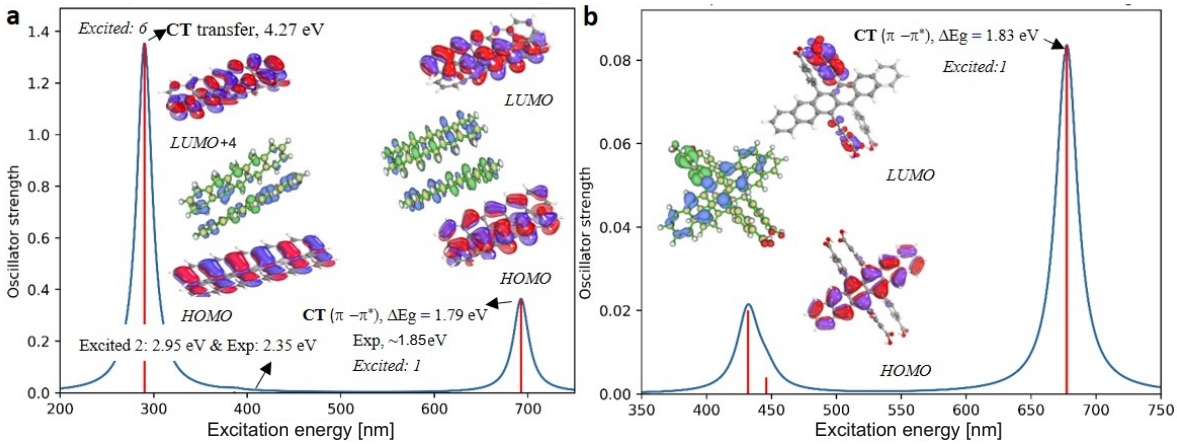

Figure 5.4: Spectra and charge density plots illustrating the CT character of electronic states in the D-A dimers within the frontier molecular orbitals a) computed PEN-spectral data compared to the experimental absorption peak positions, highlighting the most reliable values of vertical excitation energies. Molecular orbitals (MOs) and electron densities (ED) are depicted, with blue representing the hole and green representing the electron obtained by DFT/def2-TZVP. b) Spectral data for the MOF models.

Within the PEN framework, SF will occur in D-A dimers comprising a donor core, serving as the primary photon absorption site with a dominant CT contribution in its S_1 state, which transfers part of the charge density to the acceptor featuring a low-lying triplet state [107]. The electronic states corresponding to charge transfer to the triplet manifold are determined to be at 1.79 eV for S_1 (exp; 1.60 eV) [108], predominantly resulting from a HOMO→LUMO transition in the leading configuration, identified as a bright state π - π^*, while other states exhibiting local-excitation characteristics, appear to be dark (see spectral data cf. Table SA.15). In the MOF models the state ordering remains comparable, suggesting suitable charge transfer (CT) with the lowest-lying state (S_1) dominated by an H→L transition. The state of interest falls within an energy window of 1.83 eV, with the transition exhibiting a higher oscillator strength associated with a bright π - π^* transition in the MOF. The large dihedral angle between the MOF core and the substituent in the molecule slightly increases E_{S_1}, with the excitation energy (EV) distribution centred at 1.83 eV, whereas the chromophore interactions in the crystalline PEN models slightly reduce E_{S_1} = 1.79 eV. As a result, the low-lying excited states in the MOF will be primarily characterized by charge transfer within the acceptor (donor) core, thereby favouring CT. The remaining states predominantly exhibit a dark LE character (cf. Table SA.15).

Effective-electronic coupling and rate of singlet fission: The effective electronic

couplings between the S_0S_1/S_1S_0 and the ^{1}TT states are crucial for determining the rate. Table 3, presents effective coupling energies J_{eff} for SF based on calculated coupling matrix parameters (cf. Table SA.16). The calculations for the PEN models exhibit the largest coupling of 16.80 meV for the PEN-C model. This modulation in coupling may partly result from stacking changes imposed by the crystal structures. Notably, among the three derivatives, the calculated coupling constants are in reasonable agreement with those calculated by Chao et al.[109].

In the MOF models, the largest effective coupling associated with the least displacement along the long axis Δx (MOF-A) (Δx = 1.81, Δy = 1.21) is $\sim$ 21.53 meV where the coupling involving the CT states also exhibits high values (Table 3). However, a longitudinal displacement along the x-axis leads to a significant decrease in couplings, nearly vanishing at around $\sim$ 3 meV for model MOF-C. For example, the electronic coupling decreases by about -17 meV when comparing the MOF-A to the MOF-B configuration (Fig. 5.1).

	E_{S_1}[eV]	E_{CT}[eV]	E_{T_1}[eV]	J_{eff}[meV]
PEN-A	1.79	2.03	0.77	5.49
PEN-B	1.79	2.09	0.77	0.72
PEN-C	1.79	2.08	0.77	16.80
MOF-A	1.83	2.03	0.58	21.53
MOF-B	1.83	2.12	0.58	3.2
MOF-C	1.83	2.80	0.58	2.2

Table 3: The effective electronic coupling between FE and ME of PEN and MOF dimer models. Experimental values for the pentacene thin film are E_{S_1} = 1.83 eV and E_{T_1} = 0.86 eV [110]. From UV/vis measurements of ZnPn we extract E_{S_1} = 2.03 eV.

We note that the superexchange coupling may interfere destructively, potentially leading to complete cancellation through the leading configurations. It is worth noting that E_{CT} is significantly sensitive to the packing configuration of the monomer in a dimer (Table 3).

Rate of singlet fission from Marcus theory: To evaluate the feasibility of employing these dimers in organic photovoltaics (OPVs), we have calculated an estimate of the rate of formation K_{SF} of the multi-excitonic state using Eq.44. The reorganization energy and Gibbs free energy of charge transfer play a significant role in the Marcus approach. As expected, ΔG values are negative, indicating that the initial states are higher in energy than the final states. Considering that the reorganization energy of PEN is estimated to be in the range of 108-136 meV and in the MOF it is 116-201 meV, the reorganization energies vary between 30 and 80 meV for PEN and MOF models, respectively, for different configurations (cf. Figure SA.15). As a result, K_{SF} varies by two orders of magnitude among various dimer configurations.

Our findings suggest that a variation in the stacking geometry of the two molecules in the dimer can indeed have a substantial impact on the kinetics of the SF process, confirming the expected influence of the intermolecular geometry [111, 112]. It is worth noting that the variations in K_{SF} follow the trend determined by the one-electron coupling parameter J_{eff}, as shown in Table 3. In this context, PEN-C exhibits a high SF rate of approximately

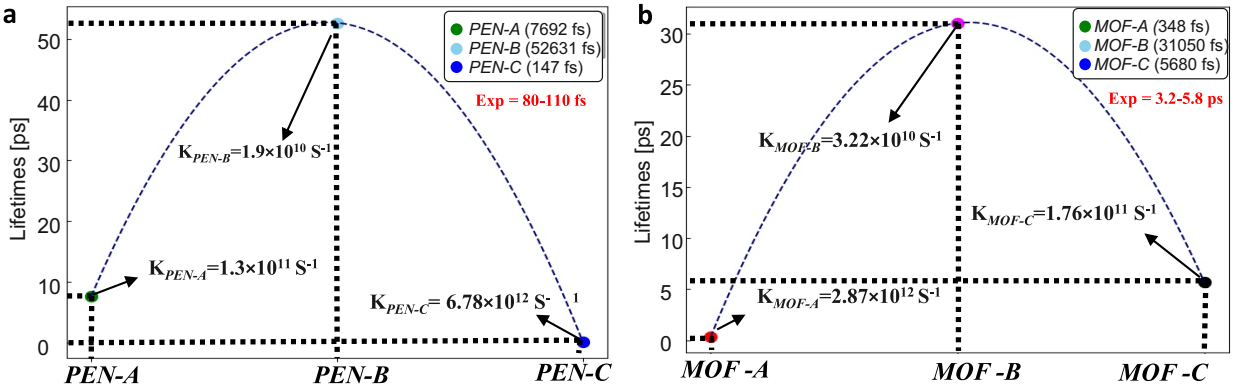

Figure 5.5: The singlet fission rates for PEN and MOF models as calculated by the Marcus rate equation.

∼147 fs and possesses the largest coupling energies (∼16 meV). Conversely, the other two molecules exhibit negligible effective coupling values of 0.72 meV and 5.47 meV, accompanied by significantly longer time constants of about ∼ 7-50 ps. The observed trend of SF rates (PEN-C > PEN-A > PEN-B) correlates closely with the trend identified for the effective coupling (Table 3). It is important to note that PEN-C and PEN-B possess very similar values of the $\pi - \pi$ distance (Table 2), yet they differ by nearly a factor of 10 in SF conversion rate. The highly favourable geometry for ultrafast SF, as exhibited by PEN-C can be rationalized by the computational results, specifically highlighting the electronic coupling between the S_1S_0 and ^{1}(TT) state. Hence, PEN-C is considered the geometry for further analysis.

Considering the MOF models, we find that MOF-A shows the highest SF conversion, while MOF-B exhibits the lowest, thereby resulting in SF rates of 0.348 ps or 31.05 ps respectively. MOF-C shows a SF rate of 5.68 ps, a value consistent with experimental findings (exp: 3.2-5.8 ps). The SF rate constant decreases in the order: MOF-A (J_{eff} = 21.53 meV) > MOF-C (J_{eff} = 2.2 meV)>MOF-B (J_{eff} = 3.2 meV). Here, the trend of rates does not follow the effective coupling, but the reorganisation energy can explain the change in order. While MOF-B and C have similar effective couplings J_{eff}, MOF-B exhibits a higher reorganisation energy (λ =201 meV) than MOF-C (λ = 132 meV), slowing down the rate in MOF-B. In summary we find that the dimer geometry of MOF-C results in the closest match between the calculated coupling strength and the experimental SF rate constant.

Excited state dynamics: After reaching the S_1 state during dynamics, three kinetically competitive excited-state deactivation pathways from S_1 to the ground state may unfold: radiative and non-radiative deactivation pathways [113]. These reaction channels were explored through nonadiabatic excited-state dynamics simulation of materials, as their significance for SF has been well established. The kinetics of the rate constants (K_{SF} and K_r) for the reference compound PEN and MOF are depicted in Fig. 5.6, which also incorporates available experimental data.

The multi-excitonic generation reaction (K_{SF}) unfolds several orders of magnitude faster than the competing fluorescence process (K_r), highlighting that the initial spectral features

arise from S_0S_1, whereas the later time features are attributed to ^{1}(TT) and (T_1+T_1) in both materials. The decorrelated (T_1+T_1) state is mediated by spin mixing with a quintet correlated triplet pair ^{5}(TT). The energy of the lowest singlet excited state $E_{S_0S_1}$, was determined as $E_{S_0S_1}$ = 1.79 and 1.83 eV for PEN and MOF respectively. Intermolecular coupling between the chromophores decreases $E_{S_0S_1}$ by approximately $\sim$ 200 meV compared to that of respective monomers. The S_1 energy changes depend on the relative orientation in both materials, as differences in the crystal structures influence dipole-dipole interactions and orbital overlap between the chromophores, ultimately altering the electronic structure in the solid state [114]. The multi-excitonic energies E_{TT}, for both materials were estimated as E_{TT} = 1.54 eV and 1.16 eV for PEN and MOF respectively. Therefore, the corresponding energy gap of $|E_{FE}$-$E_{TT}|$ is determined as ΔG_{ST} = 0.25 eV and 0.67 eV for PEN and MOF respectively. Even slight changes in the S_1-T_1 energy gap can result in significant changes in the SF dynamics. The observed CT energies reveal that the CT state energy of MOF-C is approximately 0.80 eV higher than that of PEN. As the energy of the virtual CT state decreases, the SF rate is expected to increase, but only until the CT state energy is nearly isoenergetic to or falls below that of the $S1_1$ and ^{1}(TT) states. The time constant obtained from ESD analysis shows that PEN has comparable SF efficiency with a time constant of 147 fs, consistent with experimental results indicating the formation of triplets in a few femtoseconds (exp.:80-110 fs). The MOF model features a slower triplet formation with a maximum of 31 ps for MOF-B and 5.68 ps for MOF-C which agrees best with the experimental values (exp: 3.2-5.8 ps). The excited state energies of both materials are depicted in Fig. 5.6.

5.3 Discussion

From the findings of the TA experiments and our calculation, we motivate the kinetic model for pentacene in the metal organic framework in Fig. 5.6b). For comparison the results for PEN are displayed in Fig. 5.6a). They agree well with previously published experimental and theoretical studies. We therefore believe that we can determine the relative orientation of the linkers in the MOF by comparing the calculated rates with experimental data. In the MOF we observe the generation of the triplet pair state ^{1}(T_1T_1) within a few picoseconds (4.9 ps) which is also the case for the model MOF-C (5.68 ps). This transition is promoted by the significantly polar CT character of the excited state through the superexchange mechanism. This slowdown in the rate compared to PEN (70-100 fs) can be rationalised by the higher CT state energy in the MOF model. The triplet signature peaking at 525 nm is formed from the intermediate state ^{m}(T_1T_1) with approx. 119 ps. We assign this spectrum to the state ^{m}(TT) with the assumption that m=5 due to the slipped stacked geometry, which promotes the pathway via quintets to free triplets [51]. Before the separation of the triplets, it is assumed that a spin-correlated but electronically decorrelated state with spatial separation of the excitons exists [44]. Therefore, we assign the second to last step to the state ^{5}(T$\cdots$T). As explained in the section on µs-TA, relaxation pathways to the ground state are probably responsible for the observed time constants of τ_3 =20 ns and τ_4 =352 ns. Finally, the triplet signature can be observed to decay to the ground state with a lifetime of 40 µs. Together with the observed TTA at high fluences we assume that free triplets are generated.

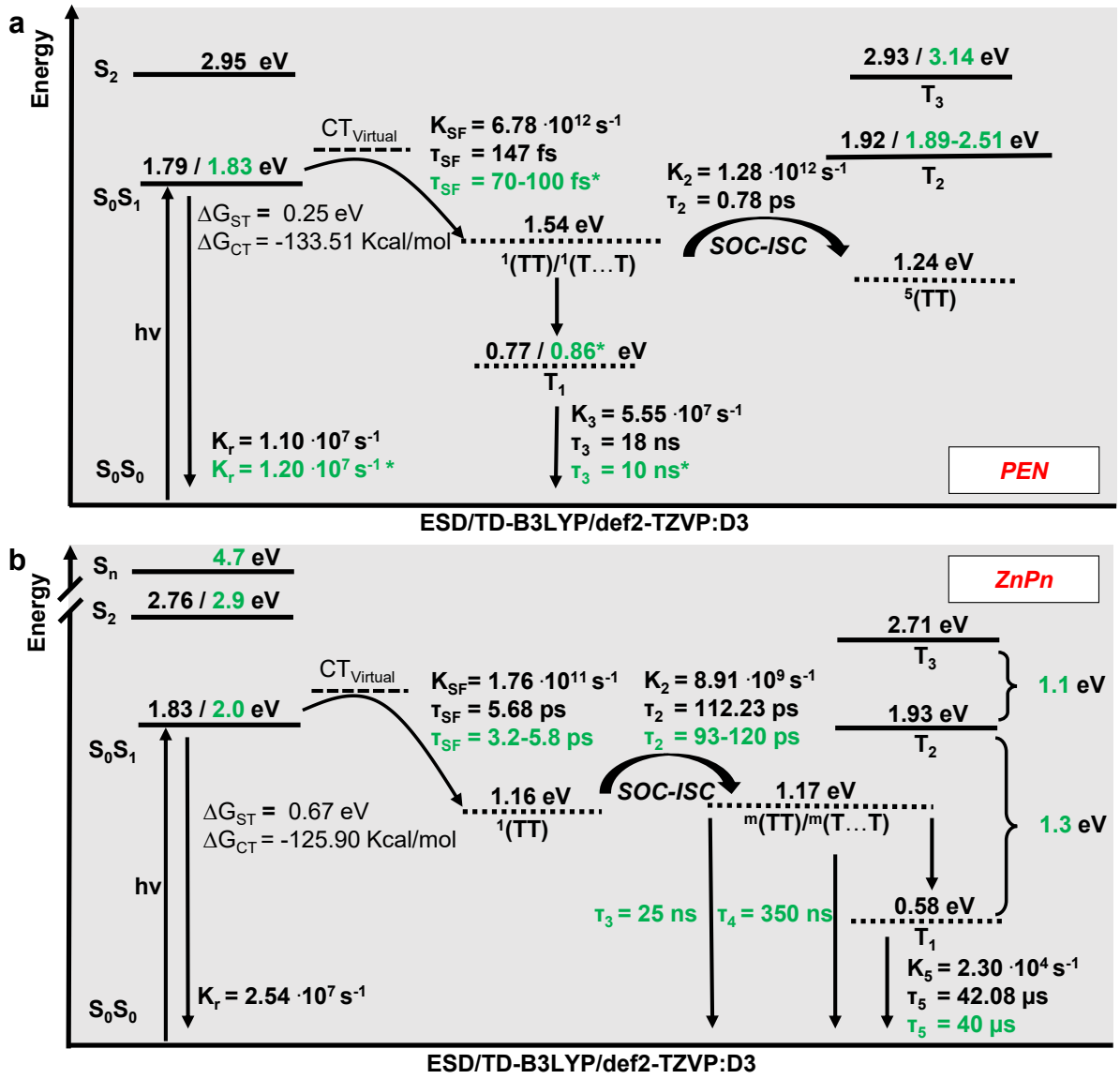

Figure 5.6: Photo-dynamic relaxation pathway illustrating the rates of radiative and non-radiative decay of a) PEN and b) ZnPn obtained from experimental (green) and theoretical simulations of the MOF-C dimer (black); internal lifetimes are computed as $\tau_r = 1/k_r$. Experimental values with a star are taken from the literature [41, 48, 110, 115].

In summary, we have used a molecular engineering approach, exploiting the conformational freedom of MOFs to arrange pentacene moieties differently than in the PEN crystal. We characterized the ultrafast optical properties by experiment and theory. Clear evidence is found for triplet exciton generation. The change in geometric arrangement compared to the thin film structure has two major impacts: It slows down the triplet-pair generation by roughly two orders of magnitude, but at the same time the triplet lifetime is extended by

almost four orders, which is an extremely promising improvement regarding the feasibility of SF materials. The ability to achieve such novel molecular arrangements inaccessible in pure organic crystals significantly enhances the SF energetics. We find that manipulation of the π-π stacking distance is pivotal for optimizing intermolecular coupling in SF and will inform the design of next-generation MOF-based materials.

5.4 Methods

5.4.1 Sample fabrication

The SURMOF (ZnPn) structure with Zn as metal nodes and the PEN linker as phenyl-carboxylate substituted pentacene at 6- and 13-positions were prepared by a spin-coating layer-by-layer method on quartz substrates, which is described elsewhere in more detail [87]. The film thickness was controlled by the number of spin-coating cycles, which amounts to 85 nm for 75 cycles in our case. For comparison neat PEN thin films were fabricated by thermal evaporation at a base pressure of $6.2 \cdot 10^{-9}$mbar and a growth rate of 6 Å min^{-1}. Both samples were sealed under nitrogen atmosphere with a second glass to minimise possible effects due to photo-degradation.

5.4.2 UV/vis and TA spectroscopy

For steady-state UV/vis spectroscopy a UV-2600i Shimadzu spectrometer was used. Transient absorption measurements were carried out with commercially available setups for short and long timescales (HELIOS and EOS, Ultrafast Systems). The output of a Ti:sapphire amplifier (Coherent Astrella) at 800 nm and a repetition rate of 4 kHz was used in a commercial optical parametric amplifier (TOPAS Prime, Light Conversion) to create the excitation pulse. The autocorrelation of the excitation pulse centred at 605 nm was about 47 fs assuming a gaussian pulse shape, measured with a commercial autocorrelator (pulseCheck, APE). For fs-TA a supercontinuum with a spectral range of 320 nm-800 nm was created by focusing the Ti:sapphire output into a CaF_2 crystal. By focusing on a sapphire crystal instead, a supercontinuum was created ranging from 820 nm to 1500 nm. The delay of up to 8 ns was controlled by a motorised delay stage. To observe longer time-dynamics up to 200 µs an electronically operated delay was employed. In this case, an external laser system (Leukos) generates a white light spectrum from 350 nm-900 nm. The cross-correlation for this setup was about 350 ps.

The samples were excited with energies of 50 nJ up to 3000 nJ corresponding to 4244 µJ cm^{-2}, and the polarisation of the pump beam was set parallel to the probe beam polarisation. Pump and probe beam were focused with parabolic mirrors and were estimated to be 300 µm and 200 µm at the sample position, respectively. Changes in absorbance ΔA we measured, therefore PIA appears as positive values and stimulated emission (SE) and ground state bleaching (GSB) as negative. The open source software Glotaran was used for global analysis of the TA data [82].

5.4.3 Computational Methods

To elucidate the mechanism of SF we employed a methodology based on density functional theory (DFT). Specifically, the equilibrium structures of singlet ground (S0) and the first triplet (T1) state of the systems were computed using Density functional theory (DFT) using the B3LYP hybrid exchange-correlation functional [116, 117, 118, 119]. Singlet (S) – Triplet (T) adiabatic energy differences and T-T couplings were computed using ground

state DFT (unrestricted wave functions were employed for triplets), which is referred to as ΔDFT. To analyse the structural minima harmonic vibrational frequencies were computed using the Aoforce program implemented in Turbomole 7.4.1 program. To assess the energetic criterion for singlet fission, vertical excitations and excited state geometry optimizations were computed using time-depended density functional theory (TD-DFT) [120]. Throughout, the valence triple zeta basis set with polarization functions (d,p) (TZVP) was chosen [121]. Dispersion interactions were incorporated using Grimme's empirical dispersion correction (D3-Correction) [122]. All optimizations were conducted without any symmetry constraints, the point group symmetry was identified as D_{2h} for Pentacene (PEN), and C_i for the Pentacene-MOF models (MOF) with D_2 and C_i symmetries determined to be the minimum energy structures for PEN and MOF respectively. All DFT/B3LYP and TD-B3LYP calculations were performed using Turbomole 7.4.1 program [123]. The electronic couplings for SF were calculated using the methodology described by Berkelbach et al[124] for the super-exchange mechanism,

$$J_{eff} = \langle S_1 S_0^1 | \widehat{V} | T_1 T_1^1 \rangle = \langle S_1 S_0^1 | \widehat{H}_{el} | T_1 T_1^1 \rangle - \frac{2(V_{LL}V_{LH} - V_{HH}V_{HL})}{E_{CT} - E_{TT} + E_{CT} - E_{S_1}} \tag{43}$$

In this expression, the first term of the right-hand side accounts for the contribution of the direct channel to the overall SF coupling while the second term accounts for the charge-transfer mediated superexchange coupling mechanism. The first term will be ignored in the subsequent analysis since the direct two-electron coupling $\langle S_1 S_0^1 | \widehat{H}_{el} | T_1 T_1^1 \rangle$ is assumed to be small compared to the four one-electron couplings, V_{if} [125, 126]. V_{LH} is the Fock matrix element between the LUMO in the donor and the HOMO in the acceptor, and the other matrix elements are defined similarly. E_{CT} and E_{TT} are the energy of the charge transfer states and of TT [$\sim$ 2E (T1)], respectively. The rate constant for the transformation of the locally excited (LE) state into the multiexcitonic ^{1}(TT) state can be calculated as,

$$k_{SF} = \frac{2\pi}{\hbar} |J_{\text{eff}}|^2 \frac{1}{\sqrt{4\pi\lambda_{if} k_B T}} e^{-\frac{(\Delta G_{if} + \lambda_{if})^2}{4\lambda_{if} k_B T}} \tag{44}$$

Here, λ is the reorganization energy, and ΔG_{if} is the Gibbs free energy difference between the initial and final states i.e, $\Delta G_{if} = E_{S_0 S_1} - E_{TT}$. Finally, the rate of intersystem crossing K_{ISC} and fluorescence K_r were benchmarked using the excited state dynamic module (ESD) implemented by Orca 5.O.4 program package [120]. The reliability of our calculations was verified by comparing them with the available experimental values of PEN demonstrating excellent agreement between the experimental and computed values (cf. Table SA.13).

Author contributions

P.T. and W.W. oversaw the project. P.L. synthesized the PEN dicarboxylic acid. Z.X. fabricated the SURMOFs. C.H. fabricated the neat PEN thin films. Transient absorption spectroscopy was carried out by M.R. and P.V.K. M.R. carried out data analysis. Simulations were carried out by M.J.K. The paper was written by M.R. and M.J.K. with equal contribution and with contributions from P.V.K., W.W. and P.T.

Competing interests

The authors declare no competing interests.

Correspondence

Correspondence and material requests should be addressed to Petra Tegeder and Christof Wöll.

Data availability

The data and code that support the findings of this study are available from the corresponding authors upon request.

5.4.4 TR-SHG on the pentacene SURMOF

For the TR-SHG experiments, a regenerative amplifier was used (RegA Coherent, 300kHz, 800 nm) which is seeded by a mode-locked Ti:sapphire. The resulting beam has a bandwidth of about 25 nm and a pulse length of about 56 fs. The beam is then split in two to prepare the pump and probe beams. The probe beam is passed through a piezo-driven stage to set a delay of up to 200 ps. To prepare the pump beam, an optical parametric amplifier (OPA) is used. Here, a central wavelength of 615 nm with a FWHM of 24 nm was used. Both beams are compressed by optical prism compressors and focused on the sample. The temporal and spatial overlap is adjusted on a GaAs sample. A cross-correlation of 68 fs was found, which corresponds to a pulse width of 48 fs assuming gaussian shaped pulses. Both beams are linearly polarized and the directions are controlled with half-wave plates. They are either set to p or s implying that the polarization is parallel or perpendicular to the plane of incidence, respectively. After reflection on the sample at an angle of incidence of 45° with respect to the surface normal, the second harmonic light is collimated, selected by a monochromator and detected with a photo multiplier tube. The fluences of pump and probe beam were 300 µJ cm^{-2} and 3000 µJ cm^{-2}, respectively. Each data set shows an average of at least 50 measurements on at least five different spots of the sample. The measurements were performed under inert gas atmosphere (N_2) at room temperature. The data were normalized to 1 before the excitation and then fitted with the following model:

$$f(t) = (A - B)e^{-kt} + B \tag{45}$$

To better describe the data, the function was additionally convolved with a Gaussian function having the width of the measured cross-correlation.

Results of SHG measurements: To increase the efficiency of solar cells through SF, the triplets must be harvested. This means that they have to diffuse from the SF material to the semiconductor of the solar cell to create an electron-hole pair. Therefore, the interface between the SF layer and the semiconductor plays a crucial role and we additionally investigated the ZnPn sample with TR-SHG, to observe what happens outside the bulk volume.

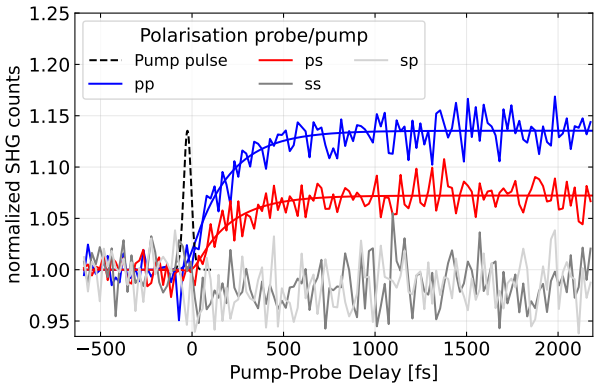

Figure 5.7: TR-SHG data of ZnPn on sapphire with an excitation centred at 615 nm.

The results are shown in Fig. 5.7, which shows the SHG intensity after excitation with a pulse centred around 615 nm. The different configurations of polarisation are indicated by p or s, where the first letter belongs to the probe, and the second to the pump beam. Within the range of the stage, the signal remains constant after the first rise, so only the first 2.2 ps are shown. It can be noticed that an s-polarised probe beam only gives minimal signal intensity, telling us that the breaking of inversion symmetry is best observed perpendicular to the surface normal. Hence, we conclude that the signal is generated at interfaces between sample and substrate, rather than at grain boundaries. Using the fit model from Eq.45 we obtain the parameters $\tau_{pp} = 201 \pm 26$ fs, $A_{pp} = 0.003 \pm 0.012$, $B_{pp} = 0.1354 \pm 0.0018$ and $\tau_{ps} = 195 \pm 34$ fs, $A_{ps} = -0.0098 \pm 0.0097$, $B_{ps} = 0.0722 \pm 0.0016$. The data with an s-polarised probe beam were not fitted. We surmise to observe SF here as well, as this is the major process to be expected in this pentacene derivative.

How come we are observing such a fast SF here? From discussions with professor Wöll it is suspected that the SURMOF structure is not fully developed within the first few nanometers. There the arrangement of the organic linkers is not constrained as in the MOF structure. Then a higher SF rate is conceivable due to a geometry favouring triplet-pair generation, although the benzoic acid side chains likely cause steric hindrance. A faster singlet fission at the interfaces might be detrimental to triplet harvesting. As pointed out by Korovina et. al and mentioned earlier, a fast triplet-pair generation often comes along with a short lifetime [30]. Therefore, the final yield might decrease due to lifetime reduction of the triplets at the interface.

6 Charge separation in a porphyrin-based metal-organic framework incorporating fullerene

In this chapter, TA spectroscopy is used to investigate the excited state dynamics of a SURMOF loaded with fullerene (C_{60}). The organic linkers are porphyrin-based, which exhibit high absorption cross sections in the visible spectral region and are good electron donors. In the previous publication by Liu et al.[62], the unloaded SURMOFs showed a low conductivity, which increased by loading with C_{60}. More interestingly, in this system the conductivity can be increased by two orders of magnitude by exciting the Soret band of porphyrin($\sim 435\,\mathrm{nm}$) with light. This is explained by a fast charge separation between the porphyrin linker and C_{60} and subsequent hole or electron conduction along the porphyrins or fullerenes in the [001] direction. The charge transfer dynamics between ZnTPP (5,15-bis-(3,4,5-trimethoxyphenyl)-10,20-bis-(4-carboxyphenyl) porphyrinato zinc(II)) and C_{60} is the subject of this section. In the following the SURMOF samples are called Zn(TPP) and C_{60}@Zn(TPP). ZnTPP refers to the linker used in the SURMOF or in general zinc tetraphenylporphyrin.

The chapter starts with an introduction to the photophysical properties of fullerenes and porphyrins and their interaction, in particular the charge transfer between the molecules. Then the sample preparation, structure and properties previously described by Liu. et al [62] are briefly reviewed in section 6.2. This is followed by the presentation of the TA experiments and their discussion. First, the excitation of the Soret band (6.3.1) and the Q-band (6.3.2) of Zn(TPP) and finally an excitation of C_{60} are described (6.3.3). The effects of the different excitation energies are compared in section 6.3.4 and the time constants obtained are discussed in section 6.4.

6.1 Introduction

Porphyrins have been intensively investigated because of their promising photophysical and electronic properties. Potential applications are in the fields of photovoltaics, photoconductivity and catalysis [62, 127, 128, 129]. The naturally occurring chlorophylls, which have porphyrin as their backbone, are considered to be the role model for the conversion of solar energy. They occur in many variations that optimise the use of solar energy. In general, porphyrins are excellent light absorbers. The so-called Soret or B band in the visible spectral range has an extraordinarily high extinction coefficient. The Soret band ($\sim 435\,\mathrm{nm}$) is assigned to the S_0-S_2 transition and the S_0-S_1 transition, named Q band ($\sim 500-700\,\mathrm{nm}$), is very weak. However, the transitions do not occur from the HOMO to LUMO, LUMO+1, etc. Instead the Soret band corresponds to the HOMO-1 to LUMO (and LUMO+1) transition and the Q band to the HOMO to LUMO (and LUMO+1) transition. The energy scheme of the orbitals is shown in Fig.6.1, which is based on the four-orbital model of M. Gouterman [130, 131]. According to this model, there are four frontier molecular orbitals and, in principle, two B bands (B_x,B_y) and two Q bands (Q_x,Q_y). The indices x and y denote the direction of the transition dipole moment in relative to a molecular coordinate system. As a complex compound with a central metal atom, the porphyin backbone is symmetrical, which

is why the transitions are degenerate in both directions. Without a central metal atom, these free base porphyrins show a splitting of the bands. The Q-band often exhibits vibronic contributions as well.

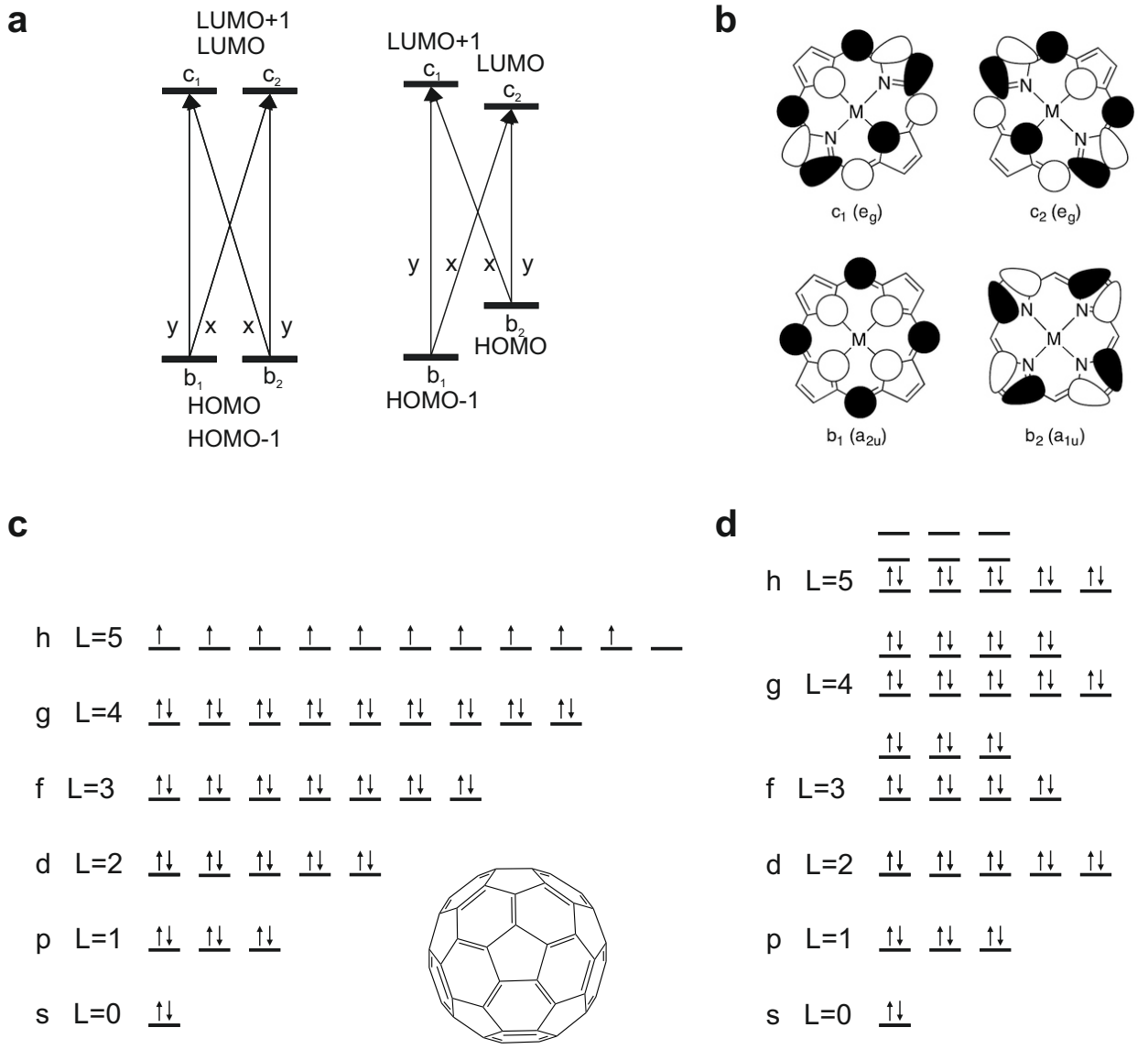

Figure 6.1: **a** Scheme of the energy levels of the four frontier orbitals involved in the photophysics of porphine based chromophores. On the right, the degeneracy of the states is lifted. **b** Illustration of the molecular orbitals on the metallated porphine. **c** Spherical harmonic energy levels with 60 electrons distributed by Hund's rule. L is the angular momentum quantum number. **d** Energy levels after invoking the icosahedral symmetry of C_{60}. Figures taken or adopted from Ref.[132] and [133].

In addition to being light absorbers, porphyrins can be used as charge and energy donors. A suitable electron acceptor is C_{60}, which can reversibly accept several electrons, which is demonstrated in numerous studies [129, 134, 135, 136, 137, 138, 139]. A consideration of the π electrons in the closed spherical potential well would lead to the conclusion that C_{60} itself is a conductor as there is an almost half filled shell, see Fig.6.1 c). However, if the icosahedral symmetry is taken into account, the level scheme in 6.1 d) arises, showing that the neutral C_{60} is an insulator. A special feature of fullerenes is the low reorganisation energy λ during charge transfer. In the context of the Markus theory, the process takes place in the normal Markus region, which means that only a low driving force (ΔG) is required to enable rapid charge separation. Charge recombination, on the other hand, takes place in the inverted Markus region. Therefore, a lower reorganisation energy causes the recombination to slow down. In both cases, the effects are therefore favourable for potential applications. Furthermore, fullerenes are interesting for various areas of organic electronics due to their electrical conductivity.

Porphyrins and C_{60} were studied intensively in combination. A wide range of dimers were analysed using both experimental and theoretical methods. Good reviews, among others, are [140, 141, 142, 143]. The compounds are realised by different interactions: Covalent bonds, π-π interactions, polar interactions, hydrogen bonds and complex formation. The electron transfer takes place in a single step and results in a C_{60} radical anion and a porphyrin radical cation. These so-called photo-induced single step electron transfer (PISET) processes are usually fast and there are no intermediate steps in which additional energy is lost. The major disadvantage, however, is that charge recombination (CR) is also comparatively fast. Photo-induced multi-step electron transfer (PIMET) processes include a further electron transfer (ET) step in which the charges are further separated from each other. This reduces the energy to be extracted from the photons in each ET process, but significantly increases the ET efficiency. This is exactly what happens in photosynthetic reaction centres with close to 100 % ET efficiency [142]. In trimers, PIMET can be realised by a third molecule and ensure extraordinarily long lifetimes of the charge separated (CS) states [135, 142]. Some results of the investigations on porhyrin-fullerene systems are briefly mentioned here: A short distance between the molecules is advantageous for fast charge separation. Common centre-to-centre distances in two-molecule systems are 6.5 to 9.5 Å [140, 141, 144]. There are various effects of metallisation of H_2TPP with zinc. A comprehensive overview of the photophysical parameters of H_2TPP and ZnTPP is given in Ref.[145]. It should be mentioned that the extinction coefficient of ZnTPP with $\epsilon = 560\,000\,\mathrm{cm^{-1}\,M^{-1}}$ is greater than that of H_2TPP with $\epsilon = 460\,000\,\mathrm{cm^{-1}\,M^{-1}}$ at a wavelength of maximum absorption. A higher extinction coefficient is beneficial for the photon conversion efficiency (PCE). In general the metallated systems show inter system crossing (ISC). Therefore, the lifetime of the singlet state is composed of the decay by fluorescence, internal conversion $S_1 \rightarrow S_0$ and ISC. In D/A systems, the generation of CS states is also possible from the respective triplet states of porphyin based donor [141]. In the context of fullerenes, a theoretical study using DFT calculations shows that the charge transfer increases with -0.01e, -0.20e and -0.38e from H_2TPP:C_{60} via MgTPP:C_{60} and ZnTPP:C_{60} [146].

6.2 Material preparation and characterisation

The SURMOF structure is depicted in Fig.6.2. The samples were prepared by Zhiyun Xu in the group of Professor Christof Wöll at in the Karlsruhe Institut für Technologie (KIT). The organic linker is ZnTPP. The sample is prepared in a layer-by-layer synthesis by spin-coating the components. Each layer consists of a cycle of spin-caoting ethanolic metal acetate solution and subsequently the ethanolic linker molecule solution. The C_{60} molecules are incorporated by a further spin-coating process after depositing the organic linker. This completes one cycle. The samples investigated here, were prepared to yield a film thickness of 60- 70 nm. For further details see Ref.[62]. The films were deposited on quartz substrates (thermo scientific, quartz microscope; slide, fused, 25.4x25.4x1.0mm).

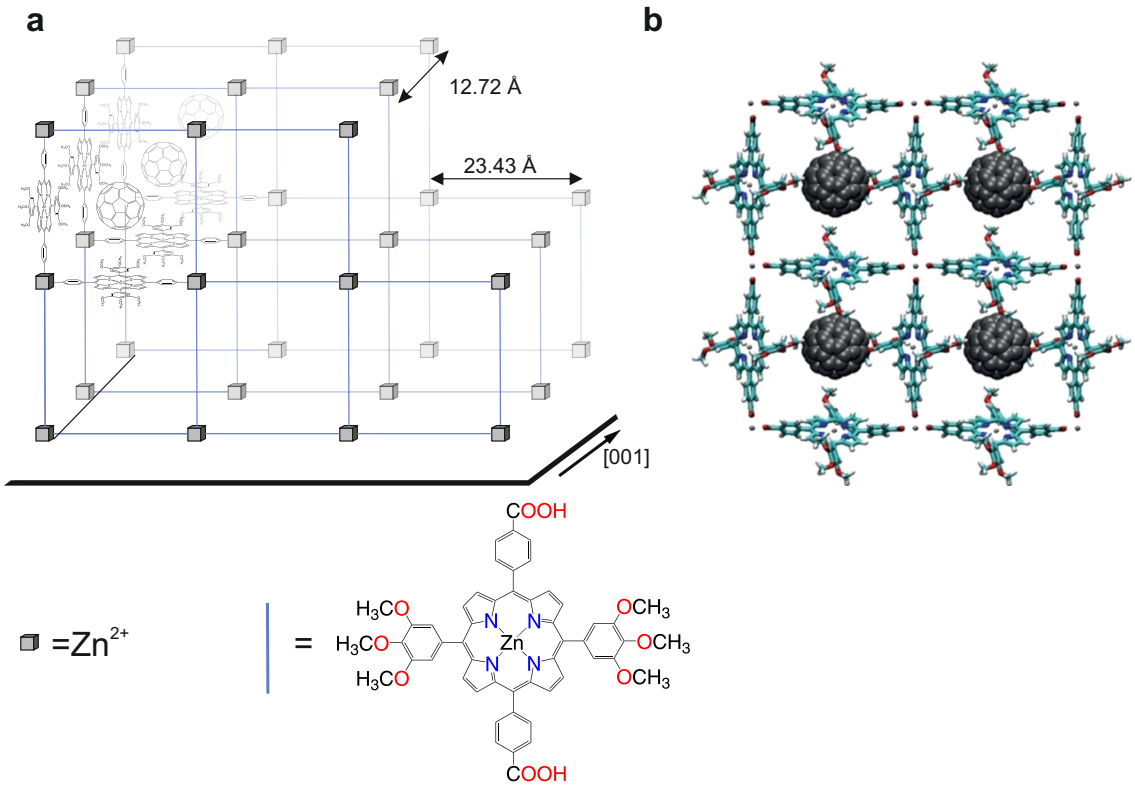

Figure 6.2: **a** Schematic of the SURMOF C_{60}@Zn(TPP). Blue rods indicate the ZnTPP linker and Zn^{2+} dimers are shown as grey cubes. **b** Molecular structure as obtained by DFT optimisation. Taken from Ref.[62].

The structure was already characterized in Ref.[62]. It was found from XRD measurements, that the SURMOFs exhibit a high degree of order and are predominantly grown along the (100) direction. They also estimated the percentage of filled pores by C_{60} to be 90-92%. AFM images show a homogeneous height distribution.

The molecular geometric and electronic structure was also investigated by computation

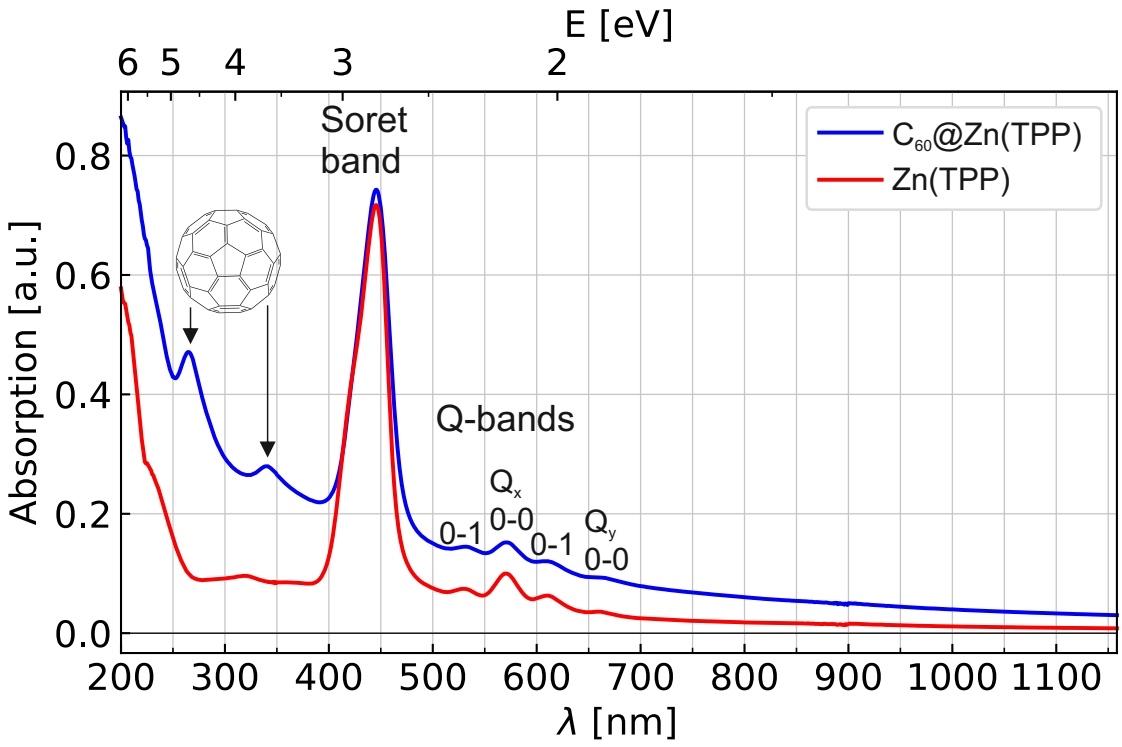

Figure 6.3: UV/vis absorption spectra of Zn(TPP) and C_{60}@Zn(TPP) SURMOFs.

[62]. Between the porphyrin linkers a closest distance of 2.27 Å and a center of mass (COM) distance of 12.72 Å was found. The COM distance of C_{60} is 12.72 Å and the closest distance is 5.78 Å. The smallest distance between C_{60} and the porphyrin linkers is 2.81 Å (compare SI of [62]). The UV/vis spectra of the SURMOF samples with C_{60} (C_{60}@Zn(TPP)) incorporated and the empty SURMOFs (Zn(TPP)) are shown in Fig.6.3. The Q- and Soret bands are clearly discernible. Non-degenerate Q_x and Q_y transitions can be observed as indicated. Furthermore the vibronic transitions (0-0) and (0-1) for both Q_x and Q_y transitions are observable. The peaks are located at 446, 531 ,571, 608 and 651 nm for C_{60}@Zn(TPP) and 445, 530 ,571, 610 and 660 nm for Zn(TPP). As described previously, the Soret band exhibits the highest extinction coefficient. For Zn(TPP) a small shoulder on the high energy side ($\sim$ 425 nm) is observable. This might be attributed to either a splitting of the LUMO levels or a vibronic transition. The double peak structure is much clearer in the TA data shown in the next section. The UV/vis spectrum of C_{60}@Zn(TPP) shows two additional absorption bands at 340 and 265 nm. They belong to the ground state absorption of the fullerene C_{60}, as can be seen by comparison to a neat film of C_{60} [147]. Furthermore, the Soret band shows a slight change of shape. This is a potential sign of electrostatic interaction of the frontier molecular orbitals of C_{60} and the porphyrin linker. This has also been observed in a D/A structure linking tetrakis (4-carboxyphenyl) zinc porphyrin (ZnTCPP) and ethylenediamine functionalized fullerene (C_{60}-EDA)[148]. However, a significant broadening of the peak as

well as a redshift was observable. The redshift points to a smaller band gap, due to electron delocalisation. Within the uncertainty there is no redshift observable in C_{60}@Zn(TPP).

6.3 Results

The samples were excited at the Q-band $\lambda_{ex} = 605\,\text{nm}$ and at the Soret band with $\lambda_{ex} = 435\,\text{nm}$. Furthermore with $\lambda_{ex} = 264\,\text{nm}$ a transition of C_{60} was adressed. First, the main absorption at the Soret band will be discussed. Then Q-band and C_{60} excitation are described afterwards.

6.3.1 Excitation of the Soret-band

Each graph is the result of two to three individual experiments to cover the spectral range shown. The UV, VIS and NIR ranges as described in the introduction were used for this purpose. Note that not all ranges were measured with the same fluence in order to obtain an improved SNR (signal to noise ratio).

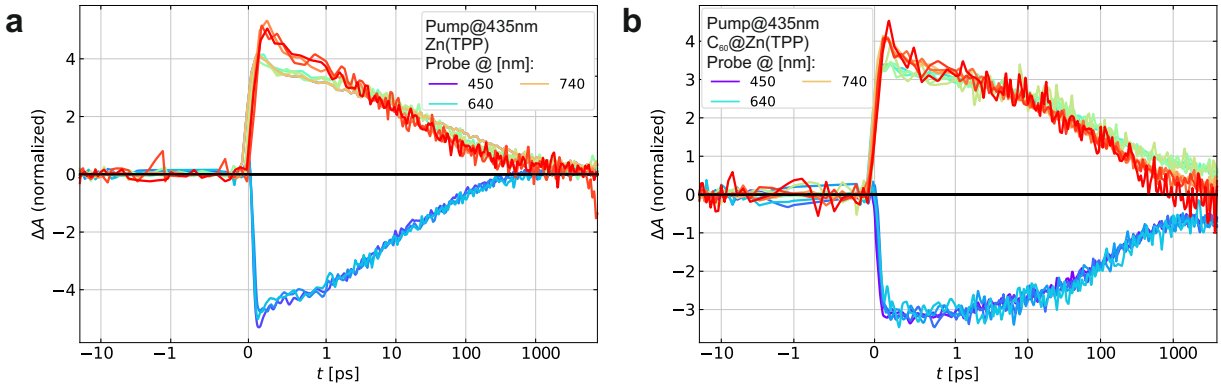

Figure 6.4: Fluence dependence of Zn(TPP) **a** and C_{60}@Zn(TPP) **b** with 25, 50, 150, 200 nJ and 25, 100, 150, 200, 320 nJ per pulse, respectively, for three different probe wavelengths. Data are normalised by dviding through the integral of the first 10 ps after excitation. Note that the delay time is given with a linear scale between -1 and 1 ps and with a logarithmic scale elsewhere.

It should therefore be established beforehand that the dynamics do not depend on the intensity of the pump beam used. For this purpose, the samples were excited with different fluences and the data obtained were normalized and superimposed. This makes it easy to show whether the dynamics vary. The time course at different wavelengths of the probe beam is shown in Fig.6.4. A dependency can be ruled out here, as the samples show no dependency on the fluence within the parameters used. A possible cause for a dependence on the fluence would be bimolecular processes such as singlet-singlet or triplet-triplet annihilation due to a high excitation density.

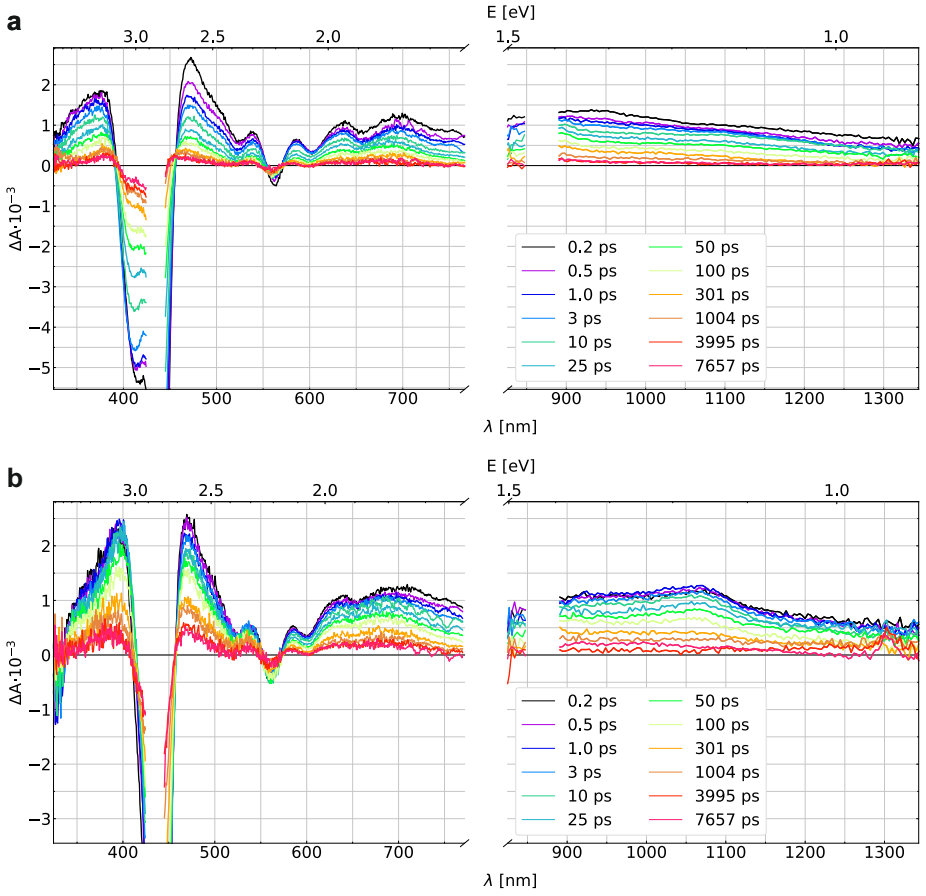

Figure 6.5: TA spectra of **a** Zn(TPP) and **b** C_{60}@Zn(TPP) after excitation with a wavelength of 435 nm. The data were obtained from several experiments to cover the whole spectral range as shown and rescaled accordingly. The data for Zn(TPP) and C_{60}@Zn(TPP) consist each of three measurement, covering the UV, visible and near infrared spectral region with 50 nJ, 200 nJ and 200 nJ, respectively. Data at 435 nm± 10 nm are removed, due to the overlaid signal from scattered pump beam light.

The TA measurements of the Soret Band excitation are shown in Fig.6.5. The GSB can be seen for Zn(TPP) in Fig.6.5 a) from 380-450 nm as a negative signal. Furthermore, some local minima can be seen, which are superimposed by a broad ESA that covers the entire observed spectrum. The ESA is composed of spectra of overlapping molecular states, which is why a clear assignment is not possible [149, 150]. The GSB of the Q bands are at 525 nm ($Q_x(1,0)$), 561 nm ($Q_x(0,0)$), 602 nm ($Q_y(1,0)$) and 658 nm ($Q_y(0,0)$) can be seen. Thus, the energy difference of the vibronic levels between $Q_x(1,0)$ and $Q_x(0,0)$ is 164 meV and between $Q_y(1,0)$ and $Q_y(0,0)$ is 180 meV. These minima blue-shift in the observed period by approximately 3 nm.

It is also noticeable that another dip can be seen at 730 nm. This cannot be explained by the ground state absorption, as the lowest transition is at 658 nm ($Q_y(0,0)$). This could be attributed to SE, as has also been observed with other porphyrin complexes [26].

The ESA in the range of 820-1300 nm is attributed to singlet-singlet absorption [135]. After the maximum delay time of approximately 8 ns the system has not yet completely returned to the ground state, which can be recognized by the GSB at 450 nm. For porphyrins, it is known that the singlet state S_1 changes to the state T_1 through ISC. The triplet state of porphyrin often shows an ESA at the lower energy side of the GSB [129, 151, 152]. This can also be observed in the TA spectrum of Zn(TPP), where the maximum of the ESA at 470 nm shifts to 460 nm for long times.

In Fig.6.5 b) the TA spectra of C_{60}@Zn(TPP) are shown. A broad ESA is detected, similar to the observed ESA in Zn(TPP). The GSB of the Soret band at 435 nm has a different shape corresponding to the ground state absorption, in particular only one minimum is recognizable. The minima of the GSB of the Q-band are at 524 nm ($Q_x(1,0)$), 562 nm ($Q_x(0, 0)$), 600 nm ($Q_y(1,0)$) and 655 nm ($Q_y(0,0)$). In contrast to Zn(TPP), no clear blue shift of the minima can be observed here. Furthermore, there is also no shift of the maximum of the ESA at 470 nm.

The influence of C_{60} in the SURMOF can be observed in the UV spectral range at 330 nm and in the NIR at 1070 nm. The negative signal at 330 nm can be assigned to the GSB of the C_{60} molecules. Fig.6.6 e) shows the evolution in time of the signal. It can be seen that the signal does not appear instantaneously, which would be the case if the corresponding state was populated directly. Instead, the signal develops over a few hundred femtoseconds. This indicates that the expected charge transfer from the porphyrin linkers to the C_{60} fullerenes is taking place in this time regime.

At 1070 nm a peak is discernible that is not present in Zn(TPP). This can be attributed to the $C_{60}^{\bullet-}$ anion absorption [153, 154]. Likewise, the signal is not present immediately after excitation and shows a rising amplitude. It should also be noted that in the associated UV/Vis spectrum, no absorption of $C_{60}^{\bullet-}$ anions can be seen in order to rule out the possibility that $C_{60}^{\bullet-}$ anions are present in the ground state. In that case a negative signal would be seen after excitation of the $C_{60}^{\bullet-}$ anions.

With the direct proof of the formation of the ESA by $C_{60}^{\bullet-}$ anions at 1070 nm, the fast charge separation as expected by Liu et al.[62] can be confirmed. A more detailed analysis of the data to get a clear picture of the dynamics will be performed in the next section.

Global anlysis after Soret band excitation of Zn(TPP)

In the following, the data are analyzed with Glotaran [82]. The difference absorption decay spectra (DADS) are calculated. This means that a sum of exponential decays is fitted. The DADS are shown in Fig.6.6 a)-d). The dynamics discussed below can also be shown in the time domain at selected wavelengths of the probe spectrum (Fig.6.6 e)-h)). At these wavelengths, significant differences occur when the SURMOF is loaded with C_{60} fullerenes.

A minimum number of four time constants is required to fit the data for Zn(TPP). The corresponding DADS are shown in Fig.6.6 a) and b) for the visible and near-infrared range. Time constants of $\tau_1 = 135\,\text{fs}$, $\tau_2 = 4\,\text{ps}$, $\tau_3 = 84\,\text{ps}$ and $\tau_4 = 6.7\,\text{ns}$ are obtained

In the literature, a state S_2' is postulated for ZnTPP in solution with a biexponential decay of 200 fs and 1 ps [26]. The S_2 state decays monoexponentially with 1.45 ps in the model. Within the S_1 state, vibrational relaxation with 5 and 12 ps takes place and with a time constant of $\tau = 2\,\text{ns}$ the state transitions to T_1 via ISC.

Another study investigated a SURMOF with 5,15-diphenyl-10,20di(4-carboxy phenyl) porphyrin. [155] The results found there should be quite comparable, since the linkers used there only lack the six methoxy groups (compare Fig.6.2 a)).The authors find three time constants with the global analysis: $\sim$1 ps, $\sim$25 ps and a long process with $>$100 ns. As in other studies on metalloporphyrins, the ultrafast transition is assigned to the internal conversion (IC) of S_2 to S_1 [152, 155]. The second time constant is attributed to vibrational relaxation in the S_1 state. The last time constant is attributed to the lifetime of the triplet state.

Therefore, the first time constant can be attributed to the IC from S_2 to S_1 with $\tau_1 = 135\,\text{fs}$. The second time constant with $\tau_2 = 4\,\text{ps}$ agrees well with rates found for vibrational relaxation. The last process has a long lifetime of 6.7 ns and is assigned to the decay to the ground state. The corresponding spectrum differs from the others due to the spectral blue shift as described above. In particular, it is noticeable that the maximum of the ESA is shifted from 470 nm to 460 nm, which could be explained by ^{3}ZnTPP* triplet ESA [148, 151, 152]. Consequently, the third time constant $\tau_3 = 84\,\text{ps}$ must be attributed to the ISC. This would make the ISC rate significantly faster than the 2.1 ns in solution [26].

A very fast ISC with τ =2 ps was found for octaethylporphyrin with copper as the central atom [156]. A mechanism involving a charge transfer state coupled with a doublet state of copper ^{2}CT is proposed here. With the closed d-shell of the electron configuration of Zn $3d^{10}4s^2$, this explanation can be rouled out. A fast ISC with τ $\sim$235 ps was also found for Zn tetraphenyltetrabenzoporphyrins in benzonitrile [157].

A fit with three time constants converges as well, but there are some deviations in the range of the first 1 ps. Only with the additional fourth lifetime of $\tau = 135\,\text{fs}$ the ultrafast relaxation discussed above is captured in the fit. This rapid dynamic can be seen very clearly in the decrease of the ESA at 475 nm within the first 500 fs in Fig. 6.6 e) or in the decrease of the GSB at 440 nm and at 560 nm in Fig.6.6 f).

Global anlysis after Soret band excitation of C_{60}@Zn(TPP)

In Fig.6.6 c) the DADS of the TA data of C_{60}@Zn(TPP) in the visible spectral region are shown. The obtained time constants are $\tau_1 = 327\,\text{fs}$, $\tau_2 = 14\,\text{ps}$, $\tau_3 = 212\,\text{ps}$, and $\tau_4 = 10.2\,\text{ns}$.

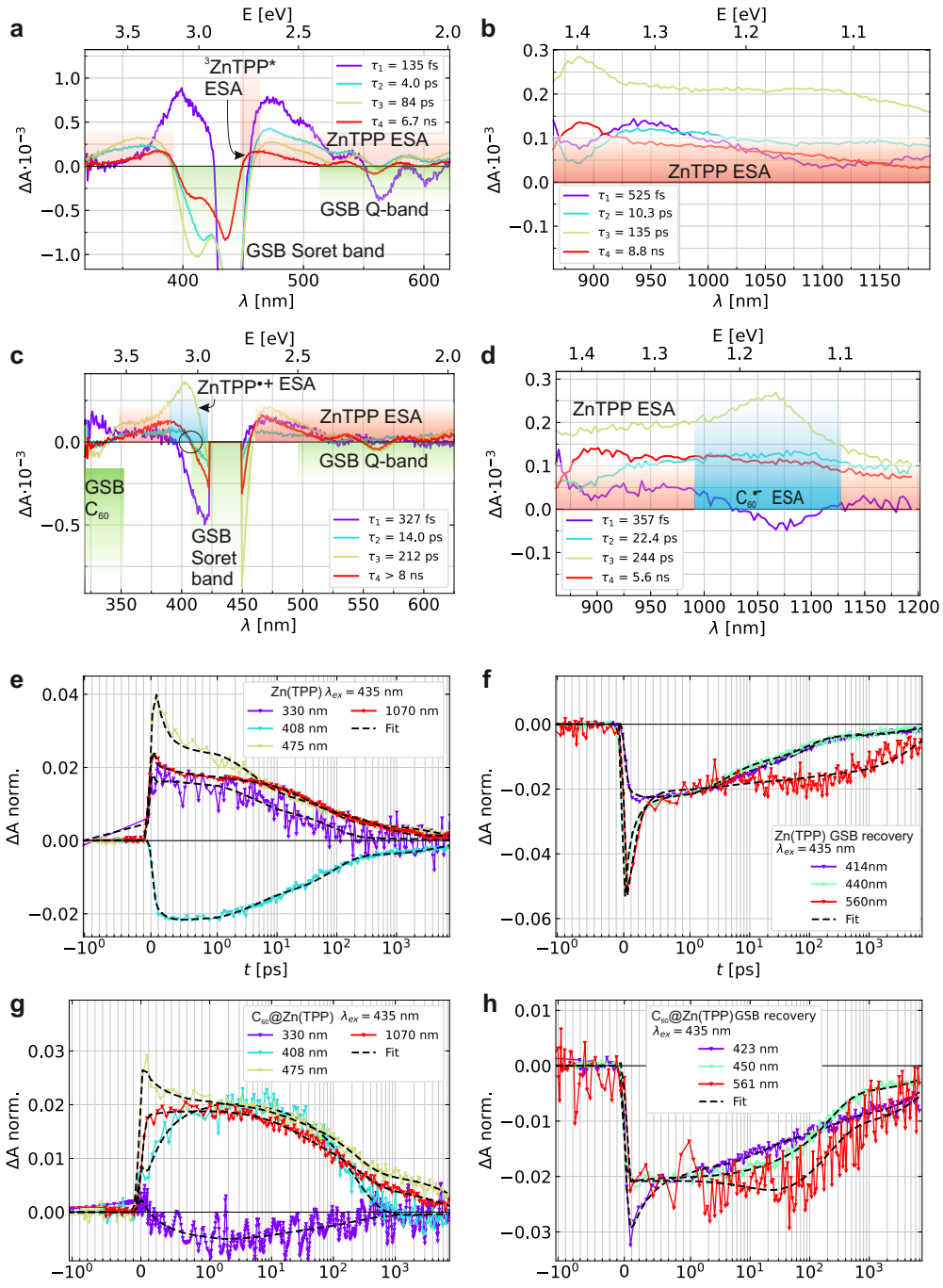

Figure 6.6: DADS of Zn(TPP) in the visible region **a** and in the NIR **b** after Soret band excitation. DADS of C_{60}@Zn(TPP) in the visible region **c** and in the NIR **d**. The data used for analysis are shown in Fig.6.5. The colored areas indicate contributions from GSB (green), ESA of the Zn(TPP) linker (red) and ESA of the cation and anion (blue). The circle in **c** marks the zero crossing mentioned in the text. **e** and **g** present the normalized difference absorption for selected wavelenghts for Zn(TPP) and C_{60}@Zn(TPP). The GSB recovery of the Soret absorption and the Q-band absorption are depicted in **e** and **g**

Since an overlap of a multitude of processes can be observed here, it cannot be assumed that all processes can be separately resolved with this model. On one hand, two porphyrin linkers are in one unit cell and only one fullerene molecule, and the loading is determined to be approximately 90% by Liu et al.[62]. Therefore, it can be assumed that even with high efficiency of charge separation, signals from excited porphyrin linkers not involved in charge separation can still be observed.

The key features of charge separation and recombination can, however, be observed. The first spectrum (purple) shows a positive signal at the position of the C_{60} ground state absorption, which means that the GSB of C_{60} builds up with the corresponding time constant of $\tau_{CS,GSB} = 327\,\text{fs}$. We tentatively ascribe this time constant to the CS process, which will be solidified with the data from the near infrared region.

The corresponding spectrum (cyan) shows characteristics of Zn(TPP) ESA. We attribute this time constant (14 ps) to internal vibrational relaxation (IVR), which also lies in the range of a few picoseconds in the SURMOF without fullerene. It is possible that the IVR can occur in the S_1 state of the ZnTPP linker or in the CS state, as investigated in a Zn–porphyrin–amino naphthalene diimide dyad [158].

As the process continues, it is expected that the CS state will recombine, so the GSB of C_{60} should recover. The DADS (yellow) shows the decay of the GSB of C_{60} (330 nm) with a time constant of $\tau_{CR,GSB} = 212\,\text{ps}$.

In Zn(TPP), we observed the formation of triplets, which was determined by the blue shift of the maximum from 470 nm to 455 nm. In C_{60}@Zn(TPP), this shift is not observed, indicating that no triplets are generated. This is also consistent with the fast charge separation. On the other hand, it has also been observed that the CS state originates from the excited porphyrin triplet state. The decay to the ground state seems to be slower in C_{60}@Zn(TPP), as τ_4 is greater.

The NIR data can also be fitted with four decay constants, see Fig.6.6 d). The resulting decay constants are $\tau_1 = 357\,\text{fs}$, $\tau_2 = 22.4\,\text{ps}$, $\tau_3 = 244\,\text{ps}$, and $\tau_4 = 5.6\,\text{ns}$.

The first DADS (purple) has a negative contribution between 1030 nm and 1100 nm, showing that the $C_{60}^{\bullet-}$ anion ESA peaking at 1070 nm builds up. With that we confirm that the observed build up of the C_{60} GSB is connected to the creation of anions as their rates match well. Similarly, as in the visible region, the second DADS (cyan) does not show features of C_{60} or the CS. Hence, we also contribute it to internal vibrational relaxation (IVR) in the porphyrin unit. The thirds DADS (yellow) has a prominet peak at the C_{60} anion absorption. From the decay of this signal we can extract the time constant for CR with $\tau_{CR,NIR} = 244\,\text{ps}$.

The temporal evolution of the ESA at 1070 nm is shown in Fig.6.7 a) for the SURMOF with and without C_{60}. Without C_{60}, a rapid decrease can be seen within the first few hundred femtoseconds. In contrast, with C_{60}, the signal builds up. Keep in mind that the scale is linear for the first picosecond. For comparison, Fig.6.7 b) shows a wavelength in the NIR that is not in the region of the anion ESA. Here, no increase in the ESA is observed.

As the rate of charge separation is almost two orders of magnitude faster than the second fastest observed rate constant, one could also attempt to fit a monoexponential function (which includes the instrument response function) to the data. This was done for the rise

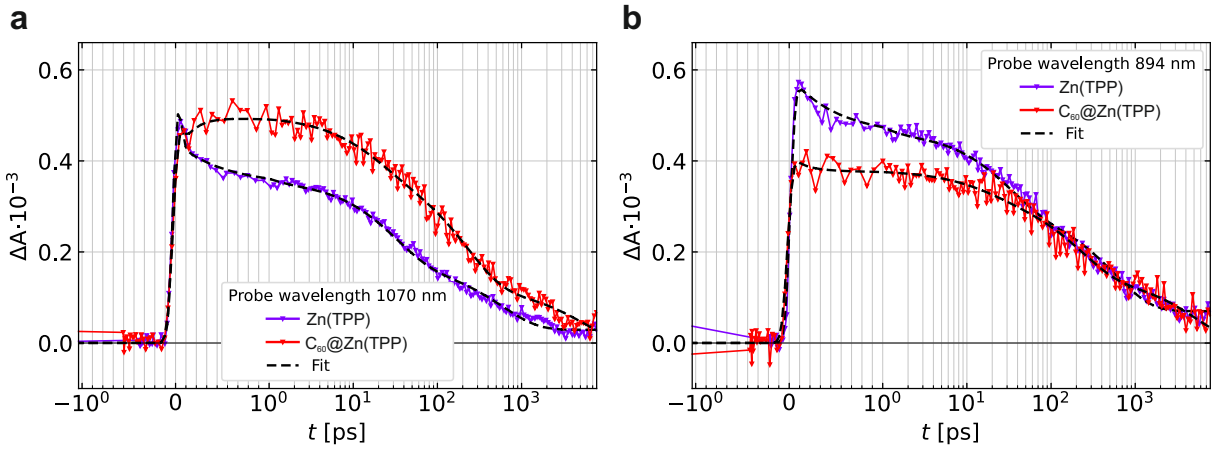

Figure 6.7: Time evolution at 1070 nm **a** and 894 nm **b** of the probe spectrum for Zn(TPP) and **C60@Zn(TPP)**. The rise in signal at 1070 nm is indicative for generation of $C_{60}^{\bullet-}$ anions.

of the anion absorption in the NIR and for the GSB of C_{60}. From that charge separation constants of $\tau_{CS,1065} = 52 \pm 7$ fs in the NIR and $\tau_{CS,330} = 128 \pm 42$ fs were obtained. These fits do not seem to agree well with the rates obtained by global analysis. This could be explained by the underlying ESA from the porphyrin linker, that also exhibits an ultrafast component.

ZnTPP radical cation absorption

With the existence of C_{60} anions, porphyrin cations should also be observable. Porpyhrine cations show absorption in the visible range between 600-700 nm [159], which cannot be clearly identified (compare Fig.6.5 b)), but the global analysis provides spectra with increased amplitude of the ESA at 650 nm, that might stem from $ZnTPP^+$ cations. Moreover, $ZnTPP^+$ absorbs in the visible range [160]. This is rarely used for identification of CS, probably due to detector limitations.

From the global analysis of C_{60}@Zn(TPP) we can conclude that the yellow DADS (Fig.6.6 c)) shows the characteristics of the CS state. A third prominent absorption with a maximum at 403 nm (see Fig.6.6 c)) is visible in the DADS. This absorption feature can be attributed to the $ZnTPP^{\bullet+}$ radical cation [160].

Interestingly, whereas the purple DADS – associated with the rise of the radical cation absorption – and the yellow DADS – associated with the decay – have high difference absorption values ΔA, the red and cyan DADS have a zero crossing. At the wavelength which is encircled in Fig.6.6 c), it should be possible to extract the charge separation and recombination dynamics without the underlying spectra, that are described by the red and cyan DADS. For that, time traces at several wavelength close to the zero crossing of the in the circle have been extracted. Since those should not contain the dynamics of the pure porphyrin dynamics, it should be possible to use a model with only two exponentials. The results are shown in Fig.6.8 and Table 4. It is indeed possible to fit the data with only two exponential functions. The obtained time constants are in good agreement with the results from the global analysis. From the RMS values (sum of squares of the errors divided by the number of degrees of freedom) in Table 4 it can be concluded that the best fits are in the range from 406.9-408.7 nm of the probe spectrum. For data with a lower wavelength, an additional long time component results in a bad fit for delay times > 300 ps, which is best observed at the probe wavelength of 404.1 nm (first graph in Fig.6.8). On the other hand, for increasing wavelength of the probe spectrum, the GSB of Zn(TPP) results in a negative ΔA contribution, which is visible for long time delays (last graph in Fig.6.8).

Energy/pulse	50 nJ			100 nJ		
λ [nm]	$\tau_1[fs]$	$\tau_2[ps]$	RMS $[10^{-5}]$	$\tau_1[fs]$	$\tau_2[ps]$	RMS $[10^{-5}]$
404.1	115 ± 110	273 ± 11	3.01	-	-	-
404.7	290 ± 123	248 ± 10	2.65	-	-	-
405.2	273 ± 103	250 ± 10	2.56	668 ± 375	229 ± 7	5.22
405.8	292 ± 131	243 ± 10	2.75	461 ± 222	224 ± 7	4.74
406.3	236 ± 80	229 ± 9	2.43	66 ± 40	202 ± 5	3.77
406.9	341 ± 64	216 ± 9	2.43	91 ± 35	194 ± 5	3.55
407.5	303 ± 69	191 ± 9	2.46	103 ± 31	185 ± 4	3.37
408.1	315 ± 69	181 ± 9	2.42	-	-	-
408.7	429 ± 51	173 ± 9	2.47	-	-	-
409.3	410 ± 90	173 ± 11	2.73	-	-	-

Table 4: Fit results for the data shown in Fig.6.8. The time constant τ_1 and τ_2 describe charge separation and recombination.

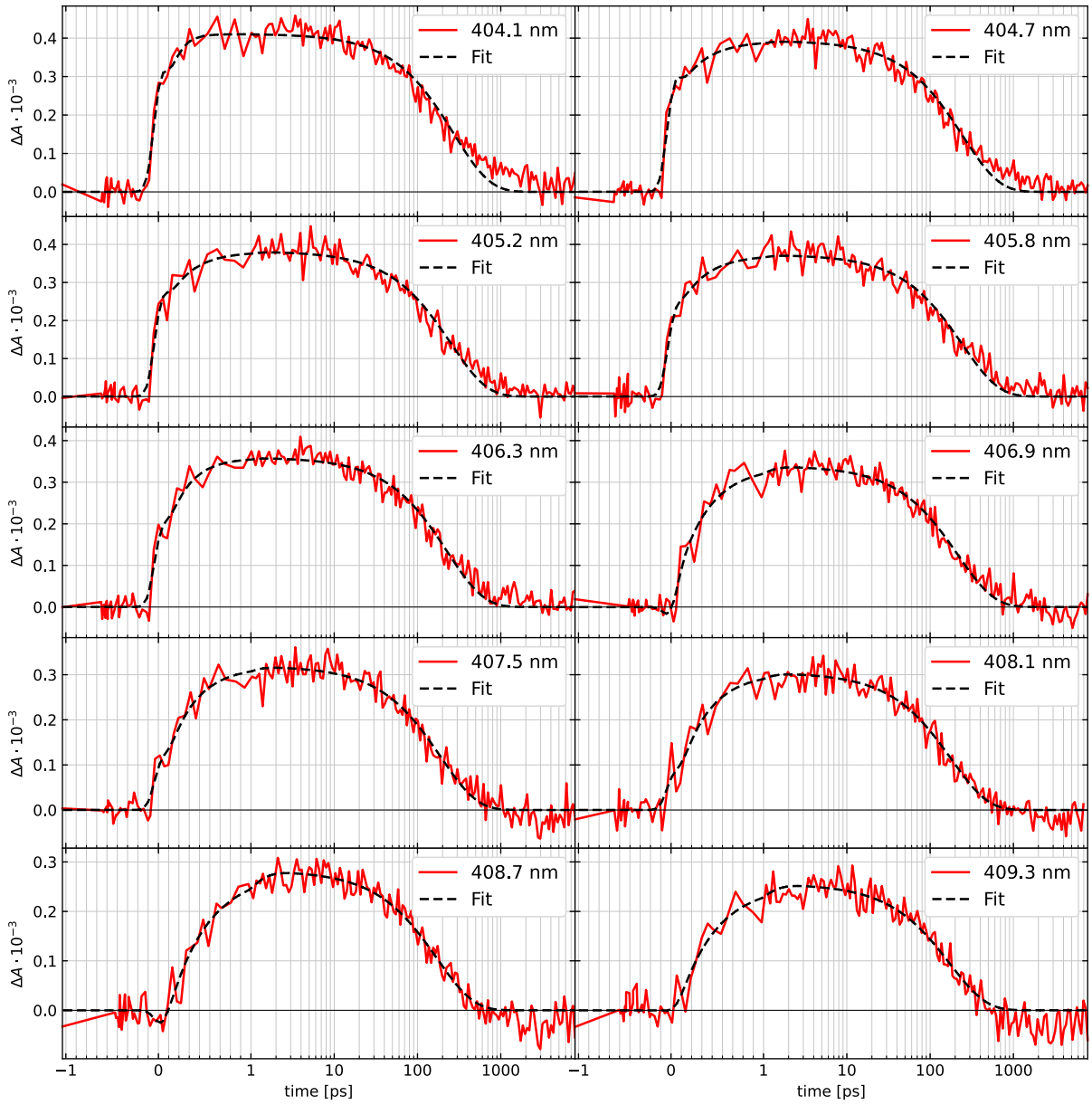

Figure 6.8: Time evolution of the radical cation absorption after excitation of the Soret band with 50 nJ per pulse. Two exponential functions are used to model the data in this spectral region.

6.3.2 Excitation of the Q-band

Fig.6.9 shows the TA spectra of Zn(TPP) and C_{60}@Zn(TPP) after excitation with laser pulses with a wavelength of 605 nm. No additional measurements were performed for the visible range, which is why the signal quality in the range 600 nm-800 nm is low. The spectra are similar to those after excitation in the Soret band, which is why the key features are not described further and instead only the differences are discussed.

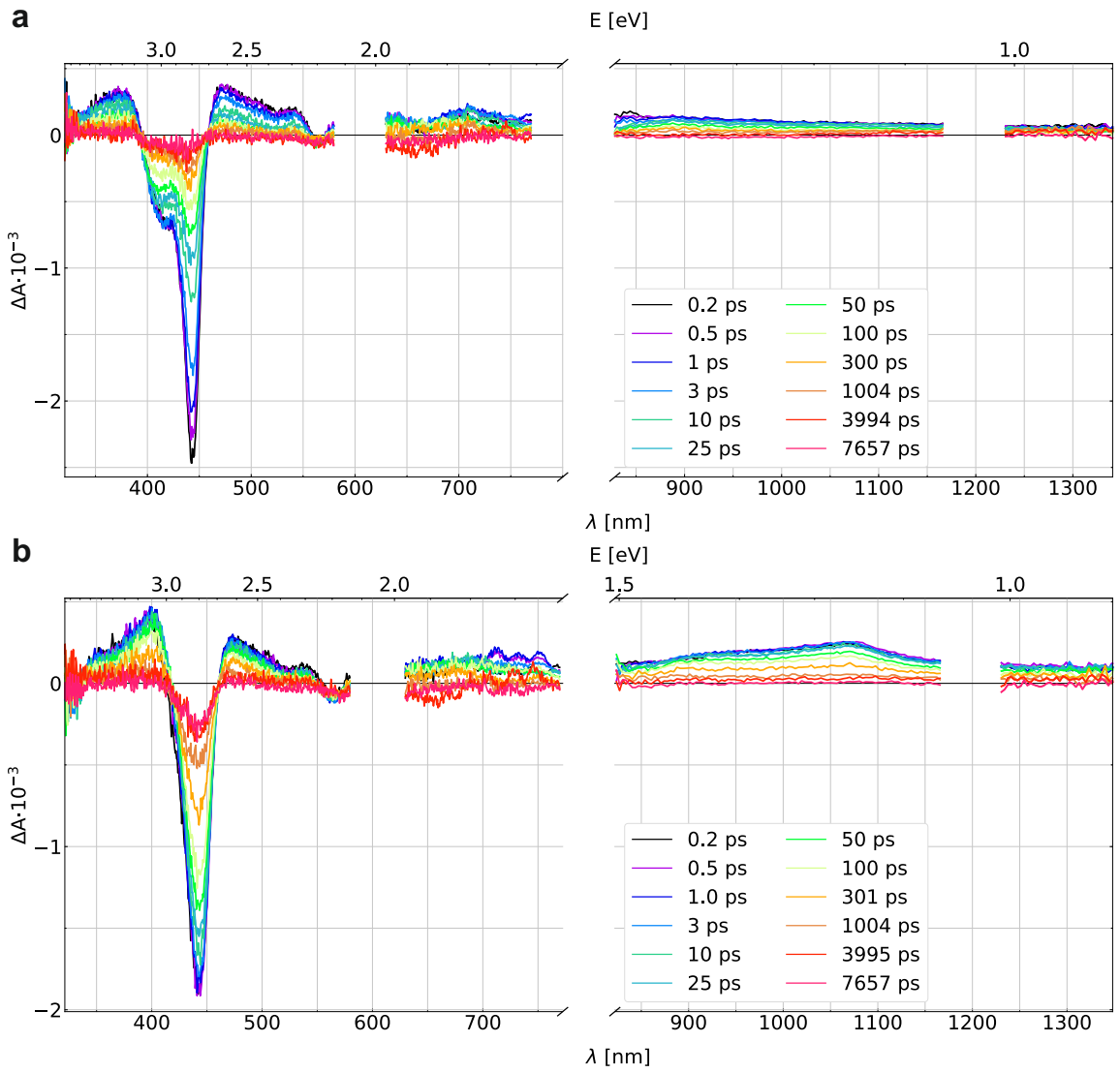

Figure 6.9: TA spectra of **a** Zn(TPP) and **b** C_{60}@Zn(TPP) after excitation with a wavelength of 605 nm. The data were obtained from several experiments to cover the whole spectral range as shown. Zn(TPP) and C_{60}@Zn(TPP) consist each of two measurements, covering the UV and near infrared spectral region each with 200 nJ. Data at 605 nm± 25 nm are removed, due to the overlaid signal from scattered pump beam light.

Since this lower-energy excitation is not sufficient to excite the S_2 state, the relaxation $S_2 \rightarrow S_1$ should be absent. In fact, the ultrafast component is no longer present in the range from 450 nm to 520 nm (see Fig.6.5 a) and Fig.6.9 a)). Furthermore, the ratio of the minima in the GSB is different for 410 nm and 440 nm. Finally, the blue shift of the maximum of the ESA at 470 nm is also less pronounced. We have attributed this shift to the transition to the triplet system by ISC. After excitation with even higher energy (λ_{ex} =264 nm), the triplet ESA is even stronger. The ISC efficiency therefore increases with the excitation energy. These three differences are discussed in more detail after the results of the excitation with λ_{ex} = 264nm have been presented.

Global anlysis after Q-band excitation of Zn(TPP)

The global analysis was carried out for Zn(TPP) with only three time constants, as it is to be expected that the relaxation $S_2 \rightarrow S_1$ is not present. The results are shown in Fig.6.10 a) and b). In the visible range, the time constants are $\tau_{1,\mathrm{VIS}}$ = 5.8 ps, $\tau_{2,\mathrm{VIS}}$ = 110 ps, $\tau_{3,\mathrm{VIS}}$ = 7.1 ns and in the NIR $\tau_{1,\mathrm{NIR}}$ = 5.5 ps, $\tau_{2,\mathrm{NIR}}$ = 110 ps, $\tau_{3,\mathrm{NIR}}$ = 7.7 ns.

We assign the time τ_1 to the IVR. We have assigned the second time constant to the ISC after excitation with λ_{ex} = 435nm. However, it appears that fewer triplets are present, which is observed by the small blue shift in the ESA at 470 nm. This also fits with the third time constant $\tau_3 \sim$ 7-8 ns, as a longer lifetime would be expected for triplets. The decay constants can therefore not be clearly assigned.

Global analysis after Q-band excitation of C_{60}@Zn(TPP)

The global analysis for C_{60}@Zn(TPP) was carried out with two time constants and an offset. In principle, very similar dynamics with charge separation and recombination, as well as parallel relaxation in the porphyrin linker should be expected. However, a fit with four times does not converge in the visible as well as in the NIR. The time constants in the visible range are determined to be τ_{IVR} = 17.5 ps and τ_{CR} = 360 ps. In the NIR, τ_{CS} = 83 fs and τ_{CR} = 263 ps. An ultrafast dynamic can therefore be observed in the NIR, having a negative amplitude with the minimum at 1070 nm. This again shows the structure of the C_{60} anion ESA, which subsequently decreases with ∼263 ps (green DADS).

Similar to the excitation with λ_{ex} = 435nm, a zero crossing of two DADS can be identified at approximately 407 nm and the ESA (green DADS), which can be attributed to the $ZnTPP^{\bullet+}$ radical cation, has its maximum at 403 nm. Therefore, we can select wavelengths of the probe spectrum where the contribution of the Zn(TPP) ESA and GSB are the smallest.

Table 5 gives an overview of fit results with only two exponentials. The table includes experiments with F =100, 200 and 300 nJ per pulse for the wavelengths λ_{probe} = 400 to 409 nm. The majority of fits for τ_{CS} return values between 100 and 300 fs when using 100 and 200 nJ per pulse. The outliers have such high errors that they still agree. For 300 nJ per pulse, greater values for τ_{CS} are obtained, but they still agree within the 3σ range. From this rather broad distribution, no conclusion can be drawn whether the CS rate is different in comparison to Soret band excitation.

However, the time constants for charge recombination are increased compared to those after Soret band excitation. All values obtained are ≥ 305 ps, whereas 212-244 ps was obtained

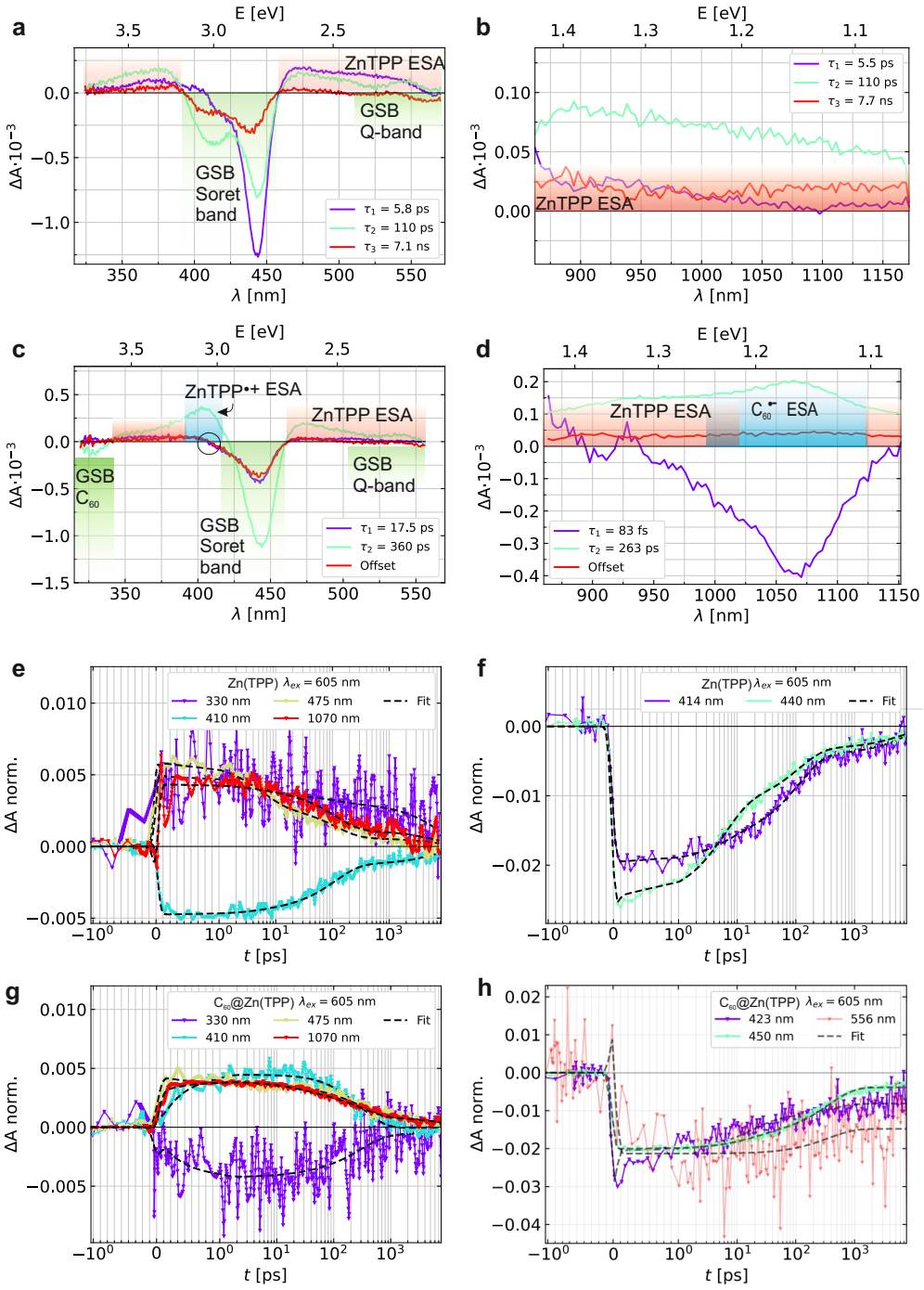

Figure 6.10: DADS of Zn(TPP) in the visible region **a** and in the NIR **b** after Q band excitation. DADS of C_{60}@Zn(TPP) in the visible region **c** and in the NIR **d**. The data used for analysis are shown in Fig.6.9. The colored areas indicate contributions from GSB (green), ESA of the Zn(TPP) linker (red) and ESA of the anions and cations (blue). The circle in **c** marks the zero crossing mentioned in the text. **e** and **g** present the normalised difference absorption for selected wavelengths for Zn(TPP) and C_{60}@Zn(TPP). The GSB recovery of the Soret absorption and the Q-band absorption are depicted in **e** and **g**

from global analysis and 181-229 ps from single fits for data after Soret band exitation. Once the CS state has been reached, it would be expected to have the same decay constant in both cases. Different dynamics could be explained by the fact that the recombination to the ground state has different dynamics if the HOMO-1 is still occupied, which is the case after excitation with λ_{ex} =605 nm. The GSB recovery has a different time evolution depending on the wavelength of the probe beam, both with and without C_{60} loading, as can be seen in Fig.6.6 f) and h) and 6.10 h). This indicates that the HOMO and HOMO-1 have different recovery dynamics.

E/pulse	100 nJ			200 nJ			300 nJ		
λ [nm]	$\tau_1[fs]$	$\tau_2[ps]$	RMS $\cdot 10^{-5}$	$\tau_1[fs]$	$\tau_2[ps]$	RMS$\cdot 10^{-5}$	$\tau_1[fs]$	$\tau_2[ps]$	RMS $\cdot 10^{-5}$
400.6	105 ± 45	483 ± 40	2.32	100 ± 112	425 ± 27	4.29	185 ± 298	436 ± 18	4.54
401.8	167 ± 57	407 ± 32	2.32	123 ± 55	368 ± 19	3.65	237 ± 140	365 ± 14	4.12
402.4	1978 ± 3044	323 ± 25	2.02	117 ± 52	368 ± 20	3.70	254 ± 137	395 ± 15	4.12
402.9	187 ± 119	311 ± 27	2.23	-	383 ± 21	3.92	320 ± 211	400 ± 16	4.40
403.5	161 ± 68	380 ± 33	2.34	164 ± 33	367 ± 19	3.56	353 ± 255	412 ± 17	4.39
404.1	207 ± 60	331 ± 26	2.12	180 ± 38	320 ± 18	3.81	442 ± 233	407 ± 16	4.35
404.7	272 ± 88	415 ± 32	2.09	173 ± 129	365 ± 22	3.90	588 ± 306	418 ± 19	4.66
405.2	270 ± 107	458 ± 39	2.28	178 ± 73	359 ± 22	3.95	516 ± 154	377 ± 16	4.33
405.8	1475 ± 835	332 ± 25	2.00	229 ± 46	321 ± 17	3.46	679 ± 200	379 ± 15	3.72
406.3	-	-	-	181 ± 67	369 ± 22	3.70	396 ± 103	379 ± 14	3.76
406.9	421 ± 308	382 ± 34	2.13	262 ± 85	321 ± 19	3.50	627 ± 147	346 ± 14	3.82
407.5	964 ± 376	390 ± 34	1.98	285 ± 70	345 ± 22	3.78	789 ± 207	349 ± 15	3.76
408.1	-	-	-	341 ± 64	308 ± 19	3.62	794 ± 160	335 ± 14	3.64
408.7	-	-	-	-	-	-	1207 ± 238	351 ± 15	3.76
409.3	-	-	-	-	-	-	1291 ± 289	322 ± 14	3.48
409.9	-	-	-	-	-	-	702 ± 70	305 ± 16	4.29

Table 5: Fit results for a model with two time components in the range of 400-410 nm of the probe spectrum for energies of 100, 200 and 300 nJ per pulse. The RMS value gives the sum of squares of the errors divided by the number of degrees of freedom [83].

6.3.3 Direct excitation of C_{60}

The light harvesting unit in a porphyrin-fullerene complex is the porphyrin unit, as it has an outstanding high exctinction coefficient in the visible spectral region. But in a D/A system it is also possible the excite the acceptor to induce the charge separation. As can be seen in Fig.6.3, the introduction of C_{60} into the SURMOF led to two new absorption peaks at 264 nm and 330 nm. An excitation wavelength of $\lambda_{ex} = 264$ nm was chosen to excite C_{60}. Of course this is not a selective excitation as ZnTPP absorbs as well in the UV and higher excited states will be populated. Hence, the dynamics will be a superposition of a multitude of processes.

Global anlysis for Zn(TPP)
Fig.6.11 a) shows the DADS of Zn(TPP) from global analysis in the visible region. The spectral evolution can be fit with $\tau_{1,\mathrm{VIS}} = 1.1$ ps, $\tau_{2,\mathrm{VIS}} = 15$ ps, $\tau_{3,\mathrm{VIS}} = 197$ ps and $\tau_{4,\mathrm{VIS}} > 8$ ns. Similarly to the dynamics observed after exciting the Soret band, the processes involved are likely to be IC from higher excited states S_n to S_1 and IVR in these states with averaged time constants of $\tau_{1,\mathrm{VIS}}$ and $\tau_{2,\mathrm{VIS}}$. The last DADS (red) with a time constant greater than 8 ns exhibits a considerably blue shifted ESA with a maximum at 450 nm, which is identified by the ESA of ^{3}ZnTPP* as before [129, 151, 152]. Therefore the third time constant $\tau_{3,\mathrm{VIS}} = 197$ ps must be ascribed to the process of ISC. The analysis in the NIR can not be brought in agreement with the results obtained in the visible region at this moment. It is however noteworthy that the longest time component is 773 ps. From that we can conclude that no ESA originating from triplets is visible in the NIR, since this would be present for longer delay times.

Global anlysis for C_{60}@Zn(TPP)
Examining the results obtained for C_{60}@Zn(TPP), similar spectral characteristics are observed, although with small deviations. As before in the visible spectral region the GSB of C_{60} can be observed at 330 nm and the ZnTPP$^{\bullet+}$ radical cation ESA at 404 nm. As indicated by the circle the DADS (red and cyan) do not cross $\Delta A = 0$ at the same wavelength. Therefore, when extracting a single or few wavelength in this region to analyse the charge separation and recombination dynamics, overlapping contributions from the Zn(TPP) excited state dynamics should be expected. Actually, the global analysis yields $\tau_{1,\mathrm{VIS}} = 987$ fs as shortest time. When analysing single traces, a fit with two time constants results in time constants $> 6ps$ for a measurement with 300 nJ. These fits clearly do not capture the rise in signal and are therefore not a good estimation of the CS rate. With a different excitation power of 100 nJ per pulse, the fit yields $\tau_{CS} = 267 \pm 211$ fs and $\tau_{CR} = 249 \pm 6$ ps. The high error $\Delta\tau_{CS}$ shows that the model is not adequate.

The maximum of the red DADS shows a blue shift of approximately 10 nm to 463 nm which could be explained by contribution to the absorption from ^{3}ZnTPP*. This means that a greater amount of triplets is generated parallel to the CS process.

In the NIR, the model with four time constants yields $\tau_{1,\mathrm{NIR}} = 1200$ fs, $\tau_{IVR,\mathrm{NIR}} = 33$ ps, $\tau_{CR,\mathrm{NIR}} = 355$ ps and $\tau_4 > 8$ ns.

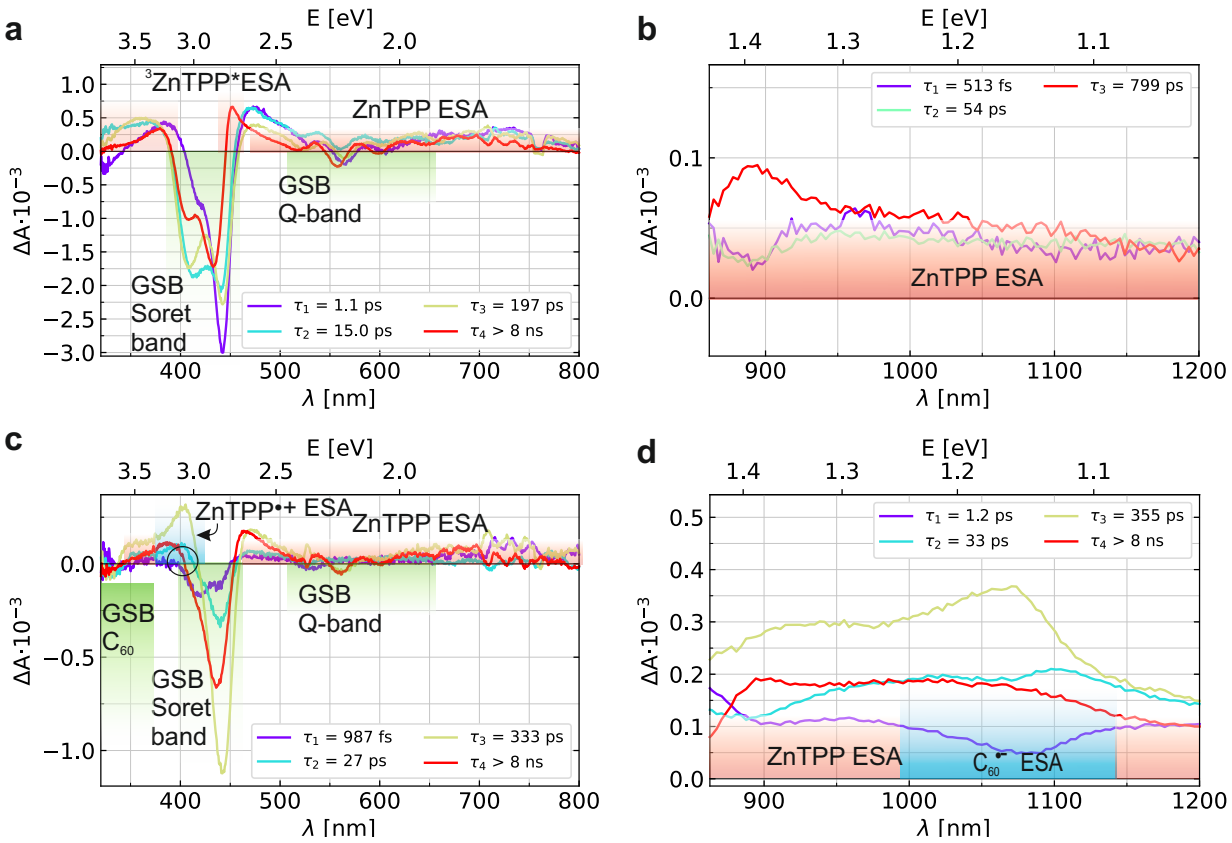

Figure 6.11: DADS of Zn(TPP) in the visible region **a** and in the NIR **b**. DADS of C_{60}@Zn(TPP) in the visible region **c** and in the NIR **d**. The samples were excited light pulses of the wavelength λ_{ex} =264 nm. The colored areas indicate contributions from GSB (green), ESA of the Zn(TPP) linker (red) and ESA of the cation and anion (blue). The circle in **c** marks the zero crossing mentioned in the text.

These times can only partially be reconciled with the existing model described before. The charge separation seems to be slowed down. This might indicate that no direct separation takes place, but separation with prior IC from higher to lower singlets states. The rates for IVR and CR are also slightly slower. Again we surmise that spectra from additional species play a role. When observing the spectral features in the NIR a seemingly minuscule difference is seen. The purple DADS does have a minimum at 1070∼1080 nm as described for lower excitation energies, however, this minimum does not have negative values. Therefore, the time evolution from this DADS does not imply a rise in signal at the absorption of the C_{60} anions. Nevertheless, it is clear that the yellow DADS shows the characteristic ESA for C_{60} anions and the decay time can be associated with the recombination process. Finally, the red spectrum in the NIR has a higher intensity compared to data with lower excitation energies, indicating long-lived species that were not observed before. From the shape of the absorption it might be attributed to ZnTPP ESA.

6.3.4 Comparison of excitation energy

In this section the major differences after exciting the samples with different excitation will be adressed. Fig.6.12 displays data of Zn(TPP) for $\lambda_{ex} = 264, 435$ and 605 nm. In Fig.6.12 a) the selected wavelength of the probe is λ_{probe} =475 nm. An ultrafast decay within the first picosecond is seen only for the higher excitation energies. This decay can be associated with the IC from higher states to S_1, as has been observed in other porphyrin based systems as well [152, 155].

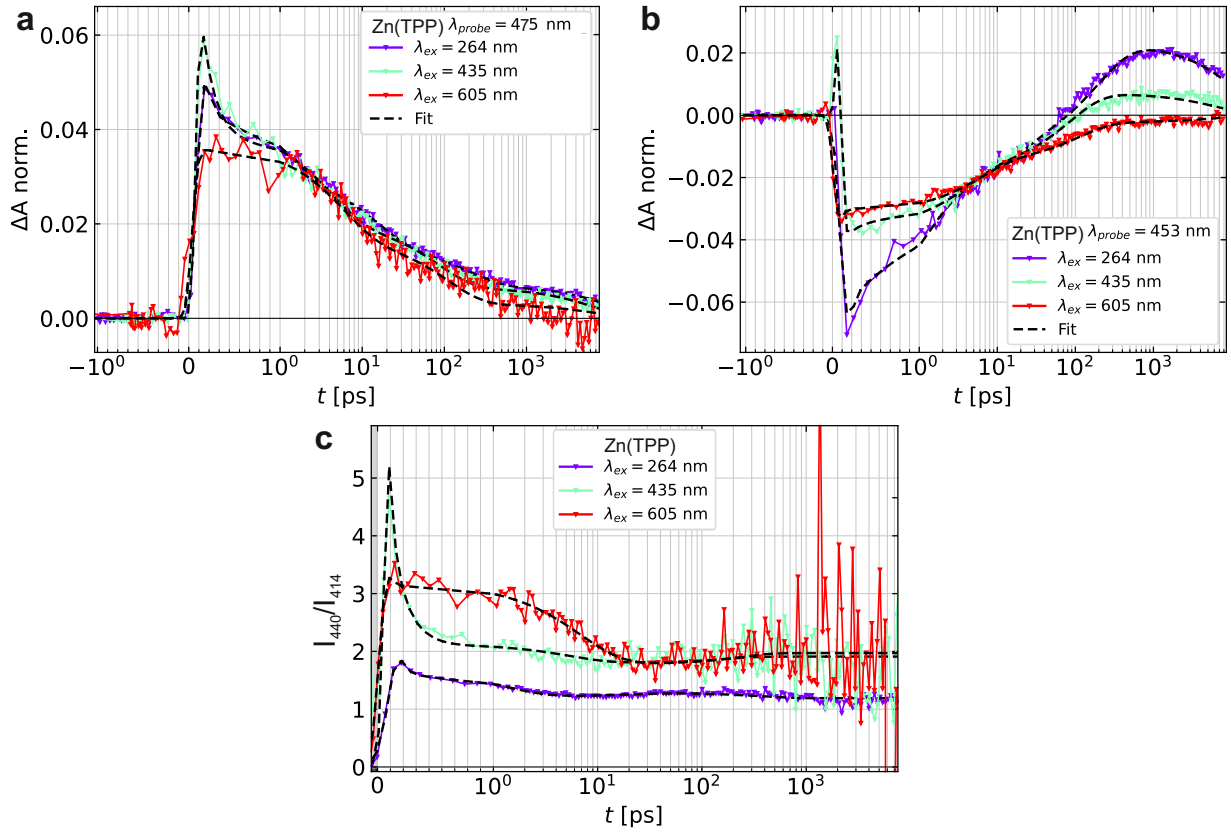

Figure 6.12: Comparison of the influence of different excitation energies on Zn(TPP). At a probe wavelength of 475 nm **a**, the ultrafast IC from higher lying states to S_1 is only absent after excitation with $\lambda_{ex} = 605$ nm. At a probe wavelength of 453 nm **b** the ESA of triplets is most prominent for long time delays. **c** Ratio $\frac{I_{440}}{I_{414}}$ of the two minima of the GSB at probe wavelengths of 440 nm and 414 nm.

Fig.6.12 b) shows the data for $\lambda_{probe} = 453$ nm which corresponds to the maximum of the DADS associated with triplet ESA as found after excitation with a wavelength of 264 nm (Fig.6.11 a)). This clearly demonstrates that the triplet yield increases with increasing excitation energy. This can be seen by the rising ΔA signal for longer time delays. For the lowest excitation energy (red) this time evolution does not show clear signs of triplet ESA. The already discussed DADS only showed a negligible spectral shift (Fig.6.10 a)). For higher

excitation energies the ΔA signal rises above zero again. Similar effects of excitation dependent ISC have been found in other systems although not including porphyrin units [161, 162]. There, several ISC pathways from higher lying states were proposed.

Fig.6.12 c) displays the ratio $\frac{\Delta A_{440}}{\Delta A_{414}}$ of the two minima of the GSB at $\lambda_{probe} = 440$ and 414 nm. The time evolution after excitation of the Soret band (green) shows an ultrafast component, which again might be caused be the IC to S_1. Then the value of the ratio stays constant ~ 2. After excitation of the Q-band, the ratio initially shows a value of ~ 3 and drops to the same value as fir the Soret band excitation at approximately 20 ps. The model proposed by us and others only show vibrational relaxation on those time scales. Therefore, the observed evolution might be associated with the $Q_y(0-1) \rightarrow Q_y(0-0)$ vibrational relaxation, as $\lambda_{ex} = 605$ nm excites the $Q_y(0-1)$ transition.

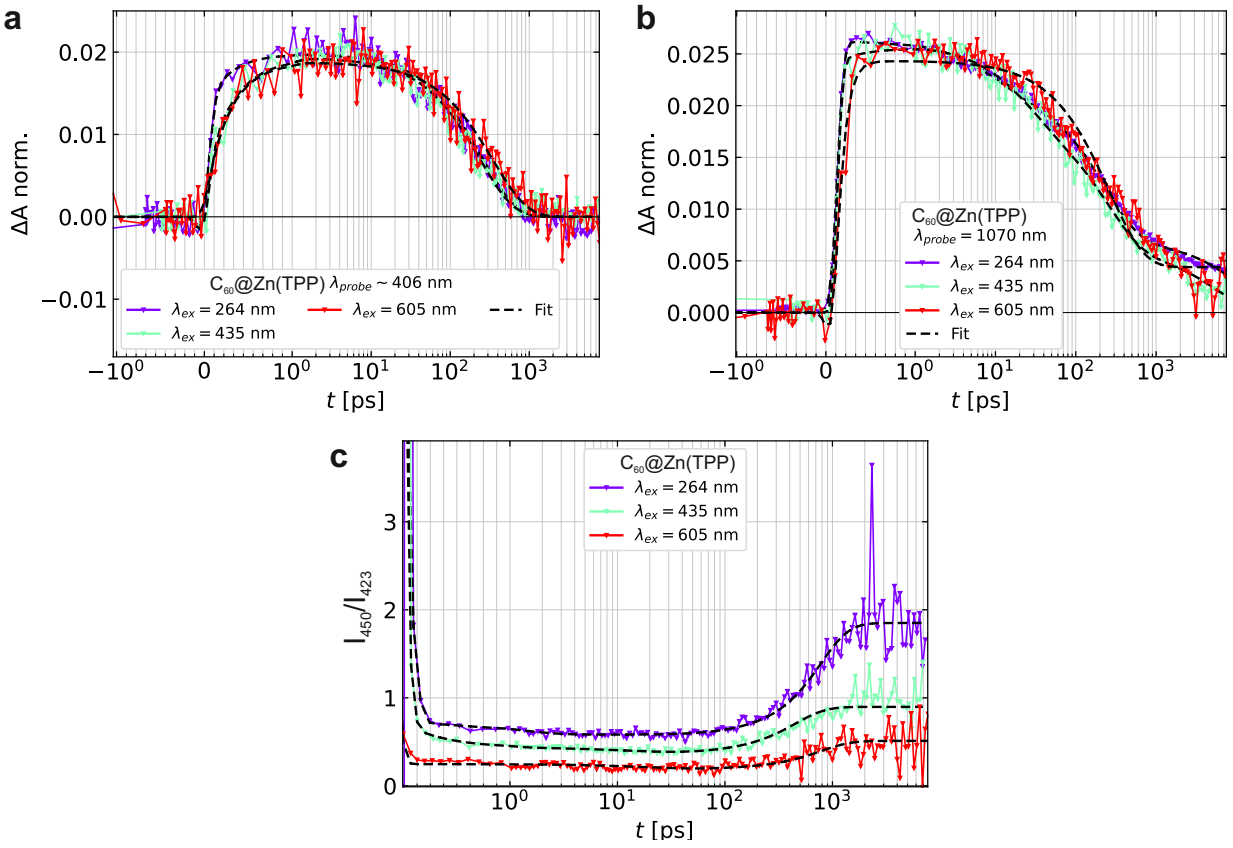

Figure 6.13: Time evolution of charge separation and recombination at **a**$\sim$ 406 nm and **b** 1070 nm for different excitation energies. **c** Ratio of difference spectra $\frac{\Delta A_{450}}{\Delta A_{423}}$ at the wavelengths 450 nm and 423 nm.

Fig.6.13 a) compares the evolution of the CS and CR in C_{60}@Zn(TPP). The probe wavelengths have been chosen to give $\Delta A \sim 0$ for long delay times ($> 1ns$). As argued in the sections above, at these wavelength the dynamics of CS and CR are singled out as other contributions are negligible or at least very small. All time traces show similar dynamics.

After excitation at with the highest energy (λ_{ex} 264 nm), the initial rise seems to be faster. Whether this is due to faster charge separation or other from contributions of higher excited states can not be clarified. Both single trace fits and global analysis give slower CR rates after excitation to the Q-band.

The dynamics as displayed by Fig.6.13 b) show the data at 1070 nm, where the C_{60} anion absorbs. For all excitation energies the rise of the signal is faster as compared to the signal rise in Fig.6.13 a) and for long delay times the signal does not decay. Both observations are explained by the fact, that underlying ESAs are present.

Fig.6.12 c) displays the ratio $\frac{\Delta A_{450}}{\Delta A_{423}}$ of the GSB at $\lambda_{probe} = 450$ and 423 nm. With higher excitation energy the ratio increases which is the invers behavior to Zn(TPP) wihtout C_{60}. This observation can not be explained so far. The rise for long delay time stems from the triplet ESA.

6.4 Discussion

Since many of the systems are not directly comparable, because of different chemical structures or different solvent, it is often useful to compare the quotient $I = \frac{k_{CS}}{k_{CR}} = \frac{\tau_{CR}}{\tau_{CS}}$ of the rates. The C_{60}@Zn(TPP) SURMOF has a ratio of $I \approx 600$. We will first report on studies of thin films of porphyrine-fullerene systems, and as the majority of publications covers dyads and more complex porpyhrine-fullerene systems in solution, a few systems in solution will also be reported.

Wang et al. studied the charge separation and recombination kinetics in crystalline nanosheets of ZnTPP-C_{70} co-crystals [163]. As C_{60}, C_{70} is also an electron acceptor and can be used to generated efficient devices [164]. Wang et al. found fast charge separation with time constants <2 ps. Interestingly, they found a biphasic decay of the anion with ∼10 ps and ∼170 ps, with a ratio of $I = 35$ for the longer lifetime. They find the reason for the biexponential decay in two distinct arrangements (face-to-face and edge-to-face) of the porphyrins and fullerenes. There are two ZnTPP linkers in a unit cell in the SURMOF. Based on its symmetry however, the dynamics of the ZnTPP linkers in C_{60}@Zn(TPP) should not be different. The absorption features of ZnTPP linkers that are oriented parallel to the substrate surface might differ from those, that are arranged perpendicularly, but this should only affect the spectral and not the kinetic properties.

The aforementioned D/A system with ZnTCPP and C_{60}-EDA arranged by electrostatic self-assembly shows a CS lifetime of 220.9 ps [148]. The charge separation takes places within a few of picoseconds. With that the ratio of rates is on the order of 10-100.

Dyadic ZnP-C_{60} systems often exhibit time constants in the pico- to nanosecond range. Functionalized C_{60} was bound to ZnTPP by metal-ligand axial coordination [136]. Here, time constants of τ_{CS} =175 ps and τ_{CR} =4 ns with $I = 23$ and τ_{CS} =127 ps and τ_{CR} =2.6 ns with $I = 21$ for differently functionalized C_{60} fullerene acceptors were found in toluene. Another dyadic system is a ZnTPP-C_{60} supramolecular assembly, which is formed by non-covalent bonds [150]. The center-to-center distance is very small with 2.77 Å, while the smallest D/A distance in C_{60}@Zn(TPP) is 2.81 Å and the COM distance is 12.7 Å. In the supramolecular assembly, τ_{CS} =1.8 ps and τ_{CR} =183 ps with $I = 102$ were determined.

Another study by Kuciauskas et al. investigated covalently bound ZnP-C_{60} and H_2P-C_{60} dyads [139]. The lifetimes of the charge-separated states of τ_{CR} =280 ps of the free base porphyrin and τ_{CR} =50 ps of the zinc analogue found there, were classified as long lived CS states.

From the above systems we see that the recombination rate of C_{60}@Zn(TPP) is on the same order as observed in other systems. However, in comparison, the rate of charge separation is quite high which is reflected in the order of magnitude bigger ratio I. It can be surmised, that a very small internal reorganisation energy is the reason for the high ratio. In the thin film no solvent reorganisation is necessary and the channels along [001] direction migth increase the charge delocalisation and therefore reduce the reorganisation energy [165].

As mentioned in the introduction, longer lifetimes of the CS state is achieved - as in natur - by a multistep transfer of the charges. The most simple architecture for that is a tryad. In both thin film or solution, the lifetimes are tremendously increased. A dendritic architecture of poprhyrins and C_{60} (C_{60}-H_2P-$(ZnP)_3$) in a Triton-100 matrix yielded a CS rate of 108 ps and a recombination rate of 460 ns (I = 4260) [137]. A supramolecular tryad in toluene consisting of a zinc phthalocyanine fused with a free-base porphyrin which are coordinated to a functionalized C_{60} fullerene, achieves a CS state that lifes for 120 ns [166].

One of the most long-lived CS states to be observed is created in a ferrocene–zinc porphyrin trimer–fullerene pentad and has a lifetime of 0.53 s [141].

In the case of possible applications such as photovoltaics, the lifetime of the charge carriers must be sufficient leave the active layer before recombination by diffusion. With a (high) exciton diffusion coefficient of $D = 0.02\,\mathrm{cm^2\,s^{-1}}$, a diffusion length $L_D = \sqrt{4Dt} = 84\,\mathrm{nm}$ is achieved in $t = 300$ ps. The active layers of organic solar cells are on the order of 100 nanometers [167]. From this estimate it can be seen that the lifetimes of the charge-separated states should be at least a few 100 ps.

6.5 Conclusion

The dynamics of charge separation and recombination have been examined in a SURMOF incorporating C_{60} fullerenes. A scheme summarising the kinetics is shown in Fig.6.14.

The dynamics in Zn(TPP) are comparable to those observed in literature. This includes ultrafast IC from the S_2 to the S_1 state (135 fs) and IVR within a few picoseconds. The triplet state is populated through intersystem crossing, however faster than in comparable systems. The arrows in Fig.6.14 a) changing from dashed to solid indicate the increase in triplet ESA that was observed, when higher excitation energies were used.

With incorporation of C_{60} the charge separation takes place on an ultrafast timescale with $\tau_{CS} = 327 - 357$ fs after excitation of the Soret band. These times are extracted from global analysis of the visible and NIR detector range. The charges recombine with a time constant of $\tau_{CR} = 212 - 244$ ps. The generation and recombination was identified by ESA of $C_{60}^{\bullet -}$ fullerene anions at 1070 nm and the GSB of C_{60} at 330 nm.

The charge separation after excitation of the Q-band has a similar or faster rate extracted from single traces. The charge recombination process was observed to be slower with $\tau_{CR} = 263 - 360$ ps from global analysis.

For both excitations, no direct evidence for ^{3}ZnTPP* ESA is found with C_{60} incorporated in the SURMOF. This indicates that CS competes with ISC, but the charge generation rate is two orders of magnitude faster, hence only very few triplet states are populated.

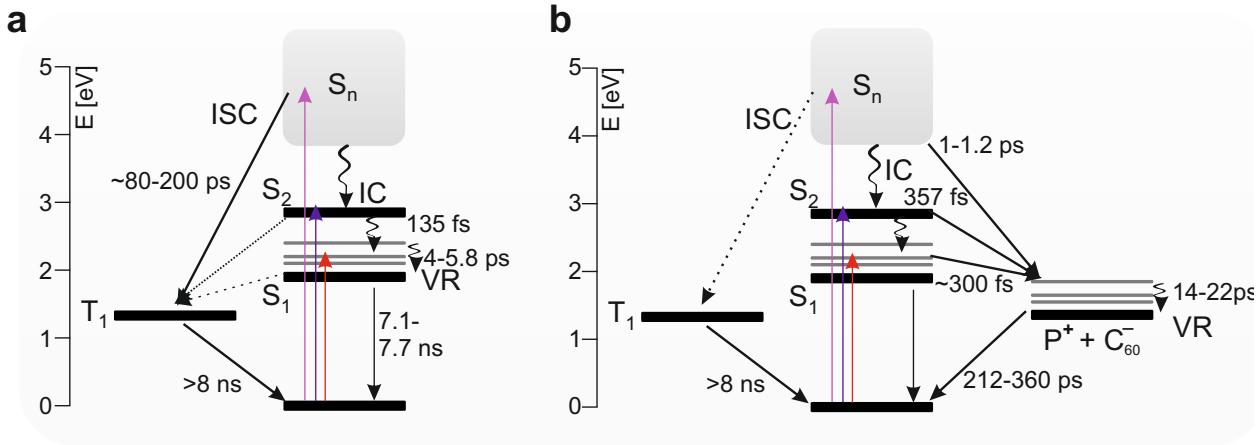

Figure 6.14: **a** Proposed kinetics for Zn(TPP) and **b** C_{60}@Zn(TPP). The coloured lines indicated excitation of the system with 605, 435 and 264 nm. The energies of S_1 and S_2 as well as the vibrational levels of S_1 are drawn according to the observed spectra. The levels of T_1 and the CS state were not obtained. The shaded area indicates higher singlet states of either ZnTPP or C_{60}. See text for further details

The dynamics of the CS can also be observed by the ESA of ZnTPP$^{\bullet +}$ radical cations. For the investigated system, global analysis allowed to identify a spectral region where the CS and CR dynamics can be disentangled from underlying spectra. Therefore the dynamics

could also be modelled including only a rise and decay rate, without the need for a more sophisticated model.

With an excitation wavelength of $\lambda_{ex} = 264\,\text{nm}$, the charge separation dynamics get partially obscured by overlapping signals. Specifically, there is an increased generation of $^3\text{ZnTPP}^*$ also in C_{60}@Zn(TPP).

Compared to other two component systems, the ratio $I = \frac{k_{CS}}{k_{CR}} = \frac{\tau_{CR}}{\tau_{CS}}$ 600 is very high, which is beneficial for efficient use of the charge carriers.

7 Pentacene-Acceptor Bilayers

In donor/acceptor systems, both doping and charge separation are key processes that need to be understood in detail. Since pentacene (PEN) has advantageous properties such as high carrier mobility [168] and the capacity for multiexciton generation through SF, it is studied intensively. Together with F4-TCNQ (2,3,5,6-tetrafluoro-7,7,8,8-tetracyanoquinodimethane) it creates a donor/acceptor system. Recently, this system was revisited, because the existing model for the doping process did not match experimental observations [10, 169, 170]. For clarification Theurer et al.[10] investigated blends of F4-TCNQ and the slightly stronger acceptor 2,2′-(perfluoronaphthalene-2,6-diylidene)- dimalononitrile (F6-TCNNQ). Here, this investigation is extended to bilayers of the donor and acceptor by means of diffraction, static and time-resolved measurements. The bilayers allow studying the process at the donor/acceptor interface. The interaction of donor and acceptor at interfaces is an important aspect of optimising bulk hetero-junctions in organic solar cells. First, a general overview of doping mechanisms for organic semiconductors (OSC) is given. The need for re-evaluation of the existing model and the new model are summarised thereafter. In section 7.2.1 the material preparation followed by the steady-state characterisation for bilayers with PEN and F4-TCNQ are presented. Section 7.2.2 discusses the fs-TA measurements. Subsequently, steady-state characterisation and fs-TA measurements for bilayers with PEN and F6-TCNNQ are discussed. A conclusion follows in section 7.4.

7.1 Introduction

A donor or acceptor can be used to dope an OSC. There are a plethora of parameters that can be altered to optimise the device performance, but first on foremost the energies of the frontier orbitals of the molecules are of interest. From that perspective two main doping mechanisms are relevant: Ion-pair and charge transfer (CT) complex formation [171].

Analogously to inorganic semiconductors, OSC can be p- or n-doped, depending on the energy level alignment of the donor and acceptor. The molecules are p-type dopants if the electron affinity (E_{EA}) is ideally equal or higher than the ionisation potential (IP) of the OSC and an electron transfers from the OSC to the dopant. For n-doping the energetic requirements are vice versa and the electron transfers from the dopant to the OSC. Hence, this process results in the formation of an ion pair and integer charge transfer (ICT). In order to serve as a charge carrier, the charges need to be separated. They are bound by an energy $E_b = \frac{e^2}{4\pi\epsilon_0\epsilon_r r}$, which results from the Coulomb force between the two charges. Typical binding energies ($\sim 1\,\mathrm{eV} > E_b > \sim 50\,\mathrm{meV}$ [21]) exceed the thermal energy at room temperature.

In the second type of doping mechanism CT complexes are created through orbital hybridisation between dopant and OSC. This is also possible for molecules where the E_{EA} and IP have a larger energy difference [172, 173]. A CT complex often leads to partial charge transfer instead of ICT. Therefore, mobile charge carriers are not produced at this step. Instead, the CT complex acts as dopant for the neutral OSC. To achieve an ICT from the OSC to the CT complex an activation energy is required, which is why only very few CT complexes contribute to the doping process [171]. F4-TCNQ is considered to be a strong

electron acceptor ($E_{EA} = 5.1 - 5.4\,eV$ [174, 175, 176, 177, 178, 179, 180]) and many studies report on its usage as a p-type dopant [181, 182]. The prevalent model was ion pair formation as describe above [10, 182]. However, high doping concentrations were needed in order to achieve an appreciable increase in conductivity [169]. Furthermore, direct evidence for polarons was missing in UPS spectra [170]. Salzmann et al.[170] proposed a CT complex formation that could explain the observed discrepancies. Further studies concluded that the system F4-TCNQ together with the OSC PEN is at the boundary of creating either ion pair or CT complexes through hybridisation [10, 169]. The values for E_{EA}, IE and also the energies of the hybridised orbitals from Ref.[170] are shown in Fig.7.1. These blends of F4-TCNQ with PEN were investigated with fourier-transform infrared (FTIR) spectroscopy, grazing-incident wide-angle X-ray scattering (GIWAXS), steady-state absorption extending to the NIR and fs-TA by Theurer et al.[10]. Both ICT and partial charge transfer were observed, depending on the ratio F4-TCNQ:PEN. The partial transfer dominated over the ICT for low (10%) concentrations of F4-TCNQ.

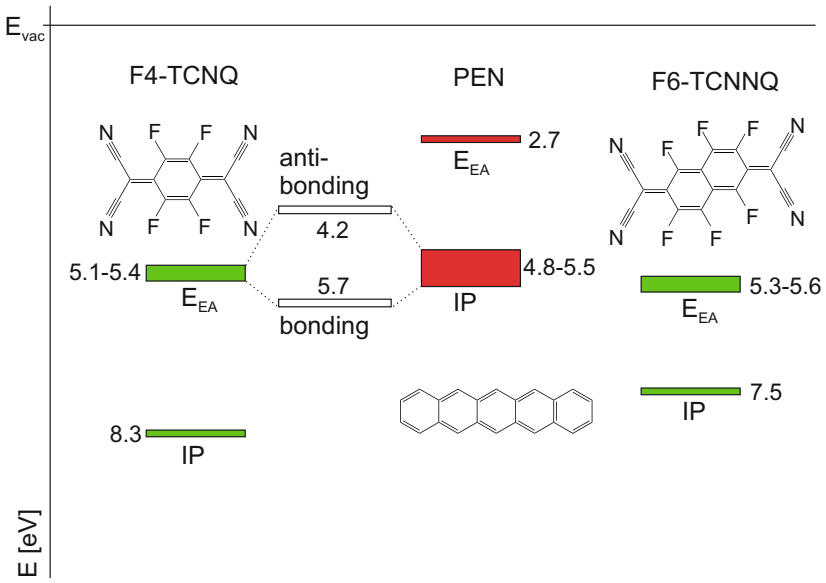

Figure 7.1: Electron affinities (E_{EA}) and ionisation potentials (IP) of F4-TCNQ, PEN [174, 175, 176, 177, 178, 179, 180] and F6-TCNNQ [174, 175, 176, 177, 178, 179]. The energy levels between F4-TCNQ and PEN belong to the bonding and antibonding orbitals after hybridization of the frontier orbitals [170].

7.2 Pentacene - F4-TCNQ bilayers

7.2.1 Material preparation and characterisation

The samples were prepared by Christoph Theurer in the group of Katharina Broch in Tübingen (Institut für Angewandte Physik, Universität Tübingen). The material was deposited

by thermal evaporation on a 150 µm thick borosilicate glass at a temperature of approximately 253 K under vacuum with a base pressure of $2 \cdot 10^{-8}$mbar, as described in [10]. The PEN thin films were prepared by Christian Huck in the group of Petra Tegeder (Physical Chemical Institute, Heidelberg) by thermal evaporation at a base pressure of $6.2 \cdot 10^{-9}$mbar and a growth rate of 6 Å min^{-1}. All samples were sealed under nitrogen atmosphere with a second glass to minimise possible effects due to photo-degradation The neat films of PEN and F4-TCNQ have a nominal thickness of 80 nm and the bilayers are 20 nm thick, with each component comprising roughly half of the thickness. The bilayers were chosen to be thin in order to keep bulk contributions as low as possible while still producing intact layers. The bilayer samples will be called **F4/PEN** and **PEN/F4** with the left component being the top layer and the right one the bottom layer (top/bottom). A PEN thin film of 10 nm thickness was also prepared for additional measurements of fs-TA, to exclude thickness dependent dynamics. The GIWAXS data were provided by Christoph Theurer and the FTIR experiments (Bruker Tensor 27 FT-IR spectrometer, Hyperion 1000 microscope) were conducted by Christian Huck.

The normalised steady-state absorption is shown in Fig.7.2 a) and b). The characteristics of the neat PEN film are described in detail in section 5.2. The bilayers for the most part show a superposition of F4-TCNQ and PEN absorption. In comparison to the neat PEN thin film, the $S_0 \rightarrow S_1$ transition is blue-shifted. The peak positions are 666 nm, 664 nm and 658 nm for PEN, **F4/PEN** and **PEN/F4**, respectively. The slight blue-shift can be caused by a disturbed crystal structure. Nonetheless, the Davydov splitting is present in both bilayers indicating that the PEN molecules are arranged in the herringbone pattern. In 7.2 b) a selected region in the NIR is displayed where absorptions of PEN cations and F4-TCNQ anions are indicated. No evidence for charges is found here. The noise at ∼860 nm stems from the change of the light source. With GIWAXS measurements information on the structure of the thin films is gained. The reciprocal space maps are shown in Fig.7.2 c) for the neat PEN film and the bilayers. PEN shows strong diffraction peaks that indicate an oriented crystal structure. The series of diffraction spots at $q_{xy} = 1.35\,\text{Å}^{-1}$, $1.67\,\text{Å}^{-1}$ and $1.98\,\text{Å}^{-1}$ correspond to Miller indices $hkl = \pm 1 \pm 1l$ (with $l = 0, 1$), $0 \pm 2l$ (with $l = 0, 1, 2$) and $\pm 1 \pm 2l$ (with $l = 0, 1$). This assignment is taken from Ref.[183]. The bilayer **F4/PEN** shows the same peaks with weaker intensity and for values on a ring $q_{xy}^2 + q_z^2 = const$ which is created by a pulver like material. This means that pentacene crystallites with herringbone structure are present. In contrast to the neat film not all of them are oriented vertically to the surface. There is an increased intensity at $q_z = 0\,\text{Å}^{-1}$, indicating that the vertical alignment is still preferential. The bilayer **PEN/F4** shows additional ring-shaped diffraction features stemming from F4-TCNQ.

For further information on the interaction in the bilayers FTIR spectroscopy measurements were conducted. Therefore, films were deposited on doubly polished, 1.5 mm thick silicon substrates [10]. The data were compared to the literature and DFT calculations to identify the prominent bands. In Fig.7.3 both bilayers show strong peaks that match with those found by Meneghetti et al.[184] for both anionic and neutral F4-TCNQ. The strongest peaks can also be brought into agreement with DFT calculations as indicated. The as-

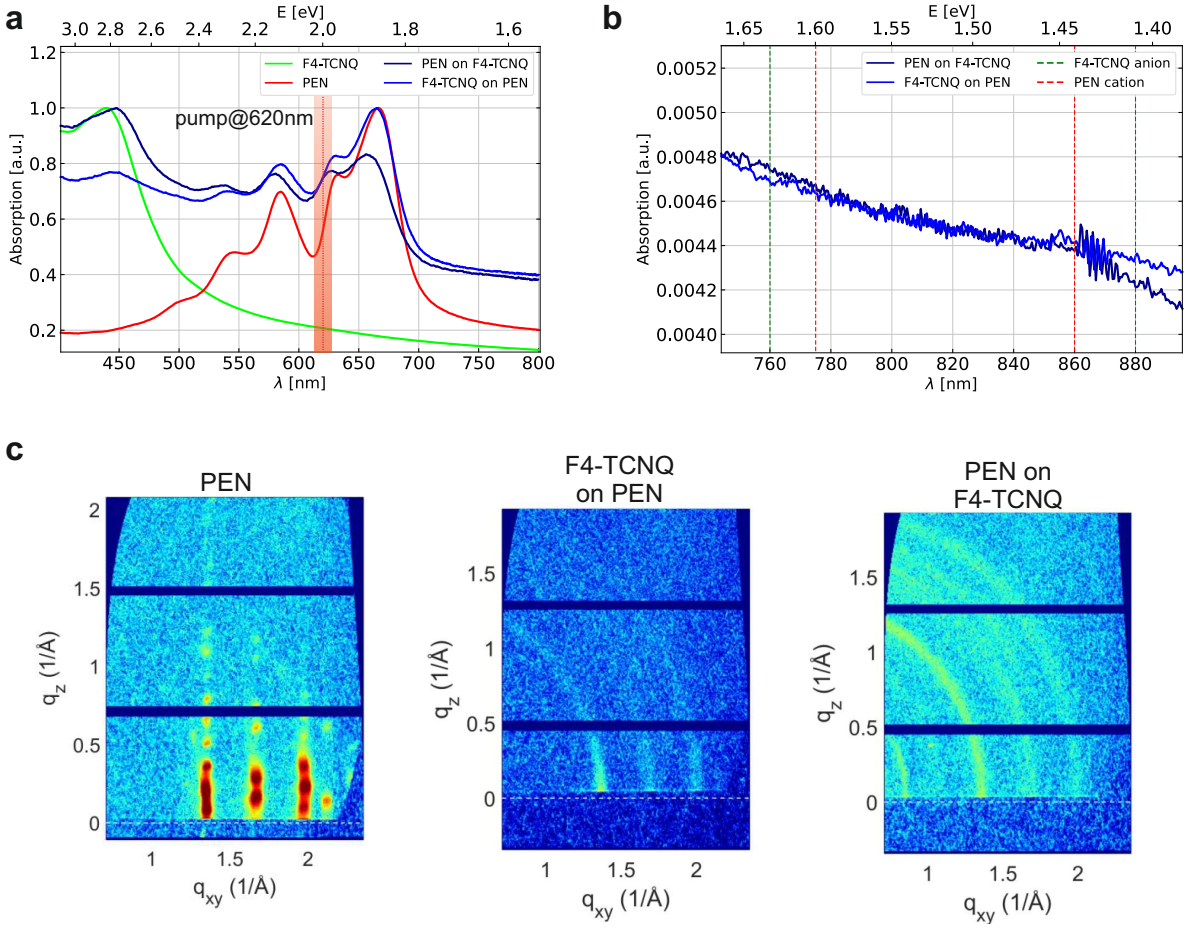

Figure 7.2: **a** UV/vis spectra of bilayers, pure PEN and F4-TCNQ thin films on quartz substrates. **b** In the NIR characteristic absorptions of possible PEN cations and F4-TCNQ anions are indicated by dashed lines. **c** Reciprocal space maps from GIWAXS measurements of PEN **F4/PEN** and **PEN/F4** (from left to right). The intensity is shown on a logarithmic scale [10].

signment of the absorption at 2194 cm^{-1} was matched with the stronger absorption of the calculation as shown in the figure, after comparison with literature. The calculation did not yield a strong absorption for neutral F4-TCNQ in this region, however, other experimental observations and calculations find bands at 2214 cm^{-1} and 2227 cm^{-1} [184, 185, 186].

Since F4-TCNQ anions are found from the spectra, pentacene cations should also be present. The band at 1395 cm^{-1} was observed from matrix-isolated pentacene cations[187] and 1501 cm^{-1} and 1541 cm^{-1} agree well with the DFT caclulation. The bands at 731 cm^{-1}, 906 cm^{-1} and 1296 cm^{-1} can be identified with absorptions of neutral PEN [188].

From the given data we can clearly conclude that F4-TCNQ anions are present in both films on the silicon substrate. On the quartz substrate they are however absent or too weak,

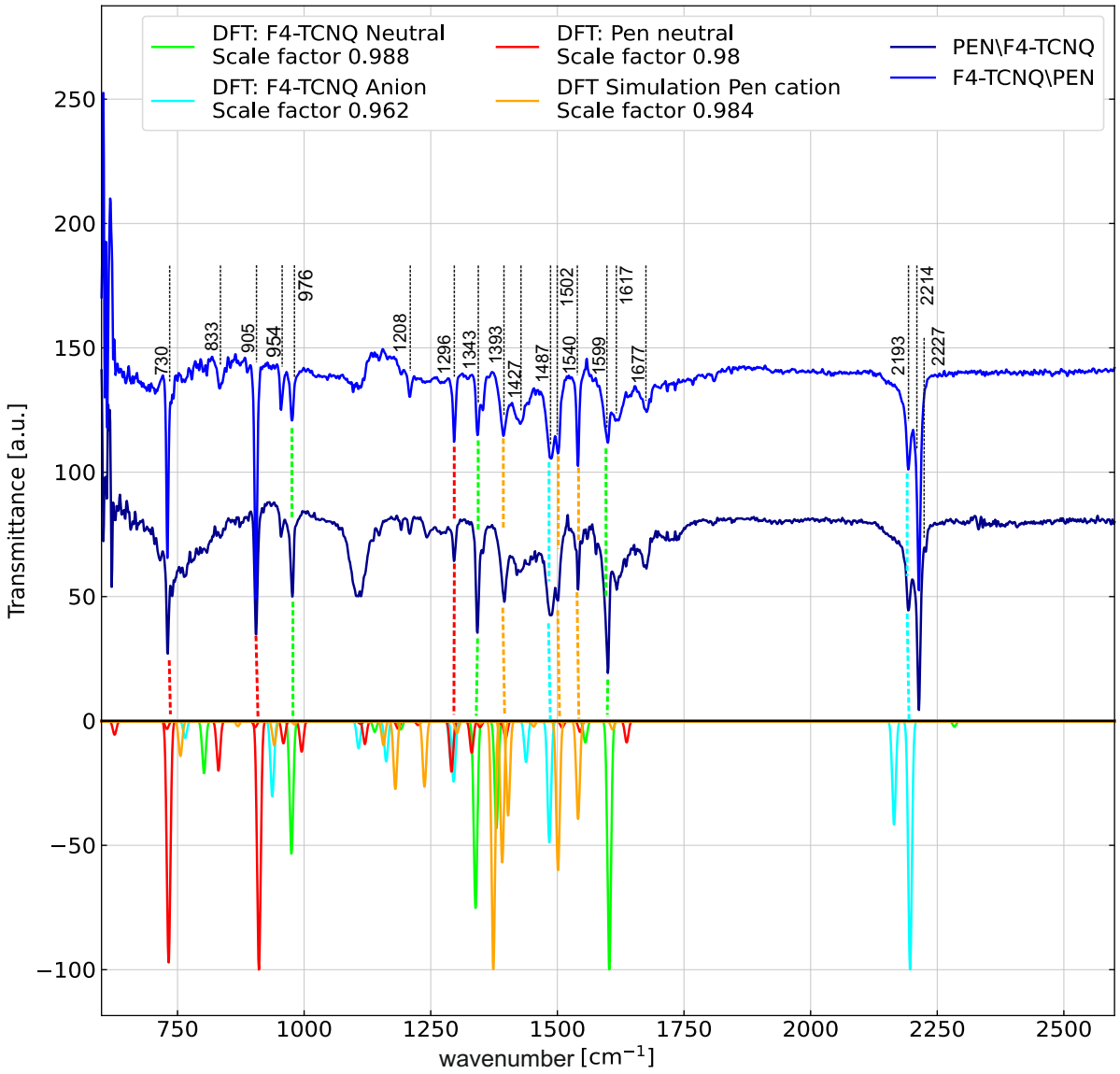

Figure 7.3: Infrared spectra of bilayers on silicon substrates measured with FTIR. The DFT calculations were performed with Gaussian with the B3LYP functional and 6-311++G** as basis set. The dashed coloured lines indicate frequencies that were used to calculate the scale factor.

to be observed.

7.2.2 Transient Absorption measurements

The samples were excited with light at a wavelength of $\lambda_{ex} = 620\,\text{nm}$, as indicated in Fig.7.2. This wavelength was chosen to excite PEN, whereas F4-TCNQ only has appreciable absorp-

tion at 450 nm or lower wavelengths. As a reminder, the model for SF in PEN is given:

$$(S_0S_1) \xrightarrow{(1)} {}^1(T_1T_1) \xrightarrow{(2)} {}^1(T_1 \cdots T_1) \xrightarrow{(3)} 2T_1, \tag{46}$$

This describes the excitation of a PEN dimer such that a singlet exciton is created on one molecule whereas the other one remains in the ground state (S_0S_1). The triplet pairs ${}^1(T_1T_1)$ and ${}^1(T_1 \cdots T_1)$ are generated after SF. The superscript on the left denotes the spin-multiplicity of the excited dimer and the dots indicate electronic dephasing and spatial separation. $2T_1$ describes two separated triplets. For more details on SF, see section 3.1.1.

The fs-TA spectra of the bilayers are shown in Fig.7.4 for the bilayers. In the visible spectrum both bilayers show characteristic spectral features that are associated with PEN (Fig.7.4 **a**, **c**). The GSB has minima at 666 and 582 nm for **F4/PEN**. The other bilayer **PEN/F4** has minima at 671 and 584 nm. The neat PEN thin film has minima at 679 and 584 nm. Above wavelengths of ∼700 nm the ESA due to the $T_1 \rightarrow T_2$ transition is visible. There is also no ESA visible that stems from the $T_1 \rightarrow T_3$ transition which is clearly observed for PEN when probed at 50° angle of incidence (compare Fig.A.2 in section A.0.2). In the NIR spectral region (Fig.7.4 **b** and **d**) the $T_1 \rightarrow T_2$ transition is observed, which extends into the visible region and has a broad maximum around 850 nm. At the same wavelength for long delay times, a weak negative contribution is detected. The $S_1 \rightarrow S_2$ transition of pentacene is seen as a broad absorption peaking at 1350 nm, compare Fig.7.4 **b** and **d**. Interestingly, it is observed for several picoseconds, yet it we claim that SF occurs in PEN within a few hundred femtoseconds. Essentially no singlet states should be occupied after a picosecond, such that an ESA due to the transition $S_1 \rightarrow S_2$ should not be observed. This observation is similar to the ESA observed for the PEN SURMOF in section 5.2 and it might be concluded that ${}^1(TT) \rightarrow S_2$ shows an absorption band resembling the $S_1 \rightarrow S_2$ absorption [35]. The features described above are similar to those observed in pure PEN, however, there are three major differences in the bilayers.

1. Both TA spectra exhibit a negative difference absorption ΔA in the range of 1400 to 1600 nm. The minimum of this absorption band is not captured by the detector of the setup. In a series of NIR spectra with F4-TCNQ and PEN a low energy absorption peaking at 1910 nm is observed that is only present in the blends [47]. The absorption is very broad and extends to values that can be observed in the fs-TA setup. Moreover the fs-TA spectra of these blends display a similar difference absorption, which is why it is attributed to the GSB of the charge transfer complex (CTC) between PEN and F4-TCNQ.

2. The triplet ESA in the NIR decays much faster in the bilayers as compared to the PEN thin film.

3. A peak emerges at 690 nm after longer time delays between 100-700 ps. We hypothesize that this kind of ESA results from the so-called electro absorption (EA).

EA as observed here, is not caused by a new absorption band but by a shift over time of an existing absorption band. This shift is caused by a static electric field which is well known

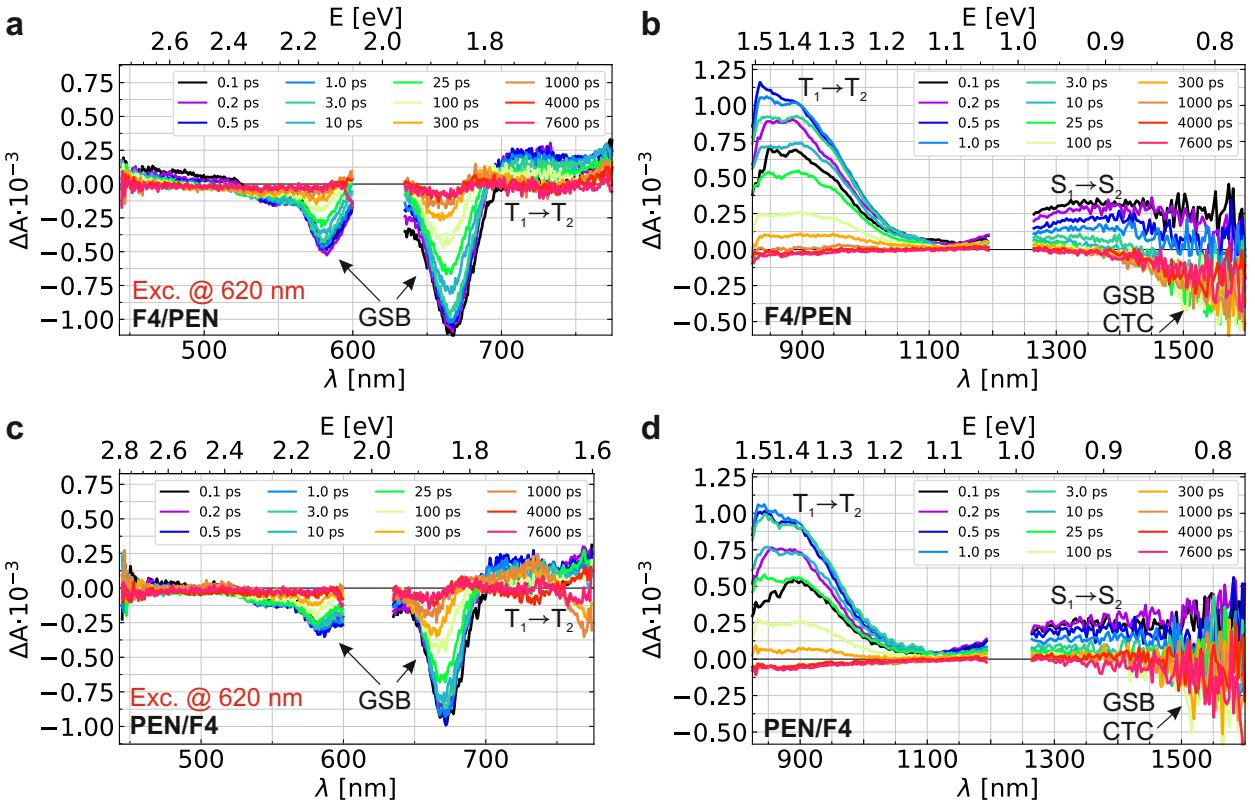

Figure 7.4: TA spectra of the **F4/PEN** bilayer in the visible range **a** and NIR **b** at a fluence of 300 nJ and 800 nJ per pulse, respectively. TA spectra of the **PEN/F4** bilayer in the visible range **a** and NIR **b** at a fluence of 150 nJ and 800 nJ per pulse, respectively. Some data points are removed due to the overlaid signal from scattered pump beam light.

in atomic spectroscopy as Stark effect. Weiser and Bässler studied the absorption spectra of pentacene and tetracene under the influence of an applied electric field [189]. The following derivation of the effect is based on their description. The transition energy E of a molecule changes in the presence of an electric field $\vec{F}$ as follows:

$$\Delta E(\vec{F}) = E(\vec{F}) - E(\vec{F}=0) = -(\vec{m_f} - \vec{m_i})\vec{F} - \frac{1}{2}\vec{F}\hat{\Delta p}\vec{F} \tag{47}$$

Here, $\vec{m}_{i,f}$ are the static dipole moments of the molecules and $\hat{\Delta p}$ is the change in polarisability upon electronic transition, which is a tensor in general. So the first term simply describes the energy of a dipole in an electric field. The second term arises when the electric field induces a dipole moment.

The change in transition energy given by Eq.(47) is relfected in a change of the extinction coefficient ϵ, which can be expressed by a taylor series:

$$\Delta\epsilon = \frac{\partial\epsilon}{\partial E}\Delta E + \frac{1}{2}\frac{\partial^2\epsilon}{\partial E^2}\Delta E^2 \tag{48}$$

The first term in Eq.(47) dominates for example if a strongly polar CT state is populated upon excitation. As we briefly mentioned already, there are CT states in our system, but the transition where EA is observed is the $S_0 \rightarrow S_1$ transition, with only weak dipole moments involved [189]. In this case the first term is neglected. In general, all transitions implicate at least a small change in polarisability Δp, which is why the quadratic term in the change of energy is neglected as well. Therefore in many systems, the *quadratic Stark effect* is present which is characterised by:

$$\Delta\epsilon = -\frac{1}{2}\bar{\Delta p}\frac{\partial\epsilon}{\partial E}\vec{F}^2, \tag{49}$$

where $\bar{\Delta p}$ includes an orientational average.

This change is seen directly in the transient absorption measurements.

$$\Delta A = -log\left(\frac{I_{ex}}{I_0}\right) = -log\left(\frac{I_0 e^{-\epsilon' c(t) d}}{I_0 e^{-\epsilon c_0 d}}\right) \tag{50}$$

$$= \epsilon c_0 d - \epsilon' c(t) d = \epsilon c_0 d - [\epsilon + \Delta\epsilon]\, c(t) d \tag{51}$$

$$= \epsilon \Delta c d - \Delta\epsilon c(t) d \tag{52}$$

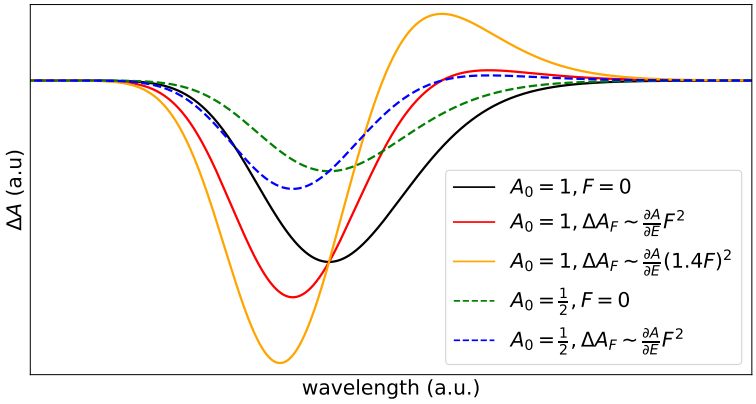

Figure 7.5: Influence of the Stark effect on transient absorption data. The ground state absorption was assumed to be Gaussian shaped with an amplitude A_0. The change in the difference absorption ΔA_F due to an electric field of magnitude F is calculated for F, an increased field strength $\sqrt{2}F$ and a reduced amplitude $\frac{1}{2}A_0$

The first term is what is observed in the TA spectra without an electric field. For a qualitative understanding a Gaussian shaped absorption is examined in Fig.7.5. In the graph, the ΔA spectrum for an amplitude of $A_0 = 1$ without and with electric field are displayed (with $\bar{\Delta p} > 0$). Here, the minimum shifts to lower wavelength, while a positive shoulder is added, that increases with the strength of the electric field.

For a lower amplitude of the GSB $A_0 = 0.5$ the minimum and maximum shift in the same manner, i.e. the position of the extrema does not depend on the amplitude, but only on

the strength of the electric field. However, the zero crossing does blueshift with decreasing amplitude.

The EA has been observed in a similar system consisting of a bilayer of PEN and C_{60}, which is a strong electron acceptor [190]. With that, the general spectral features have been described. Next, the kinetics will be elucidated with the help of global analysis.

Global analysis of PEN/F4-TCNQ bilayers

The fs-TA of Fig.7.4 were analysed with Glotaran [82]. The results are displayed in Fig.7.6. For both samples, a model with four sequential exponential decays is used to describe the data in the visible range, whereas five time constants are used in the NIR. This was chosen, since only in the NIR a sub-picosecond process could be fitted, which we attributed to SF in PEN. In the visible spectral range it is difficult to observe the SF kinetics because PEN exhibits little to no SE from the singlet state [95, 97, 191]. Moreover, the rise time of the triplet ESA is better observed in the NIR as the oscillator strength is weak in the visible spectral range. Furthermore, the process is close to the resolution limit of the setup and there is a higher level of noise in the range of 720-770 nm due to the low intensity of the probe white light spectrum. For both layers the proposed mechanism is illustrated in Fig.7.7.

With $\tau_1 = \tau_{SF} = 158$ fs for **F4/PEN** and $\tau_{SF} = 222$ fs for **PEN/F4**, the SF rate is slower than in the pure PEN thin film. This observation might be explained by the higher disorder in the bilayers, as was seen in the steady-state characterisation. The second process - electronic decoupling of the triplet pair - was claimed to be identified first in PEN derivatives [44] and from that the conclusion was suggested for the pure PEN thin film as well [47]. Again both decay constants $\tau_2 = 1.3$ ps for **F4/PEN** and $\tau_2 = 1.5$ ps for **PEN/F4** are on the same order of magnitude as for PEN (1.2 ps), yet a bit slower. The rates are taken from the NIR data, as the triplet intermediate state $^1(\mathrm{T}\cdots\mathrm{T})$ was observed by a change of shape of the triplet ESA associated with the $\mathrm{T}_1 \rightarrow \mathrm{T}_2$ transition in the NIR. In the neat PEN thin film a slight red shift was observed.Here, the blue EADS in Fig.7.6 **b** and **d** loses intensity at ~ 850 nm when changing to the green EADS. The next spectra are connected with time constants in VIS and NIR of 21 and 24 ps for **F4/PEN** and 42 and 56 ps for **PEN/F4**. While there is a weaker triplet ESA in both VIS and NIR for this spectrum, the ground state of the CTC is bleached (1400-1600 nm) and the shoulder at 690 nm due to EA can be observed. The build-up of the EA signal is depicted in Fig.7.8 **a**. The selected wavelength lies within the GSB of PEN which is why the signal is negative after excitation. For both bilayers the overlaid EA causes the signal to rise and reach a maximum at 143 ps and 663 ps for **F4/PEN** and **PEN/F4**, respectively. The maxima were extracted from the fit functions. For comparison, data of the PEN are included as well. There is data for two fluences comparable to the bilayers, since especially the triplet dynamics in PEN depend on the fluence. The data for PEN are selected from a higher probe wavelength of 707 nm, since only then any positive ΔA signal is observed. It is known for PEN to exhibit EA in pure thin films increasing with fluence [190]. For the fluences used here, the effect is seen in PEN only weakly and at a different wavelength, hence it can be excluded that the EA is an intrinsic effect of the PEN layer itself within the bilayer.

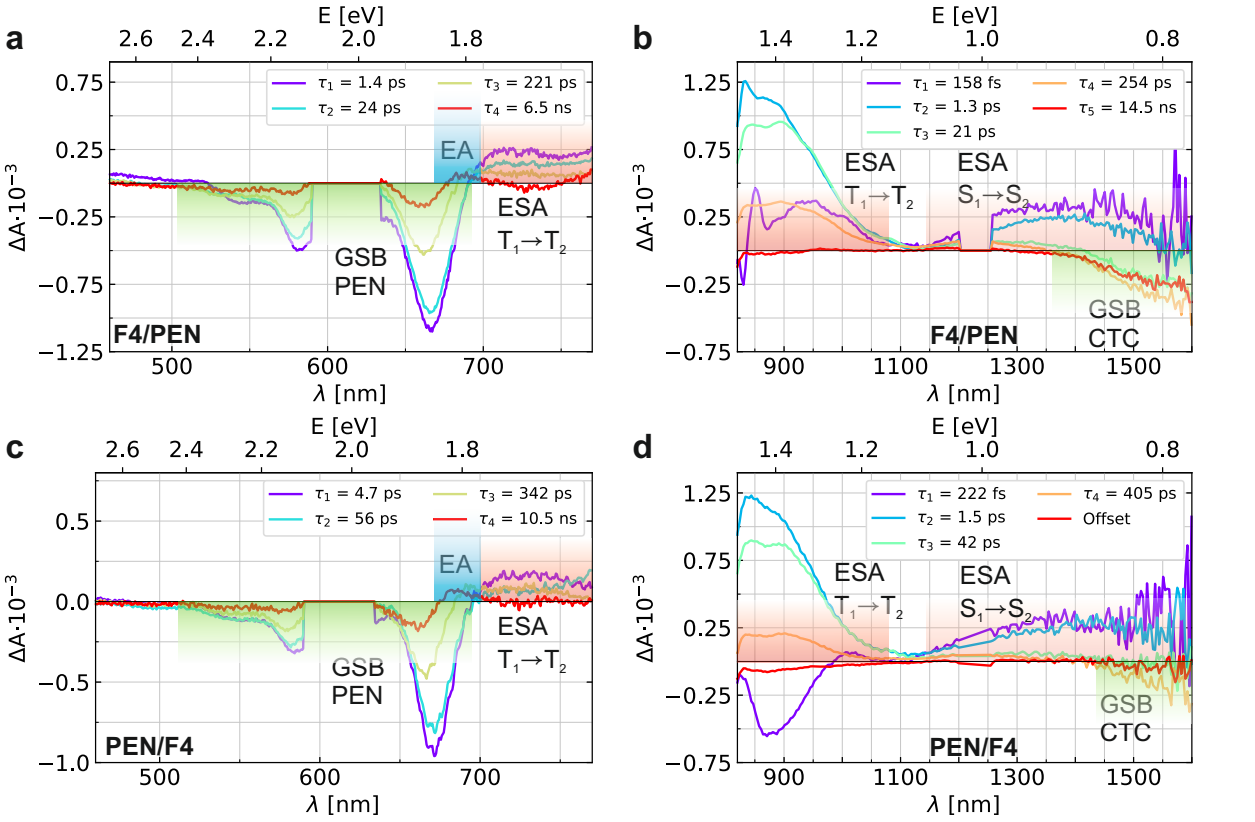

Figure 7.6: EADS of **F4/PEN a**, **b** and **PEN/F4 c** and **d**. The coloured areas indicate contributions from GSB (green), ESA (red) and electro absorption due an electric field (blue). CTC: charge transfer complex, EA: electro absorption

For the next process, the global analysis yields time constants in the visible and NIR region of 221 and 254 ps for **F4/PEN** and 342 and 405 ps for **PEN/F4**. In the visible region there are two distinct changes associated with this time constant in the spectra, which can be seen in the change from the yellow to the red EADS: The triplet ESA has essentially decayed close to zero and the EA is blue-shifted.

From the basic considerations on the Stark effect at the beginning of this section, it was seen that only the electric field strength contributes to a shift of the GSB minimum (compare Fig.7.5). Therefore, it is concluded that these decay constants of a few hundred picoseconds also contribute to the build-up of the electric field.

As in the visible, the last spectrum does not contain a contribution from the triplet ESA in the NIR, which means that all triplets have decayed to the ground state or have transferred their energy to the CTC.

The dynamics of the triplets are compared to the pure PEN thin film in Fig.7.8 **b**. As the bilayers have a total thickness of ~ 20 nm, with each PEN and F4-TCNQ comprising half of it, data for a PEN thin film of thickness $d = 10$ nm is included as well. This was done to test for any dependence on film thickness, as excitons at the surface might have different

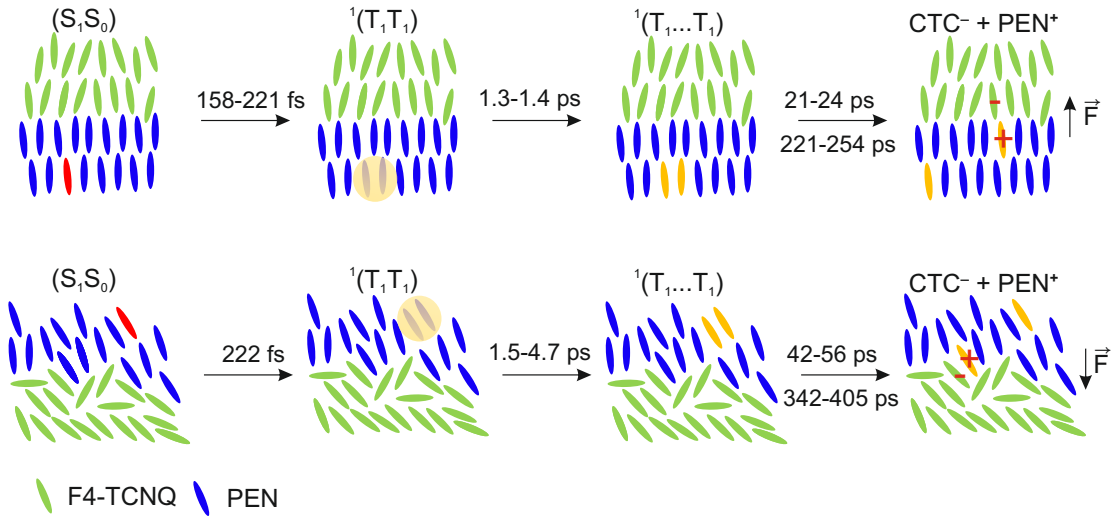

Figure 7.7: Schematic of the exciton dynamics. SF is followed by electronic decoupling of the triplet pair. The diffusion to and charge separation at the interface leads to the build-up of a static electric field $\vec{F}$. The coloured molecules indicate a singlet exciton (red) or a triplet exciton (yellow)

decay dynamics, which is not the case here. Apparently, the decay in the bilayers is sped up significantly. In principle, the decay of the triplets in PEN should be modelled via Eq.(3), which includes the decay due to triplet-triplet annihilation (TTA), but for the purpose of this comparison a bi-exponential decay is used. From that decay constants of $\tau_{PEN,T1} = 242\,\text{ps}$ and $\tau_{PEN,T2} = 2.9\,\text{ns}$ are obtained. In the bilayers the respective time constants are an order of magnitude smaller - between 21 and 56 ps and 221 and 405 ps. This points out that an additional decay channel is present and supports the idea that the triplets are responsible for populating excited states in the CTC.

Lastly, the decay of the excitation of the CTC is on the nanosecond timescale, however, the decay constants in the visible and NIR differ quite strongly. The bilayer **F4/PEN** shows a decay of 6.5 ns in the visible and 14.5 ns in the NIR. The discrepancy might be caused by the additional bleach in the range of 900-1000 nm, the origin of which is not clear. Another fit that only uses the data in the range of 1250-1600 nm yields a decay constant of 8.2 ns.

For **PEN/F4** the fit yields 10.5 ns in the visible spectrum. In the NIR region the fit only converges if a constant offset is used. The EADS in Fig.7.6 **d** shows that the main component again is the bleach between 900-1000 nm, whereas the GSB of the CTC has a low SNR and hence no conclusion for the CTC lifetime can be drawn from the NIR data. The kinetics of the GSB of the CTC in the bilayers are displayed in Fig.7.8 **d**. No comparison to the neat PEN film is made here as no absorption is observed there.

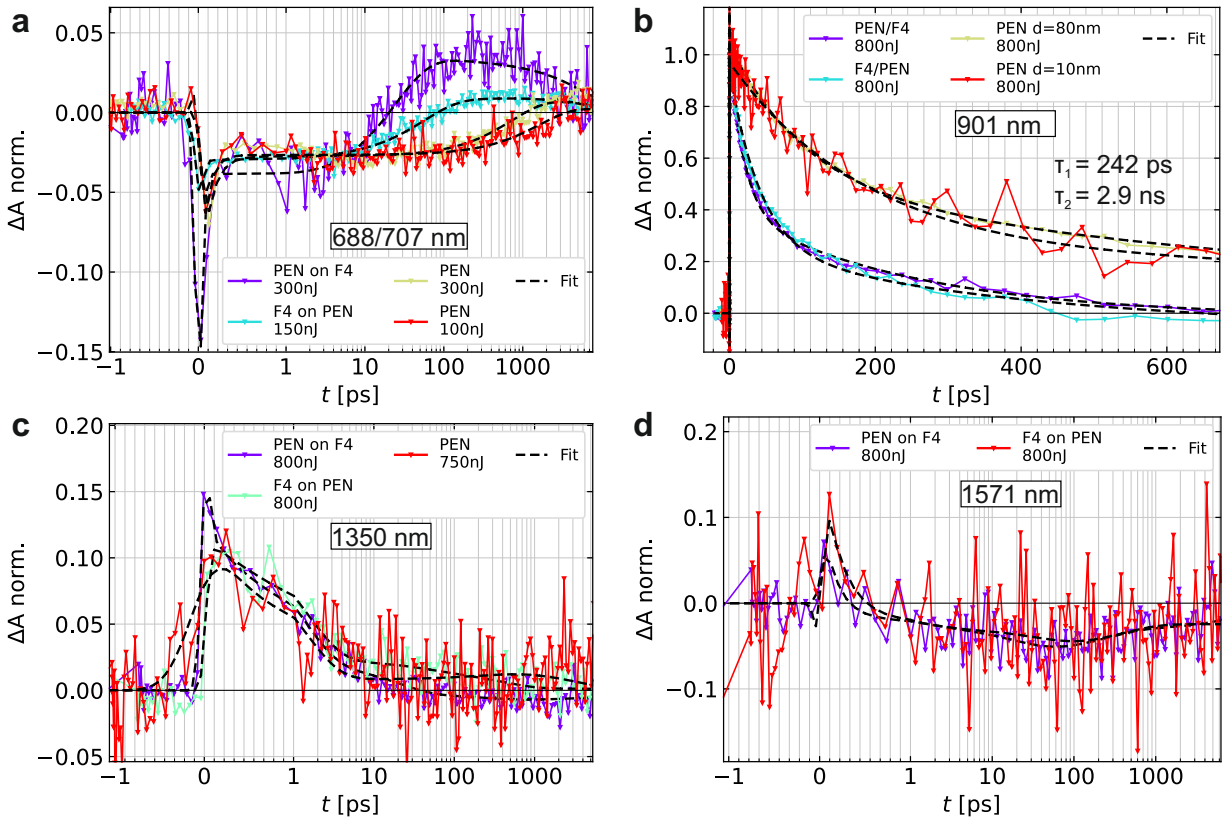

Figure 7.8: fs-TA kinetics of PEN F4-TCNQ bilayers and a neat PEN thin film. The included fits are results of the global analysis. **a** EA due to charge built-up is strongest at 688 nm for the bilayers. A positive difference absorption is observed for PEN at 707 nm for long time delays. **b** Triplet decay in PEN thin films of thickness d and bilayers observed at 901 nm. The decay constants τ_1 and τ_2 are taken from GA on the PEN thin film qith $d = 80$ nm **c** ESA at 1350 nm associated with spin singlet character. **d** GSB of the CTC observed in the bilayers.

7.3 Pentacene - F6-TCNNQ bilayers

As F6-TCNNQ is a stronger acceptor compared to F4-TCNQ, since it has a higher E_{EA}= 5.3−5.6eV (compare Fig.7.1) ICT instead of CT complex formation should be expected. This is indeed the case for the blends as verified by FTIR measurements for different PEN:F6-TCNNQ ratios [10]. With increasing ratio neutral and ionized molecules are detected.

7.3.1 Material preparation and characterisation

The UV/vis spectra of the bilayers with F6-TCNNQ **PEN/F6** and **F6/PEN** (top/bottom layer) are shown in Fig.7.9 **a** and **b**. The spectra in **a** essentially show a superposition of the spectra of the pure species. With PEN deposited on top of F6-TCNNQ the intensity of the

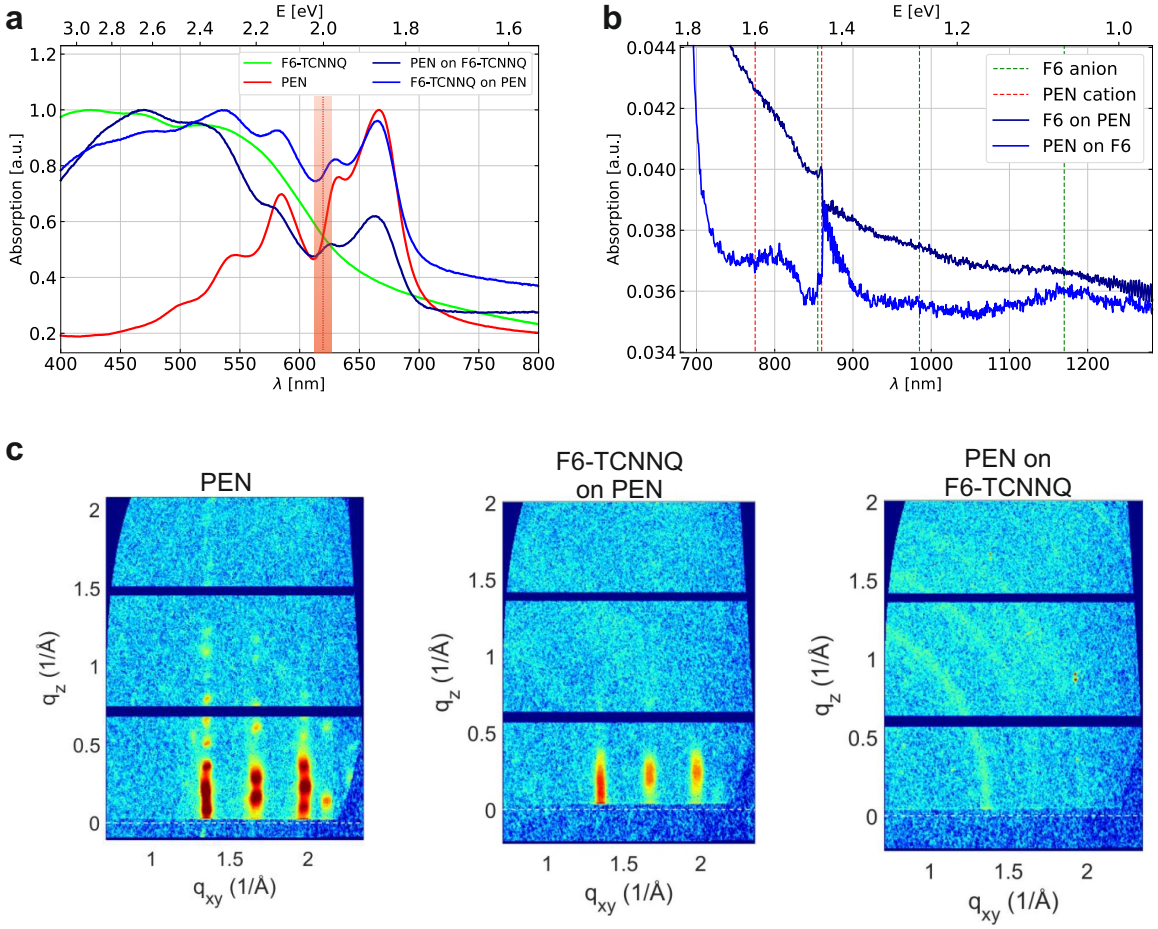

Figure 7.9: **a** Uv/Vis spectra of bilayers, pure PEN and F6-TCNNQ thin films on quartz substrates. **b** In the NIR characteristic absorptions of PEN cations and F6-TCNNQ anions are indicated by dashed lines. **c** Reciprocal space maps from GIWAXS measurements of **F6/PEN** and **PEN/F6**(from left to right). The intensity is shown on a logarithmic scale [10].

PEN absorption is decreased in comparison to the other bilayer **F6/PEN**. As the transition dipole moment of the $S_0 \rightarrow S_1$ is oriented along the short axis of the molecule, the decrease in absorption might be explained by the loss of orientation to the surface of the substrate. In the visible to NIR spectral region, absorptions of PEN cations and of F6-TCNNQ anions can be observed as indicated in Fig.7.9 **b**. For **PEN/F6** weak peaks at the F6-TCNNQ anion absorption are observed and for **F6/PEN** an even weaker absorption at 1070 nm is observed. The low intensity of these absorptions must result from the fact that only at the thin interface charges are transferred. Even further, it might be hypothesised, that **F6/PEN** does allow for less electron transfer, as no preferential relative orientation between F6-TCNNQ and PEN is achieved, due to a rigid crystalline structure of PEN, as seen from the x-ray scattering

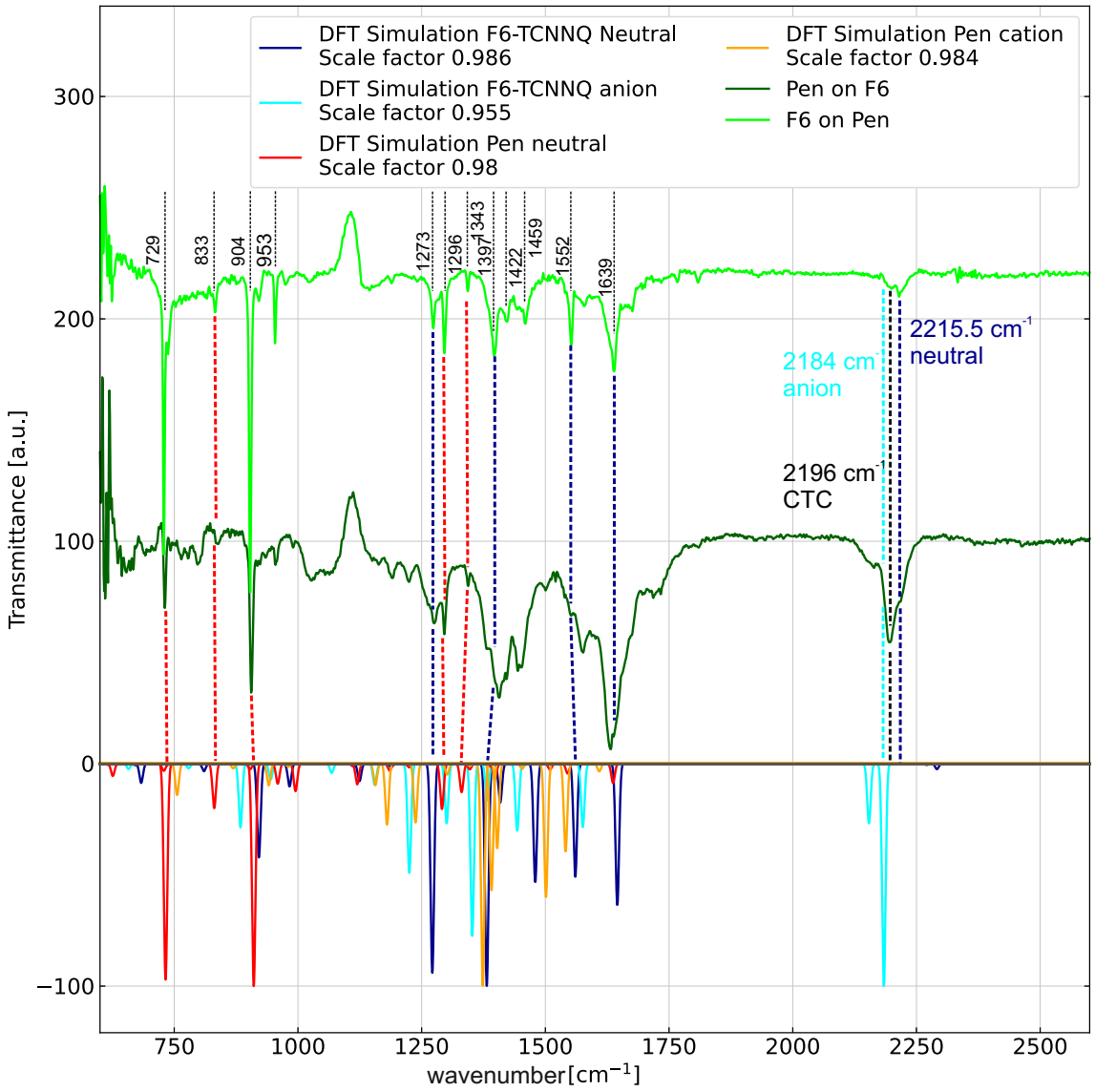

Figure 7.10: Infrared spectra of bilayers on silicon substrates measured with FTIR. The DFT calculations were performed with Gaussian with the B3LYP functional and 6-311++G** as basis set. The dashed coloured lines indicate frequencies that were used to calculate the scale factor.

experiments. The GIWAXS data for the bilayers are displayed in Fig.7.9 **c**. Apparently, the crystal structure and orientation of the PEN molecules on the surface are less disturbed in **F6/PEN** as for any other bilayer, as can be seen from the clear diffraction features at q_{xy} =1.35 Å^{-1}, 1.67 Å^{-1} and 1.98 Å^{-1}, which are at the same positions as in the neat PEN thin film, although distinct diffraction peaks are fewer.

It might be argued that the smaller F4-TCNQ molecule can interpenetrate the PEN layer better than F6-TCNNQ. On the other hand, when PEN is deposited on F6-TCNNQ the GIWAXS data again shows ring-like structures that are characteristic of a powder-like structure of PEN.

From the FTIR data in Fig.7.10 it can be inferred that the main absorption bands stem from the neutral PEN and F6-TCNNQ, which can be validated with the DFT calculation as well as other experimental results [192, 193, 194]. The main absorptions of neutral PEN in **F6/PEN** are located at 729 cm^{-1}, 903 cm^{-1} and 1296 cm^{-1}. In comparison to the other bilayers (including F4-TCNQ) the first two peaks, which stem wagging vibrations, are red-shifted by $\sim 3\,cm^{-1}$. Aditionally, all absorption bands in **PEN/F6** are broadened compared to **F6/PEN**. Again, these observations might be attributed to low distortion of the bottom PEN thin film layer in **F6/PEN**, as observed by GIWAXS. Absorption bands of neutral F6-TCNNQ are clearly visible at 1273 cm^{-1}, 1552 cm^{-1} and 1635 cm^{-1} and agree with the DFT calculation and values from the literature [193, 194]. The broad absorption band with a maximum at 2196 cm^{-1} stems from the stretching vibration of the cyano group C≡N. Although our DFT calculation does not predict a strong band for neutral F6-TCNNQ in this range, it is known from literature that an absorption at 2213-2216 cm^{-1} with minor peaks at 2222 cm^{-1}, 2204 cm^{-1} and a tail extending to lower wavenumbers is characteristic for neutral F6-TCNNQ [194]. The blends studied by Theurer et al. show clear peaks at 2191 cm^{-1} attributed to the F6-TCNNQ$^{\bullet -}$ radical anion. The F6-TCNNQ$^{\bullet -}$ radical anion has a red-shifted absorption with a maximum at 2194 cm^{-1} [194]. Another study reports an even higher red shift of 33 cm^{-1} for the anion and attributes a series of peaks with a maximum at 2189 cm^{-1} to a charge transfer degree of $\delta_C T = \frac{\Delta v_{exp}}{\Delta v_{full}} 0.81$, where $\Delta v_{exp,full}$ are the observed frequency shift and the one expected for a complete CT [193]. The authors remarked however that for F6-TCNNQ the shift of the C≡N strechting mode alone might not be a clear indicator. They observe an intensified band of the C=C stretching mode at 1389 cm^{-1}. The bilayer **F6/PEN** has a peak at 1397 cm^{-1}. With **PEN/F6** no clear identification of distinct absorption peaks is possible, but increased absorption is observed at 1381 cm^{-1} with a maximum at 1407 cm^{-1}.

7.3.2 Transient absorption measurements

The fs-TA spectra of **PEN/F6** and **F6/PEN** are displayed in Fig.7.11. The positions of the minima of the GSB are at 672 nm and 585 nm for **F6/PEN** and 672 nm and 580 nm for **PEN/F6** (679 and 584 nm in neat PEN). The blue shift of the minima of the bilayers could be explained by the disturbed crystal structure in the bilayers. It would also be possible to argue that a ground state (GS) CT would lead to electric fields and a shift of the absorption due to the Stark effect. In contrast to the development seen over time after excitation of the F4-TCNQ layers, a GS CT would not result in the positive shoulder, as the shifted absorption is present in the GS already. The triplet state $T_1 \rightarrow T_2$ absorption is seen in the visible spectrum above 700 nm and as broad absorption in the NIR.

A distinct difference between the bilayers is observed at 540 nm, which is also not seen for the F4-TCNQ layers. This ESA stems from the $T_1 \rightarrow T_3$ transition, as mentioned already

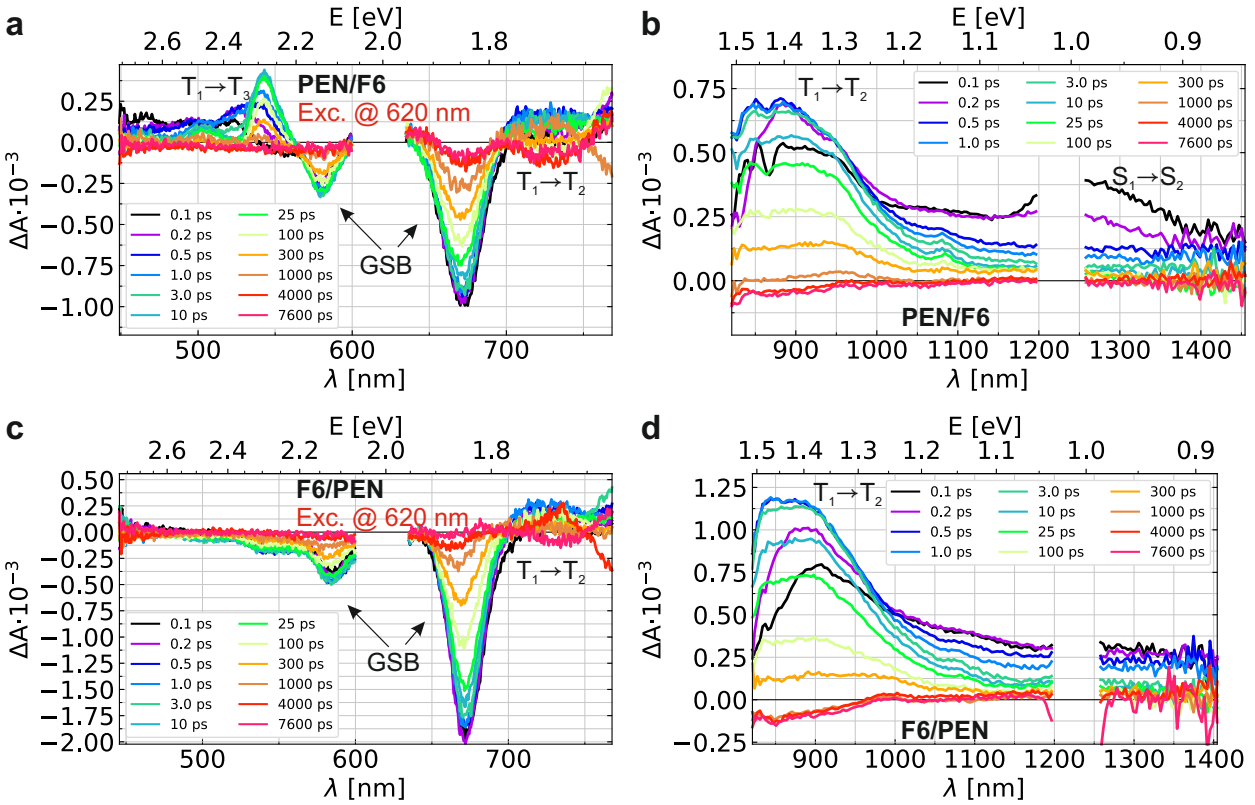

Figure 7.11: TA spectra of the **PEN/F6** bilayer in the visible range **a** and NIR **b** at a fluence of 250 nJ and 800 nJ per pulse, respectively. TA spectra of the **F6/PEN** bilayer in the visible range **a** and NIR **b** at a fluence of 200 nJ and 800 nJ per pulse, respectively. Some data points are removed due to the overlaid signal from scattered pump beam light.

in chapter 5.2.2 on the PEN thin film and PEN SURMOF. The axis of the transition dipole moment lies along the long axis of the molecule. Therefore it is not to be observed for an oriented PEN thin film, where the incident light beam and the long molecular axis are almost parallel. For **PEN/F6** the PEN layer loses its preferential upright orientation to the surface. It is also assumed that this orientational effect causes the ESA in the range of 1200 to 1400 nm, which is assigned to the transition $S_1 \rightarrow S_2$.

A weak negative ΔA signal is observed in the range of 820 to 950 nm for long time delays, which is also present in the neat F6-TCNNQ film (see Fig.D.1 c)). The EA as observed before is not specific to F4-TCNQ and arose due to PEN in the presence of static electric fields. Hence, it would be expected for F6-TCNNQ as well upon charge separation at the interface. There is no EA visible for **PEN/F6**, but there is an extremely weak EA observed in **F6/PEN** at 685 nm. There is also a blue shift of the GSB observed, which is absent in **PEN/F6**.

Global analysis of PEN/F6-TCNNQ bilayers

The DADS from global analysis are depicted in Fig.7.12. The models in the visible and NIR spectral range cannot be brought to perfect agreement. However, the SF time constants agree well with $\tau_{SF} = 145$ and 185 fs for **PEN/F6** and $\tau_{SF} = 105$ and 106 fs for **F6/PEN**. Seeing that 105 fs is close to the value of neat PEN is reasonable for this sample, since the GIWAXS data indicated a highly crystalline structure close to the native PEN thin film structure. In the NIR spectral range the model can be interpreted similar to the model for F4-TCNQ bilayers: $\tau_{2,NIR}$ describes the transition $^1(\mathrm{TT}) \rightarrow {}^1(\mathrm{T}\cdots\mathrm{T})$. The decay of the triplet ESA is captured by the time constants $\tau_{3,NIR}$ and $\tau_{4,NIR}$. For both samples they are significantly faster than the decay in neat PEN and on the same order as in the bilayers with F4-TCNQ. This indicates that the PEN triplets interact with F6-TCNNQ.

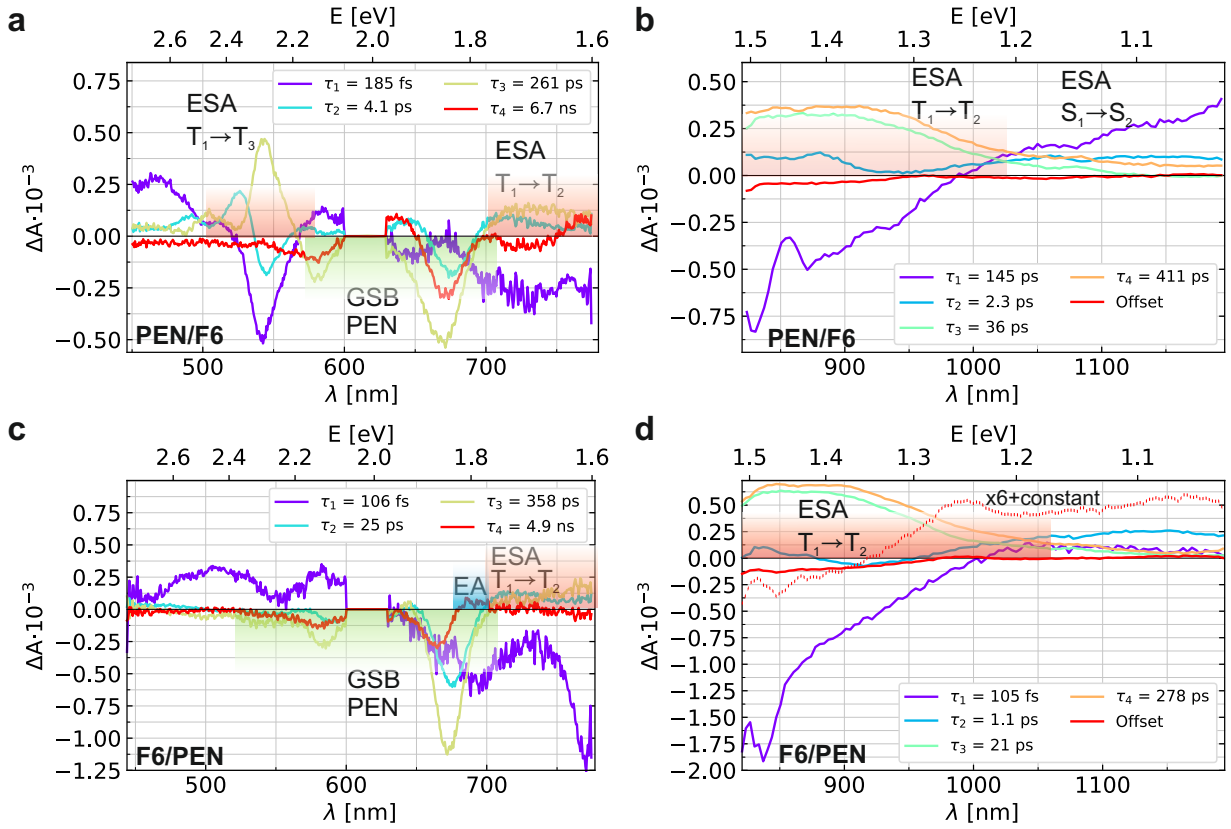

Figure 7.12: DADS of **PEN/F6 a**, **b** and **F6/PEN c** and **d**. The coloured areas indicate contributions from GSB (green), ESA (red) and electro absorption due an electric field (blue). The red dashed line in **d** shows the "Offset" spectrum (red, solid) multiplied by 6 and offset by a constant value.

As mentioned **F6/PEN** exhibits a weak EA, which is also captured in the DADS (red) in Fig.7.12 c). Hence, there should be some indication of charged species. Fig.7.12 d) includes a scaled-up version of the red DADS, which has a peak at 993 nm. F6-TCNNQ$^{\bullet-}$ anions

absorb at 985 nm and 1146 nm [195] and the PEN cation absorbs at 990 nm and it is assumed that PEN cation dimers show a broader absorption band centred at 880 nm [192]. Therefore, it can be concluded that ions are present and CS occurs in **F6/PEN** as well, although to a weaker extend. There is however no clear sign of CS in **PEN/F6**, which is surprising as the triplet decay is also sped up in this sample. An additional quenching pathway is apparently introduced in the system.

7.4 Conclusion

The properties in bilayers of F4-TCNQ and F6-TCNNQ with PEN were examined with steady-state and time-resolved spectroscopic experiments. In previous publications, it was theoretically and experimentally demonstrated that F4-TNCQ as a p-dopant is at the border of creating ion-pairs or CT complexes [10, 169, 170]. The blends of F4-TCNQ and PEN studied by Theurer et al.[10] were found to exhibit a coexistence of integer CT and CT complexes, confirming the conjecture. The structural investigation with GIWAXS showed that the bilayers exhibit diffraction features of a powder-like material. When PEN is on the bottom and therefore in direct contact with the substrate a parallel orientation of the PEN molecules to the surface normal is preferential, especially for **F6/PEN**. The FTIR data on bilayers including F4-TCNQ exhibit peaks associated with vibrations of F4-TCNQ anions and PEN cations, aside from the neutral species. This stands in contrast to the results from the fs-TA data. A possible explanation is that FITR measurements were conducted on silicon substrates, whereas the fs-TA spectra were taken on quartz substrates. On quartz substrates the PEN molecules orient upright whereas on silicon the preferred orientation is flat-lying [196, 197]. The FTIR data of the bilayer **F6/PEN** indicates very weak interaction of the molecules as mostly vibrations of neutral molecules are detected. This is not the case for **PEN/F6**, where the IR bands are broadened. From that, no clear identification is possible, despite that F6-TCNNQ is considered the stronger acceptor and ICT was expected.

The excited state dynamics (λ_{ex} = 620 nm) for the PEN-F4-TCNQ bilayers are summarized in Fig.7.7. The singlet fission process is not inhibited in this system, which is to be expected, as the PEN layers still exhibit crystalline structures. The electronic dephasing ^{1}(TT)→(T$\cdots$T) is slowed down only marginally to 1.3-1.5 ps, whereas with neat PEN a time constant of 1.2 ps is found.

The diffusion to the interface can be approximated by two exponential decays. For the bilayer **F4/PEN** time constants of 21-24 ps and 221-254 ps are obtained. With PEN on top of F4-TCNQ instead, time constants of 42-56 ps and 342-405 ps are obtained.

Since the bilayer with PEN on top shows stronger ring-like diffraction peaks, indicating less ordered structures, the difference in diffusion might be attributed to an increase in grain boundaries. That excitons reach the interface and charge separation takes place, is identified by the GSB of the CT complex in the NIR and a concomitant rise of a positive ΔA signal. The interpretation of this rising signal is, that the ground state absorption of PEN changes due to the quadratic Stark effect. The static electric field is surmised to be built up at the interface, when an electron is transferred from the PEN in a triplet excited state to the CT complex of PEN and F4-TCNQ. It should be noted on the one hand, that thin films

of pristine PEN exhibit this feature by themselves, yet for higher fluences and longer delay times. On the other hand, the blends of F4-TCNQ and PEN do show the GSB of the CT complex in the NIR, but no EA can be detected there, leading to the conclusion that the interface is responsible for the emergence of EA. Surprisingly, no evidence of CS is found in **PEN/F6** and only minor ESA due to ions is observed in **F6/PEN**. This observation might be attributed to the weak intermolecular interaction in the bilayered structure.

8 Non-linear optical studies on cubic cage compounds

This chapter includes results of SHG on chiral molecules. The theoretical fundamentals are explained in section 3.3.2, but the basic principles will be discussed in the following introduction. The experimental setup is described in section 4.2.

8.1 Introduction

Chiral molecules lack any mirror planes and therefore two so-called enantiomers exist that are mirror images of each other. Several fields have an interest in chiral molecules such as biochemistry, pharmacology and optics. The enantiomers can have drastically different properties. In biological systems often only one enantiomer is relevant (homochirality) and in some cases its mirror image can even be toxic [198, 199, 200]. Differences in the optical properties of enantiomers were already found at the beginning of the 19th century, although the connection to the molecular structure was not discovered then. The optical activity, i.e. the rotation of polarized light was first observed by J.B. Biot in 1815 [201]. He found that two forms of these optically active media exist, with the opposite sense of rotation. This effect is today known as optical rotation. Fresnel (1788-1827) explained the optical activity by decomposing linear polarized light in left and right-handed circular polarized light [202]. Under the assumption of different refractive indices of left and right-handed polarized light, a phase shift is induced due to different velocities when traversing the material. The phase shift translates to a rotation of the linear polarized light. Only in 1850, a connection was made to chiral molecules by Louis Pasteur [203].

In 1895 the French physicist Aimé Cotton observed the difference in absorption of left- and right-handed light, which is known as circular dichroism (CD).

In the context of non-linear optics similar phenomena occur, but there exist also effects that have no analogue to linear optics. Second harmonic circular dichroism (SHG-CD) is defined by $\frac{\Delta I(2\omega)}{I(2\omega)} = 2\frac{I_L(2\omega)-I_R(2\omega)}{|I_L(2\omega)+I_R(2\omega)|}$, where the indices L, R indicate left and right circular polarized light of the fundamental beam. SHG-CD relies on resonant excitation or with energy $2\hbar\omega$ [25]. The linear optical rotation has also its non-linear counterpart which is second harmonic optical rotary dispersion (SHG-ORD). Furthermore, by rotating a quarter wave plate (QWP) in front of the sample, the material response can be investigated in detail. Kauranen et al.[75] have developed a mathematical framework to describe the material response on incident light depending on the rotation angle of the QWP. From that, it is possible to characterise the second-order non-linear susceptibilities.

SHG-ORD and polarisation rotation experiments with a QWP were applied on chiral cubic cage compounds and will be presented and discussed in the following. The cages were synthesized to study chiral self-sorting. Chiral social self-sorting describes the behaviour with an increased affinity of an enantiomer to the opposite enantiomer, whereas in narcissistic self-sorting processes, the affinity is higher for the same enantiomer [204]. Here, the results serve as the first characterisation of their non-linear optical properties. Future steps aim at absorbing chiral gas molecules in the cage compounds and observing the changes in the non-linear response.

The recognition of the chirality of molecules in the gas phase is a challenging subject. Due to very similar interactions, the physical properties - aside from the discussed optical methods - are mostly identical. The interaction of enantiomers with other substances differs only if the substance itself is chiral. A fact that is used in chiral column chromatography where the stationary phase, that interacts with the molecules to be analysed is chiral itself. For chiral gas molecules, chirality recognition is complicated if the molecules only occur in trace amounts. This is especially the case in linear optical detection methods. For example, the angle of optical rotation stands in a linear correlation to the amount of chiral molecules. In non-linear optics the angle does not in principle depend on the amount of material, however, the signal intensity does [25].

As the cage compounds are highly porous, they exhibit high specific surface areas (up to $1487\,\mathrm{m^2\,g^{-1}}$ [204] and might be suited for absorption of chiral molecules. Due to the chirality of the cage compounds themselves, they could exhibit enantioselective absorption. Together with the enhanced detection capabilities of chirality in non-linear optics, chirality recognition and possibly estimation of the relative amounts of enantiomers in a gas mixture (enantiomeric excess) can be achieved with these samples in future.

8.1.1 Chiral cubic salicylimine cage compounds

The samples were prepared by Philippe Wagner in the group of Michael Mastalerz at the Institute of Organic Chemistry in Heidelberg. The synthesis and characterisation of the material can be found in Ref.[204] The cage compounds are composed of chiral 8 tris-salicylaldehydes that are linked with 12 p-phenylenediamines. The tris-salicylaldehydes adopt a bent molecular configuration as schematically illustrated Fig.8.1. In this shape they can form the vertices of a cube and the p-phenylenediamines serve as the edges. The cages have a side length of ~ 1.7nm.

The naming convention for helical chiral molecules assigns prefixes of M (minus) and P (plus). In that sense the single molecules can be prefixed with M and P, but for convenience the cage compounds themselves are simply named **M** and **P** in the following. They were dissolved in dichloromethane and films were prepared by spin-coating them on sapphire substrates (CrysTec, single crystal, S(0001) surface, both sides polished) to yield samples of 100 and 200 nm thickness. The linear molar optical rotation of the cage compounds was measured in solution to be $[\Phi] \geq \pm 13000 \cdot 10^\circ\,\mathrm{cm^2\,mol^{-1}}$. Circular dichroism (CD) measurements yield molar differences in extinction of $\Delta\epsilon = \pm 800\,\mathrm{M^{-1}\,cm^{-1}}$ [204].

8.1.2 SHG-ORD on a chiral surface

In analogy to the linear optical rotation, linear polarized light is incident on the sample. The outgoing SHG intensity is detected with respect to an analyser angle, see Fig.8.3 a). The effect of polarisation rotation can be up to six orders of magnitude larger as the linear optical rotation for the same sample [74, 205].

As linear polarized light is detected as the function of the analyser angle, the detected intensity is governed by Malus' law

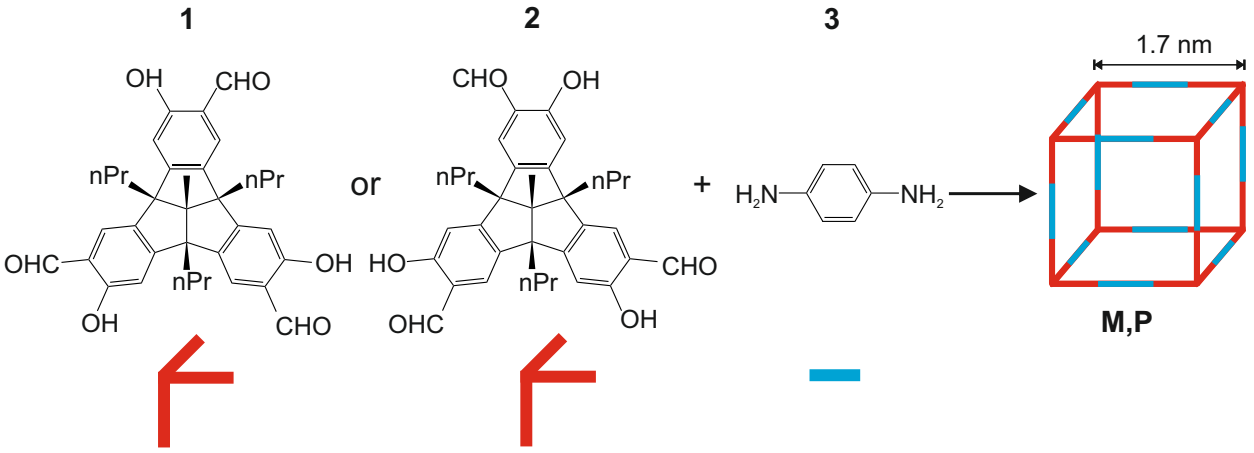

Figure 8.1: Illustration of the salicylimine cage compounds (**M**/**P**) and the constituent molecules. The tris-salicylaldehydes (M-enantiomer **1**, P-enantiomer **2**) serve as vertices and p-phenylenediamine **3** as edges. nPr = $-CH_2CH_2CH_3$.

$$I(2\omega) \sim \cos^2(\phi - \phi_0), \tag{53}$$

where ϕ is the angle of the analyser and ϕ_0 is introduced since we expect a rotation of the incident linear polarisation, such that the maximum detected intensity is at ϕ_0 instead of $\phi = 0$. Of course the squared relation between the fundamental and the second harmonic still holds, but for extracting the rotation angle ϕ_0 it does not need to be taken into account. Adjusting for a constant offset, the final fit function is given by

$$f(\phi) = A\cos^2(\phi - \phi_0) + c \tag{54}$$

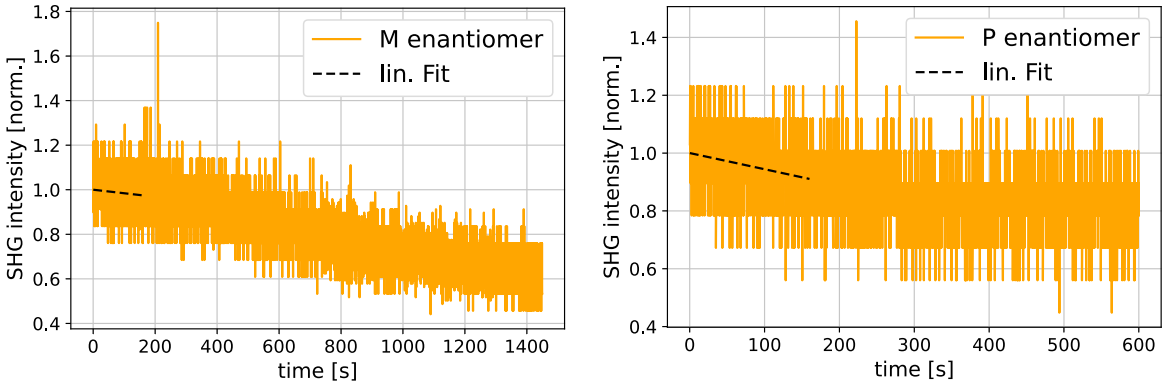

Figure 8.2: Observed photodegradtion of **M** (left) and **P** (right). The SHG intensity is normalised to the y-offset of the linear fit (dotted line).

The measurements were complicated by the degradation of the samples. Fig.8.2 shows the SHG intensity over several minutes at the same spot on the sample without rotating the analyser. The observed degradation was taken into account by adapting the measurement procedure and in the processing of the data as described in section 4.2.4. With this kind of measurement procedure a polarisation scan as shown in Fig.8.3 b) is obtained. The measured signal for **P** and **M** enantiomers is symmetric w.r.t. the p-polarisation setting (i.e. 0°, 180°, ...) which is a strong indication of chiral molecules with a random orientation on the surface [205].

The obtained rotation angles for the **M** and **P** enantiomers are $\phi_M = (24.15 \pm 0.17)°$ and $\phi_P = (22.43 \pm 0.31)°$. Possible reasons for the significant deviation $\phi_M \neq -\phi_P$ will be discussed later.

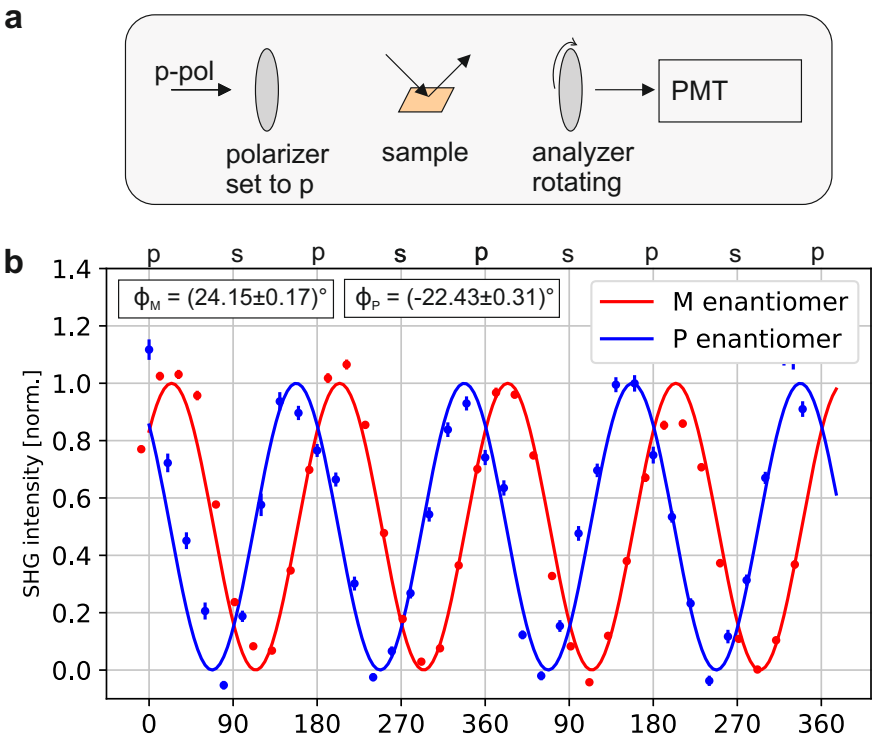

Figure 8.3: **a** Schematic of the experimental setup. **b** Polarisation rotation observed for **M** and **P**. At 0° the incident beam was p-polarised and at 90° it is s-polarised as indicated on the top of the figure. The data were modelled with $f(\phi) = A\cos^2(\phi - \phi_{M,P}) + c$.

8.1.3 Quarter wave plate rotation

The non-linear answer of chiral materials to circular polarized light also depends on the handedness of the molecules. A schematic of the setup is shown in Fig8.4 a). For details on the experimental setup refer to section 4.2. By rotating a quarter wave plate (QWP) in front of the sample, the SHG intensity can be monitored with respect to the angle of rotation ϕ:

$$I(2\omega;\phi) = |fF(\phi) + gG(\phi) + hH(\phi)|^2. \tag{55}$$

The functions F, G and H depend on the geometry of the experiment and are given in Eq(31). The complex valued fit parameters depend on the susceptibilites χ^{eee}, χ^{eem} and χ^{mee}. The superscripts indicate whether the respective transition refers to a electric-dipole (e) or magnetic-dipole (m) interactions [75]. The susceptibility χ^{mee} gives rise to a non-linear magnetisation as given in Eq.(23). In principle electric quadrupole interactions should be considered as well as they tend to be of similar order as magnetic-dipole interactions, but for chiral media magnetic-dipole were found the be of greater importance [25, 76]. The relation to the fit parameters is given by the equations (56) to (61) [75].

$$\begin{aligned}
f_{T,s}^{R,s} &= \sin\theta\left(-2\chi_{xyz}^{eee}\cos\theta - \chi_{xzx}^{eem} + \chi_{zzz}^{mee}\sin^2\theta\right. \\
&\quad \left. +\chi_{zxx}^{mee}\cos^2\theta \pm 2\chi_{xxz}^{mee}\cos^2\theta\right), && (56)\\
g_{T,s}^{R,s} &= \sin\theta(\chi_{xxz}^{eem} + \chi_{zxx}^{mee}), && (57)\\
h_{T,s}^{R,s} &= \sin\theta\left[2\chi_{zzz}^{eee} - (\chi_{xzy}^{eem} + \chi_{xyz}^{eem})\cos\theta \mp 2\chi_{xyz}^{mee}\cos\theta\right], && (58)\\
f_{T,p}^{R,p} &= \sin\theta\left(\chi_{zzz}^{eee}\sin^2\theta + \chi_{zxx}^{eee}\cos^2\theta + \mp 2\chi_{xxz}^{eee}\cos^2\theta\right. \\
&\quad \left. -\chi_{zxy}^{eem}\cos\theta \pm \chi_{xzy}^{eem}\cos\theta + 2\chi_{xyz}^{mee}\cos\theta\right), && (59)\\
g_{T,p}^{R,p} &= \sin\theta(\chi_{zxx}^{eee} - \chi_{zxy}^{eem}\cos\theta \mp \chi_{xyz}^{eem}\cos\theta), && (60)\\
h_{T,p}^{R,p} &= \sin\theta\left[\mp 2\chi_{xyz}^{eee}\cos\theta + (\chi_{zzz}^{eem} - \chi_{zxx}^{eem})\sin^2\theta\right. \\
&\quad \left. \mp(\chi_{xzx}^{eem} + \chi_{xxz}^{eem})\cos^2\theta - 2\chi_{xxz}^{mee}\right]. && (61)
\end{aligned}$$

The indices R, T, p and s stand for measurements in reflection, transmission, with p- or s-polarised light. The angle of incidence was $\theta = 45°$. With that many unknown variables, it is not possible to calculated the susceptibilities directly. First, some assumptions have to be made. For off-resonant excitations χ^{eee} can be taken to be real, whereas χ^{eem} and χ^{mee} are imaginary [75]. Furthermore, the magnitude of χ^{eee} is expected to be greater than that of χ^{eem} and χ^{mee}. Therefore, fitting with $\chi^{eem} = \chi^{mee} = 0$ was attempted, to check if magnetic-dipole interactions are needed to model the data. Assuming isotropy in the plane of the surface, only a few independent elements of the susceptibilities remain. The symmetry considerations are detailed in Ref.[25] for example and given in Table 6. This is already taken into account for the above equations, but it is interesting to note that some tensor elements are non-zero only for chiral molecules whereas others are possible for achiral media.

The results of the measurements are presented in Fig.8.4 b) to e). For both enantiomers the QWP was rotated in steps of 10 degrees and the signal was averaged of 10 seconds,

Tensor	Achiral components for all isotropic surfaces	Additional components for chiral surfaces
χ^{eee}	zzz zxx = zyy xxz = xzx = yyz = yzy	xyz = xzy = -yxz = -yzx
χ^{eem}	xyz = -yxz zxy = -zyx xzy = -yzx	zzz zxx = zyy xxz = yyz
χ^{mee}	xyz = xzy = -yxz = -yzx	zzz zxx = zyy xxz = xzx = yyz = yzy

Table 6: Non vanishing susceptibility tensor components of second order for isotropic chiral and achiral surfaces. The surface is in the x-y plane. Reproduced from Ref.[25]

while the analyser behind the sample was set to either passing p- or s-polarised light. In principle the intensity of the enantiomers is connected by the relation $I(\phi; 2\omega)_M = I(-\phi; 2\omega)_P$ [25, 205]. When detecting p-polarised light, this appears to be the case (compare Fig.8.4 c) and e)). Unfortunately, measurements with the analyser set to s-polarisation were not successful for the **P** enantiomer, as the intensity was too low at the minima.

The dashed lines in the graphs correspond to the fitted functions. For the **M** enantiomer with detection of s-polarised light, the following parameters were found:

$$f_{M,s} = -8.2 \pm 0.1 \tag{62}$$
$$g_{M,s} = 4.1 \pm 0.2 \tag{63}$$
$$h_{M,s} = (7.3 \pm 0.2) + (1.7 \pm 0.1)i \tag{64}$$

The index R is not written explicitly, as all data are from measurements in reflection; instead M is used to assign the enantiomer. A model function with $g = 0$ results in a 5-fold increase in the root mean squared error (RMS). The dashed line in Fig.8.4 b) correspond to the fit parameters above, whereas the dotted line uses $g = 0$. Allowing for an imaginary g_{im} value and vanishing real part does not give a convincing fit to the data either. The results stand in contrast to assuming that the elements of χ_{eem} and χ_{mee} can be taken as imaginary numbers, as $g_s = \sin\theta(\chi^{eem}_{xxz} + \chi^{mee}_{zxx})$. Furthermore, setting both h and f to have a zero imaginary amplitude does result in a poor fit. Including any further parameters than the ones given above will yield converging fits from arbitrary initial values and results with immense estimation errors, so the parameters are not independent from each other in that case. For the **M** and **P** enantiomer with p-polarised detection, the best fits are obtained with

$$f_{M,p} = (-6.4 \pm 0.1) + (-4.4 \pm 0.2)i \tag{65}$$
$$g_{M,p} = 4.2 \pm 0.2 \tag{66}$$
$$h_{M,p} = -3.6 \pm 0.2 \tag{67}$$

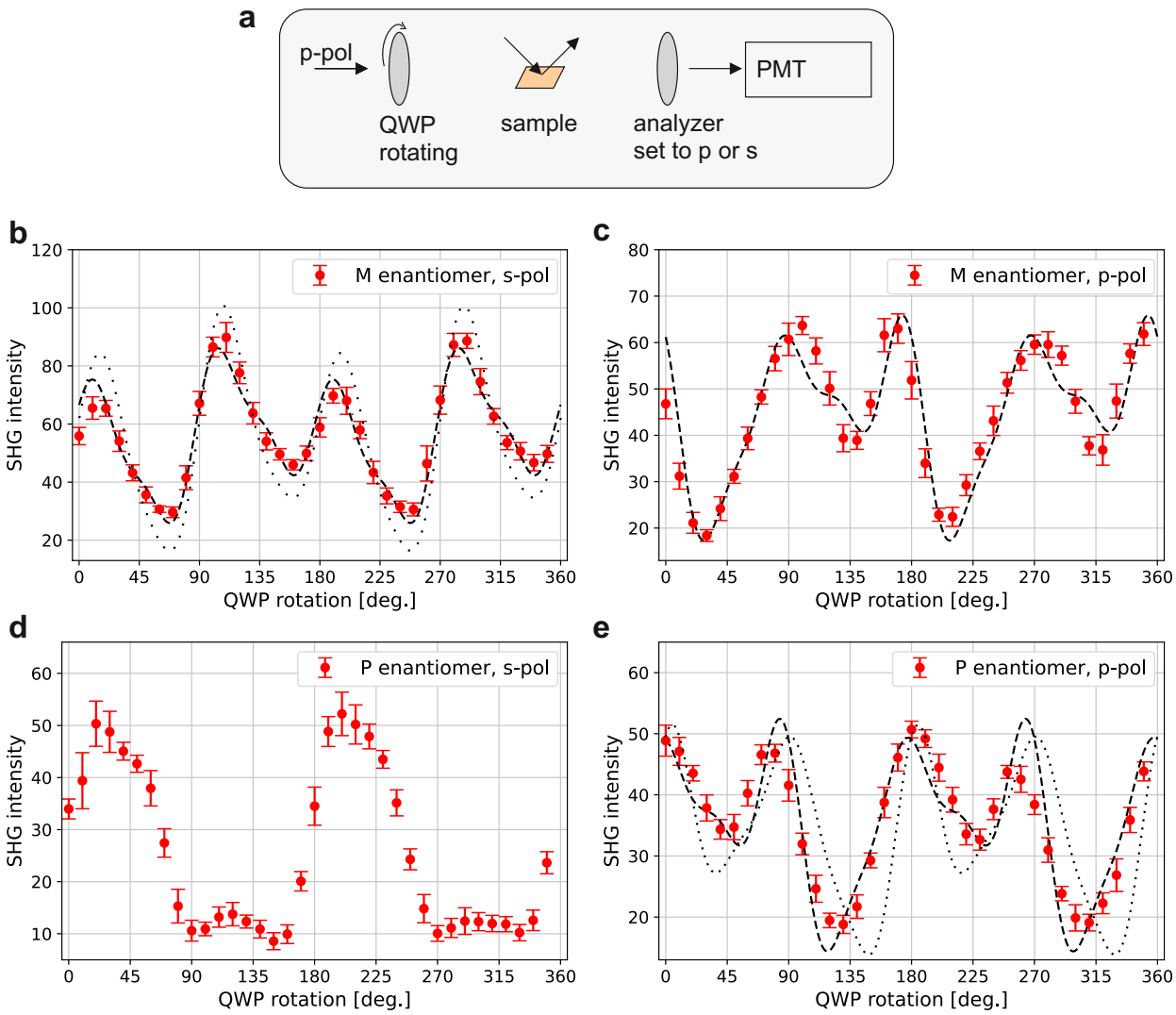

Figure 8.4: **a** Schematic of the SHG polarisation rotation experiments . **b**,**c** results for **M** with the analyser set to s- and p-polarisation , respectively. **d**,**e** results for **P** with the analyser set to s- and p-polarisation. The dotted lines in **b** uses $g = 0$. The dotted line in **e** aimed to force the relation $I(\phi)_M = I(-\phi)_P$.

and

$$f_{P,p} = (-5.9 \pm 0.1) + (3.9 \pm 0.2)i \tag{68}$$

$$g_{P,p} = 3.6 \pm 0.1 \tag{69}$$

$$h_{P,p} = -3.0 \pm 0.1 \tag{70}$$

When comparing the values for the different enantiomers all real parts of the fit parameters do not change sign and have similar magnitudes. The imaginary part of f_p does

change its sign. From literature it was expected that f_p and g_p do not change sign between the enantiomers, because they only include susceptibilities that can arise from achiral media. On the other hand h_p contains susceptibilities that are only present in chiral media (compare Table.6) and it should change sign. There exists also a second set of solutions for both enantiomers with all parameters changing sign, resulting in the same modelfunction. This does however not alleviate the observed disagreement to literature. It is interesting to note, that changing only the sign of the imaginary part of f_p is equivalent to making the transformation $\phi \rightarrow \phi - \frac{\pi}{2}$. This is only the case for real g and h: $I(\phi - \frac{\pi}{2}; f_r + f_i, g_r, h_r) = I(\phi; f_r - f_i, g_r, h_r)$. Hence it maps right- on left-handed polarisation (45° and 135°), but does not fullfill $I(\phi; f, g, h)_M = I(-\phi; f, g, h)_P$. This is the case if h alone changes sign. With different initial values a converged fit with

$$f_{P,p} = (-5.5 \pm 0.2) + (-4.4 \pm 0.2)i \tag{71}$$

$$g_{P,p} = 3.0 \pm 0.1 \tag{72}$$

$$h_{P,p} = 2.3 \pm 0.1 \tag{73}$$

is obtained, yet with a 4-fold increases in RMS (see dotted line in Fig.8.4 e)). These fit parameters show only a change of sign for h, but the model function does not fit very well.

8.2 Conclusion

The presented experiments give first results on the non-linear optical properties of chiral salicylimine cage compounds. With SHG-ORD a rotation of the incident linear polarised light of $\phi_M = (24.15 \pm 0.15)^\circ$ and $\phi_P = (-22.43 \pm 0.31)^\circ$ were observed. As expected the different enantiomers rotate the polarisation in opposite directions. With a short estimation we can compare the strength of linear and non-linear effects. What thickness d of a solution with concentration c must be traversed to rotate the light by $\phi = 24°$? Assuming a concentration comparable to that of the thin film sample of $c = \frac{8\text{molecules}}{1.7^3\text{nm}^3}$, the thickness turns out to be $d = \frac{\phi}{[\Phi]c} \sim 10^5\text{nm} = 10^3 \cdot 100\,\text{nm}$ (with $[\Phi] \geq \pm 13000 \cdot 10^\circ\,\text{cm}^2\,\text{mol}^{-1}$ [204]). So the non-linear effect is about three orders of magnitude larger. In comparison to other SHG-ORD studies, greater angles of rotation were found, for example a film of 2,20-dihydroxyl-1,10binaphthyl molecules with 38° or for a thin film of a Töger base with 66° [205, 206]. Note that for SHG-ORD the maximal rotation angle is 90°, whereas with linear optical rotation there is no limit, as the rotation angle is proportional to the length of medium that is traversed. A difference between ϕ_M and $-\phi_P$ is noticed that is significant within the experimental error. A possible reason for that is that the substrate might have an influence on the rotation angle.

The polarisation rotation experiments in the second part were conducted by rotating a quarter wave plate in front of the sample and detecting the p- and s-polarised reflected second harmonic intensity. The enantiomers reveal in principle the expected response $(\phi)_M = I(-\phi)_P$ for p-polarised detection, albeit at first glance. The fit parameters from theoretical modelling yielded best fits that could not reproduce this property exactly, however they predict opposite behaviour for left and right handed circular polarised light, i.e. **M** shows for right handed circular polarised light the same response as **P** for left handed and vice versa. The fits did unambiguously show that magnetic contributions to the non-linear optical activity are needed to explain the observed data. This can be determined, as fitting of the s-polarised signal needed the parameter $g_s = -\sin\theta(\chi^{eem}_{xxz} + \chi^{mee}_{zxx})$ to be non-zero.

The experiments successfully yielded insights into the non-linear optical properties of this newly synthesized chiral cage compound. These results encourage to pursue this research to achieve potential applications such as chiral recognition or enantiomer excess estimation as outlined in the introduction.

Further improvement of the setups is planned. Importantly the setup needs to allow for measurements in transition and reflection. With that the parameters in Eq.(56-61) in transmission can be calculated and the number of unknowns will be reduced. The angle of incidence should be adjustable, which will also help in determining the susceptibilities, but additionally this can be used to find angles where no residual SHG of the bare substrate (i.e. background) due to destructive interference is measured [205].

In Ref.[75] it is stated that the components of χ^{eem} and χ^{mee} tend to be 90° out of phase from the components of χ^{eee} and that χ^{eee} is taken to be real. Assuming that χ^{eee} is real is only valid for off-resonant excitation, which includes two photon resonance, i.e. the excitation frequency must be far away from ω_0 and $2\omega_0$. Therefore, to make use of this simplifying assumption, off-resonant excitation should be implemented by incorporating a tunable laser source.

Furthermore by choosing a suitable reference material, not only relative values of amplitudes and phases of the susceptibilities but absolute values can be obtained [25].

9 Summary

The studies in this thesis focused on the excited state dynamics in organic semiconducting materials through time-resolved spectroscopic experiments, namely sub-picosecond transient absorption (fs-TA). The four main topics were 1) experimental characterisation of singlet fission (SF) in a pentacene (PEN) based SURMOF, 2) charge separation and recombination dynamics in a porphyrin-based SURMOF incorporating C_{60}, 3) SF and charge transfer complex formation in bilayered thin films of PEN with F4-TCNQ and F6-TCNNQ and 4) improvement of the experimental setup for non-linear optics and characterisation of a thin film constituted of chiral cage compounds.

In the first study, the SF dynamics of PEN that functioned as the organic linker in a surface-anchored metal organic framework (SURMOF) were examined. The aim of this project was to study the impact of the change in geometry on the excited state dynamics. Therefore, it was compared to the dynamics of a thin film with its innate herringbone structure. The PEN thin film exhibits one of the fastest observed SF rates (70-100 fs), yet the triplet lifetime is comparatively short. There is a trade-off between the desired outcome of a longer triplet lifetime, which is advantageous for harvesting them, and fast SF. Slowing down the SF rate is especially detrimental if it allows relaxation via competing pathways. The experiments allowed to formulate a comprehensive model of the energetics and dynamics in the system.

In the SURMOF the generation of the triplet pair state $^1(T_1T_1)$ was observed within a few picoseconds (4.9 ps). This transition is promoted by the significantly polar CT character of the excited state through the super-exchange mechanism. The slowdown in the rate compared to PEN can be rationalised by the higher CT state energy in the MOF model. After creation of the triplet pair, the triplet intermediate state $^m(T_1T_1)$ with approx. 119 ps is generated, with the assumption that m=5 due to the slipped stacked geometry, which promotes the pathway via quintets to free triplets. Before the separation of the triplets, it is proposed that a spin-correlated but electronically decorrelated state $^5(T\cdots T)$ with spatial separation of the excitons exists. This can however not be observed directly, since with µs-TA no spectral changes were observed. The additional time constants that were extracted must belong to relaxation pathways to the ground state with τ_3 =25 ns and τ_4 =352 ns, since a decay of the triplet excited state absorption (ESA) was detected. Finally, the triplet signature can be observed to decay to the ground state with a lifetime of 40 µs. Together with the observed triplet-triplet annihilation (TTA) at high fluences, we assume that free triplets are generated. Excitation with a higher energy increased the generation of triplets, as identified by the increased ratio of triplet to singlet ESA. Covering a broader absorption range where SF is efficient is advantageous for solar cell devices. Lastly, the prominent absorption of excited triplet states $T_1 \rightarrow T_2$ in the PEN thin film is strongly suppressed in the PEN SURMOF, which is surprising since it was thought to be enhanced in the solid state.

The SURMOFs provided an excellent approach to arrange pentacene moieties in a parallel configuration and this change in geometric arrangement compared to the thin film structure has two major impacts: It slows down the triplet-pair generation by almost two orders of magnitude, but at the same time the triplet lifetime is extended by more than three orders of

magnitude, which is an extremely promising result regarding the utilisation of SF materials for improving solar cells. The ability to achieve such novel molecular arrangements inaccessible in pure organic crystals significantly enhances the SF energetics. The manipulation of the π-π stacking distance is pivotal for optimizing intermolecular coupling in SF.

The second topic covered charge separation and recombination dynamics in a porphyrin-based SURMOF (Zn(TPP)) that incorporates C_{60} in this highly porous material. The material was investigated previously to characterise the photo-conductivity and a fast charge generation was assumed. Since porphyrin and C_{60} form a donor/acceptor system, that is suitable for photovoltaic applications further investigations were performed with spectroscopic experiments. This was especially necessary since knowledge of the recombination dynamics is pivotal for solar cells.

The UV/vis data showed a change in the main Soret band absorption indicating a ground state (GS) interaction of Zn(TPP) and C_{60}, although no GS charge transfer. The dynamics of charge separation (CS) and recombination (CR) have been examined in the SURMOF with fs-TA and it was observed that the charge separation takes place on an ultrafast timescale with $\tau_{CS} = 327 - 357\,\text{fs}$ after excitation of the Soret band. The recombination occurs with a time constant of $\tau_{CR} = 212 - 244\,\text{ps}$. The generation and recombination was identified by the ESA of $C_{60}^{\bullet -}$ anions at 1070 nm, the ESA of $ZnTPP^{\bullet +}$ radical cations at 400-410 nm and the GSB of C_{60} at 330 nm. Since the charge separation is on the sub picosecond time scale, it can be supposed, that this lead to the reduced ESA of ^{3}ZnTPP, which are generated by a slower rate through inter system crossing. The charge separation after excitation of the Q-band has a similar rate extracted from single traces. The charge recombination process was observed to be slower with $\tau_{CR} = 263 - 360\,\text{ps}$. We surmise that the charge recombination is slower since only electrons from the HOMO and not HOMO-1 are excited after Q-band excitation. Therefore, in the case of higher excitation energies, an additional recombination pathway exists that is inaccessible for Q-band excitation With an excitation wavelength of $\lambda_{ex} = 264\,\text{nm}$, the charge separation dynamics get partially obscured by overlapping signals. Specifically, there is an increased generation of $^3ZnTPP^*$ in C_{60}@Zn(TPP).

For the investigated system, global analysis allowed to identify a spectral region where the CS and CR dynamics can be disentangled from underlying spectra. Therefore the dynamics could also be modelled including only a rise and decay rate, without the need for a more sophisticated model. The ratio $I = \frac{k_{CS}}{k_{CR}} = \frac{\tau_{CR}}{\tau_{CS}}$ can serve for comparing the material to other studied systems. With $I \approx 600$ it was found to be high for a two component system. Higher values are obtained with triadic structures that can separate the charges more effectively.

The third topic revisited the interaction of pentacene with strong acceptors. Specifically, the properties in bilayers of F4-TCNQ and F6-TCNNQ with PEN were examined with steady-state and time-resolved spectroscopic experiments. The structural characterisation with grazing-incidence wide-angle X-ray scattering (GIWAXS) showed that the bilayers exhibit diffraction features of a powder-like material. When PEN is on the bottom and therefore in direct contact with the substrate a parallel orientation of the PEN molecules to the surface normal is preferential, especially for **F6/PEN**. The FTIR data on bilayers including F4-TCNQ exhibit peaks associated with vibrations of F4-TCNQ anions and PEN cations, aside from the neutral species. This stands in contrast to the results from the fs-

TA data. The FITR measurements were conducted on silicon substrates, whereas the fs-TA spectra were taken on quartz substrates. On quartz substrates the PEN molecules orient upright whereas on silicon the preferred orientation is flat-lying, which might explain the discrepancy. The bilayer **F6/PEN** exhibits essentially only vibrations of neutral molecules indicating only weak ground state interaction. This is not the case for **PEN/F6**, where the IR bands are broadened. This could be attributed to the different structures of the films. No clear identification of the IR bands is possible for **PEN/F6**, despite that F6-TCNNQ is considered the stronger acceptor and ICT was expected.

After excitation with light of the wavelength $\lambda_{ex} = 620\,\text{nm}$, which addresses PEN, the following observations could be made. The singlet fission process is not inhibited drastically in this system, which is to be expected, as the PEN layers still exhibit crystalline structures. SF was found to take place with a time constant of 158 fs and 222 fs with PEN below and on top of F4-TCNQ, respectively (neat PEN: 70-100 fs). The electronic dephasing $^1(\text{TT}) \rightarrow (\text{T}\cdots\text{T})$ is slowed down only marginally to 1.3-1.5 ps (neat PEN: 1.2 ps).

The charge separation at the interface was identified by the GSB of the CT complex between PEN and F4-TCNQ in the NIR. Together with the bleaching of this broad transition a rise of a positive ΔA signal in the visible spectrum was observed. The interpretation of this rising signal is, that the ground state absorption of PEN changes due to the quadratic Stark effect. The static electric field is surmised to be built up at the interface, when an electron is transferred from the PEN in a triplet excited state to the CT complex. It should be noted on the one hand, that thin films of pristine PEN exhibit this feature by themselves, yet for higher fluences and longer delay times. On the other hand, blends of F4-TCNQ and PEN exhibit the GSB of the CT complex in the NIR, but no electro absorption can be detected there, leading to the conclusion that the interface is responsible for the emergence of EA. The diffusion to the interface was approximated by two exponential decays. For the bilayer **F4/PEN** time constants of 21-24 ps and 221-254 ps are obtained. With PEN on top of F4-TCNQ instead, time constants of 42-56 ps and 342-405 ps are obtained.

Lastly, the experimental setup for second harmonic generation (SHG) was extended to investigate thin films of chiral molecules. Experimental procedures were introduced and the insights will serve for improving the setup further. Furthermore, first experimental results on the non-linear optical properties of chiral salicylimine cage compounds were presented. The cage compounds called **M** and **P**, consist of 8 chiral tris-salicylaldehydes that are linked with 12 achiral p-phenylenediamines. With SHG optical rotatory dispersion (ORD) a rotation of the incident linear polarised light by angles of $\phi_M = (24.15 \pm 0.15)^\circ$ and $\phi_P = (-22.43 \pm 0.31)^\circ$ were observed. As expected the different enantiomers rotate the polarisation in opposite directions. The non-linear effect was estimated to be three orders of magnitude larger than linear optical rotation. By rotating a quarter wave plate in front of the sample and detecting the p- and s-polarised reflected second harmonic intensity, insights into the susceptibilities of second order can be gained. The enantiomers reveal in principle the expected response $(\phi)_M = I(-\phi)_P$ for p-polarised detection. The fit parameters from theoretical modelling yielded best fits that could not reproduce this property exactly, however, they predict opposite behaviour for left and right-handed circular polarised light, i.e. **M** shows for right-handed circular polarised light the same response as **P** for left-handed and vice versa. The fits

did unambiguously show that magnetic contributions to the non-linear optical activity are needed to explain the observed data. The experiments successfully yielded insights into the non-linear optical properties of this newly synthesized chiral cage compound. These results encourage to pursue this research to achieve potential applications such as chiral recognition or enantiomer excess estimation.

Regarding future investigations and applications, the PEN SURMOF has shown that the geometrical configuration is of key importance for designing SF materials. With the approach of incorporation as organic linker in a MOF, a variety of new SF materials could be examined. Concerning the PEN SURMOF specifically, future projects could include different acenes. As the excited triplet state in anthracene lies well above that of PEN, anthracene molecules could serve as impurities. This will allow to study the impact of defects in the system. With tetracene singlet heterofission, i.e. conversion of a singlet excitation to two excited triplets on different molecules, could be studied. The porphyrin fullerene system, exhibited comparatively long-lived charge separated states. After identifying the dynamics in this system, the research can be focussed on prolonging charge carrier lifetimes by modification of the side groups of the porphyrin linker or functionalisation of C_{60}. To improve this even further, adding a third component to separate the charges further could have a tremendous effect.

To summarise, materials based on OSCs were investigated for their properties - in particular the ultra-fast dynamics in the excited state. These insights will hopefully enable the design of new materials with improved properties.

References

[1] Richard Shim. Kodak, sanyo demo oled display. `https://www.cnet.com`, 2019. Retrieved 16 September 2024.

[2] C. W. Tang and S. A. VanSlyke. Organic electroluminescent diodes. *Applied Physics Letters*, 51(12):913–915, 09 1987.

[3] Wolfgang Brütting and Chihaya Adachi, editors. *Physics of Organic Semiconductors*. Wiley-VCH, Weinheim, 2nd rev. ed. edition, 2012.

[4] Luís Alcácer. *The Physics of Organic Electronics: From Molecules to Crystals and Polymers*. IOP Publishing, Bristol, UK, 2022.

[5] Kiran Sreedhar Ram and Jai Singh. Over 20% efficient and stable non-fullerene-based ternary bulk-heterojunction organic solar cell with ws2 hole-transport layer and graded refractive index antireflection coating. *Advanced Theory and Simulations*, 3(6):2000047, 2020.

[6] Martin A. Green, Yoshihiro Hishikawa, Wilhelm Warta, Ewan D. Dunlop, Dean H. Levi, Jochen Hohl-Ebinger, and Anita W.H. Ho-Baillie. Solar cell efficiency tables (version 50). *Progress in Photovoltaics: Research and Applications*, 25(7):668–676, 2017.

[7] William Shockley and Hans J. Queisser. Detailed Balance Limit of Efficiency of p-n Junction Solar Cells. *Journal of Applied Physics*, 32(3):510–519, 06 2004.

[8] M. C. Hanna and A. J. Nozik. Solar conversion efficiency of photovoltaic and photoelectrolysis cells with carrier multiplication absorbers. *Journal of Applied Physics*, 100(7), 10 2006.

[9] Ingo Salzmann, Georg Heimel, Martin Oehzelt, Stefanie Winkler, and Norbert Koch. Molecular electrical doping of organic semiconductors: Fundamental mechanisms and emerging dopant design rules. *Accounts of Chemical Research*, 49(3):370–378, 2016. PMID: 26854611.

[10] Christoph P. Theurer, Martin Richter, Debkumar Rana, Giuliano Duva, Daniel Lepple, Alexander Hinderhofer, Frank Schreiber, Petra Tegeder, and Katharina Broch. Coexistence of ion pairs and charge-transfer complexes and their impact on pentacene singlet fission. *The Journal of Physical Chemistry C*, 125(43):23952–23959, 2021.

[11] Richard S. Potember, Robert C. Hoffman, Karen A. Stetyick, Robert A. Murphy, and Kenneth R. Speck. Molecular materials for nonlinear optics. *Johns Hopkins APL Technical Digest*, 9(3):256–264, 1988. Accessed: 15 September 2024.

[12] Finn Kröger, Robert Eichelmann, Gabriel Sauter, Audrey Pollien, Petra Tegeder, Lutz H. Gade, and Eva Blasco. Two-photon laser printing of 3d multicolor emissive polymer microstructures. *RSC Appl. Polym.*, 2:847–856, 2024.

[13] Per Lind, Cesar Lopes, Kjell Öberg, and Bertil Eliasson. A qspr study on optical limiting of organic compounds. *Chemical Physics Letters*, 387(4):238–242, 2004.

[14] Robert S. Mulliken. Electronic structures of polyatomic molecules and valence. ii. general considerations. *Phys. Rev.*, 41:49–71, Jul 1932.

[15] Wolfgang Demtröder. *Experimentalphysik 3*. Springer-Lehrbuch. Springer Spektrum, Berlin ; Heidelberg, 5. aufl. 2016 edition, 2016.

[16] Sam-Shajing Sun and Larry R. Dalton, editors. *Introduction to organic electronic and optoelectronic materials and devices*. Number ARRAY(0x558f1960d238) in Optical science and engineering. CRC Press, Taylor & Francis Group, Boca Raton ; London ; New York, 2008. Literaturangaben.

[17] KENICHI FUKUI. A simple quantum-theoretical interpretation of the chemical reactivity of organic compounds, 1997.

[18] N.F. Mott. Charge transport in non-crystalline semiconductors. In O. Madelung, editor, *Festkörper Probleme IX*, pages 22–45. Pergamon, 1969.

[19] Zhigang Shuai, Weitang Li, Jiajun Ren, Yuqian Jiang, and Hua Geng. Applying Marcus theory to describe the carrier transports in organic semiconductors: Limitations and beyond. *The Journal of Chemical Physics*, 153(8):080902, 08 2020.

[20] Zhigang Shuai, Weitang Li, Jiajun Ren, Yuqian Jiang, and Hua Geng. Applying Marcus theory to describe the carrier transports in organic semiconductors: Limitations and beyond. *The Journal of Chemical Physics*, 153(8):080902, 08 2020.

[21] Lukas Schmidt-Mende, Stefan Kraner, and Azhar Fakharuddin. *Organic and Hybrid Solar Cells: An Introduction*. De Gruyter, 2nd edition, 2022.

[22] Markus Schwoerer, Hans Christoph Wolf, and William D. Brewer. *Organic molecular solids*. Physics textbook. Wiley-VCH, Weinheim, 2007. Literaturangaben ; Parallel als digitalisierte Ausg. erschienen.

[23] C. Melzer. Organic electronics - introduction to materials and analytical methods, part i: Introduction to organic semiconductors. Lecture, 2014/2015. Lecture series.

[24] Siegfried Hunklinger. Festkörperphysik, 2014.

[25] Sonja Sioncke, Thierry Verbiest, and André Persoons. Second-order nonlinear optical properties of chiral materials. *Materials Science and Engineering: R: Reports*, 42(5):115–155, 2003.

[26] Hua-Zhong Yu, J. Spencer Baskin, and Ahmed H. Zewail. Ultrafast dynamics of porphyrins in the condensed phase: Zinc tetraphenylporphyrin. *The Journal of Physical Chemistry A*, 106(42):9845–9854, 2002.

[27] J. Spencer Baskin, Hua-Zhong Yu, and Ahmed H. Zewail. Ultrafast dynamics of porphyrins in the condesnsed phase: I. free base tetraphenylporphyrin. *The Journal of Physical Chemistry A*, 106(42):9837–9844, 2002.

[28] Andrew J. Musser and Jenny Clark. Triplet-pair states in organic semiconductors. *Annual Review of Physical Chemistry*, 70(1):323–351, 2019.

[29] Rohan J. Hudson, Alexandra N. Stuart, David M. Huang, and Tak W. Kee. What next for singlet fission in photovoltaics? the fate of triplet and triplet-pair excitons. *The Journal of Physical Chemistry C*, 126(12):5369–5377, 2022.

[30] Nadezhda V. Korovina, Nicholas F. Pompetti, and Justin C. Johnson. Lessons from intramolecular singlet fission with covalently bound chromophores. *The Journal of Chemical Physics*, 152(4), 01 2020.

[31] Jingjing Li, He Cao, Zhibin Zhang, Shuo Liu, and Yuanqin Xia. Research progress on singlet fission in acenes and their derivatives. *Photonics*, 9(10), 2022.

[32] Kiyoshi Miyata, Felisa S. Conrad-Burton, Florian L. Geyer, and X.-Y. Zhu. Triplet pair states in singlet fission. *Chemical Reviews*, 119(6):4261–4292, 2019.

[33] N. Monahan and X.-Y. Zhu. Charge transfer–mediated singlet fission. *Annual Review of Physical Chemistry*, 66(1):601–618, 2015.

[34] Cory A. Nelson, Nicholas R. Monahan, and X.-Y. Zhu. Exceeding the shockley–queisser limit in solar energy conversion. *Energy Environ. Sci.*, 6:3508–3519, 2013.

[35] Akshay Rao and Richard H. Friend. Harnessing singlet exciton fission to break the shockley-queisser limit. *Nature Reviews Materials*, 2(11):17063, 2017.

[36] Samuel N. Sanders, Andrew B. Pun, Kaia R. Parenti, Elango Kumarasamy, Lauren M. Yablon, Matthew Y. Sfeir, and Luis M. Campos. Understanding the bound triplet-pair state in singlet fission. *Chem*, 5(8):1988–2005, 2019.

[37] J. C. Johnson, A. J. Nozik, and J. Michl. The role of chromophore coupling in singlet fission. *Accounts of Chemical Research*, 46:1290–1299, 2013.

[38] M. B. Smith and J. Michl. Singlet fission. *Chem Rev*, 110:6891–6936, 2010.

[39] Millicent B. Smith and Josef Michl. Recent advances in singlet fission. *Annual Review of Physical Chemistry*, 64(Volume 64, 2013):361–386, 2013.

[40] I. Paci et al. Singlet fission for dye-sensitized solar cells: Can a suitable sensitizer be found? *J Am Chem Soc*, 128:16546–16553, 2006.

[41] Mark W. B. Wilson, Akshay Rao, Jenny Clark, R. Sai Santosh Kumar, Daniele Brida, Giulio Cerullo, and Richard H. Friend. Ultrafast dynamics of exciton fission in polycrystalline pentacene. *Journal of the American Chemical Society*, 133(31):11830–11833, 2011.

[42] R.R. Alfano, S.L. Shapiro, and M. Pope. Fission rate of singlet excitons in a tetracene crystal measured with picosecond laser pulses. *Optics Communications*, 9(4):388–391, 1973.

[43] Y. Tomkiewicz, R. P. Groff, and P. Avakian. Spectroscopic Approach to Energetics of Exciton Fission and Fusion in Tetracene Crystals. *The Journal of Chemical Physics*, 54(10):4504–4507, 05 1971.

[44] Ryan D. Pensack, Evgeny E. Ostroumov, Andrew J. Tilley, Samuel Mazza, Christopher Grieco, Karl J. Thorley, John B. Asbury, Dwight S. Seferos, John E. Anthony, and Gregory D. Scholes. Observation of two triplet-pair intermediates in singlet exciton fission. *The Journal of Physical Chemistry Letters*, 7(13):2370–2375, 2016.

[45] E.L. Frankevich, V.I. Lesin, and A.I. Pristupa. Rate constants of singlet exciton fission in a tetracene crystal determined from the rydmr spectral linewidth. *Chemical Physics Letters*, 58(1):127–131, 1978.

[46] Ryan D. Pensack, Andrew J. Tilley, Christopher Grieco, Geoffrey E. Purdum, Evgeny E. Ostroumov, Devin B. Granger, Daniel G. Oblinsky, Jacob C. Dean, Grayson S. Doucette, John B. Asbury, Yueh-Lin Loo, Dwight S. Seferos, John E. Anthony, and Gregory D. Scholes. Striking the right balance of intermolecular coupling for high-efficiency singlet fission. *Chem. Sci.*, 9:6240–6259, 2018.

[47] Christoph P. Theurer, Martin Richter, Debkumar Rana, Giuliano Duva, Daniel Lepple, Alexander Hinderhofer, Frank Schreiber, Petra Tegeder, and Katharina Broch. Coexistence of ion pairs and charge-transfer complexes and their impact on pentacene singlet fission. *The Journal of Physical Chemistry C*, 125(43):23952–23959, 2021.

[48] Andrey D. Poletayev, Jenny Clark, Mark W. B. Wilson, Akshay Rao, Yoshitaka Makino, Shu Hotta, and Richard H. Friend. Triplet dynamics in pentacene crystals: Applications to fission-sensitized photovoltaics. *Advanced Materials*, 26(6):919–924, 2014.

[49] Eric A. Margulies, Claire E. Miller, Yilei Wu, Lin Ma, George C. Schatz, Ryan M. Young, and Michael R. Wasielewski. Enabling singlet fission by controlling intramolecular charge transfer in pi-stacked covalent terrylenediimide dimers. *Nature Chemistry*, 8(12):1120–1125, 2016.

[50] Murad J. Y. Tayebjee, Samuel N. Sanders, Elango Kumarasamy, Luis M. Campos, Matthew Y. Sfeir, and Dane R. McCamey. Quintet multiexciton dynamics in singlet fission. *Nature Physics*, 13(2):182–188, 2017.

[51] Daphné Lubert-Perquel, Enrico Salvadori, Matthew Dyson, Paul N. Stavrinou, Riccardo Montis, Hiroki Nagashima, Yasuhiro Kobori, Sandrine Heutz, and Christopher W. M. Kay. Identifying triplet pathways in dilute pentacene films. *Nature Communications*, 9(1):4222, 2018.

[52] Sarah R. E. Orsborne, Jeffrey Gorman, Leah R. Weiss, Akshay Sridhar, Naitik A. Panjwani, Giorgio Divitini, Peter Budden, David Palecek, Seán T. J. Ryan, Akshay Rao, Rosana Collepardo-Guevara, Afaf H. El-Sagheer, Tom Brown, Jan Behrends, Richard H. Friend, and Florian Auras. Photogeneration of spin quintet triplet–triplet excitations in dna-assembled pentacene stacks. *Journal of the American Chemical Society*, 145(9):5431–5438, 2023.

[53] Souratosh Khan and Sumit Mazumdar. Theory of transient excited state absorptions in pentacene and derivatives: Triplet–triplet biexciton versus free triplets. *The Journal of Physical Chemistry Letters*, 8(23):5943–5948, 2017.

[54] Ryan D. Pensack, Geoffrey E. Purdum, Samuel M. Mazza, Christopher Grieco, John B. Asbury, John E. Anthony, Yueh-Lin Loo, and Gregory D. Scholes. Excited-state dynamics of 5,14- vs 6,13-bis(trialkylsilylethynyl)-substituted pentacenes: Implications for singlet fission. *The Journal of Physical Chemistry C*, 126(23):9784–9793, 2022.

[55] Peyman Z. Moghadam, Aurelia Li, Seth B. Wiggin, Andi Tao, Andrew G. P. Maloney, Peter A. Wood, Suzanna C. Ward, and David Fairen-Jimenez. Development of a cambridge structural database subset: A collection of metal–organic frameworks for past, present, and future. *Chemistry of Materials*, 29(7):2618–2625, 2017.

[56] A. J. Brown, N. A. Brunelli, K. Eum, F. Rashidi, J. R. Johnson, W. J. Koros, C. W. Jones, and S. Nair. Interfacial microfluidic processing of metal–organic framework hollow fiber membranes. *Science*, 345:72–75, 2014.

[57] Y. Peng, Y. S. Li, Y. J. Ban, H. Jin, W. M. Jiao, X. L. Liu, and W. S. Yang. Metal–organic framework nanosheets as building blocks for molecular sieving membranes. *Science*, 346:1356–1359, 2014.

[58] T. Rodenas, I. Luz, G. Prieto, B. Seoane, H. Miro, A. Corma, F. Kapteijn, F. X. L. I. Xamena, and J. Gascon. Metal–organic framework nanosheets in polymer composite materials for gas separation. *Nat. Mater.*, 14:48–55, 2015.

[59] R. C. Huxford, J. Della Rocca, and W. Lin. Metal-organic frameworks as potential drug carriers. *Current Opinion in Chemical Biology*, 14(2):262–268, April 2010. Epub 2010 Jan 12.

[60] Chun Gu, Hang Zhang, Pengxian You, Qiao Zhang, Guoqiang Luo, Qiang Shen, Zhengbang Wang, and Jianbo Hu. Giant and multistage nonlinear optical response in porphyrin-based surface-supported metal–organic framework nanofilms. *Nano Letters*, 19(12):9095–9101, 2019. PMID: 31765163.

[61] Lars Heinke and Christof Wöll. Surface-mounted metal–organic frameworks: Crystalline and porous molecular assemblies for fundamental insights and advanced applications. *Advanced Materials*, 31(26):1806324, 2019.

[62] Xiaojing Liu, Mariana Kozlowska, Timur Okkali, Danny Wagner, Tomohiro Higashino, Gerald Brenner-Weiß, Stefan M. Marschner, Zhihua Fu, Qiang Zhang, Hiroshi Imahori, Stefan Bräse, Wolfgang Wenzel, Christof Wöll, and Lars Heinke. Photoconductivity in metal–organic framework (mof) thin films. *Angewandte Chemie International Edition*, 58(28):9590–9595, 2019.

[63] George Porter. Flash photolysis and spectroscopy. a new method for the study of free radical reactions. *Proceedings of the Royal Society of London. Series A, Mathematical and Physical Sciences*, 200:284–300, 1950. NA3240.

[64] Thomas Gaumnitz, Arohi Jain, Yoann Pertot, Martin Huppert, Inga Jordan, Fernando Ardana-Lamas, and Hans Jakob Wörner. Streaking of 43-attosecond soft-x-ray pulses generated by a passively cep-stable mid-infrared driver. *Opt. Express*, 25(22):27506–27518, Oct 2017.

[65] Rudi Berera, Rienk van Grondelle, and John T. M. Kennis. Ultrafast transient absorption spectroscopy: principles and application to photosynthetic systems. *Photosynthesis Research*, 101(2):105–118, 2009.

[66] P. A. Franken, A. E. Hill, C. W. Peters, and G. Weinreich. Generation of optical harmonics. *Phys. Rev. Lett.*, 7:118–119, Aug 1961.

[67] Robert W. Boyd. *Nonlinear Optics*. Academic Press, 3rd edition, 2008.

[68] Richard L. Sutherland. *Handbook of Nonlinear Optics*. Marcel Dekker, Inc, 2nd edition, 2003.

[69] Franz X. Kärtner and Oliver D. Mücke. Nonlinear optics. Center for Free-Electron Laser Science, DESY, Department of Physics, University of Hamburg, January 22, 2018.

[70] Marc Hänsel. Ultrafast excited state dynamics and functional interfaces probed by second harmonic generation, 2017.

[71] Michael Schulze. Second harmonic generation: Probing photochromic interfaces and ultrafast charge transfer processes, October 2014. Im Fachbereich Physik eingereichte Dissertation.

[72] Vipilan Sivanesan. Ultrafast excited state dynamics in organic semiconducting systems, 2021.

[73] Sven Van Elshocht, Thierry Verbiest, Martti Kauranen, André Persoons, B. M. W. Langeveld-Voss, and E. W. Meijer. Direct evidence of the failure of electric-dipole approximation in second-harmonic generation from a chiral polymer film. *The Journal of Chemical Physics*, 107(19):8201–8203, 11 1997.

[74] Peer Fischer and François Hache. Nonlinear optical spectroscopy of chiral molecules. *Chirality*, 17(8):421–437, Oct 2005.

[75] Martti Kauranen, Thierry Verbiest, Jeffery J. Maki, and André Persoons. Second-harmonic generation from chiral surfaces. *The Journal of Chemical Physics*, 101(9):8193–8199, 11 1994.

[76] E. W. Meijer, E. E. Havinga, and G. L. J. A. Rikken. Second-harmonic generation in centrosymmetric crystals of chiral molecules. *Phys. Rev. Lett.*, 65:37–39, Jul 1990.

[77] Katrin Elisabeth Oberhofer. Femtosecond spectroscopy on technically and pharmaceutically relevant organic molecules, June 2020.

[78] E. U. Condon. Theories of optical rotatory power. *Rev. Mod. Phys.*, 9:432–457, Oct 1937.

[79] Jeffrey D. Byers and Janice M. Hicks. Electronic spectral effects on chiral surface second harmonic generation. *Chemical Physics Letters*, 231(2):216–224, 1994.

[80] G. J. Simpson. Molecular origins of the remarkable chiral sensitivity of second-order nonlinear optics. *Chemphyschem*, 5(9):1301–1310, September 2004.

[81] Audrius Dubietis, Gintaras Tamošauskas, Rosvaldas Šuminas, Vytautas Jukna, and Arnaud Couairon. Ultrafast supercontinuum generation in bulk condensed media (invited review), 2017.

[82] Joris J. Snellenburg, Sergey Laptenok, Ralf Seger, Katharine M. Mullen, and Ivo H. M. van Stokkum. Glotaran: A java-based graphical user interface for the r package timp. *Journal of Statistical Software*, 49(3):1–22, 2012.

[83] Joris-Joost Snellenburg. Glotaran: a tool for interactive global target analysis of time-resolved spectroscopy and microscopy data, November 2010.

[84] Joris J. Snellenburg, Sergey Laptenok, Ralf Seger, Katharine M. Mullen, and Ivo H. M. van Stokkum. Glotaran: A java-based graphical user interface for the r package timp. *Journal of Statistical Software*, 49(3):1–22, 2012.

[85] Ivo H.M. van Stokkum, Delmar S. Larsen, and Rienk van Grondelle. Global and target analysis of time-resolved spectra. *Biochimica et Biophysica Acta (BBA) - Bioenergetics*, 1657(2):82–104, 2004.

[86] C. Ruckebusch, M. Sliwa, P. Pernot, A. de Juan, and R. Tauler. Comprehensive data analysis of femtosecond transient absorption spectra: A review. *Journal of Photochemistry and Photobiology C: Photochemistry Reviews*, 13(1):1–27, 2012.

[87] Ritesh Haldar, Mariana Kozlowska, Michael Ganschow, Samrat Ghosh, Marius Jakoby, Hongye Chen, Farhad Ghalami, Weiwei Xie, Shahriar Heidrich, Yusuke Tsutsui, Jan Freudenberg, Shu Seki, Ian A. Howard, Bryce S. Richards, Uwe H. F. Bunz, Marcus Elstner, Wolfgang Wenzel, and Christof Wöll. Interplay of structural dynamics and electronic effects in an engineered assembly of pentacene in a metal–organic framework. *Chem. Sci.*, 12:4477–4483, 2021.

[88] R. Hesse, W. Hofberger, and H. Bāssler. Absorption spectra of disordered solid tetracene and pentacene. *Chemical Physics*, 49(2):201–211, 1980.

[89] Rui He, Nancy G. Tassi, Graciela B. Blanchet, and Aron Pinczuk. Fundamental optical recombination in pentacene clusters and ultrathin films. *Applied Physics Letters*, 87(10):103107, 08 2005.

[90] T Jentzsch, H.J Juepner, K.-W Brzezinka, and A Lau. Efficiency of optical second harmonic generation from pentacene films of different morphology and structure. *Thin Solid Films*, 315(1):273–280, 1998.

[91] Alexander Hinderhofer, Ute Heinemeyer, Alexander Gerlach, Stefan Kowarik, Robert M. J. Jacobs, Youichi Sakamoto, Toshiyasu Suzuki, and Frank Schreiber. Optical properties of pentacene and perfluoropentacene thin films. *The Journal of Chemical Physics*, 127(19):194705, 11 2007.

[92] Christine C. Mattheus, Anne B. Dros, Jacob Baas, Auke Meetsma, Jan L. de Boer, and Thomas T. M. Palstra. Polymorphism in pentacene. *Acta Crystallographica Section C*, 57(8):939–941, Aug 2001.

[93] Mark W. B. Wilson, Akshay Rao, Bruno Ehrler, and Richard H. Friend. Singlet exciton fission in polycrystalline pentacene: From photophysics toward devices. *Accounts of Chemical Research*, 46(6):1330–1338, 2013.

[94] H. Yamagata, J. Norton, E. Hontz, Y. Olivier, D. Beljonne, J. L. Brédas, R. J. Silbey, and F. C. Spano. The nature of singlet excitons in oligoacene molecular crystals. *The Journal of Chemical Physics*, 134(20):204703, 05 2011.

[95] Akshay Rao, Mark W. B. Wilson, Sebastian Albert-Seifried, Riccardo Di Pietro, and Richard H. Friend. Photophysics of pentacene thin films: The role of exciton fission and heating effects. *Phys. Rev. B*, 84:195411, Nov 2011.

[96] Chaw Keong Yong, Andrew J. Musser, Sam L. Bayliss, Steven Lukman, Hiroyuki Tamura, Olga Bubnova, Rawad K. Hallani, Aurélie Meneau, Roland Resel, Munetaka Maruyama, Shu Hotta, Laura M. Herz, David Beljonne, John E. Anthony, Jenny Clark,

and Henning Sirringhaus. The entangled triplet pair state in acene and heteroacene materials. *Nature Communications*, 8(1):15953, 2017.

[97] H. Marciniak, M. Fiebig, M. Huth, S. Schiefer, B. Nickel, F. Selmaier, and S. Lochbrunner. Ultrafast exciton relaxation in microcrystalline pentacene films. *Phys. Rev. Lett.*, 99:176402, Oct 2007.

[98] Samuel N. Sanders, Andrew B. Pun, Kaia R. Parenti, Elango Kumarasamy, Lauren M. Yablon, Matthew Y. Sfeir, and Luis M. Campos. Understanding the bound triplet-pair state in singlet fission. *Chem*, 5(8):1988–2005, 2019.

[99] Johannes Zirzlmeier, Dan Lehnherr, Pedro B. Coto, Erin T. Chernick, Rubén Casillas, Bettina S. Basel, Michael Thoss, Rik R. Tykwinski, and Dirk M. Guldi. Singlet fission in pentacene dimers. *Proceedings of the National Academy of Sciences*, 112(17):5325–5330, 2015.

[100] Samuel N. Sanders, Elango Kumarasamy, Andrew B. Pun, M. Tuan Trinh, Bonnie Choi, Jianlong Xia, Elliot J. Taffet, Jonathan Z. Low, John R. Miller, Xavier Roy, X.-Y. Zhu, Michael L. Steigerwald, Matthew Y. Sfeir, and Luis M. Campos. Quantitative intramolecular singlet fission in bipentacenes. *Journal of the American Chemical Society*, 137(28):8965–8972, 2015.

[101] M. Tuan Trinh, Andrew Pinkard, Andrew B. Pun, Samuel N. Sanders, Elango Kumarasamy, Matthew Y. Sfeir, Luis M. Campos, Xavier Roy, and X.-Y. Zhu. Distinct properties of the triplet pair state from singlet fission. *Science Advances*, 3(7):e1700241, 2017.

[102] Rasmus Ringström, Fredrik Edhborg, Zachary W. Schroeder, Lan Chen, Michael J. Ferguson, Rik R. Tykwinski, and Bo Albinsson. Molecular rotational conformation controls the rate of singlet fission and triplet decay in pentacene dimers. *Chem. Sci.*, 13:4944–4954, 2022.

[103] Ilias Papadopoulos, Johannes Zirzlmeier, Constantin Hetzer, Youn J. Bae, Matthew D. Krzyaniak, Michael R. Wasielewski, Timothy Clark, Rik R. Tykwinski, and Dirk M. Guldi. Varying the interpentacene electronic coupling to tune singlet fission. *Journal of the American Chemical Society*, 141(15):6191–6203, 2019.

[104] Kiyonori Kuroda, Kohei Yazaki, Yuya Tanaka, Munetaka Akita, Hayato Sakai, Taku Hasobe, Nikolai V. Tkachenko, and Michito Yoshizawa. A pentacene-based nanotube displaying enriched electrochemical and photochemical activities. *Angewandte Chemie International Edition*, 58(4):1115–1119, 2019.

[105] Wai-Lun Chan, Manuel Ligges, and X.-Y. Zhu. The energy barrier in singlet fission can be overcome through coherent coupling and entropic gain. *Nature Chemistry*, 4(10):840–845, 2012.

[106] Natalie A. Pace, Dylan H. Arias, Devin B. Granger, Steven Christensen, John E. Anthony, and Justin C. Johnson. Dynamics of singlet fission and electron injection in self-assembled acene monolayers on titanium dioxide. *Chem. Sci.*, 9:3004–3013, 2018.

[107] E. Busby et al. A design strategy for intramolecular singlet fission mediated by charge-transfer states in donor-acceptor organic materials. *Nat Mater*, 14:426–433, 2015.

[108] V. O. Kim et al. Singlet exciton fission via an intermolecular charge transfer state in coevaporated pentacene-perfluoropentacene thin films. *Journal of Chemical Physics*, 151, 2019.

[109] C. H. Yang and C. P. Hsu. First-principle characterization for singlet fission couplings. *Journal of Physical Chemistry Letters*, 6:1925–1929, 2015.

[110] J. Burgos, M. Pope, Ch. E. Swenberg, and R. R. Alfano. Heterofission in pentacene-doped tetracene single crystals. *physica status solidi (b)*, 83(1):249–256, 1977.

[111] M. A. Castellanos and P. Huo. Enhancing singlet fission dynamics by suppressing destructive interference between charge-transfer pathways. *Journal of Physical Chemistry Letters*, 8:2480–2488, 2017.

[112] N. Renaud, P. A. Sherratt, and M. A. Ratner. Mapping the relation between stacking geometries and singlet fission yield in a class of organic crystals. *Journal of Physical Chemistry Letters*, 4:1065–1069, 2013.

[113] M. Fujitsuka et al. Properties of triplet-excited [n]cycloparaphenylenes (n = 8-12): Excitation energies lower than those of linear oligomers and polymers. *Journal of Physical Chemistry A*, 118:4527–4532, 2014.

[114] N. J. Hestand and F. C. Spano. Molecular aggregate photophysics beyond the kasha model: Novel design principles for organic materials. *Acc Chem Res*, 50:341–350, 2017.

[115] N. Nijegorodov, V. Ramachandran, and D.P. Winkoun. The dependence of the absorption and fluorescence parameters, the intersystem crossing and internal conversion rate constants on the number of rings in polyacene molecules. *Spectrochimica Acta Part A: Molecular and Biomolecular Spectroscopy*, 53(11):1813–1824, 1997.

[116] A. D. Becke. Density-functional exchange-energy approximation with correct asymptotic behavior. *Physical Review A*, 38, 1988.

[117] A. D. Becke. Density-functional thermochemistry. iii. the role of exact exchange. *J Chem Phys*, 98:5648–5652, 1993.

[118] L. Wilk A N and D. M. Nusair. Accurate spin-dependent electron liquid correlation energies for local spin density calculations: A critical analysis. *J. Phys*, 58, 1980.

[119] Chengteh Lee, Weitao Yang, and Robert G. Parr. Development of the colle-salvetti correlation-energy formula into a functional of the electron density. *Phys. Rev. B*, 37:785–789, Jan 1988.

[120] F. Wennmohs. *ORCA-An Ab Initio, DFT and Semiempirical SCF-MO Package*, Year.

[121] F. Weigend and R. Ahlrichs. Balanced basis sets of split valence, triple zeta valence and quadruple zeta valence quality for h to rn: Design and assessment of accuracy. *Physical Chemistry Chemical Physics*, 7:3297–3305, 2005.

[122] S. Grimme, J. Antony, S. Ehrlich, and H. Krieg. A consistent and accurate ab initio parametrization of density functional dispersion correction (dft-d) for the 94 elements h-pu. *Journal of Chemical Physics*, 132, 2010.

[123] *Turbomole Program Package for Ab Initio Electronic Structure Calculations USER'S MANUAL*, 2018.

[124] T. C. Berkelbach, M. S. Hybertsen, and D. R. Reichman. Microscopic theory of singlet exciton fission. ii. application to pentacene dimers and the role of superexchange. *Journal of Chemical Physics*, 138, 2013.

[125] Y. J. Bae et al. Substituent effects on energetics and crystal morphology modulate singlet fission in 9,10-bis(phenylethynyl)anthracenes. *Journal of Chemical Physics*, 151, 2019.

[126] S. Ito, T. Nagami, and M. Nakano. Design principles of electronic couplings for intramolecular singlet fission in covalently-linked systems. *Journal of Physical Chemistry A*, 120:6236–6241, 2016.

[127] Taku Hasobe, Prashant V. Kamat, Mark A. Absalom, Yukiyasu Kashiwagi, Joseph Sly, Maxwell J. Crossley, Kohei Hosomizu, Hiroshi Imahori, and Shunichi Fukuzumi. Supramolecular photovoltaic celss based on composite molecular nanoclusters: Dendritic porphyrin c60, porhyrin dimer and c60, and porphyrin-c60 dyad. *The Journal of Physical Chemistry B*, 108(34):12865–12872, 2004.

[128] Paul C. Dastoor, Christopher R. McNeill, Holger Frohne, Christopher J. Foster, Benjamin Dean, Christopher J. Fell, Warwick J. Belcher, Wayne M. Campbell, David L. Officer, Iain M. Blake, Pall Thordarson, Maxwell J. Crossley, Noel S. Hush, and Jeffrey R. Reimers. Understanding and improving solid-state polymer/c60-fullerene bulk-heterojunction solar cells using ternary porphyrin blends. *The Journal of Physical Chemistry C*, 111(42):15415–15426, 2007.

[129] Jianfang Jing, Junshan Li, Yiguo Su, and Yongfa Zhu. Non-covalently linked donor-acceptor interaction enhancing photocatalytic hydrogen evolution from porphyrin assembly. *Applied Catalysis B: Environmental*, 324:122284, 2023.

[130] Martin Gouterman. Spectra of porphyrins. *Journal of Molecular Spectroscopy*, 6:138–163, 1961.

[131] Martin Gouterman, Georges H. Wagnière, and Lawrence C. Snyder. Spectra of porphyrins: Part ii. four orbital model. *Journal of Molecular Spectroscopy*, 11(1):108–127, 1963.

[132] J. Otsuki. Supramolecular approach towards light-harvesting materials based on porphyrins and chlorophylls. *J. Mater. Chem. A*, 6:6710–6753, 2018.

[133] Frank Rioux. Quantum mechanics, group theory and c60, 2024.

[134] Chandra B. KC, Gary N. Lim, and Francis D'Souza. Multi-modular, tris(triphenylamine) zinc porphyrin–zinc phthalocyanine–fullerene conjugate as a broadband capturing, charge stabilizing, photosynthetic 'antenna-reaction center' mimic. *Nanoscale*, 7:6813–6826, 2015.

[135] Sairaman Seetharaman, Jorge Follana-Berná, Luis Martín-Gomis, Georgios Charalambidis, Adelais Trapali, Paul A. Karr, Athanassios G. Coutsolelos, Fernando Fernández-Lázaro, Ángela Sastre-Santos, and Francis D'Souza. Sequential, ultrafast energy transfer and electron transfer in a fused zinc phthalocyanine-free-base porphyrin-c60 supramolecular triad. *ChemPhysChem*, 20(1):163–172, 2019.

[136] Sushanta K. Das, Baiyun Song, Andrew Mahler, Vladimir N. Nesterov, Angela K. Wilson, Osamu Ito, and Francis D'Souza. Electron transfer studies of high potential zinc porphyrin–fullerene supramolecular dyads. *The Journal of Physical Chemistry C*, 118(8):3994–4006, 2014.

[137] Sebastian Schlundt, Gregory Kuzmanich, Fabian Spaenig, Gustavo de Miguel Rojas, Christian Kovacs, Miguel A. Garcia-Garibay, Dirk. M. Guldi, and Andreas Hirsch. Dendritic porphyrin–fullerene conjugates: Efficient light-harvesting and charge-transfer events. *Chemistry – A European Journal*, 15(45):12223–12233, 2009.

[138] Austen Moss, Youngwoo Jang, Jacob Arvidson, Hong Wang, and Francis D'Souza. Highly coupled heterobicycle-fused porphyrin dimers: Excitonic coupling and charge separation with coordinated fullerene, c60. *ChemSusChem*, 16(8):e202202289, 2023.

[139] Darius Kuciauskas, Su Lin, Gilbert R. Seely, Ana L. Moore, Thomas A. Moore, Devens Gust, Tatiana Drovetskaya, Christopher A. Reed, and Peter D. W. Boyd. Photoinduced electron transfer in porphyrin-fullerene dyads. *The Journal of Physical Chemistry*, 100(39):15926–15932, 1996.

[140] Mohamed E. El-Khouly, Osamu Ito, Phillip M. Smith, and Francis D'Souza. Intermolecular and supramolecular photoinduced electron transfer processes of fullerene–porphyrin/phthalocyanine systems. *Journal of Photochemistry and Photobiology C: Photochemistry Reviews*, 5(1):79–104, 2004.

[141] Hiroshi Imahori. Porphyrin–fullerene linked systems as artificial photosynthetic mimics. *Org. Biomol. Chem.*, 2:1425–1433, 2004.

[142] Hiroshi Imahori. Porphyrin–fullerene linked systems as artificial photosynthetic mimics. *Org. Biomol. Chem.*, 2:1425–1433, 2004.

[143] Neha Agnihotri. Computational studies of charge transfer in organic solar photovoltaic cells: A review. *Journal of Photochemistry and Photobiology C: Photochemistry Reviews*, 18:18–31, 2014.

[144] Vladimir A. Basiuk. Interaction of porphine and its metal complexes with c60 fullerene: A dft study. *The Journal of Physical Chemistry A*, 109(16):3704–3710, 2005. PMID: 16839037.

[145] Masahiko Taniguchi, Jonathan S. Lindsey, David F. Bocian, and Dewey Holten. Comprehensive review of photophysical parameters of tetraphenylporphyrin (h2tpp) and zinc tetraphenylporphyrin (zntpp) – critical benchmark molecules in photochemistry and photosynthesis. *Journal of Photochemistry and Photobiology C: Photochemistry Reviews*, 46:100401, 2021.

[146] E. G. Donenko O. E. Kvyatkovskii and I. B. Zakharova. Electronic structure and optical properties of charge-transfer fullerene-porphyrin complexes: ab initio calculations. *Fullerenes, Nanotubes and Carbon Nanostructures*, 16(5-6):530–533, 2008.

[147] Teguh Endah Saraswati, Umam Hasan Setiawan, Mohammad Rifki Ihsan, Isnaeni Isnaeni, and Yuliati Herbani. The study of the optical properties of c60 fullerene in different organic solvents. *Open Chemistry*, 17(1):1198–1212, 2019.

[148] Jianfang Jing, Junshan Li, Yiguo Su, and Yongfa Zhu. Non-covalently linked donor-acceptor interaction enhancing photocatalytic hydrogen evolution from porphyrin assembly. *Applied Catalysis B: Environmental*, 324:122284, 2023.

[149] Baxter Abraham, Jesus Nieto-Pescador, and Lars Gundlach. Ultrafast relaxation dynamics of photoexcited zinc-porphyrin: Electronic-vibrational coupling. *The Journal of Physical Chemistry Letters*, 7(16):3151–3156, 2016. PMID: 27482847.

[150] Arthur J. Harrison. Investigating electron-transfer processes of supramolecular donor-acceptor complexes using femtosecond transient absorption spectroscopy, 2019.

[151] Katrin Peuntinger, Theodore Lazarides, Dimitra Dafnomili, Georgios Charalambidis, Georgios Landrou, Axel Kahnt, Randy Pat Sabatini, David W. McCamant, Daniel T. Gryko, Athanassios G. Coutsolelos, and Dirk M. Guldi. Photoinduced charge transfer in porphyrin–cobaloxime and corrole–cobaloxime hybrids. *The Journal of Physical Chemistry C*, 117(4):1647–1655, 2013.

[152] Maximilian Wolf, Joana I. T. Costa, Martin B. Minameyer, Thomas Drewello, Augusto C. Tomé, and Dirk M. Guldi. Efficient low driving force charge separation in an electron deficient zn-porphyrin-fullenen donor-acceptor conjugate. *The Journal of Physical Chemistry C*, 123(46):28093–28099, 2019.

[153] Dirk M. Guldi and Maurizio Prato. Excited-state properties of c60 fullerene derivatives. *Accounts of Chemical Research*, 33(10):695–703, 2000. PMID: 11041834.

[154] Susana Iglesias-Groth Franco Cataldo and Arturo Manchado. On the radical anion spectra of fullerenes c60 and c70. *Fullerenes, Nanotubes and Carbon Nanostructures*, 21(6):537–548, 2013.

[155] Xiaoxin Li, Chenghuan Gong, Gagik G. Gurzadyan, Maxim F. Gelin, Jinxuan Liu, and Licheng Sun. Ultrafast relaxation dynamics in zinc tetraphenylporphyrin surface-mounted metal organic framework. *The Journal of Physical Chemistry C*, 122(1):50–61, 2018.

[156] Minh-Huong Ha-Thi, Niloufar Shafizadeh, Lionel Poisson, and Benoit Soep. An efficient indirect mechanism for the ultrafast intersystem crossing in copper porphyrins. *The Journal of Physical Chemistry A*, 117(34):8111–8118, 2013. PMID: 23675770.

[157] Garusinghe Nepali Rajapakse. Photophysical properties of metallotetraphenyltetrabenzoporphyrins: Insights from experimental and theoretical studies, 2008.

[158] Marina V. Rogozina, Vladimir N. Ionkin, and Anatoly I. Ivanov. Kinetics of charge separated state population produced by intramolecular electron transfer quenching of second excited state. *Journal of Photochemistry and Photobiology A: Chemistry*, 301:55–61, 2015.

[159] Hiroshi Imahori and Yoshiteru Sakata. Fullerenes as novel acceptors in photosynthetic electron transfer. *European Journal of Organic Chemistry*, 1999(10):2445–2457, 1999.

[160] Masanori Yamamoto, Jens Föhlinger, Jonas Petersson, Leif Hammarström, and Hiroshi Imahori. A ruthenium complex–porphyrin–fullerene-linked molecular pentad as an integrative photosynthetic model. *Angewandte Chemie International Edition*, 56(12):3329–3333, 2017.

[161] Guoyan Li, Yexin Li, Xiaofeng Yang, Jinling Miao, Yu Cui, Yong Nie, Shuaijun Yang, Wei Liu, and Guoxin Sun. N-to-s substitution induced fluorescence-to-phosphorescence dominant emission with excitation-dependent intersystem crossing. *J. Mater. Chem. C*, 12:2585–2592, 2024.

[162] Kai Li, Glenna So Ming Tong, Jia Yuan, Chensheng Ma, Lili Du, Chen Yang, Wai-Ming Kwok, David Lee Phillips, and Chi-Ming Che. Excitation-wavelength-dependent and auxiliary-ligand-tuned intersystem-crossing efficiency in cyclometalated platinum(ii) complexes: Spectroscopic and theoretical studies. *Inorganic Chemistry*, 59(20):14654–14665, 2020. PMID: 32806020.

[163] Bingzhe Wang, Shushu Zheng, Avishek Saha, Lipiao Bao, Xing Lu, and Dirk M. Guldi. Understanding charge-transfer characteristics in crystalline nanosheets of fullerene/(metallo)porphyrin cocrystals. *Journal of the American Chemical Society*, 139(30):10578–10584, 2017. PMID: 28686429.

[164] L. Benatto, C.F.N. Marchiori, T. Talka, M. Aramini, N.A.D. Yamamoto, S. Huotari, L.S. Roman, and M. Koehler. Comparing c60 and c70 as acceptor in organic solar cells: Influence of the electronic structure and aggregation size on the photovoltaic characteristics. *Thin Solid Films*, 697:137827, 2020.

[165] Nikolay V. Tkachenko, Claudia Guenther, Hiroshi Imahori, Koichi Tamaki, Yoshiteru Sakata, Shunichi Fukuzumi, and Helge Lemmetyinen. Near infra-red emission of charge-transfer complexes of porphyrin–fullerene films. *Chemical Physics Letters*, 326(3):344–350, 2000.

[166] Sairaman Seetharaman, Jorge Follana-Berná, Luis Martín-Gomis, Georgios Charalambidis, Adelais Trapali, Paul A. Karr, Athanassios G. Coutsolelos, Fernando Fernández-Lázaro, Ángela Sastre-Santos, and Francis D'Souza. Sequential, ultrafast energy transfer and electron transfer in a fused zinc phthalocyanine-free-base porphyrin-c60 supramolecular triad. *ChemPhysChem*, 20(1):163–172, 2019.

[167] Ardalan Armin, Marappan Velusamy, Pascal Wolfer, Yuliang Zhang, Paul L Burn, Paul Meredith, and Almantas Pivrikas. Quantum efficiency of organic solar cells: Electro-optical cavity considerations. *ACS Photonics*, 1(3):173–181, 2014.

[168] Chuan Yu Han, Wing Man Tang, and Pui-To Lai. High-mobility pentacene organic thin-film transistors achieved by reducing remote phonon scattering and surface-roughness scattering. *Applied Surface Science*, 544:148656, 2021.

[169] Jing Li, Gabriele D'Avino, Anton Pershin, Denis Jacquemin, Ivan Duchemin, David Beljonne, and Xavier Blase. Correlated electron-hole mechanism for molecular doping in organic semiconductors. *Phys. Rev. Mater.*, 1:025602, Jul 2017.

[170] Ingo Salzmann, Georg Heimel, Steffen Duhm, Martin Oehzelt, Patrick Pingel, Benjamin M. George, Alexander Schnegg, Klaus Lips, Ralf-Peter Blum, Antje Vollmer, and Norbert Koch. Intermolecular hybridization governs molecular electrical doping. *Phys. Rev. Lett.*, 108:035502, Jan 2012.

[171] Alberto D. Scaccabarozzi, Aniruddha Basu, Filip Aniés, Jian Liu, Osnat Zapata-Arteaga, Ross Warren, Yuliar Firdaus, Mohamad Insan Nugraha, Yuanbao Lin, Mariano Campoy-Quiles, Norbert Koch, Christian Müller, Leonidas Tsetseris, Martin Heeney, and Thomas D. Anthopoulos. Doping approaches for organic semiconductors. *Chemical Reviews*, 122(4):4420–4492, 2022. PMID: 34793134.

[172] Henry Méndez, Georg Heimel, Stefanie Winkler, Johannes Frisch, Andreas Opitz, Katrein Sauer, Berthold Wegner, Martin Oehzelt, Christian Röthel, Steffen Duhm, Daniel

Többens, Norbert Koch, and Ingo Salzmann. Charge-transfer crystallites as molecular electrical dopants. *Nature Communications*, 6(1):8560, 2015.

[173] Henry Mendez, Georg Heimel, Andreas Opitz, Katrein Sauer, Patrick Barkowski, Martin Oehzelt, Junshi Soeda, Toshihiro Okamoto, Jun Takeya, Jean-Baptiste Arlin, Jean-Yves Balandier, Yves Geerts, Norbert Koch, and Ingo Salzmann. Doping of organic semiconductors: Impact of dopant strength and electronic coupling. *Angewandte Chemie International Edition*, 125(30):7905–7909, 2013.

[174] H. Yoshida, K. Yamada, J. Tsutsumi, and N. Sato. Complete description of ionization energy and electron affinity in organic solids: Determining contributions from electronic polarization, energy band dispersion, and molecular orientation. *Physical Review B*, 92:075145, 2015.

[175] K. Kanai, K. Akaike, K. Koyasu, K. Sakai, T. Nishi, Y. Kamizuru, Y. Ouchi, and K. Seki. Determination of electron affinity of electron accepting molecules. *Applied Physics A*, 95:309–313, 2009.

[176] P. K. Koech, A. B. Padmaperuma, L. Wang, J. S. Swensen, E. Polikarpov, J. T. Darsell, J. E. Rainbolt, and D. J. Gaspar. Synthesis and application of 1,3,4,5,7,8-hexafluorotetracyanonaphthoquinodimethane (f6-tnap): A conductivity dopant for organic light-emitting devices. *Chemistry of Materials*, 22:3926–3932, 2010.

[177] Y. Karpov, T. Erdmann, M. Stamm, U. Lappan, O. Guskova, M. Malanin, I. Raguzin, T. Beryozkina, V. Bakulev, F. Günther, et al. Molecular doping of a high mobility diketopyrrolopyrrole-dithienylthieno[3,2-b]thiophene donor-acceptor copolymer with f6tcnnq. *Macromolecules*, 50:914–926, 2017.

[178] F. Zhang and A. Kahn. Investigation of the high electron affinity molecular dopant f6-tcnnq for hole-transport materials. *Advanced Functional Materials*, 28:1703780, 2018.

[179] W. Gao and A. Kahn. Controlled p-doping of zinc phthalocyanine by coevaporation with tetrafluorotetracyanoquinodimethane: A direct and inverse photoemission study. *Applied Physics Letters*, 79:4040–4042, 2001.

[180] D. Gerbert, F. Maaß, and P. Tegeder. Extended space charge region and unoccupied molecular band formation in epitaxial tetrafluorotetracyanoquinodimethane films. *Journal of Physical Chemistry C*, 121:15696–15701, 2017.

[181] Hans Kleemann, Christoph Schuenemann, Alexander A. Zakhidov, Moritz Riede, Björn Lüssem, and Karl Leo. Structural phase transition in pentacene caused by molecular doping and its effect on charge carrier mobility. *Organic Electronics*, 13(1):58–65, 2012.

[182] Sieu D. Ha and Antoine Kahn. Isolated molecular dopants in pentacene observed by scanning tunneling microscopy. *Phys. Rev. B*, 80:195410, Nov 2009.

[183] Dmitrii Nabok, Peter Puschnig, Claudia Ambrosch-Draxl, Oliver Werzer, Roland Resel, and Detlef-M. Smilgies. Crystal and electronic structures of pentacene thin films from grazing-incidence x-ray diffraction and first-principles calculations. *Phys. Rev. B*, 76:235322, Dec 2007.

[184] Moreno Meneghetti and Cesare Pecile. Charge–transfer organic crystals: Molecular vibrations and spectroscopic effects of electron–molecular vibration coupling of the strong electron acceptor tcnqf4. *The Journal of Chemical Physics*, 84(8):4149–4162, 1986.

[185] Lingyun Zhu, Eung-Gun Kim, Yuanping Yi, and Jean-Luc Brédas. Charge transfer in molecular complexes with 2,3,5,6-tetrafluoro-7,7,8,8-tetracyanoquinodimethane (f4-tcnq): A density functional theory study. *Chemistry of Materials*, 23(23):5149–5159, 2011.

[186] Patrick Pingel, Lingyun Zhu, Kue Surk Park, Jörn-Oliver Vogel, Silvia Janietz, Eung-Gun Kim, Jürgen P. Rabe, Jean-Luc Brédas, and Norbert Koch. Charge-transfer localization in molecularly doped thiophene-based donor polymers. *The Journal of Physical Chemistry Letters*, 1(13):2037–2041, 2010.

[187] Jan Szczepanski, Christine Wehlburg, and Martin Vala. Vibrational and electronic spectra of matrix-isolated pentacene cations and anions. *Chemical Physics Letters*, 232(3):221–228, 1995.

[188] Yoshinobu Hosoi, Koshi Okamura, Yasuo Kimura, Hisao Ishii, and Michio Niwano. Infrared spectroscopy of pentacene thin film on sio2 surface. *Applied Surface Science*, 244(1):607–610, 2005. 12th International Conference on Solid Films and Surfaces.

[189] L. Sebastian, G. Weiser, and H. Bässler. Charge transfer transitions in solid tetracene and pentacene studied by electroabsorption. *Chemical Physics*, 61(1):125–135, 1981.

[190] Akshay Rao, Mark W. B. Wilson, Justin M. Hodgkiss, Sebastian Albert-Seifried, Heinz Bässler, and Richard H. Friend. Exciton fission and charge generation via triplet excitons in pentacene/c60 bilayers. *Journal of the American Chemical Society*, 132(36):12698–12703, 2010. PMID: 20735067.

[191] Henning Marciniak, Igor Pugliesi, Bert Nickel, and Stefan Lochbrunner. Ultrafast singlet and triplet dynamics in microcrystalline pentacene films. *Phys. Rev. B*, 79:235318, Jun 2009.

[192] M. Brinkmann, V. S. Videva, A. Bieber, J. J. André, P. Turek, L. Zuppiroli, P. Bugnon, M. Schaer, F. Nuesch, and R. Humphry-Baker. Electronic and structural evidences for charge transfer and localization in iodine-doped pentacene. *The Journal of Physical Chemistry A*, 108(40):8170–8179, 2004.

[193] Giuliano Duva, Paul Beyer, Reinhard Scholz, Valentina Belova, Andreas Opitz, Alexander Hinderhofer, Alexander Gerlach, and Frank Schreiber. Ground-state charge-transfer interactions in donor:acceptor pairs of organic semiconductors – a spectroscopic study of two representative systems. *Phys. Chem. Chem. Phys.*, 21:17190–17199, 2019.

[194] Yevhen Karpov, Tim Erdmann, Manfred Stamm, Uwe Lappan, Olga Guskova, Mikhail Malanin, Ivan Raguzin, Tetyana Beryozkina, Vasiliy Bakulev, Florian Günther, Sibylle Gemming, Gotthard Seifert, Mike Hambsch, Stefan Mannsfeld, Brigitte Voit, and Anton Kiriy. Molecular doping of a high mobility diketopyrrolopyrrole–dithienylthieno[3,2-b]thiophene donor–acceptor copolymer with f6tcnnq. *Macromolecules*, 50(3):914–926, 2017.

[195] Vishnu Vijayakumar, Pablo Durand, Huiyan Zeng, Viktoriia Untilova, Laurent Herrmann, Patrick Algayer, Nicolas Leclerc, and Martin Brinkmann. Influence of dopant size and doping method on the structure and thermoelectric properties of pbttt films doped with f6tcnnq and f4tcnq. *J. Mater. Chem. C*, 8:16470–16482, 2020.

[196] D. Choudhary, P. Clancy, and D.R. Bowler. Adsorption of pentacene on a silicon surface. *Surface Science*, 578(1):20–26, 2005.

[197] Takashi Minakata, Hideaki Imai, Masaru Ozaki, and Kentaro Saco. Structural studies on highly ordered and highly conductive thin films of pentacene. *Journal of Applied Physics*, 72(11):5220–5225, 12 1992.

[198] Weiping Liu, Kunde Lin, and Jianying Gan. Separation and aquatic toxicity of enantiomers of the organophosphorus insecticide trichloronate. *Chirality*, 18(9):713–716, 2006.

[199] Brad J. Konwick, Aaron T. Fisk, Arthur W. Garrison, Jimmy K. Avants, and Marsha C. Black. Acute enantioselective toxicity of fipronil and its desulfinyl photoproduct to ceriodaphnia dubia. *Environmental Toxicology and Chemistry*, 24(9):2350–2355, 2005.

[200] Silas W. Smith. Chiral Toxicology: It's the Same Thing. . . Only Different. *Toxicological Sciences*, 110(1):4–30, 05 2009.

[201] J. B. Biot. Phenomene de polarisation successive, observés dans des fluides homogenes. *Bulletin des Sciences, par la Société Philomatique de Paris*, pages 190–192, 1815. Phenomenon of successive polarization, observed in homogeneous fluids.

[202] Augustin-Jean Fresnel. Mémoire sur la double réfraction que les rayons lumineux éprouvent en traversant les aiguilles de cristal de roche suivant les directions parallèles à l'axe, 1866. extrait first published in *Bulletin de la Société philomathique* for 1822, pp. 191–198.

[203] Louis Pasteur. Mémoires sur la relation qui peut exister entre la forme crystalline et la composition chimique, et sur la cause de la polarisation rotatoire. *Comptes Rendus de l'Académie des Sciences*, 26:535–538, 1848.

[204] Philippe Wagner, Frank Rominger, Wen-Shan Zhang, Jürgen H. Gross, Sven M. Elbert, Rasmus R. Schröder, and Michael Mastalerz. Chiral self-sorting of giant cubic [8+12] salicylimine cage compounds. *Angewandte Chemie International Edition*, 60(16):8896–8904, 2021.

[205] Philipp Heister, Tobias Lünskens, Martin Thämer, Aras Kartouzian, Sabine Gerlach, Thierry Verbiest, and Ueli Heiz. Orientational changes of supported chiral 2,2′-dihydroxy-1,1′binaphthyl molecules. *Phys. Chem. Chem. Phys.*, 16:7299–7306, 2014.

[206] F. Hache, T. Boulesteix, M. C. Schanne-Klein, M. Alexandre, G. Lemercier, and C. Andraud. Polarization rotation in a second harmonic reflection experiment from an isotropic surface of chiral troeger base. *The Journal of Physical Chemistry B*, 107(22):5261–5266, 2003.

[207] Python Software Foundation, Guido van Rossum. Python, 2021.

[208] G. Porter and M. W. Windsor. The triplet state in fluid media. *Proceedings of the Royal Society of London. Series A, Mathematical and Physical Sciences*, 245(1241):238–258, 1958.

[209] A. Vollmer, H. Weiss, S. Rentenberger, I. Salzmann, J.P. Rabe, and N. Koch. The interaction of oxygen and ozone with pentacene. *Surface Science*, 600(18):4004–4007, 2006. Berlin, Germany: 4–9 September 2005.

[210] Ashok Maliakal, Krishnan Raghavachari, Howard Katz, Edwin Chandross, and Theo Siegrist. Photochemical stability of pentacene and a substituted pentacene in solution and in thin films. *Chemistry of Materials*, 16(24):4980–4986, 2004.

[211] Lin Ma, Peng Hu, Hui Jiang, Christian Kloc, Handong Sun, Cesare Soci, Alexander A. Voityuk, Maria E. Michel-Beyerle, and Gagik G. Gurzadyan. Single photon triggered dianion formation in tcnq and f4tcnq crystals. *Scientific Reports*, 6(1):28510, 2016.

[212] Brandon J. Barrett, Simran S. Saund, Rachel A. Dziatko, Tylar L. Clark-Winters, Howard E. Katz, and Arthur E. Bragg. Spectroscopic studies of charge-transfer character and photoresponses of f4tcnq-based donor–acceptor complexes. *The Journal of Physical Chemistry C*, 124(17):9191–9202, 2020.

A Supplementary information on PEN SURMOF

Enhancing singlet fission lifetimes through molecular engineering

Martin Richter[1], Muhammed Jeneesh Kariyottukuniyil[2], Zhiyun Xu[3], Philipp Ludwig[4], Pavel V. Kolesnichenko[1], Christian Huck[1], Uwe Bunz[4], Christof Wöll[3], Wolfgang Wenzel[2] and Petra Tegeder[1]

[1]*Physikalisch-Chemisches Institut, Ruprecht-Karls-Universität Heidelberg, Im Neuenheimer Feld 253 , 69120 Heidelberg, Germany*
[2]*Institute of Nanotechnology, Karlsruher Institut für Technologie, Hermann-von-Helmholtz-Platz 1, 76131 Karlsruhe, Germany*
[3]*Institut für Funktionelle Grenzflächen, Karlsruher Institut für Technologie, Hermann-von-Helmholtz-Platz 1, 76131 Karlsruhe, Germany*
[4]*Organisch-Chemisches Institut, Ruprecht-Karls-Universität Heidelberg, Im Neuenheimer Feld 271, 69120 Heidelberg, Germany*

A.0.1 Femtosecond transient absorption

Transient absorption measurements have been carried out as described in the "Experimental" section. The fits are all calculated with Glotaran. For plotting the data a self-written Python [207] script is used. For the data with time-zero correction an interpolation is implemented. Therefore there might be data points shown that lie in between the acquired data points. This is however solely for display purposes and does not affect the analysis with Glotaran, which uses the non-interpolated data. When normalised data is shown, it means that the signal is divided by the integral of 0 to 50 ps. Be aware that plots over time use a semi-logarithmic scale, i.e. linear between -1 and 1 ps and logarithmic elsewhere.

A.0.2 fsTA on pentacene thin film

To gain more insights on the PIA probed at 340 nm, a test on fluence dependence as well as a variation of the angle of incidence were carried out. It is noticeable that the new PIA, just like the GSB, increases instantaneously - within the time resolution - while the PIAs which are assigned to the triplets rise more slowly. However, the signal then does increase further in the same way as the triplet PIAs until approx. 10 ps. For long pump-probe delays, the signal decay is similar to that of the triplet PIAs and it also shows a significant reduction in lifetime in the same manner upon increasing fluence, suggestive of TTA (Fig. SA.1). Measurements with an angle of incidence of 50° show a clear increase in ΔA compared to 0° (Fig. SA.2), which is also the case for triplet PIAs at 540 nm and 750 nm. Higher triplet state energies of PEN in solution are observed at 385 nm (weak) and 305 nm (strong) [208]. Thus we attribute the transition at 340 nm also to a triplet-triplet transition at.

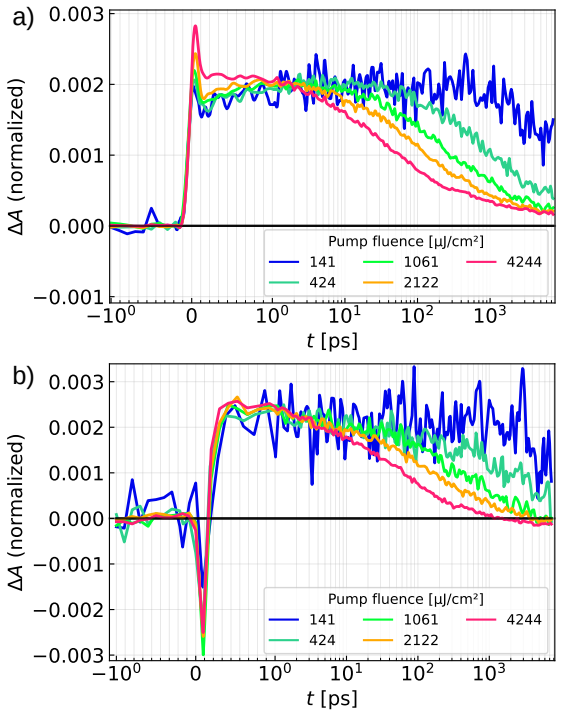

Figure A.1: Fluence dependence of the pentacene thin film for a probe wavelength of a) 340 nm and b) 750 nm. Excitation was centered around 620 nm and traces are averaged over a range of 4 nm.

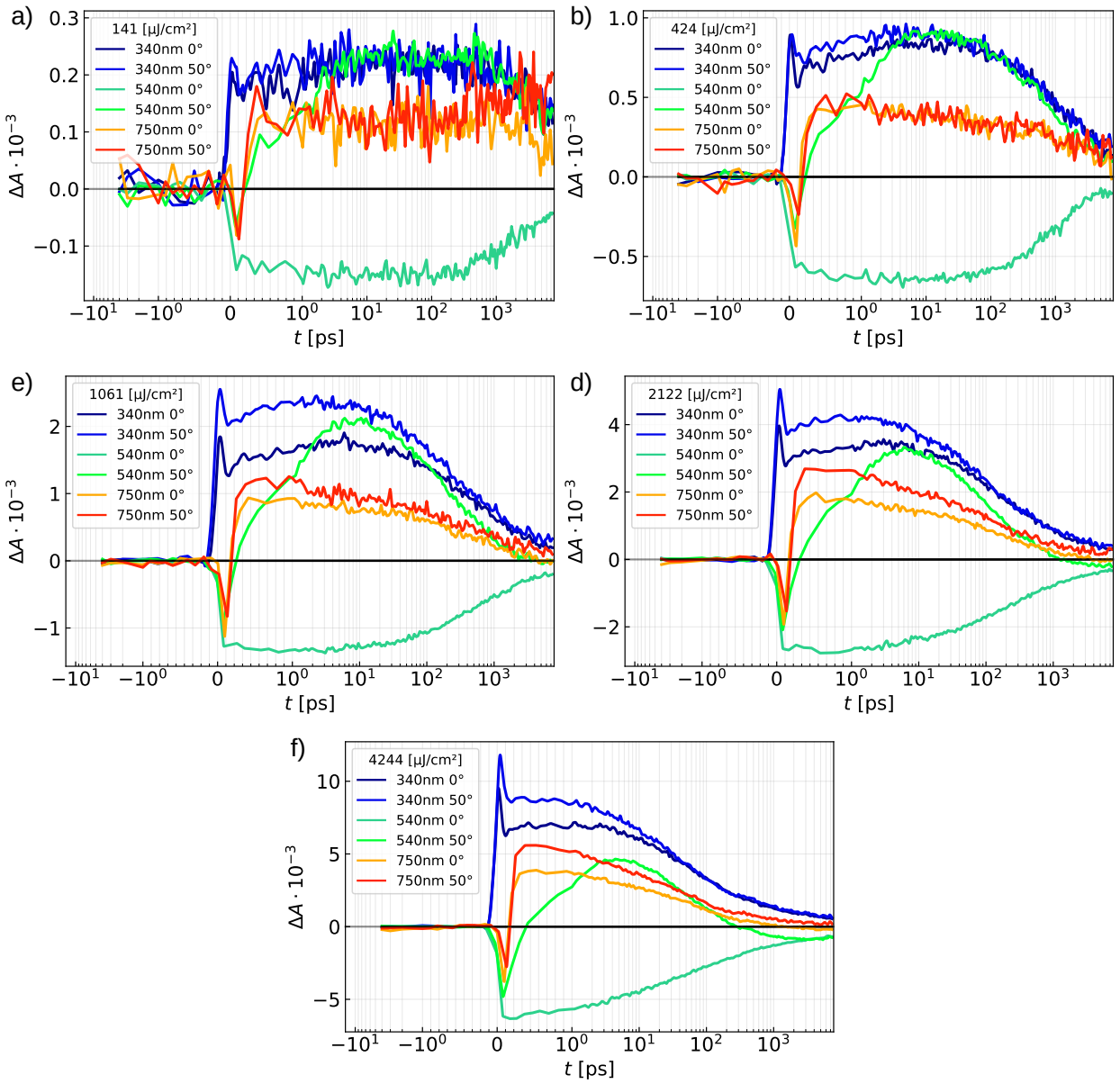

Figure A.2: Comparison of angles of incidence for pentacene thin film. The newly observed PIA is centered at 340 nm.

A.0.3 fsTA on pentacene embedded in a SURMOF

The results shown in the main text were obtained by extracting the first two rates from a constrained range (410 nm-450 nm), where the Evolution Associated Difference Spectra (EADS) of the third rate is close to zero and then obtain the full fit with these two rates held fixed, see Fig. SA.3 and Fig. SA.4 for the GA results. This was done because the overlapping spectra together with the fluence dependence gave varying rates for triplet-pair generation, which should not be affected since only TTA and no singlet-singlet annihilation were observed. For completeness fits with free parameters are also included in Fig. SA.5. A fit with a constant offset was also attempted, but did not yield reasonable results.

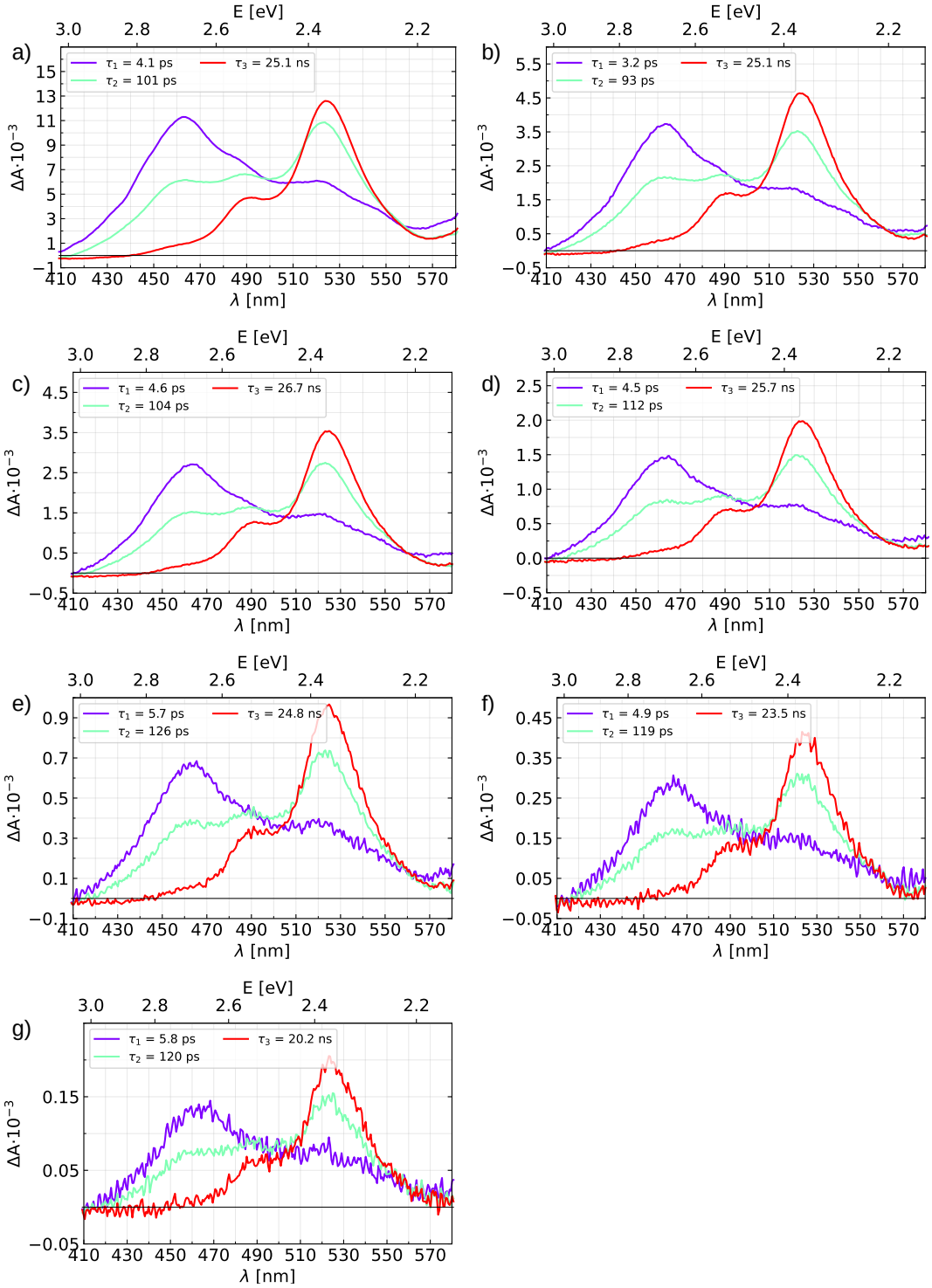

Figure A.3: EADS from global fits for ZnPn excited at 605 nm for different pump fluences of 4244, 2122, 1061, 566, 283 and 141 µJ cm^{-2} from a) to g). The first two rates were obtained from GA in the range of 410-450 nm, where the triplet PIA (red) is close to zero. A subsequent fit from 410-580 nm yielded the results that are shown.

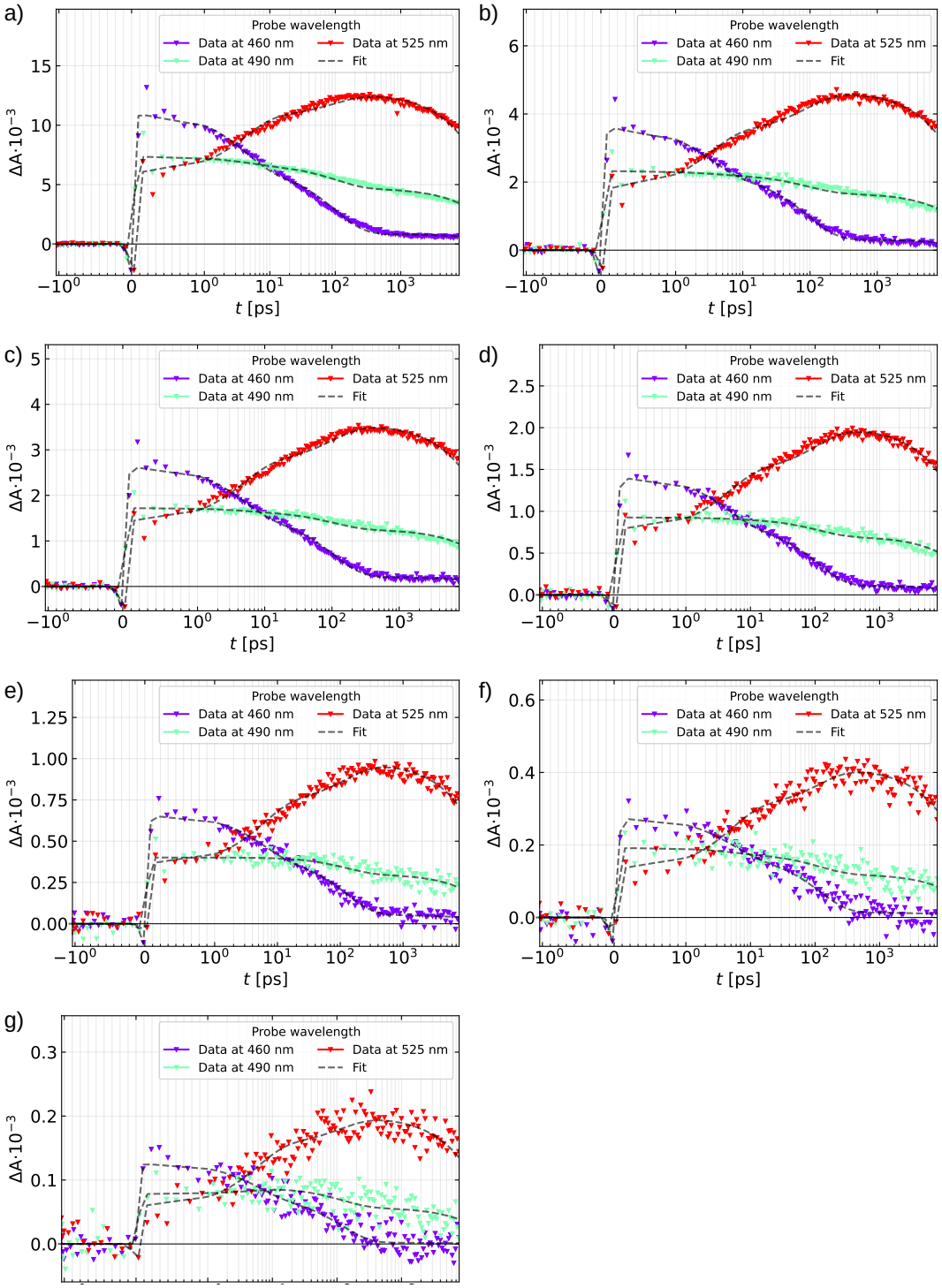

Figure A.4: Dynamics and fits that are associated with the results shown in Fig. SA.3.

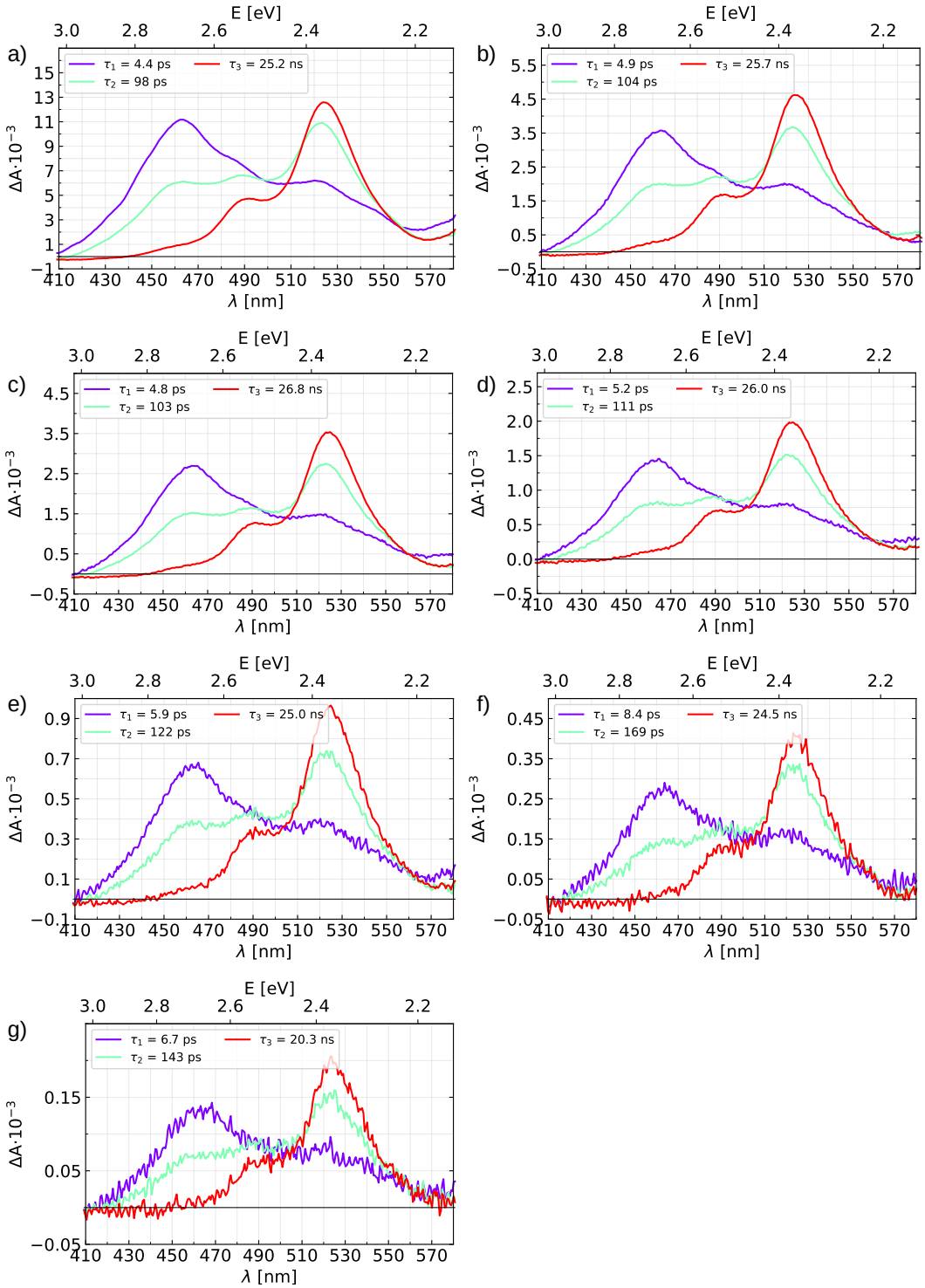

Figure A.5: EADS from global fits for ZnPn excited at 605 nm for different pump fluences of 4244, 2122, 1061, 566, 283 and 141 µJ cm^{-2} from a) to g). All rates were kept unconstrained.

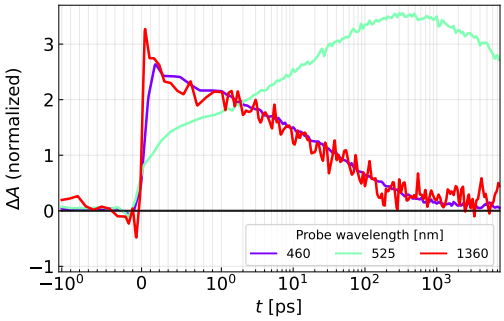

Figure A.6: Time traces of fsTA data of ZnPn excited at 605 nm with 424 µJ cm^{-2} at selected wavelenghts. Data at 460 nm and 1360 nm are associated with singlet PIA and at 525 nm with triplet PIA.

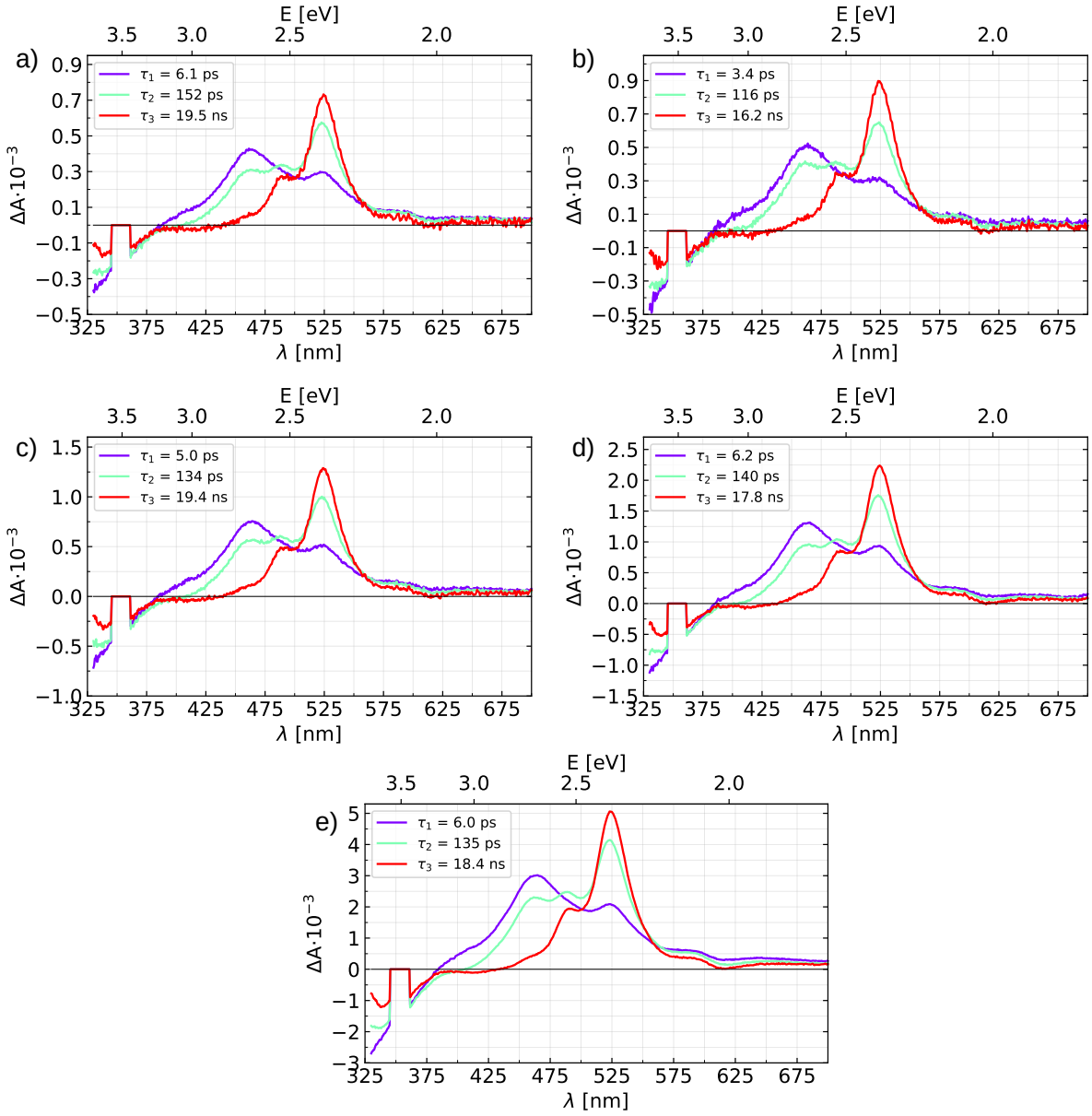

Figure A.7: EADS from global fits for ZnPn excited at 355 nm for different pump fluences of from 141, 86, 57, 42 and 14 µJ cm^{-2} a) to e). All rates were kept unconstrained.

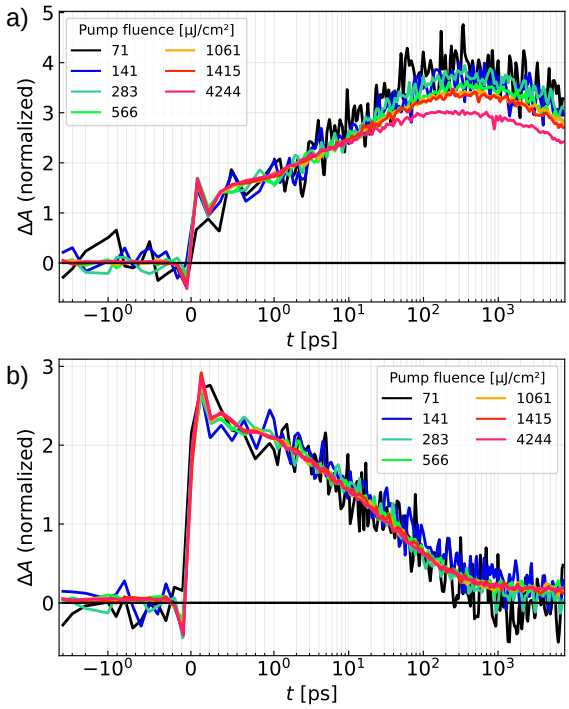

Figure A.8: a) Fluence dependence of transient absorption spectra of ZnPn excited at 605 nm probed at a) 525 nm and b) 460 nm, which are associated with triplet and singlet exciton PIAs, respectively. Notice that only the triplet signature is affected, which is indicative for TTA.

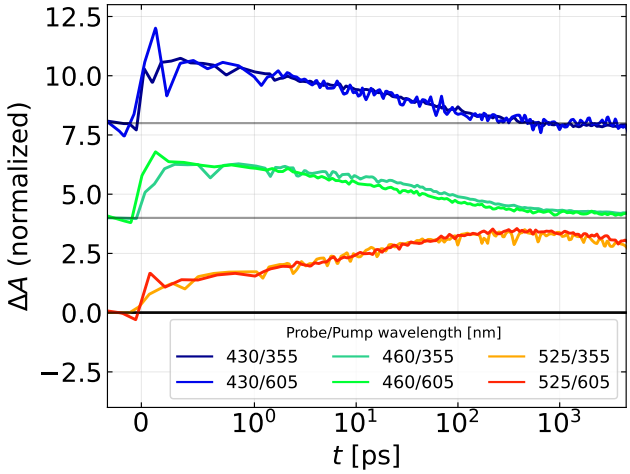

Figure A.9: Comparison of normalised kinetics of ZnPn excited at a wavelength of either 605 nm or 355 nm. The maximum absorption of the singlet and triplet excited species is at 460 nm and 525 nm, respectively. The data are offset by a constant value for clarity

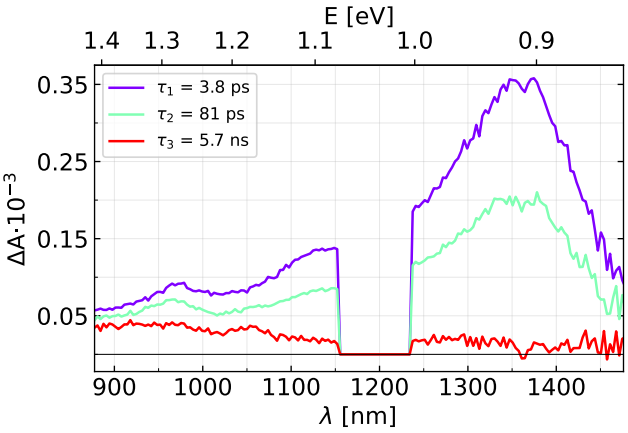

Figure A.10: EADS of ZnPn excited at a wavelength of 605 nm and probed in the NIR. For analysis it was necessary to include a fit for the coherent artifact.(In Glotaran: CohSpec→ ModelType: Mix; Number of seq starting values 1; value=20.59)

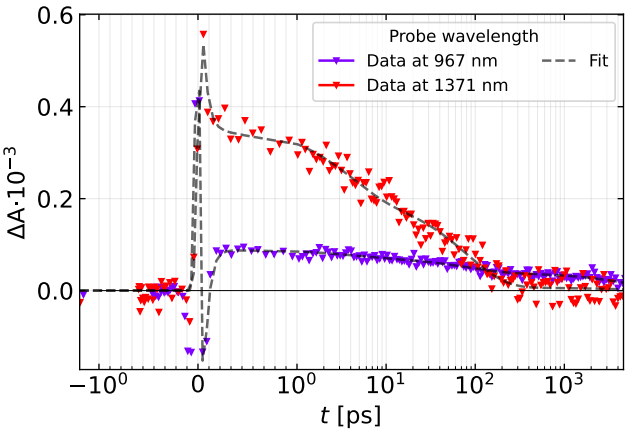

Figure A.11: Dynamics of ZnPn excited at a wavelength of 605 nm. The fit results correspond to the values shown in Fig. A.10. Notice the coherent artifact at t=0 s, which needs to be modelled.

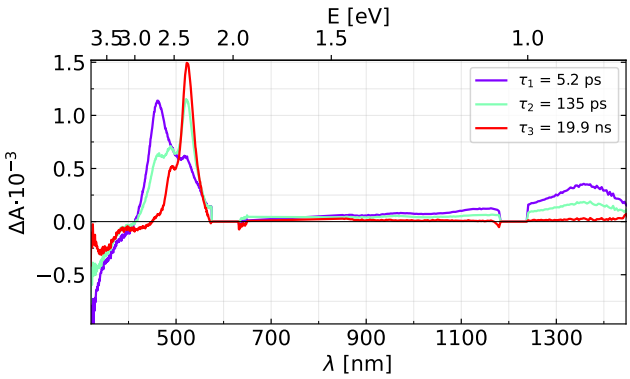

Figure A.12: EADS of ZnPn excited at a wavelength of 605 nm. The data of the whitelight probe in UV in NIR were merged after dispersion correction. Notice that the second spectrum (green) assigned to ^{1}(TT) has a contribution in the NIR aswell. GA included modelling of the coherent artifact. (In Glotaran: CohSpec→ ModelType: Mix; Number of seq starting values 1; value=9.76)

A.0.4 Computational study

The values in Fig.SA.14 were quantified by using orbital (Λ) and density-based metrics (Δ_μ)

$$\Lambda = \frac{\sum_{ia} K_{ia}^2 \int |\phi_a(r)||\phi_i(r)|dr}{\sum_{ia} K_{ia}^2}, \tag{74}$$

where K_{ia} is the exchange integral in the localized natural orbital (LNO) basis calculated by CASCI method.

	Pentacene (*PEN*)		**Pentacene (*MOF*)**	
	Theory	Exp	Theory	Exp
$E(S_1)$	1.79 eV	1.85, 1.96	1.83 eV	*
$E(T_1)$	0.77 eV	0.86 eV [1]	0.58 eV	*
Charge-Transfer (CT)	2.08 eV	*	2.80 eV	*
Reorganization energy (λ)	126 meV	96 meV	136 meV	*
Radiative - decay (K_r)	1.10×10^7 S^{-1}	1.20×10^7 S^{-1} [3]	2.54×10^7 S^{-1}	*
K_{SF}	6.78×10^{12} S^{-1}	*	1.76×10^{11} S^{-1}	*
SF- Lifetime	147 fs	80-110 fs [7]	5.68 ps	3.2-5.8 ps
ΔG_{if}	-0.22 eV	*	-0.18 eV	*
Energy Gap (ΔE_g)	2.09 eV	*	2.14 eV	*
$E(T_2) - E(T_1)$	1078 nm	750-1200 nm	918 nm	*
$E(T_3) - E(T_1)$	574 nm	540 nm	582 nm	525 nm
$E(S_2) - E(S_1)$	1068 nm	1653 nm	1333 nm	1350 nm
$^1(TT) \rightarrow {}^5(TT)$	0.78 ps	*	112.23 ps	93-120 ps
ISC ($T_1 - S_0$)	18 ns	10 ns [4]	42.08 µs	40 µs

Figure A.13: Experimental and computed data of pentacene (PEN) and pentacene model MOF-C (MOF) [41, 48, 110, 115].

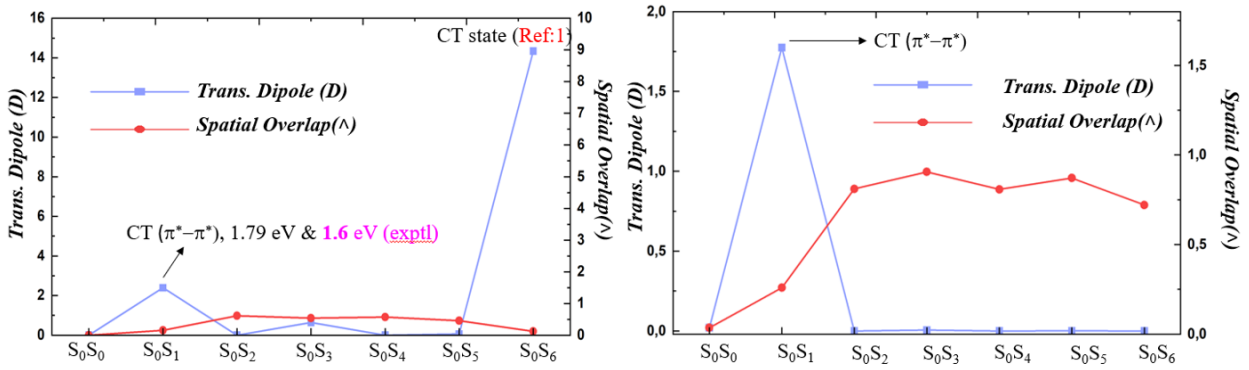

Figure A.14: Computed spatial overlap and transition dipole moment for both materials.

PEN	*ΔE (ev)*	**Orbital contribution**	*f*
S_0 S_0	0.00		
S_0S_1 (CT)	1.79 **(Exp: ~1.6)** [51]	H⟶ L	0.4090
S_0S_2 (LE)	2.95**(Exp:~2.35)** [61]	H-1⟶ L	0.01
S_0S_3 (LE)	3.20	H-2⟶ L	0.00498
S_0S_4 (LE)	3.21	H-1⟶ L	0.00005
S_0S_5 (LE)	3.98	H-3⟶ L	0.002
S_0S_6 (CT)	4.27	H⟶ L+4	1.126

MOF	*ΔE (ev)*	**Orbital contribution**	*f*
S_0 S_0	0.00		
S_0S_1 (CT)	1.83	H⟶ L	0.0839
S_0S_2 (LE)	2.76	H⟶ L+1	0.02
S_0S_3 (LE)	2.78	H⟶ L+2	0.004
S_0S_4 (LE)	2.87	H-1⟶ L	0.001
S_0S_5 (LE)	3.12	H-2⟶ L	0.00
S_0S_6 (LE)	3.16	H-1⟶ L	0.00

Figure A.15: Spectral data for both materials, obtained by TD-B3LYP/def2-TZVP:D3

	V_{HH} (meV)	V_{LL} (meV)	V_{HL} (meV)	V_{LH} (meV
PEN-A	-48	-82	59	59
PEN-B	82	76	-51	-51
PEN-C	-51	76	61	51
MOF-A	89	73	-54	92
MOF-B	-48	-82	59	59
MOF-C	-38	46	-32	89

Figure A.16: Coupling tensors of Fock-matrix elements for PEN and MOF models.

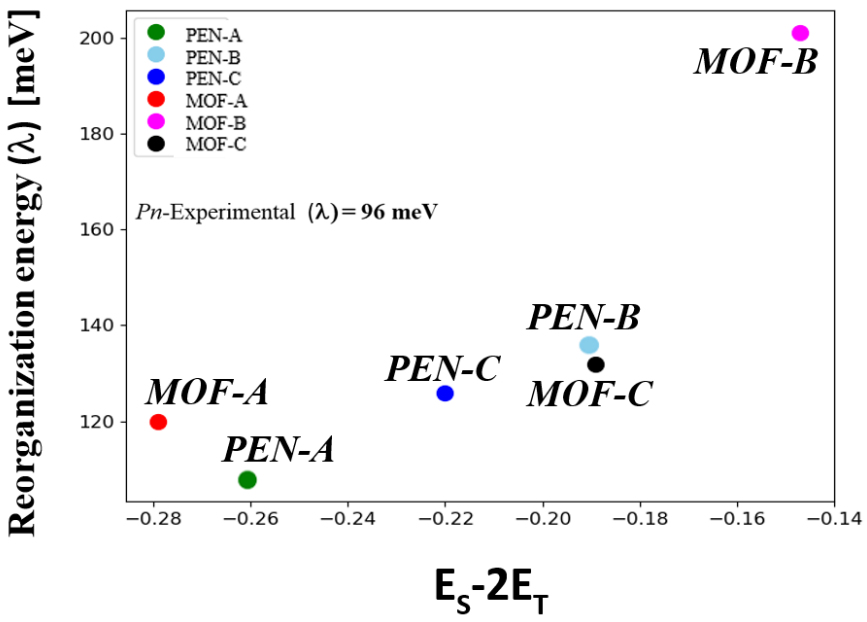

Figure A.17: Calculated ΔG and λ for each molecule, obtained by DFT/def2-TZVP:D3 method.

B Photo-degradation of the PEN SURMOF

The data shown in chapter 5 are obtained with an encapsulated sample. This means that an additional quartz glass covers the thin film. The glass was glued to the sample with a two-component adhesive under nitrogen atmosphere to prevent oxygen from being trapped. PEN is known to be subject to photo-degradation. In particular, the 6 and 13 positions of PEN are prone to oxidise under illumination (especially UV light) and the presence of oxygen [209]. Furthermore, it was found that alkynyl functionalisation at the 6 and 13 positions of PEN to yield 6,13-Bis(triisopropylsilylethynyl)pentacene reduces photo-degradation [210].

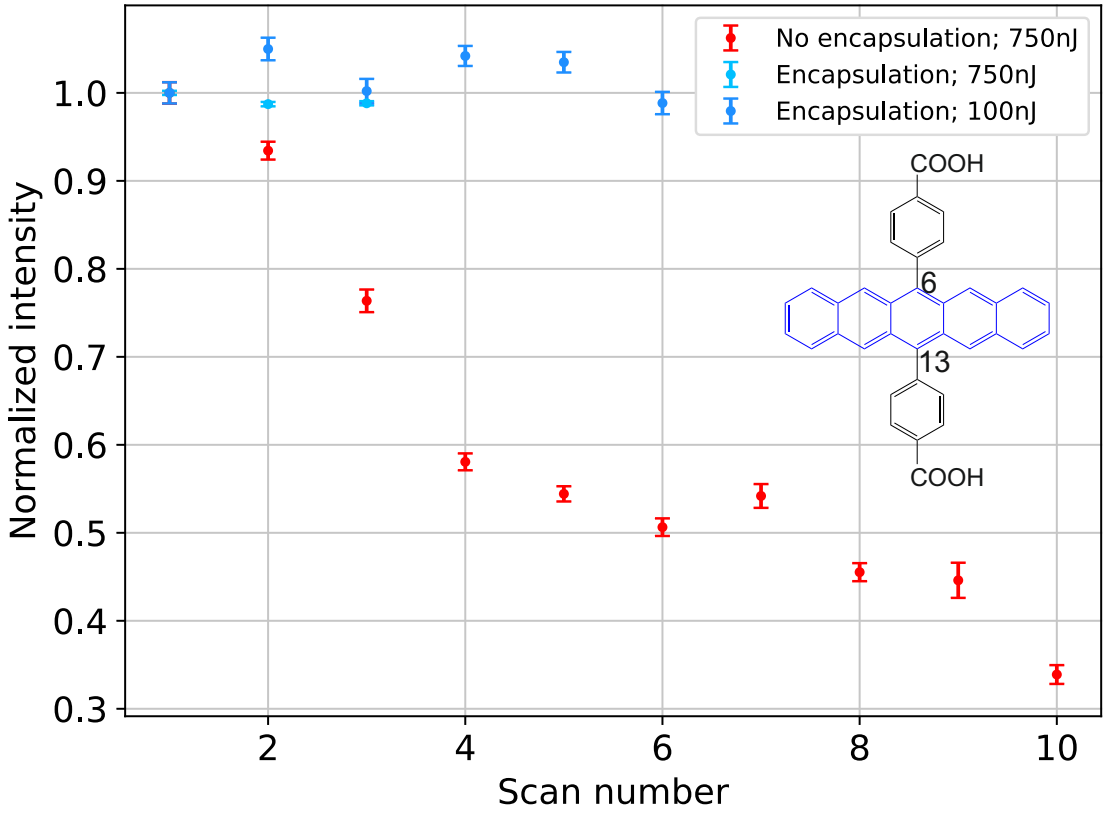

Figure B.1: Test for photo-degradation of PEN SURMOF in TA experiments. The data points shown correspond to the averaged ΔA intensity between $700 < t < 1300$ fs and $520 < \lambda < 530$ nm. The energy per pulse is given in the legend in nJ. The chemical structure of the functionalised PEN linker is shown and the 6 and 13 positions are indicated.

Therefore, the functionalised PEN linker used in the SURMOF (compare Fig.B.1) might exhibit reduced photo-degradation as well. Unfortunately, this was not the case, as can be seen in Fig.B.1. Successive scans (each taking $\sim$ 6-8 min) in TA experiments reveal a drastic loss in signal amplitude. With encapsulation, no degradation is observed.

C SHG setup: beam profiles

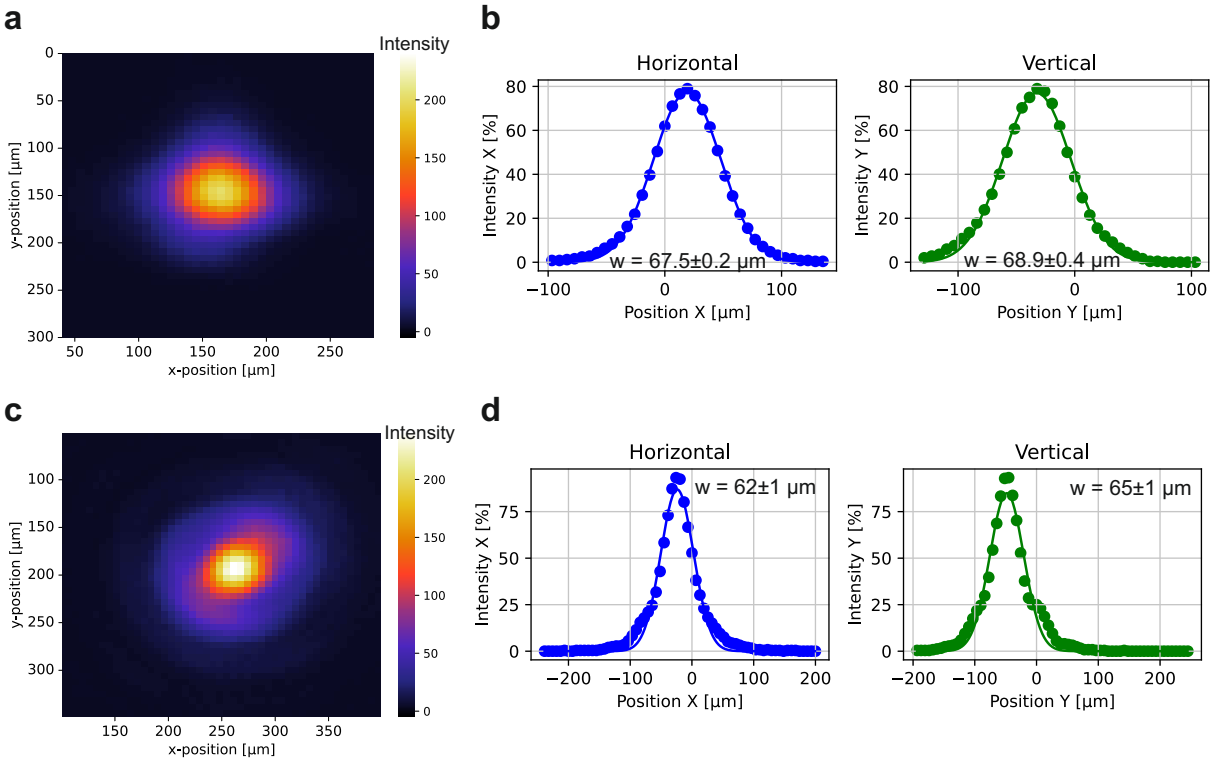

Figure C.1: Beam profiles of **a,c** the probe (centred at 800 nm) and pump (centred at 565 nm) beam with horizontal and vertical cuts through the maximum **b,d** ,respectively. Measured at the position of the sample. The fit uses a Gaussian function with a FWHM denoted as w.

D TA spectra of neat F4-TCNQ/F6-TCNNQ

The neat film of F4-TCNQ excited at $\lambda_{ex} = 400\,\text{nm}$ are shown in Fig.D.1 a). The negative signal corresponds to the GSB of F4-TCNQ. The shift of the GSB and the concomitant rise of the ESA at 560 nm is likely to be associated with the formation of dianions F4-TCNQ$^{\bullet 2-}$ from anions F4-TCNQ$^{\bullet -}$ [211, 212]. F6-TCNNQ was excited at a wavelength of $\lambda_{ex} = 495\,\text{nm}$. The resulting fs-TA data for the VIS and NIR spectral region are shown in D.1 b) and c). The GSB of F6-TCNNQ has a minimum at 595 nm. The peaks at 985 nm and 1146 nm correspond well with the observed absorption of F6-TCNNQ$^{\bullet -}$ [195].

corresponds to ions of

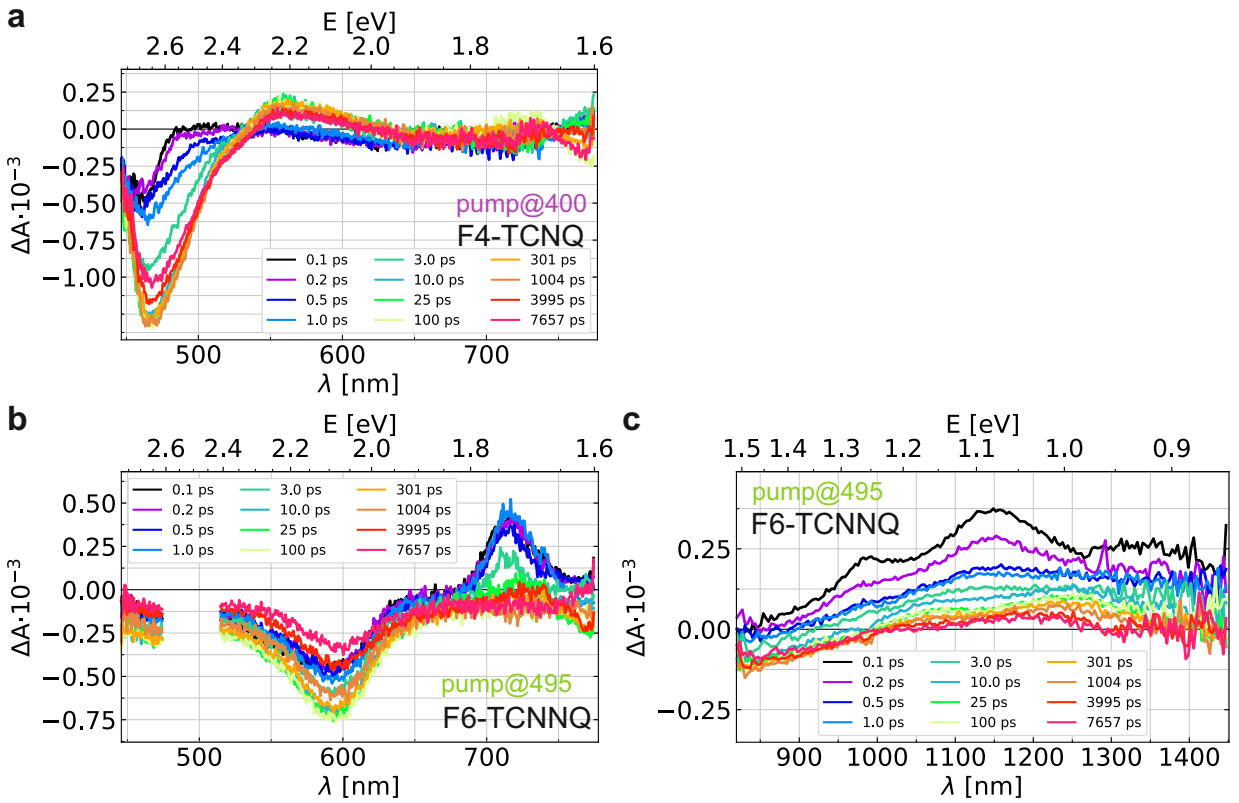

Figure D.1: TA spectra of F4-TCNQ excited at $\lambda_{ex} = 400\,\text{nm}$ in the visible spectral region **a** and TA spectra of F6-TCNNQ excited at $\lambda_{ex} = 495\,\text{nm}$ in the visible and NIR spectral region **b** and **c**, respectively.

E Publications and conference contributions

Publications related to the thesis:

Coexistence of Ion Pairs and Charge-Transfer Complexes and Their Impact on Pentacene Singlet Fission
Christoph P. Theurer, Martin Richter, Debkumar Rana, Giuliano Duva, Daniel Lepple, Alexander Hinderhofer, Frank Schreiber, Petra Tegeder and Katharina Broch
The Journal of Physical Chemistry C

Enhancing singlet fission lifetimes through molecular engineering
Martin Richter, Muhammed Jeneesh Kariyottukuniyil, Zhiyun Xu, Philipp Ludwig, Pavel V. Kolesnichenko, Christian Huck, Uwe Bunz, Christof Wöll, Wolfgang Wenzel and Petra Tegeder
submitted

Charge separation in a porphyrin-based metal organic framework incorporating C_{60} fullerenes
Martin Richter, Xiaojing Liu, Pavel Kolesnichenko, Christof Wöll and Petra Tegeder
in preparation

Charge Transfer and Singlet Fission in Pentacene/Acceptor thin films
Martin Richter, Christoph Theurer, Debkumar Rana, Katharina Broch, and Petra Tegeder
in preparation

Publications not related to the thesis:

Short-range organization and photophysical properties of CdSe quantum dots coupled with aryleneethynylenes
Christoph P Theurer, Antonia Weber, Martin Richter, Markus Bender, Patrick Michel, Debkumar Rana, Krishan Kumar, Uwe Bunz, Marcus Scheele, Petra Tegeder
Nanotechnology - IOPscience

Conference contributions related to the thesis:

Singlet Fission and charge separation in Pentacene/Acceptor thin films
Martin Richter, Christoph P. Theurer, Debkumar Rana, Katharina Broch, Petra Tegeder
Poster
ISPF2 -2022, 3rd International symposium on singlet fission and photon fusion

Charge Transfer and Singlet Fission in Pentacene/Acceptor thin films
Martin Richter, Christoph Theurer, Debkumar Rana, Katharina Broch, and Petra Tegeder
Talk
DPG-Frühjahrstagung der Sektion Kondensierte Materie (SKM) 2022, Regensburg

Singlet fission and triplet dynamics in pentacene embedded in a surface-anchored metal-organic framework
Martin Richter, Zhiyun Xu, Philipp Ludwig, Pavel Kolesnichenko, Uwe Bunz, Christof Wöll and Petra Tegeder
Talk
DPG-Frühjahrstagung der Sektion Kondensierte Materie (SKM) 2023, Dresden

Charge separation in a porphyrin-based metal organic framework incorporating C_{60} fullerenes
Martin Richter, Xiaojing Liu, Pavel Kolesnichenko, Christof Wöll and Petra Tegeder
Talk
87. Jahrestagung der DPG und DPG-Frühjahrstagung der Sektion Kondensierte Materie (SKM) 2024, Berlin

Singlet fission and triplet dynamics in pentacene embedded in a surface-anchored metal-organic framework
Martin Richter, Zhiyun Xu, Philipp Ludwig, Pavel Kolesnichenko, Uwe Bunz, Christof Wöll and Petra Tegeder
Poster
87. Jahrestagung der DPG und DPG-Frühjahrstagung der Sektion Kondensierte Materie (SKM) 2024, Berlin

Acknowledgments

Ich möchte mich an dieser Stelle bei allen bedanken, die mich im Laufe meiner Promotion begleitet und unterstützt haben. Insbesondere danke ich

Prof. Dr. Petra Tegeder für die Möglichkeit, in ihrer Arbeitsgruppe am Physikalisch-Chemischen Institut in Heidelberg zu promovieren, sowie für die ausgezeichnete Betreuung während meiner Promotion. Insbesondere möchte ich mich für die Unterstützung bei der Teilnahme an zahlreichen Konferenzen vielmals bedanken.

Herrn Prof. Dr. Rüdiger Klingeler für die freundliche Übernahme der offiziellen Erstbetreuung und für die Erstellung des Erstgutachtens.

Meinen vielen Kooperationspartnern mit welchen ich im Rahmen dieser Arbeit zusammenarbeiten durfte und ohne jene die Arbeit in der vorliegenden Form nicht möglich gewesen wäre. Insbesondere danke ich: Pavel Kolesnichenko, der mich bei vielen TA Experimenten unterstützt hat, viele Verbesserungen zum Manusskript vorgeschlagen hat und für Diskussionen immer Zeit hatte. Ich danke Christoph P. Theurer für die Bereistellung der Bilagen (PEN/Akzeptor) und zusammen mit Debkumar Rana für eine erste Einweisung in TA Spektroskopie. Zhiyun Xu und Xiaojing Liu danke ich für die Bereitstellung der SURMOFs, die in der Arbeitsgruppe von Prof. Christof Wöll angefertigt wurden. Weiterhin danke Muhammed Jeneesh Kariyottukuniyil für die theoretische Modellierung. Prof. Wolfgang Wenzel danke ich für die Zusammenarbeit und klärenden Diskussion bzgl. des Pentacen SURMOFs. Außerdem möchte ich Philippe Wagner für die Herstellung der Proben der chiralen Käfigverbindungen danken.

Für die Unterstützung bei administrativen Tätigkeiten danke ich Angelika Neuner, Marina Sommer und Anja Ihli. Ich möchte mich auch bei allen Studierenden bedanken, die ich betreuen durfte und die mich im Labor sowie bei der Interpretation der Messungen unterstützt und mit neuen Ideen bereichert haben.

Desweiteren möchte ich meinen langjährigen Kommilitonen Jan Eberhardt und Benjamnin Weinläder für das Gegenlesen einiger Abschnitte danken. Ich möchte mich bei Diren Usta für seine motivierende Unterstützung bedanken.

Ein großes Dankeschön gilt meinen Kolleginnen und Kollegen, die mir tatkräftig geholfen haben und für anregende und ausgiebige Diskussionen immer offen waren: Jakob Roth, Michael Tzschoppe, Jakob Steidel, Vipilan Sivanesan, Gabriel Sauter, Tanja Schmitt, Christian Huck, Nadine von Coelln, Mohsen Ajdari.

Besonders danke ich Vipilan Sivanesan, der mich in den experimentellen Aufbau für NLO eingewiesen hat und mich hilfsbereit unterstützt hat.

Ich danke ganz besonders Charlotte Uhlenbrock für ihre Unterstützung. Nicht zuletzt gebührt meinen Eltern und meinem Bruder für ihre immerwährende Unterstützung ein herzliches Dankeschön.